Microscopy-based High-content Analyses Identify Novel Chromosome Instability Genes including *SKP1*

by

Laura L. Thompson

A Thesis submitted to the Faculty of Graduate Studies of

The University of Manitoba

In partial fulfillment of the requirements of the degree of

Doctor of Philosophy

Department of Biochemistry and Medical Genetics

University of Manitoba

Winnipeg, Manitoba, Canada

ABSTRACT

Cancer is a devastating disease responsible for ~80,000 deaths in Canada each year. Chromosome instability (CIN) is an abnormal phenotype frequently observed in cancer, characterized by an increase in the rate at which chromosomes or chromosomal fragments are gained or lost. CIN underlies the development of aggressive, drug resistant cancers, disease recurrence, and poor prognoses. Despite this, the majority of CIN genes have yet to be elucidated, highlighting the need for studies aimed at identifying the defective genes that underlie CIN.

This thesis describes the development and utilization of imaged-based assays designed to detect CIN phenotypes (*i.e.* nuclear size changes and micronucleus formation) following gene silencing. Mitotic chromosome spread analyses validated that changes in CIN phenotypes corresponded with numerical and structural chromosome defects by silencing the established CIN gene, *SMC1A* (*Chapter 3*). The assays were multiplexed in a high-content, siRNA-based screen of 164 candidate genes in hTERT and HT1080, which identified 148 putative CIN genes. Validation of 10 genes (*e.g. SKP1*) was performed in hTERT and HCT116, which confirmed gene silencing induced chromosome changes (*Chapter 4*). SKP1 is a component of the SKP1-CUL1-F-box protein (SCF) E3 ubiquitin ligase complex, which regulates degradation of numerous proteins within pathways that maintain chromosome stability. Accordingly, the aberrant biology underlying CIN in *SKP1* silenced cells was investigated further using immunofluorescence, microscopy, and biochemical techniques (*Chapter 5*). A high-content screen of all 68 F-box genes was performed to determine which F-box proteins/SCF complexes regulate chromosome stability. *EMI1*, *SKP2*, and *FBXL7* induced CIN phenotypes similar to *SKP1*, suggesting that the corresponding SCF complexes are required for chromosome stability.

Increases in the levels of SCF substrates Survivin and CCNE1, were detected in *SKP1* silenced cells. Replication stress, DNA damage, centromeric protein mislocalization, and centrosome defects were also observed, all of which are mechanisms known to underlie CIN. Significantly, a novel screen for CIN phenotypes was developed and employed in this study, which expedited human CIN gene identification and provided critical insights into the fundamental biological mechanisms that regulate chromosome stability. Importantly, characterizing the aberrant genes/mechanisms that underlie CIN and oncogenesis could ultimately reveal novel cancer therapeutic targets.

ACKNOWLEDGEMENTS

First, I would like to express my sincerest gratitude to my supervisor Dr. Kirk McManus for his time, mentorship, scientific advice, and continuous support throughout my graduate studies. I am extremely fortunate to have had the opportunity to work, learn, and grow in the McManus lab. I would also like to thank my advisory committee; Dr. Mark Nachtigal, Dr. Yvonne Myal, and Dr. Tamra Werbowetski-Ogilvie, for their critical assessments of my research project, challenging questions, valuable input, support, and career advice.

I would like to acknowledge all members of the McManus lab, past and present; Zelda Lichtensztejn, Sajesh Babu, Brent Guppy, Amy Cisyk, Erin McAndrew, Yasamin Asbaghi, Lucile Jeusset, Nicole Wilson, Chloe Lepage, Manisha Bungsy, Claire Morden, and all summer and co-op students that I have had the pleasure of working with. Thank you for your friendship, support, and for making the McManus lab a wonderful place to work. I would especially like to thank Zelda, Sajesh and Brent for training me in the laboratory and providing extensive technical assistance and trouble-shooting advice. I am extremely grateful to Allison Baergen, my summer student of three years, for her hard work and significant contributions to this research project.

This research would not have been possible without the financial support of NSERC, Research Manitoba, University of Manitoba, CancerCare Manitoba, Terry Fox Institute and the Research Institute in Oncology and Hematology. I would also like to thank the donors that provided funding for the Caroline A. Cope Award for Excellence in Oncology Research, Mindel Rady Olenick Fellowship in Human Genetics, Emil & Lynette Hain Oncology Award, Human Genetics Endowment Fund Award, Mindel & Tom Olenick Research Studentship in Medicine, Sheu L. Lee Family Scholarship in Oncology Research, Nancie J. Mauro Scholarship in Oncology Research, and Phyllis J. McAlpine Graduate Fellowship.

I am truly grateful to my family; Dad, Mom, Steve, Debbie, Travis, Janene, Troy, Brianna, Rob, Lucille, Robbie, and Sarah for their encouragement and support in all aspects of my life and studies. Lastly, I would like to extend a special thank you to Mike for his unwavering love, patience, and support. Thank you for always being there for me.

TABLE OF CONTENTS

LIST OF ABBREVIATIONS

%	percentage
~	approximately
<	less than
>	greater than
±	plus or minus
°C	degrees Celsius
µL	microliter(s)
µm	micrometer(s)
µM	micromolar
ρmol	picomolar
βTRCP	Beta-Transducin Repeat Containing E3 Ubiquitin Protein Ligase
γH2AX	gamma-histone variant H2AX (phosphorylated at serine 139)
γTURC	gamma-tubulin ring complex
2D	two-dimensional
3D	three-dimensional
5-FU	5-fluorouracil
6-OAP	6-O-angeloylplenolin
APC	Adenomatous Polyposis Coli
APC/C	Anaphase Promoting Complex/Cyclosome
ARL2	Adenosine Diphosphate (ADP)-Ribosylation Factor-Like 2
ATM	Ataxia Telangiectasia-mutated
ATR	Ataxia Telangiectasia and Rad3-related
ATRIP	ATR Interacting Protein
au	arbitrary units
BAX	BCL2 Associated X, Apoptosis Regulator
BCA	Bicinchoninic Acid
BIRC5	Baculoviral IAP Repeat Containing 5 (Survivin)
bp	base pair(s)
BPNT1	Bisphosphate 3-Nucleotidase 1
BRCA1/2	Breast Cancer 1/2
BSA	bovine serum albumin
BTB/POZ	broad complex, tramtrack and bric à brac/poxviruses and zinc finger
BUB1	Budding Uninhibited By Benzimidazoles 1
BUB3	Budding Uninhibited By Benzimidazoles 3
BUBR1	MAD3/BUB1-Related Protein Kinase
Cas9	CRISPR-associated Protein 9
CATD	centromere targeting domain
CCAN	constitutive centromere-associated network
CCCI-01	5-Nitro-N-(3-pyridinylmethyl)-2-furancarboxamide
CCD	charge-coupled device
CCNE1	Cyclin E1
CCNF	Cyclin F
CCP110	Centriolar Coiled-Coil Protein 110
CDC20	Cell Division Cycle 20
CDC45	Cell Division Cycle 45

CDC6	Cell Division Cycle 6
CDK2	Cyclin Dependent Kinase 2
CDT1	Chromatin Licensing And DNA Replication Factor 1
CENPA	Centromeric Protein A
CETN1	Centrin
CHEK1	Checkpoint Kinase 1
CHEK2	Checkpoint Kinase 2
CIM	cell invasion/migration
CIMP	CpG island methylator phenotype
CIN	chromosome instability
cm	centimeter
CO_2	carbon dioxide
CPTS	copper phthalocyanine 3,4',4'',4'''-tetrasulfonic acid tetrasodium salt
CRC	colorectal cancer
CRISPR	clustered regularly interspaced short palindromic repeat
CT	computerized tomography
C-terminal	carboxy-terminal
CUL1	Cullin 1
CUL7	Cullin 7
CY3	cyanin 3
DAPI	4',6-diamidino-2-phenylindole
DNA	deoxyribonucleic acid
DSB(s)	double strand break(s)
DSN1	DSN1 homolog, MIS12 kinetochore complex component
E1	E1 ubiquitin-activating enzyme
E2	E2 ubiquitin-conjugating enzyme
E3	E3 ubiquitin-protein ligase
ECL	enhanced chemiluminescence
EDTA	ethylenediaminetetraacetic acid
EdU	5-ethynyl-2'-deoxyuridine
EMI1	Early Mitotic Inhibitor 1
EPCAM	Epithelial Cell Adhesion Molecule
ERCC5	Excision Repair Cross-Complementation Group 5
ESCO1/2	Establishment Of Sister Chromatid Cohesion N-Acetyltransferase 1/2
ESPL1	Extra Spindle Pole Bodies Like 1 (Separase)
FANCC	Fanconi Anemia Complementation Group C
FAP	familial adenomatous polyposis
FBS	fetal bovine serum
FC	fold change
FI	fold increase
FISH	fluorescence *in situ* hybridization
FITC	fluorescein isothiocyanate
FOBT	fecal occult blood test
FOLFIRI	folinic acid, 5-fluorouracil and irinotecan
FOLFOX	folinic acid, 5-fluorouracil and oxaliplatin
GAPDH	Glyceraldehyde-3-Phosphate Dehydrogenase

GARS	Glycyl-tRNA Synthetase
GFP	green fluorescent protein
GINS	GINS Complex Subunits 1-4
GPI	glycosylphosphatidylinositol
GTP	guanosine triphosphate
h	hour(s)
HBSS	Hank's balanced salt solution
HCl	hydrochloric acid
HECT	homologous to the E6-AP carboxyl terminus
HJURP	Holliday Junction Recognition Protein
HNPCC	hereditary nonpolyposis colorectal cancer
HRP	horseradish peroxidase
HRR	homologous recombination repair
HSF1	Heat Shock Transcription Factor 1
HSP90B	Heat Shock Protein HSP 90-Beta
hTERT	human telomerase reverse transcriptase
HU	hydroxyurea
IHC	immunohistochemistry
IIF	indirect immunofluorescence
INCENP	Inner Centromere Protein
ITH	intratumoral heterogeneity
KCl	potassium chloride
kDa	kilodalton(s)
KIF11	Kinesin Family Member 11
KMN	KNL1-MIS12-NDC80
KNL1	Kinetochore Scaffold 1
KO	knockout
KS	Kolmogorov-Smirnov
MAD1	Mitotic Arrest Deficient Like 1
MAD2	Mitotic Arrest Deficient 2 Like 1
MAT	mating type
MAU2	MAU2 Sister Chromatid Cohesion Factor
MCM10	Minichromosome Maintenance Complex Component 10
MCM2-7	Minichromosome Maintenance Complex Component 2-7
MCM5	Minichromosome Maintenance Complex Component 5
METAP2	Methionyl Aminopeptidase 2
min	minute(s)
MIS12	MIS12 Kinetochore Complex Component
MIS18	MIS18 Kinetochore Protein A
mL	milliliter(s)
MLH1	MutL Homolog 1
mM	millimolar
MN	micronucleus
MNi	micronuclei
MPS1	Monopolar Spindle 1
MRE11A	Meiotic Recombination 11 Homolog A

MRN	MRE11-RAD50-NBS1
mRNA	messenger RNA
MSH2	MutS Homolog 2
MSH3	MutS Homolog 3
MSH6	MutS Homolog 6
MSI	microsatellite instability
MYC	MYC Proto-Oncogene, BHLH Transcription Factor
NA	nuclear area
NBS1	Nijmegen Breakage Syndrome 1 (Nibrin)
NDC80	Nuclear Division Cycle 80
ng	nanogram(s)
NHEJ	non-homologous end-joining
NIPBL	NIPBL (Nipped-B-Like Protein) Cohesin Loading Factor
nm	nanometer(s)
nM	nanomolar
NOD/SCID	non-obese diabetic/severe combined immunodeficient
NUF2	NUF2 NDC80 Kinetochore Complex Component
ODF2/1	Outer Dense Fiber Of Sperm Tails 2 (Cenexin 1)
ORC1-6	Origin Recognition Complex Subunit 1-6
PAGE	polyacrylamide gel electrophoresis
PARP	poly(ADP-ribose) polymerase
PBS	phosphate buffered saline
PCM	pericentriolar material
PCNT	Pericentrin
PDS5	PDS5 Cohesin Associated Factor
PHD	plant-homeo-domain
PI3K	Phosphatidylinositol-3-Kinase
PIGS	phosphatidylinositol glycan anchor biosynthesis class S
PLC1	Phospholipase C Gamma 1
PLK1	Polo Like Kinase 1
PLK4	Polo Like Kinase 4
PMS2	PMS1 Homolog 2, Mismatch Repair System Component
PP2A	Protein Phosphatase 2 Phosphatase Activator
pre-RC	pre-replicative complex
PROTACs	proteolysis targeting chimeras
PSMA4	Proteasome Subunit Alpha 4
PSMA6	Proteasome Subunit Alpha 6
PSMD12	Proteasome 26S Subunit, Non-ATPase 12
PSMD4	Proteasome 26S Subunit, Non-ATPase 4
PTTG1	Pituitary Tumor-Transforming 1
PVDF	polyvinylidene difluoride
RAD17	RAD17 Checkpoint Clamp Loader Component
RAD21	RAD21 Cohesin Complex Component
RAD50	RAD50 Double Strand Break Repair Protein
RAD51	RAD51 Recombinase
RAD54B	RAD54 Homolog B

RAS	Ras Proto-Oncogene, GTPase
RBX1	Ring-Box1
RECQL4	RecQ Like Helicase 4
RING	Really Interesting New Gene
RIPA	radioimmunoprecipitation assay
RNA	ribonucleic acid
RNAi	ribonucleic acid interference
RPA	replication protein A
RT	room temperature
RTCA	real-time cellular analysis
S15	serine 15
SAC	spindle assembly checkpoint
SCF	SKP1-CUL1-F-box Protein
SD	standard deviation
SDS	sodium dodecyl sulfate
SGO1	Shugoshin 1
SHMT2	Serine Hydroxymethyltransferase 2
shRNA	short hairpin ribonucleic acid
siRNA	short interfering ribonucleic acid
SKP1	S-phase Kinase Associated Protein 1
SKP2	S-Phase Kinase Associated Protein 2
SL	synthetic lethal
SMC1A	Structural Maintenance Of Chromosomes 1A
SMC2	Structural Maintenance Of Chromosomes 2
SMC3	Structural Maintenance Of Chromosomes 3
SPC24	Spindle Pole Body Component 24 Homolog
SSB	single strand breaks
ssDNA	single stranded deoxyribonucleic acid
STAG1/2	Stromal Antigen 1/2
TBS	tris buffered saline
TBST	tris buffered saline with tween-20
TCGA	The Cancer Genome Atlas
TGFBR2	Transforming Growth Factor Beta Receptor 2
TIFF	tagged image format
TNM	tumor size, lymph node involvement, and metastasis
TOPBP1	DNA Topoisomerase II Binding Protein 1
TP53	Tumor Protein P53
tRNA	transfer ribonucleic acid
UICC	Union Internationale Contre le Cancer
UPS	ubiquitin-proteasome system
V	volts
vs.	versus
W	watts
WAPL	WAPL (Wings Apart-Like Homolog) Cohesin Release Factor
WGA	wheat germ agglutinin
WRN	Werner Syndrome

LIST OF TABLES

LIST OF FIGURES

USED WITH PERMISSION and CONTRIBUTION OF AUTHOR

PREFACE:

This thesis contains data, material, and/or ideas published in two peer-reviewed journals, of which Laura Thompson was first author. Each journal applies the Creative Commons Attribution (CC BY) license to articles and other works, such that articles can be reused in whole or in part for any purpose.

CONTRIBUTION OF AUTHOR

CHAPTER 3:

Thompson, L.L., and McManus, K.J. A Novel Multiplexed, Image-based Approach to Detect Phenotypes that Underlie Chromosome Instability in Human Cells. *PLOS ONE.* April 2015. Impact Factor 2.806.

Contribution: Laura Thompson performed experiments, analyzed data, created figures and tables, and wrote first draft of manuscript.

CHAPTER 6:

Thompson, L.L., Jeusset, L.M-P., Lepage C.C., and McManus, K.J. Evolving Therapeutic Strategies to Exploit Chromosome Instability in Cancer. *Cancers.* November 2017. Impact Factor 4.64.

Contribution: Laura Thompson wrote the first draft and edited the manuscript.

RESEARCH RATIONALE AND HYPOTHESES

Rationale

Chromosome instability (CIN) (*i.e.* increases in the gain or loss of chromosomes or chromosome fragments [*see Section 1.2.2*]) is a characteristic of virtually all cancer types, including colorectal cancer (CRC)[1], and drives cancer progression, tumor evolution, the acquisition of drug resistance, and poor patient outcomes[2-4]. Developing a better understanding of the aberrant molecular mechanisms that drive CIN and oncogenesis is critical for the development of new therapeutic strategies designed to exploit those aberrations and better treat highly-aggressive, chromosomally unstable cancers. As proper transmission of chromosomes to daughter cells is essential for organism survival, many genes (*i.e.* CIN genes) and molecular mechanisms that normally function to maintain chromosome stability are evolutionarily conserved. Thus, the human orthologs of previously established budding yeast CIN genes represent potential human CIN gene candidates. As detailed in the following chapters, nuclear size (*i.e.* volumes or areas) changes and micronucleus (MN) increases (*i.e.* small extra-nuclear bodies containing chromosomes or chromosome fragments) are indicative of the large and small-scale chromosomal changes characteristic of CIN, and can provide valuable prognostic and diagnostic insights in cancer. Accordingly, assessing human candidate CIN genes identified by cross-species approaches in a high-content screen for changes in nuclear area (NA) and MN formation following gene silencing represents a promising strategy that will facilitate human CIN gene identification and expedite the characterization of genes that contribute to CIN and cancer.

Hypotheses

The hypothesis of this thesis is that a high-content screen assessing NA and MN changes following candidate gene silencing will allow for rapid identification of putative human CIN genes. Further, the validation and characterization of a subset of these genes will provide novel insights into the fundamental biology and altered mechanisms implicated in CIN and oncogenesis.

Research Aims

The following three critical research aims were generated to test these hypotheses and are addressed in Chapters 3-5 (Results):

AIM 1: To establish assays capable of detecting CIN phenotypes including nuclear size and MN changes that are amenable to a high-content screen (*Chapter 3*).

AIM 2: To execute a high-content screen of human candidate CIN genes selected through cross-species approaches, using the assays developed in *Aim 1*, to identify and validate a subset of novel human CIN genes (*Chapter 4*).

AIM 3: To characterize the aberrant mechanisms that drive CIN in cells with diminished expression of S*KP1,* a CIN gene identified by the high-content screen and validated in *Aim 2* (*Chapter 5*).

Significance

The identification and characterization of novel human CIN genes will provide critical insights into fundamental biology and the aberrant mechanisms underlying CIN and oncogenesis. A list of validated human CIN genes represents a valuable research resource that can be utilized in subsequent translational studies (*i.e.* "bench to bedside") to develop novel cancer therapies that selectively exploit CIN.

CHAPTER 1: INTRODUCTION

1.0.0. Cancer Burden

1.0.1. The Global and National Impact of Cancer

According to the International Agency for Research on Cancer[5], there are more than 14 million new cancer diagnoses and over 8 million deaths attributed to this disease each year. In fact, 1 out of every 7 deaths worldwide is due to cancer, which is equivalent to ~22,000 cancer-associated deaths each day. Approximately 35% and 65% of cancer-related deaths occur in high-income and economically developing countries, respectively[5,6]. In economically developed countries like Canada or the United States, the most frequently diagnosed cancers and the greatest contributors to cancer-related deaths are prostate, lung, and colorectal in males, and breast, colorectal, and lung in females[5]. In economically transitioning countries where lifestyles are shifting towards those of high-income countries with greater exposure to cancer risk factors (*e.g.* smoking, poor diet, sedentary lifestyle and excess body weight) cancers such as lung, breast, and colorectal are increasing, and are expected to continue on this trend[6]. As a consequence of the growing and aging population, global cancer incidence and mortality rates are projected to increase to 22 million diagnoses and 13 million deaths annually by the year 2030[5,6].

Cancer is the leading cause of death in Canada, responsible for ~30% of all deaths[7]. While ~50% of all Canadians develop cancer in their lifetime, ~25% will inevitably succumb to the disease. These numbers translate to more than 200,000 cancer diagnoses and 80,000 cancer-related deaths among Canadians each year[7]. Lung, breast, colorectal and prostate cancer alone, constitute ~50% of all new diagnoses and are responsible for ~50% of all cancer-associated deaths in both sexes combined. In 2012, cancer was the leading cause of disease-associated death

in children younger than 15, and represents the primary cause of premature mortality based on potential years of life lost[7]. Although cancer significantly impacts the lives of younger individuals, cancer is typically considered a disease of the elderly, as ~90% of Canadian cancer patients are older than 50 years of age[7]. With Canada's growing and aging population, the average number of Canadians older than 65 years of age, is expected to increase more than 220% from 4.2 million (2003-2007) to 9.4 million (2028-2032)[7]. Accordingly, similar to the global trends described above, the average number of annual Canadian cancer diagnoses in 2028-2032 is projected to increase 84% for males and 74% for females relative to the 2003-2007 rates[8]. It is apparent from the above statistics that cancer represents a significant national and global health issue. Thus, research that seeks to better understand the molecular pathogenesis of cancer is critical to develop novel cancer therapies with enhanced specificity and efficacy, to achieve the ultimate goal of diminishing cancer morbidity/mortality rates in Canada and throughout the world.

1.0.2. Colorectal Cancer Burden

Worldwide, colorectal cancer (CRC) accounts for 9% of all cancer diagnoses, with ~1.4 million new cases in 2012[5]. CRC represents the second and third most commonly diagnosed cancer type in men and women, respectively[5,9]. With ~700,000 deaths globally each year, CRC contributes to 8% of all cancer deaths, ranking fourth in men and third in women[5,9]. Approximately 55% of all CRC cases occur in economically developed countries, with North American countries amongst those with the highest incidence rates[9]. Overall, morbidity and mortality rates associated with CRC are expected to increase with the growing and aging population. Additionally, the transition of economically developing countries and other countries

with historically low CRC rates (*e.g.* Japan)[6,9] to Westernized lifestyles with increased CRC risk factor exposures (*listed in Section 1.1.2*), will further increase the global CRC burden.

According to the 2017 Canadian Cancer Society Statistics[7], CRC is the second most prevalent cancer in Canada, comprising ~13% of all diagnoses. A total of 27,000 new CRC cases were estimated for 2017 alone[7]. It is predicted that 1 in 13 Canadian males and 1 in 16 females will be diagnosed with CRC in their lifetime[7]. Furthermore, CRC is the second leading cause of cancer-associated mortality in males and third in females, accounting for 12% of all cancer deaths. Overall, Canadian males and females have a 1 in 29 and 1 in 34 chance of dying from CRC, respectively[7]. Thus, identifying and characterizing the pathogenic mechanisms underlying CRC is a critical step towards the development of new treatment strategies with the potential to improve outcomes for a large proportion of cancer patients.

1.1.0. Overview of Colorectal Cancer

1.1.1. Clinical Features

CRC can originate anywhere within the proximal colon (cecum, ascending or transverse colon), distal colon (descending or sigmoid colon), or rectum[10]. Individuals may inherit genetic alterations and predisposition syndromes conferring an increased risk for CRC development (~20-30% CRC cases), while others develop CRC sporadically through somatically acquired alterations (~70-80% CRC cases)[11]. The majority of CRCs are classified as adenocarcinomas[12] and the classic Fearon and Vogelstein 'adenoma to carcinoma sequence' describes the step-wise progression from normal, to dysplastic colonic epithelial cells, to adenomatous polyp, and ultimately to adenocarcinoma[13]. Although initially only conventional tubular adenomatous polyps were proposed to harbor malignant potential, additional morphological lesion types

including serrated polyps have been identified as precursor lesions, which progress through an alternative pathway of hyperplastic polyps, to serrated neoplasms, to CRC[14,15]. CRC is now recognized as a complex, heterogeneous disease that develops from a lesion, or polyp, typically over the course of a decade[12] through a variety of distinct molecular pathways (*see Section 1.2.0*). Thus, our understanding of CRC pathogenesis has since evolved beyond the original adenoma to carcinoma model[13]. Interestingly, as proximal and distal regions of the colon differ with respect to embryologic origin, microenvironment, morphology, physiology, and function, the etiologic origins and molecular pathogenesis of proximal and distal CRC are often distinct (*see Section 1.2.0*)[16,17].

1.1.2. Risk Factors and Screening

There are a number of risk factors associated with CRC including increased age, family history, inflammatory bowel disease (*e.g.* Crohn's Disease), obesity, diabetes, physical inactivity, smoking, and consumption of alcohol, refined sugars, or red and processed meat[18]. For CRC screening purposes, the population is divided into individuals with average, or increased CRC risk. Individuals considered at increased risk for CRC are those with a family history of CRC including one or more first-degree relatives with CRC, but who do not meet the criteria for hereditary CRC syndromes, which require distinct screening protocols (s*ee Section 1.1.3*). The Canadian Task Force on Preventive Health Care recommends that asymptomatic adults aged 50-74 years who are at average risk for CRC should be screened via the fecal occult blood test (FOBT) every 2 years or by flexible sigmoidoscopy every 10 years[19]. An FOBT test uses a guaiac-based chemical reaction or an antibody-based immunoassay to detect hemoglobin in the feces[20], which can arise from bleeding due to CRC or polyps larger than 1 cm in size[21]. An abnormal FOBT or sigmoidoscopy should be followed up within 8 weeks by colonoscopy[22,23].

Conversely, for asymptomatic individuals with an increased CRC risk, screening by colonoscopy should be initiated at the earlier of age 50, or 10 years prior to the age their relative was diagnosed. Following a normal colonoscopy result (*i.e.* no polyps or adenomas), individuals at increased risk should be re-screened every 5 years if their first degree relative was diagnosed prior to age 60, and every 10 years if diagnosis was at age 60 or older[24,25].

As of 2017, all 10 Canadian provinces have implemented, or are in the process of implementing standardized CRC screening programs. However, participation rates vary between existing organized programs, and none meet the target of 60% compliance[7]. This may contribute to the fact that even with the current CRC screening approaches, more than 50% of new diagnoses occur in patients with late stage disease (III or IV)[26], with ~20% presenting with distant metastases at the time of diagnosis[27]. Unfortunately, ~50% of patients initially diagnosed with early stage CRC (I or II), inevitably progress to metastatic disease[28]. The 5 year relative survival rate for patients with metastatic disease is only 6-13% compared to 70-90% for those with early stage CRC[29,30]. Thus, novel CRC treatments targeting both primary and metastatic disease are required.

1.1.3. Diagnosis and Staging

Colonoscopy is considered the gold standard for detection of colonic lesions or polyps and for CRC diagnosis[31]. A lesion is a region of atypical cellular growth that may be benign or cancerous, including hyperplastic precursor lesions, classical tubular-shaped polyps, and non-classical polyp types including sessile serrated polyps. If lesions or polyps are detected during a colonoscopy, endoscopic or surgical resection (polypectomy) is performed for treatment and diagnostic evaluation[32]. The resected specimen is assessed by histopathological examination for diagnosis and to determine whether further colonic resection or treatment is required. With

successful polypectomy, the patient is recommended to undergo routine surveillance colonoscopy after 3-5 years, according to size, number, and histological results of the polyps[33]. If a hereditary cancer predisposition syndrome is suspected, individuals diagnosed with CRC are referred for follow-up, genetic testing for germline mutations that will allow for a definitive diagnosis. For familial adenomatous polyposis (FAP) patients (*see Section 1.2.0*) that typically develop hundreds of colonic polyps, a total colectomy is the standard of care[34].

CRC staging at diagnosis is critical to determine prognosis and appropriate treatment strategies. Staging is based on the TNM classification system, where tumor size (T), lymph node involvement (N), and metastasis (M) are evaluated to assess local tumor invasion, progression, and the presence of local or distant metastasis[35]. These parameters are assessed and combined to give an overall Union Internationale Contre le Cancer (UICC) stage definition of CRC Stage 0 – IV[33,35]. Generally, Stage 0 is carcinoma *in situ* where cancer cells are restricted to the innermost lining of the colon or rectum. Stage I and II are considered early disease and are characterized by local tumor growth through the mucosa with invasion into (Stage I) or beyond (Stage II) the colonic muscular layer, without evidence for lymph node involvement or metastases. Lymph node involvement without metastases is indicative of Stage III, while Stage IV CRC has progressed not only to lymph nodes but metastasized to distant organs such as the liver or lungs[33]. Additional examinations including abdominal ultrasound, chest X-ray, and abdominal, pelvic, or thoracic computerized tomography (CT) scans are commonly employed for patients with Stage II – IV CRC to establish the extent of the disease and the presence/location of metastases[24,25,18].

1.1.4. Current Standard of Care

Treatment for Stage 0 – I CRC patients is often curative and involves surgical resection of the lesion or tumor. Stages II – IV are often treated with surgical resection of the primary tumor and metastases when possible, along with adjuvant chemotherapy[18,36]. Currently, the standard of care for CRC employs combinatorial chemotherapeutic regimens, administering conventional cytotoxic chemotherapies with molecularly targeted biologic agents. The standard cytotoxic regimens include FOLFOX, consisting of folinic acid, the anti-metabolite nucleoside analog fluoropyrimidine 5-fluorouracil (5-FU), and the platinum compound oxaliplatin, as well as FOLFIRI, comprised of folinic acid, 5-FU, and the topoisomerase inhibitor, irinotecan[18]. FOLFOX and FOLFIRI are considered the mainstays of CRC treatment to which molecularly targeted agents including inhibitors of vascular endothelial growth factor (*e.g.* Bevacizumab), epidermal growth factor receptor (*e.g.* Cetuximab) or intracellular kinases (*e.g.* Regorafenib) can be added, typically improving efficacy, response rates, and patient survival[37]. Despite the significant advances in CRC therapy, a large proportion of patients (~90% of those with metastatic disease) develop multi-drug resistance, progress to more advanced disease and/or relapse following an initial therapeutic response[38-40]. As such, a comprehensive understanding of the mechanisms underlying the acquisition of drug resistance in CRC is required, such that treatment approaches can be devised that will mitigate the potential for drug resistance.

1.2.0. Molecular Pathogenesis of Colorectal Cancer

The etiological factors and molecular pathogenic mechanisms underlying CRC are heterogeneous and differ according to precursor lesion, proximal versus distal position, inherited versus sporadic disease, and molecular subtype as discussed below. CRC can be divided into

familial disease, associated with hereditary predisposition syndromes, or sporadic (somatically acquired) CRC. The familial genetic aberrations that underlie ~10% of CRCs are well established[11,41], and the list of genes and inherited syndromes that predispose to CRC continues to increase[42]. The two most common hereditary syndromes that predispose individuals to CRC are hereditary nonpolyposis colorectal cancer (HNPCC, also known as Lynch syndrome) and FAP[41], which account for 2-5% and < 1% of all CRC cases, respectively[11]. HNPCC is characterized by germline mutations in genes that mediate DNA mismatch repair including *MLH1* (50% of cases), *MSH2* (40%), *MSH6* (7-10%), *PMS2* (< 5%), and *EPCAM* (1-3%)[30,43,44], which confer a lifetime CRC risk of 52-82%[33]. FAP patients harbour germline mutations in the cell signalling gene Adenomatous Polyposis Coli (*APC*), and ~95% exhibit colonic adenomas by age 35 that will inevitably progress to CRC without colectomy[33]. Both are considered autosomal dominant cancer predisposition diseases, where oncogenesis is initiated upon somatic alteration of the second wild-type allele. Conversely, sporadic or randomly occurring disease accounts for ~85% of all CRCs, and arises from multiple somatically acquired genomic alterations, often within the same molecular pathways that drive HNPCC and FAP (*see Section 1.2.1).* For example, the adenoma to carcinoma model[13] describes the acquisition and clonal amplification of genomic alterations that favour oncogenesis through activation of proto-oncogenes like *RAS*, inhibition of tumor suppressor genes such as *APC* and *TP53*, aberrant methylation of DNA, and promotion of invasion into the extracellular matrix[45]. Genome instability underlies these changes and is a defining feature of both familial and sporadic CRC as described below[46].

1.2.1. Genome Instability in Colorectal Cancer

Genome instability is an abnormal state characterized by the high prevalence of genomic alterations, including mutations in nucleic acid sequence, aberrant chromatin modifications,

chromosome rearrangements, or aneuploidy[47]. As these genomic changes drive the acquisition of the classical cancer hallmarks, genome instability is considered an enabling feature of cancer[48]. As such, genome instability is associated with virtually all cancer types, and is arguably best described in CRC where it differentiates normal from neoplastic colonic epithelium. Genome instability can arise through aberrations in different molecular pathways[46] including microsatellite instability (MSI), CpG island methylator phenotype (CIMP), or chromosome instability (CIN), the primary focus of this thesis (*see Section 1.2.2*).

MSI results from defects in DNA mismatch repair proteins (*e.g.* MLH1, *see Section 1.2.0*), which normally function to identify, excise, and repair misincorporated deoxyribonucleotides and slippage errors that occur during DNA replication[49]. DNA mismatch repair dysfunction is observed in ~15% of sporadic CRCs and results in genetic hypermutability of microsatellite regions (*i.e.* repetitive sequences of 1-6 base pairs (bp) dispersed throughout the genome[50]) or base mismatches that occur during DNA replication or repair. DNA mismatch repair defects result in the accumulation of insertions and deletions in microsatellites, and can generate coding sequence alterations or frameshift mutations resulting in truncated or aberrant protein products. Alterations derived from MSI involving tumor suppressor or oncogenes (*e.g. TGFBR2* and *BAX*) drive oncogenesis[51]. MSI is considered a positive prognostic marker associated with less aggressive tumors and improved patient outcomes, as well as 5-FU-based adjuvant chemotherapy resistance, which should be avoided in treatment of these patients[52]. While germline mutations in DNA mismatch repair deficiencies are associated with the development of HNPCC as described above, sporadic MSI CRCs most often result from transcriptional silencing of *MLH1* via promotor methylation[49].

Although altered DNA methylation is present in virtually all CRCs, ~10-20% exhibit extensive hypermethylation of CpG island loci (*i.e.* CIMP). DNA methyltransferases mediate the addition of methyl group to the 5C position of cytosine nucleotides, which recruits histone deacetylases and chromatin remodelling complexes that promote DNA/chromatin compaction. As DNA sequences consisting of CpG nucleotide repeats are frequently located in the 5' promoter regions of human genes, hypermethylation of these islands can induce transcriptional silencing. Although the aberrant mechanisms underlying CIMP are not clearly delineated, hypermethylation can transcriptionally silence tumor suppressor genes, and contribute to oncogenesis. As CpG promoter hypermethylation can induce transcriptional silencing of the DNA mismatch repair genes, ~50% of CIMP-positive CRCs exhibit both MSI and CIMP[53]. Interestingly, proximal CRCs more frequently exhibit MSI and CIMP than distal CRCs, which often arise from polyposis-associated alterations and frequently exhibit CIN[17]. As mentioned previously (*Section 1.1.1*), this may be related to inherent biological differences between the proximal and distal colon (*e.g.* distinct embryologic origins derived from midgut and hindgut, respectively) in combination with different environmental exposures (*e.g.* bowel contents and microbiota) that predispose different colonic regions to different CRC subtypes.

1.2.2. Chromosome Instability

CIN is the predominant form of genomic instability, defined as an increase in the rate at which whole chromosomes (numerical CIN) or chromosomal fragments (structural CIN) are gained or lost, and typically results in aneuploidy or abnormal DNA content[54,55]. CIN is a characteristic of virtually all cancer types including both hematologic and solid cancers (*e.g.* ~85% of all CRC cases)[1,54]. Conceptually, numerical CIN underlies aneuploidy and leads to gene copy number alterations for contiguous gene sets, while structural CIN can induce specific gene

amplifications, deletions or translocations[55]. CIN collectively promotes oncogenesis by increasing the rate at which proto-oncogenes, tumor suppressors, DNA repair, apoptotic and other genes associated with oncogenesis, metastasis and drug resistance, are gained, lost, or altered[56]. As such, CIN-positive tumors (*i.e.* those acquiring chromosomal changes at an increased rate) often harbor extensive chromosomal intratumoral heterogeneity (ITH)[57]. Thus, cells harboring alterations that promote tumor growth, metastasis, cell survival, and drug resistance (*e.g.* inhibit drug uptake, drive drug efflux, inactivate/metabolize the drug, or alter cell signalling to mitigate the effects of the drug[57]) are more likely to be present/acquired within CIN-positive tumors[4].

Overall, CIN is considered an early event in oncogenesis, and is associated with cellular transformation[2,58], ITH[59], cancer progression to metastasis[3], multi-drug resistance[4,60], tumor recurrence[4,60] and poor patient prognosis[4,61]. Despite these many associations, the aberrant genes that underlie the CIN phenotype in human cells (*i.e.* CIN genes) remain largely unknown[47]. Accordingly, it is essential that novel CIN genes are identified and characterized in order to gain a greater understanding of the normal biological pathways that mediate and maintain chromosome stability. Furthermore, characterizing the altered genes and molecular mechanisms that drive CIN and oncogenesis is critical as it may identify new cancer prognostic or diagnostic markers, or reveal novel therapeutic targets that could be exploited in precision medicine approaches. In principle, therapies that selectively exploit the aberrant genes or pathways leading to CIN would be effective in a myriad of cancers (at both primary and metastatic sites) and could potentially reduce and/or eliminate many of the off-target toxicities associated with current chemotherapeutics. Unfortunately, traditional cytogenetic methods (*e.g.* mitotic chromosome spread analyses) used to identify human CIN genes are time consuming and unsuitable for

assessing large gene sets[62-64], and thus, novel approaches to rapidly identify and characterize novel CIN genes are needed.

1.3.0. Chromosome Instability in Yeast and Cross-Species Approaches

As CIN genes mediate balanced transmission of chromosomes to daughter cells, which is critical for chromosome stability and organism survival, CIN genes are often conserved throughout evolution[65]. Thus, studies in model organisms such as budding yeast (*Saccharomyces cerevisiae*) provide important insights into the genes and molecular mechanisms that contribute to CIN in humans. In the past, complementary screening assays have been employed to identify CIN genes in yeast and include the chromosome transmission fidelity, bi-mater, A-like faker, and gross chromosomal rearrangement assays[66]. Briefly, the chromosome transmission fidelity assay monitors the loss of a non-essential chromosome fragment and detects whole chromosome instability when a gene of interest is knocked-out. Bi-mater and A-like faker assays monitor changes to the mating type (MAT) locus, based on mating capacity in candidate CIN gene knockout (KO) mutants and determines whether the knocked-out gene induces whole chromosome loss, gene conversion, or chromosomal rearrangements. The gross chromosomal rearrangement assay detects terminal chromosomal deletions and chromosome rearrangements as a result of candidate CIN gene KO, based on acquired resistance to counter-selection drugs[66]. Employing these CIN assays in combination with techniques designed to evaluate both essential and non-essential genes, has enabled assessment of virtually all yeast genes.

In 2011, Stirling *et al*[65] generated a comprehensive list of 692 budding yeast CIN genes. Overall, similar absolute numbers of essential and non-essential yeast CIN genes were identified, with proportionally more essential (323/1,156; 28%) than non-essential genes (369/4,800; 7.7%)

uncovered[65]. The diversity of CIN genes identified suggests that a myriad of biological pathways are necessary to maintain chromosome stability under normal conditions. Approximately 40% of yeast CIN genes function in predictable biological pathways (described below), including mitosis, DNA replication and DNA repair. The remaining 60% of yeast CIN genes encode functions in biological pathways with less established connections to CIN, such as proteasomal degradation, RNA processing, glycosylphosphatidylinositol (GPI)-anchor or tRNA synthesis[65]. Overall, 11.5% the ~6,000 total *S. cerevisiae* genes (692/6,000) were identified as CIN genes. If these values are extrapolated to humans (~20,000 total genes), it is estimated that ~2,300 CIN genes (11.5%) may exist within the human genome; however, only a small proportion have been identified and characterized to date[2]. Accordingly, the 692 CIN genes identified in yeast serve as a valuable cross-species resource that can be exploited to aid in the identification of conserved human orthologs that may be implicated in CIN and oncogenesis.

1.4.0. Biological Pathways that Maintain Chromosome Stability

Studies from yeast have provided valuable insights into the altered genes and cellular pathways that may contribute to CIN in humans. Although the majority of human CIN genes remain unknown, numerical and/or structural chromosome alterations associated with CIN often occur as a result of defects in intuitive biological pathways that include sister chromatid cohesion defects (*see Section 1.4.1*), mitotic spindle assembly (*e.g.* kinetochore-microtubule attachment and centrosome dynamics) (*Sections 1.4.2-4*), DNA replication (*Section 1.4.5*) and DNA damage repair (*Section 1.4.6*)[67,68]. As revealed in yeast, less intuitive pathways (*see Section 1.4.7*), such as proteasomal degradation, may also induce CIN in human cells. A brief description of these pathways and their roles in chromosome stability is detailed below.

1.4.1. Sister Chromatid Cohesion

Sister chromatid cohesion is a cellular mechanism mediated by Cohesin that is necessary for proper chromosome congression during metaphase and accurate segregation during anaphase (reviewed in Losada[69]). Cohesin is a ring-shaped complex consisting of four core subunits, SMC1A, SMC3, RAD21, and STAG1/2, that encircles sister chromatids following DNA replication to maintain cohesion[69] (Figure 1-1). Cohesin prevents sister chromatid entanglement and premature chromatid segregation, thereby maintaining chromosome stability[70]. A number of accessory proteins regulate Cohesin loading, establishment, maintenance, and dissolution (reviewed in Mirkovic and Oliveira[71]). Briefly, Cohesin loading and unloading is regulated by NIPBL-MAU2 and PDS5-WAPL heterodimers, respectively. During S phase, ESCO1/2 and Sororin establish cohesion through SMC3 lysine head group acetylation and stabilize the Cohesin ring structure (Figure 1-1). In prophase, STAG1/2 and Sororin phosphorylation by PLK1 allows for Cohesin removal from non-centromeric DNA regions. Cohesin is maintained at the centromere by recruitment of SGO1-PP2A, which counteracts Sororin phosphorylation. At anaphase onset, the activated Anaphase Promoting Complex/Cyclosome (APC/C) degrades Securin (PTTG1) (*see Section 1.4.4*), allowing Separase (ESPL1) to cleave RAD21 and open the Cohesin ring[69-72] (Figure 1-1). Separation and segregation of sister chromatids to opposite spindle poles positioned at either end of the cell (*i.e.* bipolar mitotic spindle [*see Section 1.4.3*]) during anaphase ensures chromatids are equally partitioned between daughter cells and thus, maintains chromosome stability.

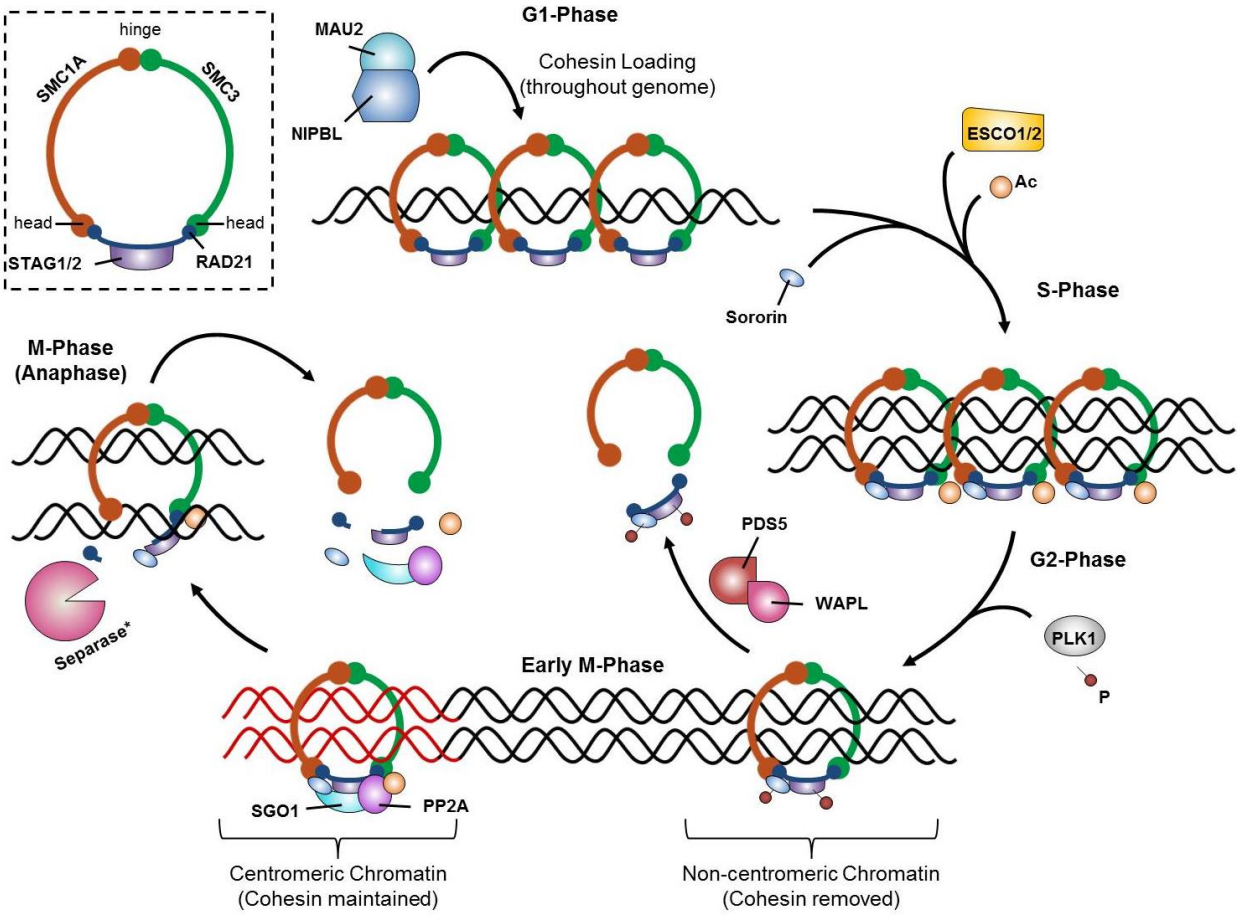

Figure 1-1. Cohesin Mediates Sister Chromatid Cohesion
Schematic presenting the four core components SMC1A, SMC3, RAD21 and STAG1/2 that comprise Cohesin (top left) and the process by which Cohesin is added and removed from chromatin throughout the cell cycle. Cohesin maintains sister chromatid cohesion following DNA replication, and must be cleaved at anaphase onset to allow for chromatid segregation (*see text for details*). SMC1A, Structural Maintenance Of Chromosomes 1A; SMC3, Structural Maintenance Of Chromosomes 3; RAD21, RAD21 Cohesin Complex Component; STAG1/2, Stromal Antigen 1/2; NIPBL, (Nipped-B-Like Protein) Cohesin Loading Factor; MAU2, Sister Chromatid Cohesion Factor; ESCO2, Establishment Of Sister Chromatid Cohesion N-Acetyltransferase 2; Ac, Acetyl group; PLK1, Polo Like Kinase 1; P, Phosphate group; PDS5, Cohesin Associated Factor; WAPL, (Wings Apart-Like Protein Homolog) Cohesin Release Factor; SGO1, Shugoshin 1; PP2A, Protein Phosphatase 2 Scaffold Subunit Alpha, Active Separase (*see Section 1.4.4*) indicated with (*).

Aberrations involving Cohesin or the above regulatory proteins have the potential to induce premature or delayed Cohesin release, impairing chromosome segregation and inducing numerical CIN. For example, short interfering (si)RNA-mediated knockdown of Cohesin components *SMC1A* and *STAG2* in the CRC cell line HCT116, induce cohesion defects visualized by sister chromatid separation at the centromere (*i.e.* primary constriction gaps), corresponding with significant DNA and chromosome content increases according to flow cytometry and mitotic chromosome spread analysis[62]. Interestingly, additional roles for Cohesin in DNA replication, DNA damage repair, telomere maintenance and gene transcription have also been described[69,70]. Thus, Cohesin-associated defects have the potential to induce both numerical and structural CIN, contributing to the genomic changes that promote oncogenesis. In fact, Barber *et al*[62] found that at least one gene encoding the Cohesin components or the accessory proteins that regulate Cohesin, is somatically altered in > 20% of CRCs[62].

1.4.2. Centromere and Kinetochore Protein Recruitment and Regulation

Centromeric aberrations that hinder kinetochore complex assembly or function may also prevent accurate chromosome congression and sister chromatid segregation, leading to CIN (reviewed in Stellfox *et al*[73]). Centromeres are heterochromatic chromosomal regions 0.2-5.0 megabases in size, consisting of repetitive, non-coding α-satellite DNA sequence arrays[74]. Active centromeric sites are epigenetically defined through integration of alternate histone octamers containing the histone H3 variant, Centromeric Protein A (CENPA)[75] (Figure 1-2). The Holliday Junction Recognition Protein (HJURP) assembly factor binds CENPA-Histone H4 in a prenucleosomal complex by interacting with the unique centromere targeting domain (CATD) in the histone fold motif of CENPA[76,77] (Figure 1-2). Following centromeric recruitment of MIS18

in telophase, CENPA deposition is initiated in G1 by creating a chromatin state permissive for HJURP-CENPA, presumably through histone acetylation[77].

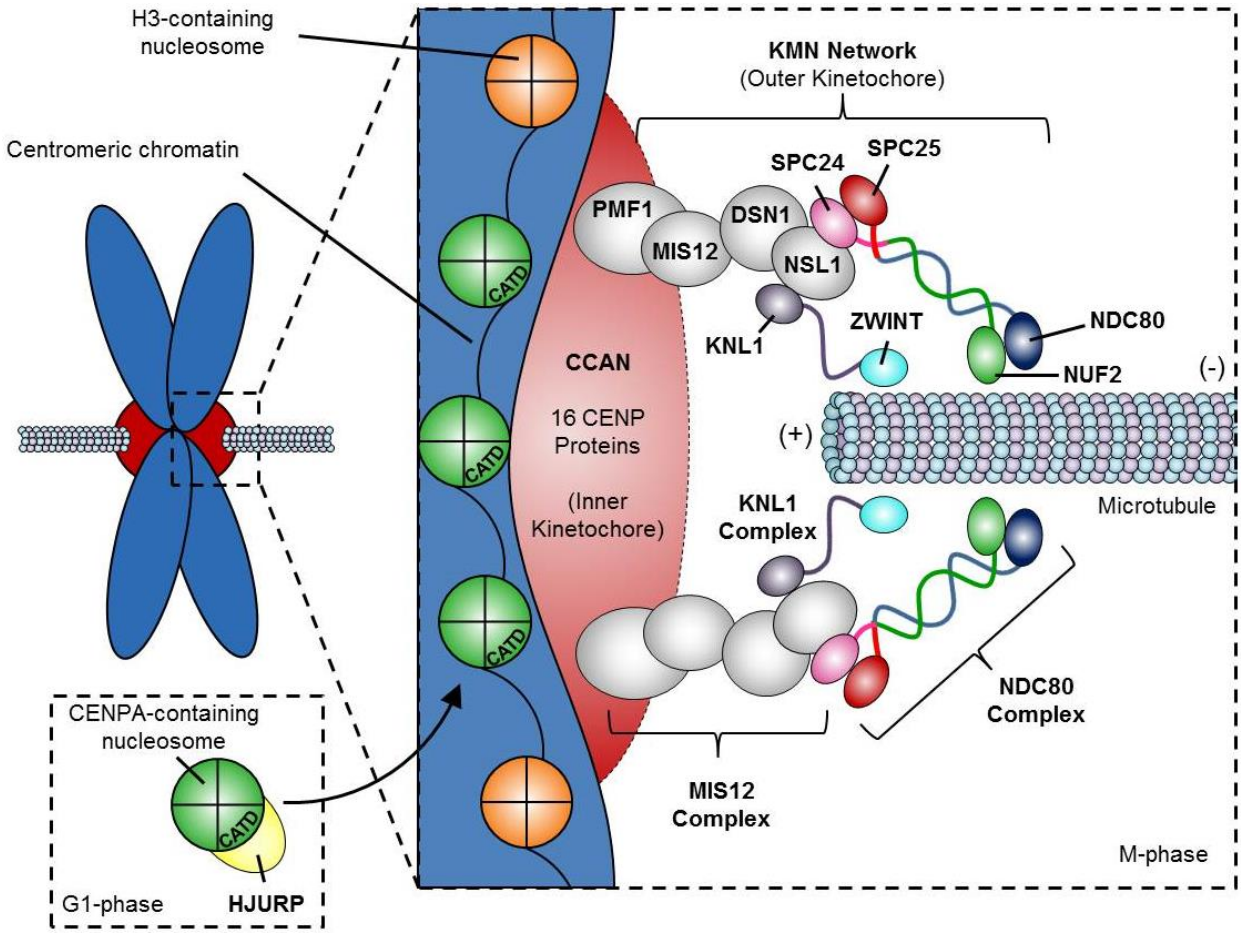

Figure 1-2. Centromeric and Kinetochore Complexes Mediate Microtubule Attachment
CENPA-containing histones integrated within centromeric chromatin recruit proteins of the CCAN, comprised of 16 CENP proteins. The CCAN recruits outer kinetochore complexes including the MIS12 Complex (PMF1, MIS12, DSN1 and NSL1), the KLN1 Complex (KLN1 and ZWINT) and the NDC80 Complex (SPC24, SPC25, NDC80 and NUF2). These multiprotein complexes regulate microtubule attachment (*see text for details*). Note this is simplified schematic as typically 20-30 microtubules attach to each centromere. CATD, centromere targeting domain; CENPA, Centromeric Protein A; HJURP, Holliday Junction Recognition Protein; CCAN, constitutive centromere-associated network; PMF1, Polyamine Modulated Factor 1; MIS12, MIS12 Kinetochore Complex Component; DSN1, DSN1 homolog MIS12 kinetochore complex component; NSL1, NSL1 MIS12 Kinetochore Complex Component; SPC24, Spindle Pole Body Component 24; SPC25, Spindle Pole Body Component 25 Homolog; NDC80, Nuclear Division Cycle 80; NUF2, NUF2 NDC80 Kinetochore Complex Component; KNL1, Kinetochore Scaffold 1.

In G1, HJURP assembles and integrates CENPA-containing octameric nucleosomes into a left-handed coil of DNA, in a similar manner to canonical H3 nucleosomes[78] (Figure 1-2). The CATD of CENPA is not only critical for centromeric localization and incorporation, but creates a chromatin structure that facilitates downstream protein recruitment, and directly binds components of the constitutive centromere-associated network (CCAN)[79]. The CCAN is a large-multiprotein complex consisting of 16 centromere proteins (CENPC, H, I, K-U, W, and X), which constitutes the inner kinetochore and recruits outer kinetochore proteins during mitosis[73,80] (Figure 1-2). Thus, altered expression or localization of CENPA can hinder kinetochore assembly and function leading to CIN and oncogenesis.

CENPA overexpression and misregulation induces ectopic CENPA incorporation, sequestering downstream centromere/kinetochore and Cohesin proteins (*e.g.* CENPC and SMC1A) at non-centromeric sites. This hinders proper centromeric kinetochore complex assembly, promotes CIN, and drives oncogenesis[75]. Normally, ectopically integrated CENPA is recognized by its CATD, removed, and degraded to maintain CENPA localization solely at the centromere. CENPA degradation is suspected to occur through a ubiquitin-mediated mechanism; however, the specific E3 ubiquitin ligase involved in humans remains unknown[73]. The CATD of centromeric CENPA is protected from E3 ligases and proteolytic degradation by binding of HJURP and CCAN components. In fact, HJURP knockdown in human cells corresponds with decreased CENPA levels, as HJURP can no longer effectively prevent degradation of CENPA[81]. Additionally, altered HJURP, CENPA, and histone H4 ratios were found to correspond with chromosome missegregation[82]. Overexpression of HJURP and CENPA occurs in numerous cancer types[83-89] and induces CIN phenotypes including mitotic defects, lagging chromosomes and extra-nuclear bodies found outside the primary nucleus, termed micronuclei (MNi) (*see*

Section 1.6.2 below)[82,90]. For example, CENPA has been found highly overexpressed (1.5 - 32.5-fold) and mislocalized relative to the alpha-satellite DNA-specific centromeric binding protein CENPB[91], in CRC patient samples[89]. Emerging evidence also suggests HJURP and CENPA may play a role in DNA double strand break (DSB) repair, sister chromatid segregation and cell survival[92] and are critical for maintaining chromosome stability in human cells.

The mature kinetochore complex is assembled in a hierarchal manner and contains two core networks: the inner kinetochore CCAN (discussed above) and the outer kinetochore KNL1-MIS12-NDC80 network (KMN), which mediates chromosome-spindle microtubule attachment[93] (Figure 1-2). MIS12 is the innermost multiprotein complex that links the CCAN to KNL1 and NDC80 complexes. The KNL1 complex serves as a scaffold for recruitment of Spindle Assembly Checkpoint (SAC) components (*Section 1.4.4 below*). Further, the KNL1 complex recruits dynein and dynactin, which are required for chromosome migration, and removes SAC proteins once the microtubule is effectively bound. Thus, kinetochore complex assembly is a prerequisite for proper chromosome-microtubule attachment, chromosome congression at the metaphase plate, and accurate segregation of sister chromatids into daughter cells in anaphase[75].

1.4.3. Centrosome Regulation and Microtubule Dynamics

CIN can also result from defects associated with the centrosome, microtubules, or mitotic spindle (reviewed in Fukasawa[94]). Microtubules are dynamic cytoskeletal filaments that establish cell morphology/polarity and facilitate intracellular trafficking via molecular motor proteins, mitotic spindle formation, chromosome segregation, and cell division[95]. α- and β-tubulin heterodimers bind longitudinally to form polar protofilaments (with plus- and minus-ends), 13 of which, align laterally to form the cylindrical microtubule structure[96,97] (Figure 1-3). αβ-tubulin

dimers are added in a guanosine triphosphate (GTP)-dependent manner to the microtubule plus-end for extension[96] (Figure 1-3).

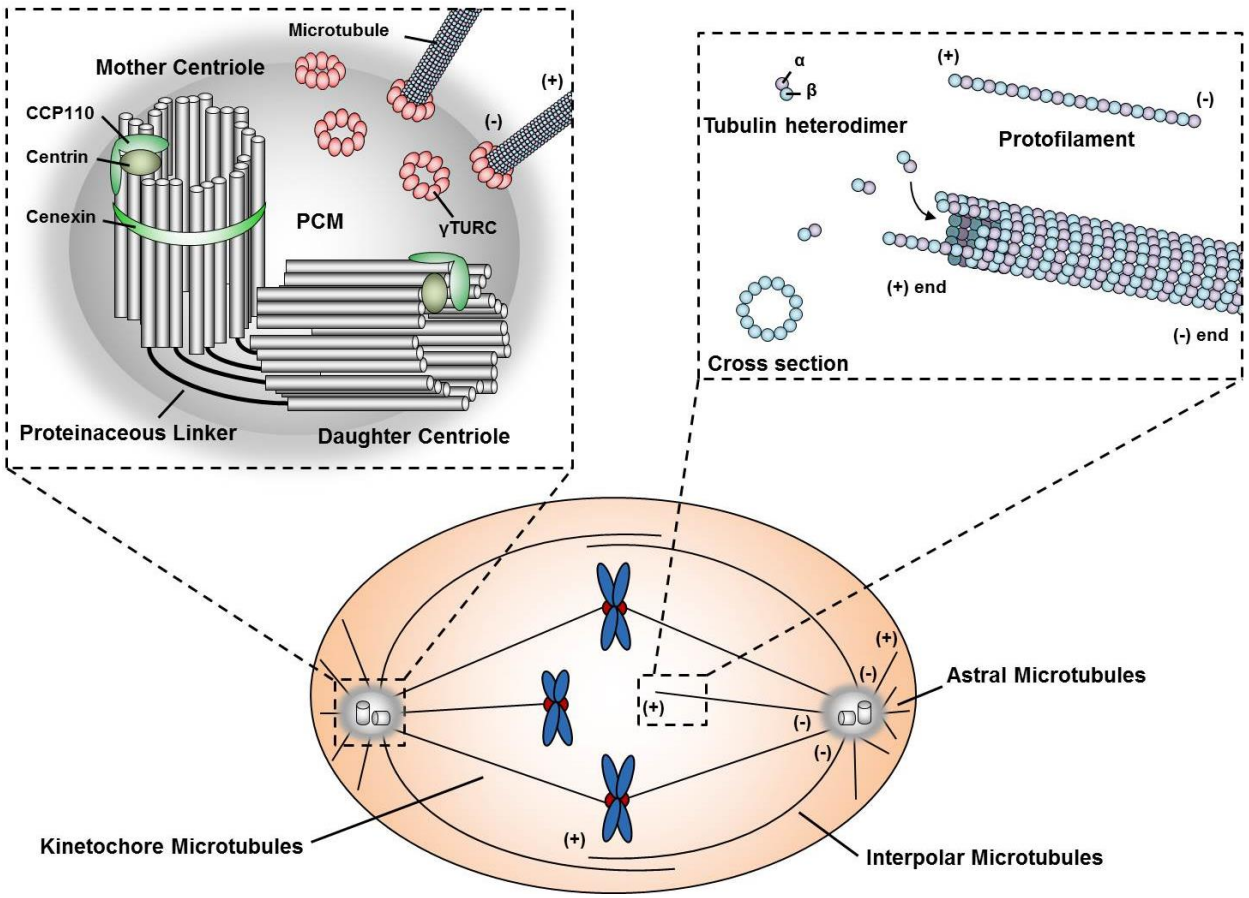

Figure 1-3. Mitotic Spindle Apparatus
Schematic of the bipolar mitotic spindle generated from centrosomes at opposite poles of the cell that organize microtubules to assemble the mature spindle apparatus. The centrosome serves as the microtubule organizing center and nucleation site. Top left magnified image presents the structure of the centrosome consisting of mother and daughter centrioles, accessory proteins (*e.g.* CCP110, Centrin and Cenexin) and γTURC microtubule nucleation sites embedded within the PCM. Three categories of microtubules comprise the mitotic spindle including kinetochore, interpolar and astral microtubules (*see text*). Magnified image of a microtubule on the top right shows αβ-tubulin heterodimers being added to (+) end for microtubule elongation. CCP110, Centriolar Coiled-Coil Protein 110; γTURC, γ-tubulin ring complex.

The centrosome serves as the microtubule organizing centre for mammalian cells. The centrosome contains a pair of orthogonally positioned "mother" and "daughter" centrioles each consisting of triplet microtubules arranged in cylindrical structures with nine-fold symmetry[95] (Figure 1-3). The mother centriole harbors distinct proteins from that of the daughter including the sub-distal appendage protein Cenexin, which recruits downstream proteins and regulates centriole structural integrity, spindle orientation, and centrosome positioning within the cell[98]. Centrioles are embedded in pericentriolar material (PCM) comprised of scaffolding proteins such as Pericentrin[99], which recruits γ-tubulin ring complex (γ-TURC) structures to serve as nucleation sites for microtubule assembly and anchor the microtubule minus-ends to the centrosome[100] (Figure 1-3). Three types of microtubules emanate from the centrosome to assemble the mitotic spindle (Figure 1-3). Astral and interpolar microtubules mediate centrosome positioning within the cell and bipolar spindle assembly, while kinetochore microtubules attach to kinetochore complexes for chromosome segregation (reviewed in Meunier and Vernos[97]).

To generate a bipolar spindle, the centrioles/centrosome must be duplicated precisely once per cell cycle (reviewed in Fu *et al*[101]). In G1, mother and daughter centrioles contained within a single centrosome disengage but remain connected throughout interphase by a fibrous linker. In a semi-conservative manner, new pro-centrioles are assembled perpendicular to each disengaged centriole beginning at G1/S. PLK4 is considered a master regulator of the centrosome and mediates centriole duplication[102]. Over- or under-expression of *PLK4* induces centriole over- and under-duplication, respectively[103,104]. Interestingly, centrosome and DNA replication are concurrent and are mediated by many of the same regulatory complexes including Cyclin E1 (CCNE1)/CDK2, which phosphoactivates centrosomal proteins such as CCP110 (involved in centrosome duplication and centriolar length determination)[105]. CCNE1 also interacts with the

DNA replication protein MCM5 independently of CDK2, to regulate centrosome duplication[106]. Centriolar linker proteins are cleaved at mitotic entry, allowing new centriole pairs to separate into distinct centrosomes that migrate to opposite poles through the action of motor proteins on interpolar microtubules that generate forces to drive the centrosomes apart and establish the bipolar mitotic spindle[107]. Defects in the above processes (*i.e.* centriole or centrosome duplication, regulation, migration) can prevent proper mitotic spindle assembly and result in CIN[108].

Centrosomal aberrations are typically classified as either numerical or structural (reviewed in Godhino and Pellman[109]) and are frequently observed in both solid and hematologic cancers. Centrosome defects correlate with CIN, cancer recurrence, metastatic progression, and poor prognoses (reviewed in Chan[108]). Numerical aberrations characterized by supernumerary (> 2) centrosomes can result from misregulation of centrosome or centriole regulatory factors (*e.g.* PLK4 or CCNE1), *de novo* centriole assembly, mitotic slippage, or cytokinesis errors, effectively increasing the number of centrosomes per cell. Structural defects can include alterations associated with centriole or PCM structure or size. Common structural centriole defects are increases in centriole length, or increases in the heterogeneity of centriole lengths. Components of the mature centriole (*e.g.* Cenexin, CCP110, and Centrin) and/or PCM (*e.g.* Pericentrin) can be immunofluorescently labelled to evaluate structural and/or numerical centrosomal defects *in vitro* and in patient tumor samples[99]. For example, primary CRC cells have been found to exhibit intense Pericentrin labelling with centrosomal size, structure, and number alterations, correlating with morphological nuclear abnormalities and CIN according to centromeric fluorescence *in situ* hybridization (FISH) probe analysis[110].

1.4.4. Spindle Assembly Checkpoint

The above biological processes including sister chromatid cohesion (*Section 1.4.1*), centromeric/kinetochore complex assembly (*Section 1.4.2*) and mitotic spindle assembly (*Section 1.4.3*) are intricately linked and regulated by the SAC (reviewed in Lara-Gonzalez *et al*[111]). The SAC is the primary surveillance mechanism that functions to delay Cohesin cleavage and anaphase onset until all kinetochores are properly attached to mitotic spindle microtubules, and chromosomes are aligned at the metaphase plate with the appropriate tension to bi-orient sister chromatids towards opposite poles[112] (Figure 1-4). Kinetochores that are not properly attached to microtubules recruit mitotic checkpoint components including BUB1, BUB3, BUBR1, MAD1, MAD2, and MPS1 which convert MAD2 to its open, activated form[113]. As part of the Mitotic Checkpoint Complex, activated MAD2 prevents CDC20 from activating APC/C, thereby preventing Securin degradation, Separase activation, and Cohesin release, as described above. The cell cycle becomes arrested prior to anaphase, ensuring premature sister chromatid segregation does not occur (Figure 1-4). SAC components function in coordination with the Chromosome Passenger Complex, comprised of Aurora B, INCENP, Borealin and Survivin, which destabilizes aberrant kinetochore-microtubule attachments and promotes bipolar attachments[114]. When all kinetochores are properly attached to microtubules, MAD2 is inactivated (*i.e.* closed conformation), releasing inhibition of CDC20, and APC/C drives Securin degradation, Separase-mediated Cohesin cleavage, anaphase progression, and chromosome segregation[113] (Figure 1-4). Misexpression, misregulation, or mislocalization of SAC proteins may permit chromosome missegregation and CIN. In fact, *Mad2* overexpression in mice has been shown to induce CIN and tumorigenesis[115]. In humans, *MAD2* is overexpressed in various cancer types including retinoblastoma, bladder, and neuroblastoma and correlates with poorer

patient outcomes[116]. BUB1 mutations and overexpression of Securin, which can induce numerical and structural CIN, have also been reported in CRC[117-119].

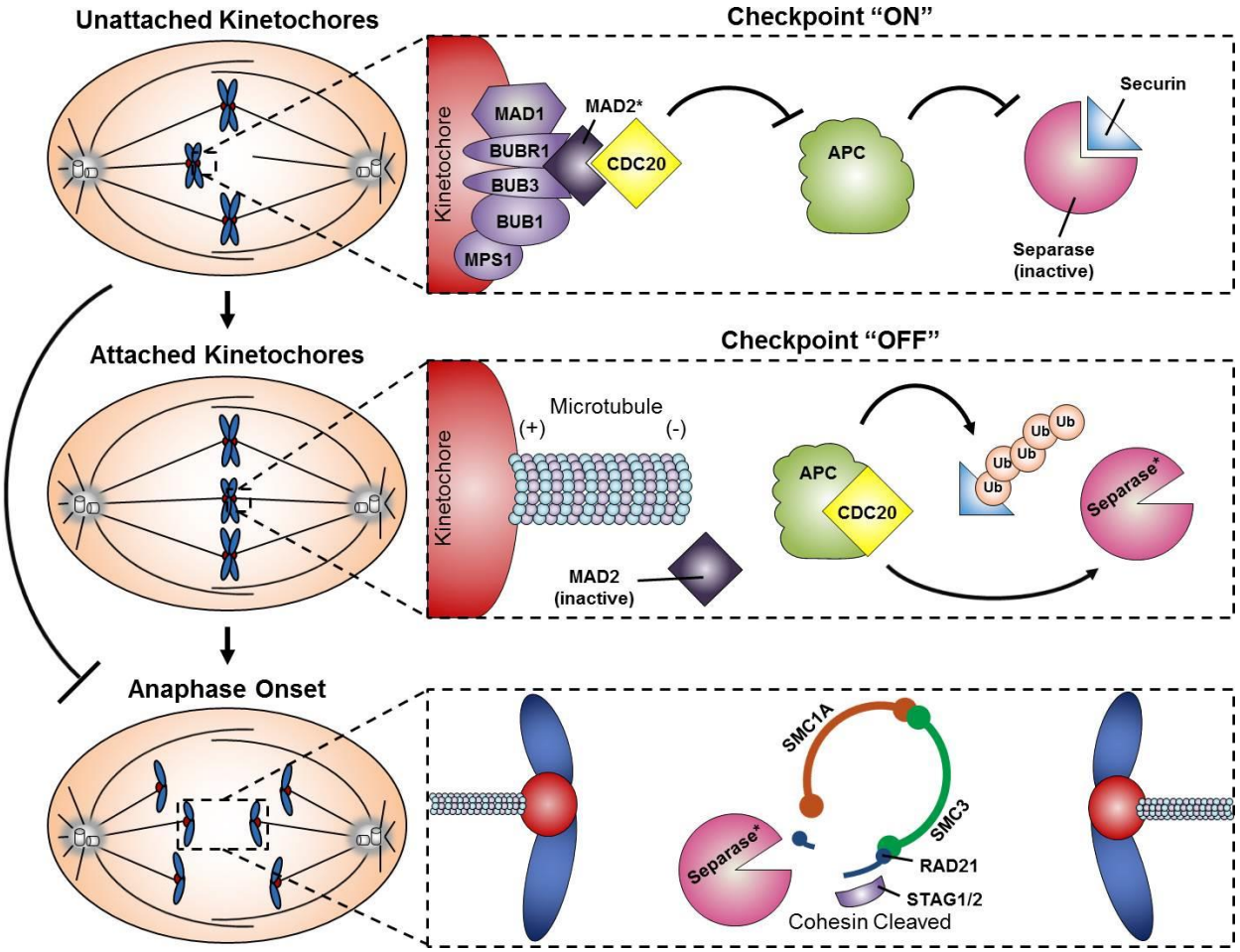

Figure 1-4. Spindle Assembly Checkpoint Ensures Kinetochore-Microtubule Attachment Prior to Anaphase

SAC is "on" when kinetochores are not attached to microtubules and lack tension. SAC is turned "off" once kinetochores are properly attached to microtubules. Separase is activated, which cleaves Cohesin and allows sister chromatid segregation in anaphase (*see text for details*). MAD1, Mitotic Arrest Deficient Like 1; MAD2, Mitotic Arrest Deficient 2 Like 1; BUBR1, MAD3/BUB1-Related Protein Kinase; BUB3, Budding Uninhibited by Benzimidazoles 3 Homolog; BUB1, Budding Uninhibited By Benzimidazoles 1; MPS1, Monopolar Spindle 1; CDC20, Cell Division Cycle 20; APC, Anaphase Promoting Complex; Ub, Ubiquitin; SMC1A, Structural Maintenance Of Chromosomes 1A; SMC3, Structural Maintenance Of Chromosomes 3; RAD21, RAD21 Cohesin Complex Component; STAG1/2, Stromal Antigen 1/2. Active forms of MAD2 and Separase are indicated with (*).

1.4.5. DNA Replication

DNA replication is a tightly controlled process regulated by numerous protein complexes that ensure replication origin licensing, firing, and genome replication occurs once per cell cycle, without inducing DNA damage, gene amplification, polyploidy, or other genomic abnormalities (reviewed in Fragkos *et al*[120]). First, the pre-replicative complex (pre-RC) is recruited to DNA replication origins throughout the genome in G1-phase (*i.e.* origin licensing). The pre-RC consists of the origin of replication complex components ORC1-6, CDC6, and CDT1, which recruit hexameric MCM2-7 helicases[121] (Figure 1-5). Origin firing is initiated at G1/S by kinases that phosphoactivate MCM2-7 and additional proteins (*e.g.* RECQL4 helicase, MCM10, CDC45, GINS, DNA primase and polymerases), which unwind the DNA and ultimately form the mature replisomes[120]. Replisomes synthesize DNA bi-directionally from DNA primers in the 5' to 3' direction on both leading and lagging strands for complete replication of the genome in S-phase[120] (Figure 1-5).

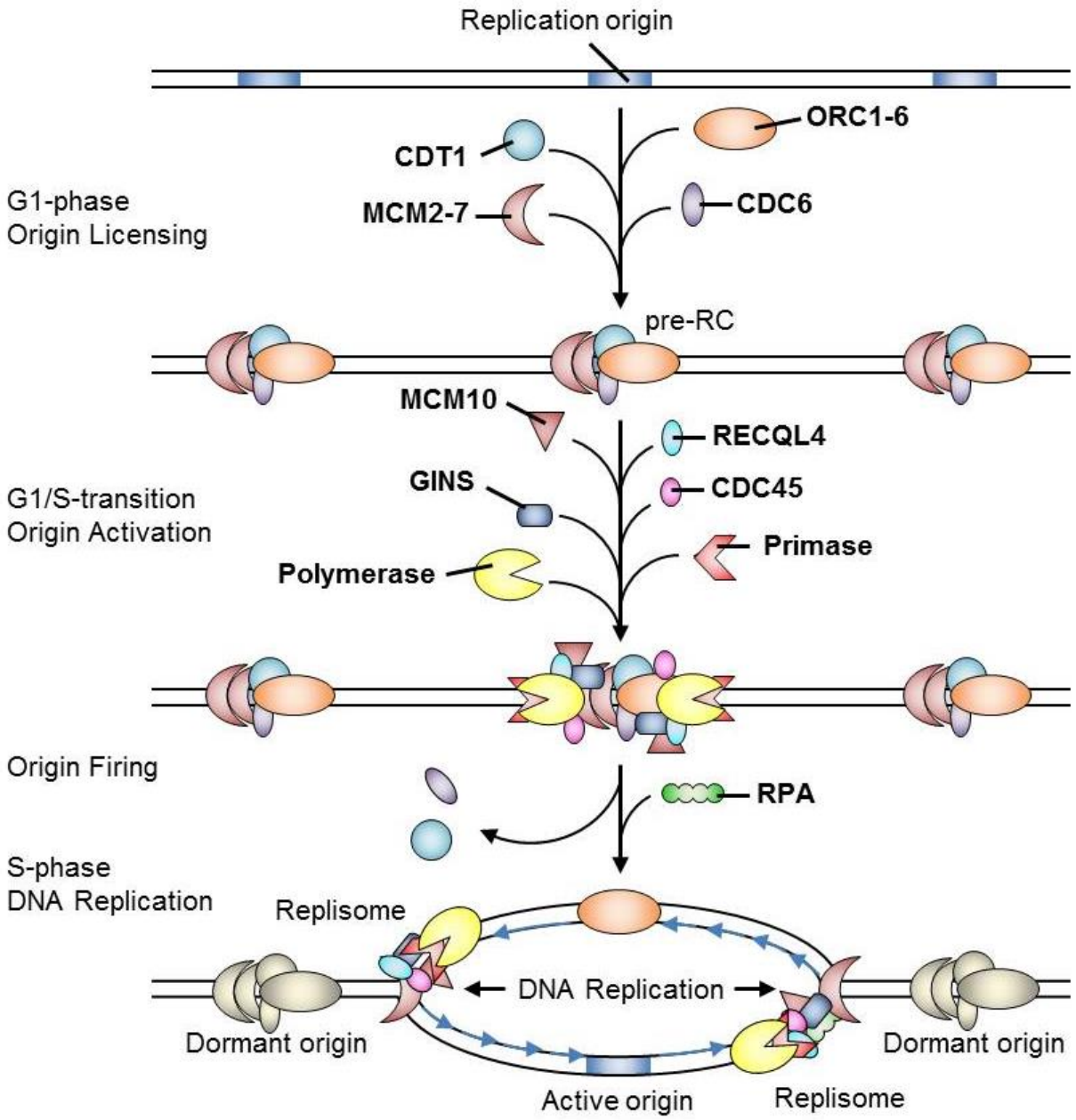

Figure 1-5. Regulation of DNA Replication Ensures Accurate Duplication of the Genome
Origins are licensed in G1-phase by recruitment of the pre-RC, comprised of ORC1-6, CDC6, CDT1 and MCM2-7 helicases. Additional replication factors including RECQL4, MCM10, CDC45, GINS, DNA primase and DNA polymerases are recruited to the origins, forming the mature replisomes that fire at G1/S for DNA replication in S-phase (*see text for details*). RPA is recruited to stabilize single stranded DNA intermediates generated during DNA replication or to recruit DNA repair enzymes during replication stress. CDT1, Chromatin Licensing and DNA Replication Factor 1; ORC1-6, Origin Recognition Complex Subunits 1-6; CDC6, Cell Division Cycle 6; MCM2-7, Minichromosome Maintenance Complex Components 2-7; pre-RC, pre-replicative complex; MCM10, Minichromosome Maintenance Complex Component 10; RECQL4, RecQ Like Helicase 4; GINS, GINS Complex Subunits 1-4; CDC45, Cell Division Cycle 45; RPA, Replication Protein A. Figure adapted from Fragkos *et al*[120].

Replication stress or replisome slowing/stalling can occur when replication forks encounter obstacles such as DNA damage, secondary DNA structures, aberrant protein-DNA interactions, transcription machinery, or as a result of nucleotide deficiency (reviewed in Zeman and Cimprich[122]). During G1, MCM2-7 complexes are normally recruited to replication origins in excess to create dormant origins that can fire if replication stress in encountered to ensure that DNA replication is completed. Additionally, Replication Protein A (RPA) binds and stabilizes single stranded DNA (ssDNA) intermediates during replication to prevent reannealing, recombination, nuclease degradation and DNA damage[123]. As replication stress increases ssDNA regions, immunofluorescent labeling and signal assessment of RPA is frequently utilized as an indicator of replication stress. If replication stress is not relieved, it can prevent complete duplication of the genome, generate chromosome breakages or rearrangements (structural CIN), and/or create structurally abnormal chromosomes that missegregate (numerical CIN)[55].

Replication defects and CIN can arise not only from replication stress but from replication origin under-usage (too few origins fire), over-usage (too many origins fire), or re-usage (the same origins fire multiple times per cell cycle), which can cause under- or over-duplication of the genome or genomic regions (reviewed in Hills and Diffley[124]). Over- or re-use of replication origins can also deplete the available pools of substrates or accessory proteins required for replication such as deoxyribonucleotides or RPA, ultimately inducing replication stress[124]. Normally, improper usage of replication origins is inhibited by proteins such as Early Mitotic Inhibitor 1 (EMI1), which inhibits APC/C and allows the accumulation of proteins (*e.g.* CCNE1) that function to drive replication but prevent re-replication or endoreduplication[121]. Additionally, the CDT1 licensing factor is inhibited by Geminin to prevent MCM2-7 loading outside of G1-phase, which can cause the same replication origins to fire more than once per cycle. In cancer

cells, activation of oncogenes like CCNE1 promotes rapid proliferation and replication checkpoints are often circumvented, driving cell cycle progression, regardless of replication stress, leading to replication defects[125].

1.4.6. DNA Damage Response

Misregulation of the DNA damage response is frequently observed in cancer and is a common mechanism that leads to the generation/persistence of DNA double strand breaks (DSBs), chromosome fragments, and CIN (reviewed in Hosoya and Miyagawa[126]). Normally, DNA damage repair mechanisms monitor the genome for defects such as DSBs, ssDNA regions, or single strand breaks (SSB) (often converted into DSBs) that are derived from exogenous or endogenous sources such as ionizing radiation or oxidative and replication stress. The MRE11-RAD50-NBS1 (MRN) complex binds to DSBs and recruits the Ataxia Telangiectasia-mutated (ATM) kinase[126,127]. Autophosphorylation and activation of ATM allows phosphoactivation of numerous downstream substrates including CHEK2, BRCA1/2, TP53, and histone H2AX[127]. Histone H2AX is an alternate histone H2A variant that is phosphorylated on serine residue 139 (γH2AX). Immunofluorescent labelling of γH2AX and assessment of nuclear γH2AX foci is commonly employed as a surrogate marker of DSBs[128]. Overall, the phosphorylation cascade initiates a cell cycle arrest, permitting the cell to either repair damaged DNA (*e.g.* by non-homologous end-joining [NHEJ] or homologous recombination repair [HRR]) or initiate cell death[126]. In response to ssDNA regions, RPA recruits ATRIP, RAD17, 9-1-1 complex, and TOPBP1 which activate the Ataxia Telangiectasia and Rad3-related (ATR) kinase (Figure 1-6). ATR phosphoactivates downstream substrates including CHEK1 and TP53, coordinating a cell cycle arrest, replication fork stabilization, and restart. Additionally, nearby dormant origins licensed with MCM2-7 are stimulated to fire, ensuring complete replication of the genome[129].

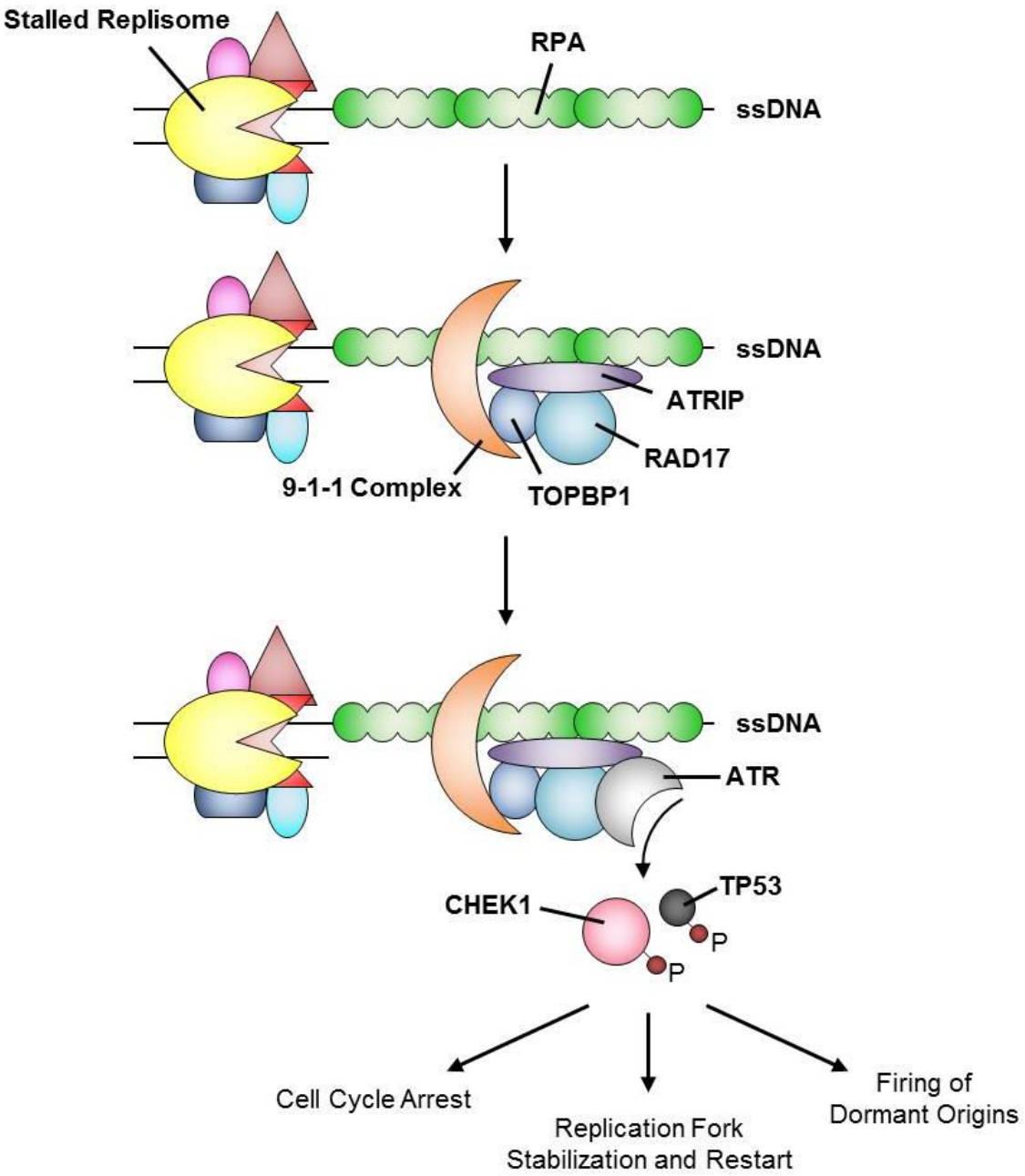

Figure 1-6. DNA Damage Response to Replication Stress
Schematic summarizing the DNA damage response to ssDNA intermediates generated from replication stress (*see text for details*). RPA binds ssDNA, which recruits ATRIP, RAD17, TOPBP1 and the 9-1-1 complex to activate ATR. ATR phosphoactivates downstream substrates, such as CHEK1 and TP53, which coordinate the appropriate cell response. RPA, Replication Protein A; ATRIP, ATR Interacting Protein; RAD17, RAD17 Checkpoint Clamp Loader Component; TOPBP1, DNA Topoisomerase II Binding Protein 1; ATR, ATR Serine/Threonine Kinase; TP53, Tumor Protein P53; CHEK1, Checkpoint Kinase 1; P, Phosphate group.

The above DNA damage response proteins are frequently altered in cancer. For example, *TP53* is mutated in > 40% of the 12 most common cancer types, including 40-50% of sporadic CRCs[130] and upwards of 95% of serous ovarian carcinomas[131]. Defects in the DNA damage response permit cells to bypass DNA damage checkpoints and proceed through the cell cycle, regardless of DNA damage or replication errors. This promotes rapid acquisition of mutations, and structural and numerical CIN.

1.4.7. Ubiquitin-dependent Proteasomal Degradation

The causal relationship between defects in the above biological pathways (*Sections 1.4.1-6*) and CIN are readily apparent, however genes with a less intuitive connection to CIN such as those involved in proteasomal degradation, were also identified as CIN genes in budding yeast (*see Section 1.3.0*). The relationship between aberrant proteasomal degradation and CIN appears to be conserved in humans, as diminished expression of proteasomal subunits PSMA6, PSMA4, PSMD4 and PSMD12 in HCT116 CRC-derived cells, induced increases in chromosome number and DNA content according to mitotic chromosome spread analyses and flow cytometry, respectively[132]. Further, as many proteins involved in the above CIN-associated pathways (*e.g.* CCNE1 [*see Sections 1.4.3 and 1.4.5*]) are regulated by proteasomal degradation, it is possible that proteasomal defects can indirectly induce CIN through misregulation of the above pathways. Thus, further investigation into biological pathways like proteasomal degradation that may be indirectly linked to DNA/chromosome regulation and mitosis are required to effectively evaluate their role in CIN and cancer.

Proteasomal degradation directs substrate turnover and maintains downstream proteins at an appropriate cellular level via the ubiquitin-proteasome system (UPS) (reviewed in Kleiger and Mayor[133]). The UPS is characterized by two successive steps; covalent attachment of ubiquitin

molecules to a target protein, followed by degradation of the polyubiquitinated protein by the 26S proteasome[133] (Figure 1-7). The 26S proteasome is a large (2.5 MDa) macromolecular structure consisting of a cylindrical 20S catalytic subunit, which harbours peptidase activity, and the ring-shaped 19S regulatory subunit, consisting of structural components, ubiquitin-receptors, and ATPases that bind, denature, and translocate substrates into the 20S proteolytic core[134]. Substrate polyubiquitination provides a high degree of specificity for the system and is carried out by the consecutive action of three enzymes, an E1 ubiquitin-activating enzyme, E2 ubiquitin-conjugating enzyme, and E3 ubiquitin ligase[135] (Figure 1-7). These enzymes are responsible for ATP-dependent ubiquitin activation (E1), covalent attachment to E2, and transfer of ubiquitin moieties to the target substrate (E3), creating a polyubiquitin chain linked through lysine 48 (K48)-glycine 76 (G76) isopeptide bonds[135]. As the E3 component dictates substrate specificity for the UPS, a large number of E3 ubiquitin ligases (up to 1000) are predicted to exist in humans (reviewed in Deshaies and Joazeiro[136]). The E3 ubiquitin ligases are divided into four main groups, the Homologous to the E6-AP Carboxyl Terminus (HECT), U-box, Plant-homeo-domain (PHD)-finger, or Really Interesting New Gene (RING)-finger type, according to the E2-binding structural motif that they harbour (Figure 1-7). The RING-finger type E3 ubiquitin ligases are further categorized into subfamilies, the largest of which is the Cullin-based subfamily[137]. The SKP1-CUL1-F-box Protein E3 Ubiquitin ligase (SCF) complex is considered the prototypical Cullin-based, RING-finger type E3 enzyme and is the primary focus of this thesis.

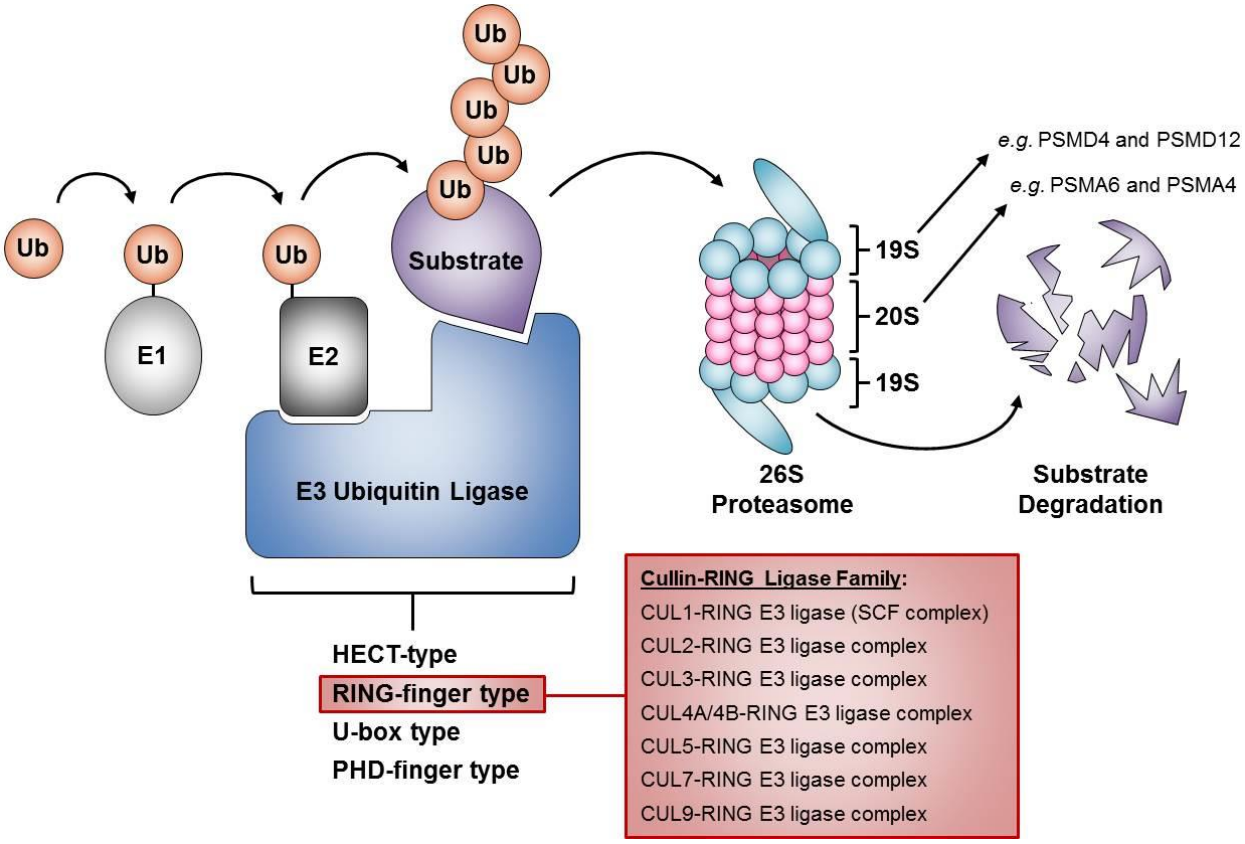

Figure 1-7. Ubiquitin-Proteasome System
Substrates intended for degradation by the 26S proteasome are polyubiquitinated through the concerted activity of the E1 ubiquitin-activating enzyme, E2 ubiquitin-conjugating enzyme, and E3 ubiquitin-protein ligase. Four major families of E3 ubiquitin ligases (HECT, RING-finger, U-box, and PHD-finger) are listed. Examples of the RING-finger type Cullin-based ligases are listed including the prototypic CUL1-based SCF complex. Ub, Ubiquitin; HECT, Homologous to the E6-AP Carboxyl Terminus; PHD, Plant-homeo-domain; RING, Really Interesting New Gene; PSMD4, Proteasome 26S Subunit Non-ATPase 4; PSMD12, Proteasome 26S Subunit Non-ATPase 12; PSMA6, Proteasome Subunit Alpha 6; PSMA4, Proteasome Subunit Alpha 4.

1.5.0. The SCF Complex

The SCF complex consists of three core components including the ring-finger protein Ring-Box1 (RBX1) responsible for recruiting the E2 ubiquitin-conjugating enzyme, the scaffolding protein Cullin 1 (CUL1), and the invariable adaptor component S-phase Kinase Associated Protein 1 (SKP1)[138] (Figure 1-8). SKP1 recruits the variable, substrate-recognition F-box protein subunit by binding its 40 amino acid F-box domain[139]. F-box proteins are classified into three main groups according to their substrate recognition domains, FBXW, FBXL, and FBXO. These protein groups harbour WD40 repeats (*e.g.* FBXW7), leucine-rich repeats (*e.g.* FBXL1/SKP2), or other domains (*e.g.* FBXO28) respectively, in addition to their characteristic F-box domain[137]. Each F-box protein recruits substrates[140], typically those that are phosphoactivated, to the core SCF complex, facilitating several rounds of ubiquitin conjugation and degradation by the 26S proteasome, thereby tightly regulating substrate expression levels[141] (Figure 1-8). As there are 68 F-box proteins encoded in the human genome, there are potentially 68 different SCF complexes, each responsible for regulating distinct subsets of target proteins[137]. Additionally, CUL7 can interact with SKP1 and FBXW8 in a non-canonical SCF-like complex[142] that regulates distinct substrates from canonical SCF^{FBXW8}. Thus, SKP1 may be involved in > 68 different E3 ubiquitin ligase complexes. Unfortunately, the substrates and functions for the majority of human F-box-proteins and SCF complexes have yet to be elucidated. The few F-box proteins characterized to date (*e.g.* SKP2, CCNF, βTRCP) regulate substrates such as CCNE1[143], CDC6[144], and PLK4[145] that are involved in key CIN-associated cellular processes including centrosome regulation, DNA replication and DNA damage repair as described above. As such, future studies that seek to functionally characterize the remaining F-box proteins and SCF complexes are highly warranted.

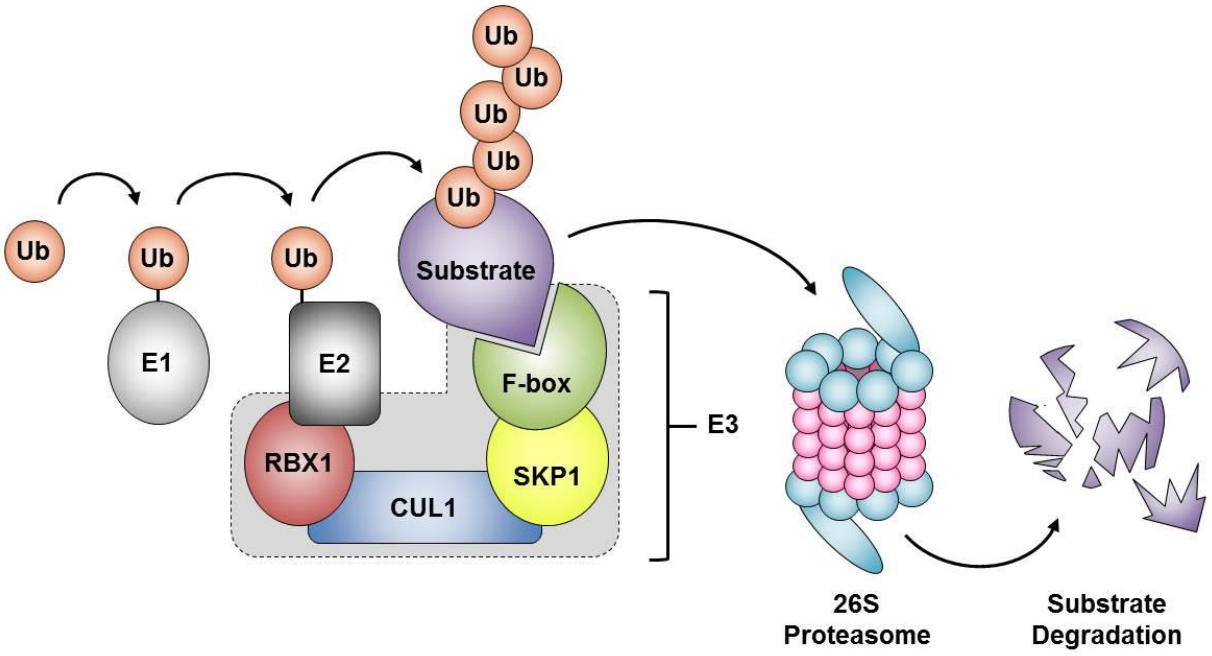

Figure 1-8. The SCF Complex Regulates Protein Degradation
Schematic of the SCF E3 ubiquitin ligase complex, which consists of four components, namely SKP1, RBX1, CUL1, and the variable F-box protein (*e.g.* SKP2). The F-box protein recognizes the targeted substrates (*e.g.* CCNE1) and facilitates transfer of ubiquitin moieties to the substrate protein by the E2 ubiquitin-conjugating enzyme (*see text for details*). Polyubiquitin demarcates substrates for degradation by the 26S proteasome. E1, E1 ubiquitin-activating enzyme; E2, E2 ubiquitin-conjugating enzyme; E3, E3 ubiquitin-protein ligase; RBX1, Ring-Box 1; CUL1, Cullin 1; SKP1, S-Phase Kinase Associated Protein 1, Ub, Ubiquitin.

Gaining a greater understanding of specific E3 ubiquitin ligase components (*e.g.* SKP1) is especially important, as alterations involving E3 subunits can have detrimental consequences for the cell and are often implicated in the pathogenesis of human disease. The mutation or misregulation of the invariable E3 adaptor component, SKP1, may be particularly damaging as this could hinder SCF complex formation, F-box protein recruitment, substrate polyubiquitination, and impact numerous downstream pathways, culminating in cellular dysfunction and disease. Indeed, underexpression of *SKP1* is implicated in the pathogenesis of sporadic Parkinson's Disease[146], and suspected to play a role in development of Sjögren's Syndrome (a chronic inflammatory autoimmune disease)[147]. Further, both over- and under-expression of SKP1 occurs in cancer[148], as detailed below (*Section 1.5.2*). Thus, understanding the role of SKP1 and the SCF complex in various cellular contexts is imperative, as it may provide important insights into the pathogenesis of different cancer types, disease management, identification of new diagnostic/prognostic indicators, or for designing novel treatment strategies.

1.5.1. S-Phase Kinase Associated Protein 1

The human *SKP1* locus spans 28,097 bp on chromosome 5q31.1, and encodes two protein coding mRNA transcripts of different lengths, 2,028 bp and 2,714 bp that are generated through alternative splicing[149]. The transcripts are translated into two protein isoforms, 163 (Isoform B) and 160 (Isoform A) amino acids in size, respectively, which differ only in their carboxy-terminal regions. A study in *S. cerevisiae* revealed that the tryptophan residue at position 159, which is present only in human Isoform B, is essential for *in vivo* function[150]. As Trp159 is highly evolutionarily conserved in orthologs from yeast to humans, these experimental findings suggest that Isoform B is the functional isoform in humans[150-152]. The encoded protein is ~18

kDa in size[149] and harbours a 128 residue domain at the amino-terminus resembling the α-helix/β-sheet structure of a BTB/POZ (broad complex, tramtrack and bric à brac/poxviruses and zinc finger) fold domain, but with an α-helical insertion (αH4)[150] (Figure 1-9). This domain is essential for heterodimerization and is required for the binding of CUL1 to SKP1. Additionally, SKP1 harbours a two-helix, carboxy-terminal extension (αH7 and αH48) that can cooperate with elements from the BTB/POZ fold to create a variable interaction motif that can bind F-box domains and thus, a multitude of F-box proteins (Figure 1-9). These interactions are crucial for the formation of the mature SCF E3 ubiquitin ligase complex[140,153]. Thus, the ability of SKP1 to interact with CUL1 and F-box proteins is critical and highly conserved throughout evolution.

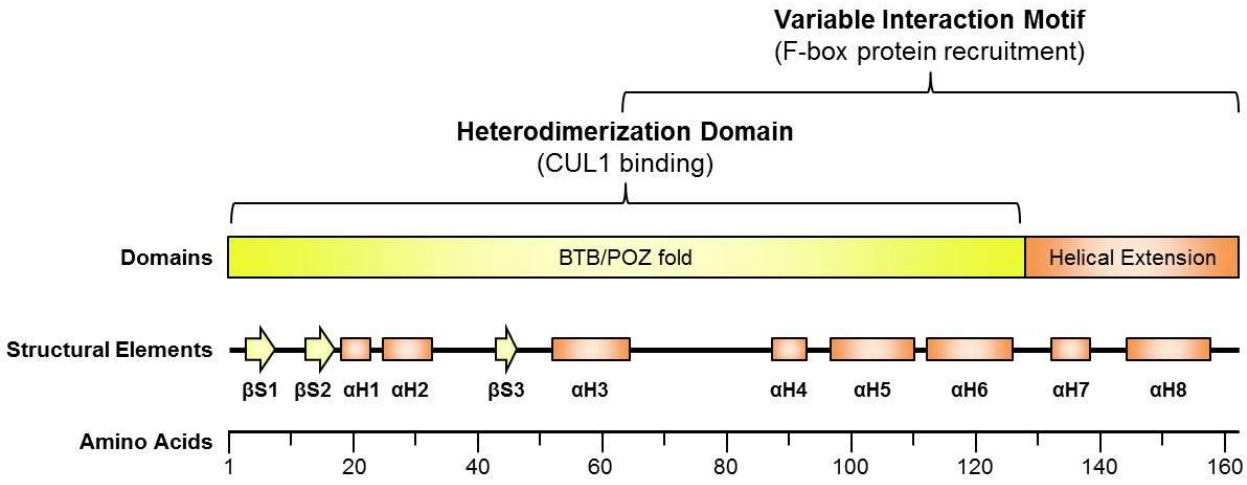

Figure 1-9. SKP1 Structure Enables Binding to a Myriad of F-box Proteins
Schematic depicting the secondary structural elements and protein domains of SKP1 that enable binding to CUL1 and numerous F-box proteins to form the SCF complex. BTB/POZ domain consists of all three βS and six αH elements, while αH7 and αH8 make up the helical extension domain. Scale bar represents the entire length (163 amino acids) of SKP1. CUL1, Cullin 1; βS, beta-sheet; αH, alpha-helix; BTB/POZ, broad complex, tramtrack and bric à brac/poxviruses and zinc finger.

1.5.2. *SKP1* Alterations in Cancer

As the SCF complex is critical for regulating proteins within the key biological pathways discussed above, alterations involving the invariable SCF component SKP1 may result in extensive cellular dysfunction, CIN, and oncogenesis. Although, *SKP1* transgenic mice have yet to be generated, studies in mice have provided insights into the implications of SKP1 and SCF misregulation *in vivo*. For example, Piva and colleagues[154] developed mice that express a Cul1 mutant (Cul1-N252) in the T-lymphoid lineage. This dominant negative Cul1 mutant, binds, sequesters, and functionally inactivates Skp1. Initially, Cul-N252 deletion mice presented with reduced cellular proliferation, lymphoid organ hypoplasia, supernumerary centrosomes, mitotic spindle aberrations and chromosome missegregation. Following the initial proliferation lag, >80% of Cul-N252 mice developed T-cell lymphomas, suggesting that SKP1 and the SCF complex are required to prevent oncogenesis in lymphoid tissues[154]. While studies in mouse models support *SKP1* as a CIN- and cancer-associated gene, studies investigating the pathogenic impact of *SKP1* alterations in human cancers are lacking. *In silico* queries of the cBioPortal for Cancer Genomics database[155,156] reveal that *SKP1* is misexpressed in a variety of cancer types including ~10% of prostate[157], serous ovarian[158], and bladder cancers[159], and is often both under- and overexpressed within a given cancer type. Presumably, this reflects the fact that as a member of the SCF complex, SKP1 has vital roles regulating both tumor suppressor and oncoprotein substrates, and SKP1 levels must be precisely regulated to prevent oncogenic transformation and cancer progression. This highlights the merit of investigating human candidate CIN genes like *SKP1*, to identify novel genes and pathways that induce CIN when misregulated and drive oncogenesis.

1.6.0. CIN Phenotypes

In order to identify novel human CIN genes, traditional cytogenetic methods are often employed. Typically, a gene of interest is altered by mutation, silencing, or overexpression, and mitotic chromosome spreads are generated and analyzed to determine whether gene alteration resulted in numerical or structural chromosomal defects that are indicative of CIN. As chromosome assessment and enumeration is time-consuming and costly, novel approaches designed to rapidly detect the phenotypes that underlie CIN are in dire need. As discussed in the preceding sections, CIN can manifest as large or small-scale chromosome content changes, depending on the biological pathways that are impacted by CIN gene alteration. Thus, in a manner analogous to the yeast screens described above (*see Section 1.3.0*), complementary assays capable of detecting different CIN phenotypes indicative of large or small-scale chromosome content changes in a human cellular context are required.

1.6.1. Nuclear Size Changes as an Emerging Indicator for Large-scale DNA Content Changes in Cancer

As described above, CIN gene alterations that induce large-scale chromosome missegregation or endoreduplication can result in extensive numerical chromosomal changes or polyploidy. While nuclear morphology and size changes are frequently assessed in patient tumor samples for diagnostic/grading and prognostic purposes in the clinic, it has become increasingly evident that nuclear size changes are also indicative of DNA content changes in numerous cancer types. In fact, increases in nuclear areas (NAs) and perimeters are sufficient to distinguish cancer from non-cancerous cells in the pancreas, and were found to correlate with increased DNA ploidy in endocrine and solid pseudopapillary pancreatic tumors[160]. Similarly, NAs, aneuploidy, hyperploidy, and proliferation index are significantly correlated in serous and mucinous ovarian

cancer with increasing nuclear area (NA) associated with poorer overall and progression-free survival[161]. In both non-small cell and small cell lung cancers, increasing nuclear size (diameters), nuclear size heterogeneity, and the presence of giant nuclei (maximal nuclear diameter > 20μm) correlate with increasing DNA content and significantly poorer patient outcomes[162]. Similar findings are observed in bladder cancer where mean nuclear volume correlates with DNA content and pathologic grade[163]. Nuclear enlargement was also found to correlate with extensive submucosal invasion in CRC and when assessed in combination with additional factors (*e.g.* multilayered nuclei), this allowed for differential diagnoses between minimally invasive and highly invasive CRCs[164]. Evidently, nuclear size changes are indicative of DNA content changes in numerous cancer types, and may provide valuable diagnostic or prognostic information. As aneuploidy and polyploidy are a primary consequence of CIN, nuclear size represents a surrogate marker that could be monitored following alteration of a suspected CIN gene to rapidly identify putative CIN genes that may contribute to oncogenesis.

1.6.2. Micronucleus Formation as an Indicator for Small-scale DNA Content Changes

MNi are small, extra-nuclear bodies containing chromosomes or chromosomal fragments that fail to incorporate within a primary daughter nucleus following mitosis and nuclear membrane re-assembly[165,166]. Generally, two classes of events give rise to micronucleus (MN) formation termed aneugenic or clastogenic[165]. Mitotic aberrations leading to chromosome mal-segregation, lagging chromosomes or chromosomes that are physically separated from the bulk of the DNA, are considered aneugenic events that can result in the formation of MNi containing whole chromosomes. In contrast, clastogenic events include increased chromosomal breakages and inadequate DNA DSB repair, which can generate acentric chromosome fragments. As these chromosome fragments lack a centromere, they are unable to attach to the mitotic spindle and

segregate with the remaining chromosomes, and typically result in MNi harbouring chromosomal fragments[165]. Ultimately, alterations that induce CIN by adversely impacting mitotic spindle assembly, kinetochore-microtubule attachment, centrosome regulation, and DNA replication or damage repair, can also generate MNi. As such, MNi are indicative of CIN and are frequently observed in cancer[165-168]. In fact, MN formation is often assessed in the clinic and has emerged as a biomarker for screening and risk prediction with potential diagnostic and prognostic value. For instance, increased MN frequency within peripheral blood lymphocytes is predictive of increased risk for colorectal, urogenital, gastrointestinal, or lung cancer[169-171]. A retrospective study found that increased MN formation in urine cytology smears with atypical cells was sufficient for a definitive urothelial cancer diagnosis[172]. In oral squamous cell carcinoma, MN formation correlated with increasing tumour grade, and was proposed as a candidate grading biomarker[173]. Additionally, increased MN formation in erythropoietic bone marrow cells corresponded with decreased acute non-lymphocytic leukemia patient survival, compared to those with low MN formation[174]. The results of the above studies reflect the relationship between MN formation and CIN, and highlight the value of MN assessment in cancer. Accordingly, increases in MN formation following alteration of a gene of interest would serve as a surrogate marker for CIN and represents a valuable tool that can be exploited to identify genes with a potential role in CIN and oncogenesis. A MN enumeration screen would complement nuclear size assessments, as MN formation is indicative of small-scale numerical or structural CIN[165,175], while nuclear size changes presumably reflect large-scale chromosome content changes. A multiplexed screen capable of rapidly and simultaneously assessing these phenotypes would dramatically expedite the identification of novel human CIN genes.

CHAPTER 2: MATERIALS AND METHODS

2.1.0. Reagents

See Appendix A for a complete list of solutions and reagents employed in this study.

2.2.0. Cell Culture

The characteristic features of the three adherent, karyotypically-stable human cell lines utilized in this study are summarized in Table 2-1. HT1080 fibrosarcoma and immortalized (telomerase) normal skin fibroblast hTERT cell lines, were generously provided by Drs. J. Chubb (University College, London) and C. P. Case (University of Bristol, Bristol), respectively. The epithelioid colorectal carcinoma HCT116 cell line was purchased from American Type Culture Collection (Rockville, MD). Cell line authentication was validated based on cell viability, growth, morphology, and spectral karyotyping[176]. HT1080 and hTERT cells were cultured in Dulbecco's modified Eagle's medium/High glucose media (HyClone) and HCT116 was cultured in modified McCoy's 5A (HyClone, Logan, UT). All media was supplemented with 10% fetal bovine serum (FBS) (Sigma-Aldrich).

Table 2-1. Properties of Human Cell Lines Utilized in this Study

Cell Line	HT1080	hTERT	HCT116
Organism	Human	Human	Human
Tissue	Connective Tissue, Fibrosarcoma, Transformed	Foreskin, Fibroblast, Immortalized (Telomerase)	Colon, Epithelial, Colorectal cancer, Transformed
Properties	Adherent	Adherent	Adherent
Gender	Male	Male	Male
Required Medium	DMEM + 10% FBS	DMEM + 10% FBS	McCoys 5A + 10% FBS
Doubling Time	~22 hours	~36 hours	~22 hours
Karyotype	Diploid 46 XY, Stable	Diploid 46 XY, Stable	Near Diploid 45 XY, Stable
Source	Dr. J. Chubb (University College London, UK)	Dr. C. P. Case (University of Bristol, Bristol, UK)	American Type Culture Collection (Rockville, MD)

2.2.1. Cell Passaging

Cells were grown and maintained at subconfluent levels on 10 cm tissue culture dishes (Sarstedt) in a 37°C incubator with 5% CO_2, humidified with Milli-Q water containing cupric sulfate pentahydrate to prevent microbial/fungal growth (Appendix A), and were passaged in a biological safety cabinet every 2 – 3 days. Media was aspirated from the tissue culture dish and adhered cells were rinsed with sterile phosphate buffered saline (1× PBS) (Appendix A). To detach cells from the tissue culture dish, 2 mL of 0.05% trypsin containing ethylenediaminetetraacetic acid (EDTA) (Gibco; Life Technologies) was added for 5 minutes (min) for HCT116 and 8 min for HT1080 and hTERT at 37°C. Cell detachment was monitored with an inverted ID03 microscope (Zeiss) equipped with a 10× objective. Trypsin was neutralized in 2 mL of complete media and 2 mL 1× PBS, which was used to wash cells from the bottom of the plate. Suspended cells were collected and transferred to a 15 mL conical (Sarstedt)

and pelleted by centrifugation at 140 ×g at 21°C for 5 min in a Legend XFR centrifuge (Thermo Scientific). The supernatant was aspirated and the cell pellet was resuspended in 5 mL of 1× PBS. Approximately 1 mL of cell suspension was added back to the 10 cm plate containing 10 mL of fresh complete media and cell culture dishes were returned to the incubator.

2.2.2. Cell Counting and Seeding

Accurate cell counting is required to calculate and subsequently seed appropriate cell densities into the corresponding vessels (Table 2-2). First, cells were harvested as described above (*Section 2.2.1*). Following centrifugation and aspiration, the cell pellet was resuspended in ~5 mL of 1× PBS and passed through a 40 µm strainer to eliminate cell aggregates and obtain a single cell suspension. Cell suspension (40 µL) was added to a 0.5 mL microcentrifuge tube and mixed with an equal volume of 0.2% trypan blue stain (Gibco). Viable cells with intact cellular membranes will exclude the dye, whereas dead or dying cells with compromised membrane integrity will stain blue. Next, 10 µL of the trypan blue – cell suspension was dispensed in duplicate into the cell counter Cedex Smart Slide (Roche) compartments. The Cedex XS (Roche) cell counter captures images of the cells within both compartments of the Cedex slide, distinguishes between live and dead cells according to trypan blue exclusion, and provides the average concentration of viable cells in the PBS solution. This value was utilized to calculate the appropriate volumes of cell solution to be diluted in complete media, such that the desired number of cells can be seeded in the corresponding vessels for all experiments (Table 2-2).

Table 2-2. Cell Seeding Protocols Employed with Corresponding Experimental Approaches

Treatment	Cell Line	Experimental Approach[A]	Plate Format	Days[B]	Cells ($\times 10^3$) (Exp)[C]	Cells ($\times 10^3$) (Control)[D]
Forward Transfection (Direct Tests)	HT1080	NA, MN	6-well plate	4	50	40
	hTERT	NA, MN,WB, IIF, MS	6-well plate	6	40	20 - 35
	HCT116	NA, MN,WB, IIF, MS	6-well plate	4	75 - 220	40 - 75
Reverse Transfection (High-Content)	HT1080	NA, MN	96-well plate	4	2	2
	hTERT	NA, MN	96-well plate	6	2	2
	HCT116	NA, MN, IIF	96-well plate	4	2	2

[A]Abbreviations of experiments/analyses performed: NA (nuclear area assay), MN (micronucleus enumeration assay), WB (western blot), IIF (indirect immunofluorescence), and MS (mitotic chromosome spread analyses).
[B]Days = Experiment time course (post-transfection). Note: All western blots performed 4 days post-transfection.
[C]Cell numbers (in thousands) seeded in experimental wells (*e.g.* Putative CIN gene silencing).
[D]Cell numbers (in thousands) seeded in control wells (*e.g.* Untreated and si*GAPDH*).

2.3.0. siRNA-based Gene Silencing

Forward short interfering (si)RNA transfection (cells seeded prior to transfection) and reverse transfection (cells seeded simultaneously with transfection) were employed for direct silencing tests (*Chapters 3-5*) and high-content screening (*Chapters 4 and 5*) respectively, to execute the corresponding experimental approaches and analyses listed in Table 2-2. Optimal siRNA and transfection reagent conditions were experimentally determined as those that cause efficient gene silencing according to western blot analyses (*Section 2.6.0*) but also maintain cell viability. Sequences are proprietary, belonging to Dharmacon, and not listed in this thesis.

2.3.1. siRNA-based Gene Silencing by Forward Transfection

To perform a forward transfection, cells were processed and counted as described above (*Sections 2.2.1 and 2.2.2*). Appropriate cell densities for each cell type (HT1080, hTERT or

HCT116) and condition were seeded in complete media into each well of 6-well tissue culture plate (Cellstar; Greiner Bio-one) containing 70% Ethanol-sterilized (Appendix A) coverslips (18 x 18; Fisherbrand) for all microscopy-based analyses, or a 6-well plate (Falcon; Corning) without coverslips for western blot analyses (Table 2-2). Cells were allowed to attach to the bottom of the vessel and grow for 24 hours (h) before transient transfection by standard, RNAiMAX (Invitrogen) lipid-based transfection as detailed below.

Sets of four ON-TARGETplus siRNA duplexes targeting distinct mRNA coding regions for each gene of interest and the Glyceraldehyde-3-Phosphate Dehydrogenase (*GAPDH*) control were purchased from Dharmacon. All four siRNA duplexes for each gene were resuspended in 1× siRNA buffer (Dharmacon; Appendix A) to a stock concentration of 20 µM and a working dilution of 10 µM. A 10 µM siRNA pool for each gene was prepared by combining equal volumes of all four distinct 10 µM siRNA duplexes. Small ~10 µL siRNA aliquots were stored at -80ºC to minimize freeze-thaw cycles. To silence the gene of interest in cells within each well of a 6-well tissue culture plate, 1 µL of 10 µM siRNA was added to 250 µL serum-free media and separately, 6 µL RNAiMAX was added to 250 µL serum-free media. The siRNA and RNAiMAX solutions were mixed in a 1:1 ratio, inverted gently and allowed to incubate at room temperature (RT) for 20 min. The total 500 µL volume for each condition was then added to the appropriate well. Plates were rocked gently and returned to the incubator for the duration of the experiment (Table 2-2), at which point they were treated accordingly, depending on the experimental approach to follow (protein extraction, fixation, *etc.*). For all genes of interest, silencing efficiency was validated by western blot analyses as in Section 2.6.0.

2.3.2. siRNA-based Gene Silencing by Reverse Transfection

For high-content screening, custom-arrayed 96-well reverse transfection format plates were ordered from Dharmacon. Each well contains a desiccated pool of 4 distinct siGENOME siRNA duplexes (6.25 ρmol total) that target distinct mRNA regions of specific genes of interest, and in separate wells, the appropriate positive, negative, or transfection controls. Desiccated siRNAs were rehydrated in 25 µL of DharmaFECT Cell Culture Reagent (Thermo Scientific) containing 0.2 µL of DharmaFECT 2 transfection reagent (Thermo Scientific) for 30 min. HT1080 and hTERT (*Chapter 4*) or HCT116 (*Chapter 5*) cells were processed as described above (*see Sections 2.2.1 and 2.2.*2) and the appropriate cell numbers were seeded in 100 µL complete media into each well containing rehydrated siRNA and DharmaFECT mixture. Plates were gently rocked, allowed to sit at RT for 30 min until cells began to settle on the bottom of the plate, and returned to the incubator to grow over 4 (HT1080 or HCT116) or 6 (hTERT) days at 37˚C. Following incubation, equal volumes of 8% paraformaldehyde (VWR Canlab) (Appendix A) was added to media within each well (4% final concentration), and cells were fixed for 10 min. Fixative was carefully aspirated, cells were rinsed with 1× PBS and counter-stained with 200 µL of 300 ng/mL Hoechst (Thermo Scientific) in 1× PBS (Appendix A) to visualize DNA. Plates were imaged and analyzed (*see Sections 2.5.2-5*). HCT116 cells of the high-content screen (*Chapter 5*) were fixed and immunofluorescently labelled as described in Section 2.4.2. High-content screens were executed once per cell line in Chapter 4 (N = 1) and twice in HCT116 in Chapter 5 (N = 2).

2.4.0. Fluorescent Labelling of Human Cells

Fluorescent labelling was employed throughout this study to visualize cellular components including nuclei, MNi, cell membranes, and proteins of interest using fluorescent microscopy.

2.4.1. Standard DNA Labeling for NA and MN Analyses

Following siRNA-based gene silencing by forward transfection (*Section 2.3.1*), media from each well was aspirated and cells were fixed in 1.5 mL of 4% paraformaldehyde (Appendix A) for 10 min at RT. Cells were washed twice in 1× PBS and cell membranes were permeabilized in ~2 mL of 0.5% Triton X in 1× PBS (Appendix A) for 10 min at RT, then rinsed with 1× PBS. Coverslips were applied slowly cell-side-down to an 8 µL droplet of 0.5 µg/mL DAPI (Sigma-Aldrich) in Vectashield Mounting Media (Vector Laboratories) adhering the coverslips to the glass slides. Slides were stored at 4°C protected from light for at least 24 h before proceeding with microscopy to ensure uniform DAPI labeling.

2.4.2. Indirect Immunofluorescence Labelling

For protein labeling using indirect immunofluorescence (IIF), cells were fixed and permeabilized as described above. Following permeabilization, coverslips were incubated cell-side-down on parafilm containing 30 µL aliquots of primary antibody targeted against the protein of interest in 1× PBS, for 1 h in a humidified chamber. Cells were washed with 0.1% Triton X in 1× PBS (Appendix A) and twice with 1× PBS. Coverslips were incubated on a 30 µL aliquot of fluorescently labelled secondary antibody targeted against the primary. See Table 2-3 for the complete list of primary and secondary antibodies and the corresponding dilutions utilized throughout this thesis for IIF. Following a 1 h incubation in the humidified chamber protected from light, 0.1% Triton X (1×) and 1× PBS (2×) washes were performed and cells were counterstained with 8 µL of DAPI Mounting Media and affixed to glass slides.

Table 2-3. List of Antibodies Utilized in this Study

Protein of Interest[A]	Species	Catalog Number	[WB][B]	[IIF][C]
Primary Antibodies				
α-Tubulin*	Mouse	Abcam; ab7291	1:4,000	-
ARL2	Rabbit	Abcam; ab183510	1:5,000	-
BUB3	Rabbit	Abcam; ab4180	1:5,000	-
CCNE1	Rabbit	Abcam; ab133266	1:5,000	1:200
CCP110	Rabbit	Abcam; ab99337	-	1:800
CENPA	Mouse	Abcam; ab13939	-	1:200
CENPB	Rabbit	Abcam; ab27534	-	1:200
CETN1 (Centrin)	Rabbit	Abcam; ab101332	-	1:800
Cyclophilin B*	Rabbit	Abcam; ab16045	1:50,000	-
DSN1	Rabbit	Thermo Fisher; PA534879	1:1,000	-
EMI1	Mouse	Abcam; ab215765	1:2,000	-
GARS	Rabbit	Abcam; ab42905	1:5,000	-
GART	Rabbit	Abcam; ab169550	1:5,000	-
γH2AX	Rabbit	Abcam; ab2893	-	1:1,000
HJURP	Rabbit	Abcam; ab220016	1:4,000	1:500
NUF2	Rabbit	Abcam; ab176556	1:20,000	-
ODF2/1 (Cenexin)	Rabbit	Abcam; ab43840	-	1:800
PCNT (Pericentrin)	Mouse	Abcam; ab28144	-	1:200
PIGS	Rabbit	Abcam; ab113817	1:5,000	-
RPA32/RPA2	Mouse	Abcam; ab2175	-	1:200
SHMT2	Rabbit	Abcam; ab180786	1:1,000	-
BIRC5 (Survivin)	Rabbit	Abcam; ab76424	1:4,000	1:200
SKP1	Mouse	Abcam; ab124473	1:5,000	-
SPC24	Rabbit	Abcam; ab157184	1:5,000	-
Secondary Antibodies				
Anti-Rabbit HRP	Goat	Jackson Immunoresearch; 111-035-144	1:10,000	-
Anti-Mouse HRP	Goat	Jackson Immunoresearch; 115-035-146	1:10,000	-
Anti-Rabbit AlexaFluor488	Goat	Abcam; ab150081	-	1:200
Anti-Mouse CY3	Goat	Abcam; ab150117	-	1:200

[A]The protein targeted by the antibody. Note: Proteins listed with an asterisk represent western blot loading controls. HRP = horse radish peroxidase.
[B]Concentration of antibody employed for western blot analyses.
[C]Concentration of antibody employed for indirect immunofluorescence.

The IIF labelling protocol above was modified for centrosomal protein labeling (*Chapter 5*). Cells were fixed with 1.5 mL of ice-cold 100% Methanol for 10 min at RT. Cells were washed twice in 1× PBS and permeabilized with 0.5% Triton X (10 min) and rinsed with 1× PBS. Coverslips were subjected to a 1.5 h blocking step, incubating cell-side-down on 30 µL of 1% Bovine Serum Albumin (BSA) in 1× PBS (Appendix A) prior to antibody incubation. Excess blocking solution was blotted from coverslips, which were transferred to 30 µL aliquots of primary antibody in 1% BSA in 1× PBS blocking solution, for 3 h in a humidified chamber. Standard 0.1% Triton X (1×) and 1× PBS (2×) washes were performed and coverslips were incubated on a 30 µL droplet of the appropriate secondary antibody in blocking solution for 1 h protected from light in the humidified chamber. Cells were washed and counterstained with DAPI as above.

For IIF labelling following reverse transfection in a 96-well plate (*Chapter 5*), cells were fixed with 4% paraformaldehyde as described in Section 2.3.2, rinsed with 1× PBS and permeabilized for 10 min in 150 µL of 0.5% Triton X. Cells were rinsed twice with 1× PBS, and 60 µL of the desired primary antibody diluted in 1× PBS was added to each well and allowed to incubate overnight in a humidified chamber. Subsequently, cells were washed with 0.1% Triton X, twice with 1× PBS, and 60 µL of the appropriate secondary antibody diluted in 1× PBS was applied to each well and incubated protected from light for 2 h at RT. The 0.1% Triton X and 1× PBS washes were repeated and cells were counterstained with 300 ng/mL Hoechst as described in Section 2.3.2.

2.4.3. Co-Labelling to Visualize DNA Synthesis and Cell Membranes

To identify multinucleated cells and assess DNA synthesis within multinucleated cells (*Chapter 4*), the Click-iT™ 5-ethynyl-2'-deoxyuridine (EdU) Alexa Fluor™ 647 Imaging Kit

(Thermo Scientific) and Wheat Germ Agglutinin (WGA) Alexa Fluor™ 488 Conjugate Labelling Kit (Thermo Scientific) were utilized in combination. hTERT cells were cultured and transfected on ethanol-sterilized coverslips for 6 days as above. Media (1 mL) from each well was removed and 1 mL of pre-warmed 20 μM EdU in complete media (Appendix A) was added for a final concentration of 10 μM EdU per well (Appendix A). Cells were returned to the incubator for 20 min and EdU-containing media was removed. Cells were fixed in 1.5 mL of 4% paraformaldehyde for 10 min at RT. Paraformaldehyde was removed and cells were rinsed 3× with 1.5 mL Hank's balanced salt solution (1× HBSS) for mammalian cells (Thermo Scientific). Coverslips were incubated cell-side down on parafilm containing 30 μL aliquots of 5 μg/mL WGA solution prepared from 1 mg/mL stock (Appendix A) for 10 min at RT. When cell membrane labeling was complete, cells on coverslips were washed twice with 1× HBSS and permeabilized in ~2 mL of 0.5% Triton X for 10 min at RT, and rinsed twice with 1× PBS. Coverslips were incubated cell-side down on parafilm containing 30 μL aliquots of Click-iT® Reaction Cocktail (Appendix A) for 30 min protected from light. Coverslips were washed once with 1 mL of 1× PBS, counterstained with 8 μL of DAPI Mounting Media and affixed to glass slides.

2.5.0. Fluorescent Microscopy Imaging and Assessment

Fluorescent microscopy was performed manually to image cells on coverslips from direct silencing tests (*Chapters 3-5*), and automated microscopy was employed for imaging 96-well plates in high-content screening (*Chapters 4 and 5*).

2.5.1. Manual Fluorescent Microscopy Imaging for Direct Tests

Images were acquired using an AxioImager Z1 Microscope (Zeiss) equipped with an AxioCam HR charge-coupled device (CCD) camera (Zeiss). Objective lenses employed included a 20× Plan-Neofluar lens (0.5 numerical aperture), a 40× EC Plan-Neofluar oil immersion lens (1.30 numerical aperture), and a 63× Plan-Apochromat oil immersion lens (1.40 numerical aperture). Immersol 518F immersion oil (Zeiss) with a 1.518 refractive index was utilized with 40 and 63× oil immersion objectives. Filter cubes including the Filter Set 49HE DAPI, 38HE FITC, and 43HE CY3 (Zeiss) were employed when appropriate to acquire DAPI, Alexafluor488, and CY3 channels, respectively. Exposure times were independently optimized for each channel and the dynamic range was set to 85% to eliminate the potential for channel saturation. For quantitative analyses, exposure times for each channel were maintained constant throughout image acquisition for all conditions. For three-dimensional (3D) image acquisitions, a series of images spanning the entire thickness of the nuclei were acquired at 0.4 μm intervals. To assess subcellular structures, 3D image series were imported into AutoQuant X3 (Media Cybernetics) for deconvolution prior to image analysis. Images were processed by maximum-likelihood expectation deconvolution using a constrained iterative algorithm and theoretical point spread functions for each channel. Conversely, a single image in the focal plane was acquired for two-dimensional (2D) image acquisitions. All images were imported into Imaris v7.7.2 (Bitplane) image visualization software and analyzed as detailed below (*see Sections 2.5.3 and 2.5.5*). Representative images were exported into Photoshop Creative Suite 6 (Adobe) where figure panels were assembled.

2.5.2. Automated High-Content Fluorescent Microscopy Imaging

Imaging of 96-well plates was performed using a Cytation 3 Cell Imaging Multi-Mode Reader (Bio-Tek) equipped with a 16-bit, gray scale, charge-coupled device camera (Sony) and an Olympus 20x lens (0.45 numerical aperture). Using Gen5 Software (Bio-Tek), exposure times were optimized for the Hoechst channel (Semrock DAPI filter) and when appropriate (*Chapter 5*), the AlexaFluor488 channel (Semrock GFP filter). The Auto Focus with Optional Scan feature was employed for image acquisition. A total of 9 non-overlapping (3×3 matrix) 2D images were acquired from each well and imported into Imaris for analysis. Representative images were exported into Photoshop CS6 and figure panels were assembled.

2.5.3. Quantification of Nuclear Volumes or Nuclear Areas

The Surfaces function of the Imaris software was employed to automatically generate surface renderings of interphase nuclei based on the Hoechst/DAPI signal, from which nuclear volumes (3D images) or NAs (2D images) were calculated. To ensure that only complete nuclei were included in the analyses, an XY boundary exclusion filter (< 1 μm) was employed to remove partial nuclei located along the image periphery, while inclusion filters were employed for area (250 μm^2 > 2800 μm^2) and mean DAPI intensity (4500 < 5×10^4 au) to eliminate small, brightly stained nuclear debris (*i.e.* apoptotic bodies) and mitotic cells. In general, a minimum of 100 nuclei were assessed for each condition. Nuclear volume/NA data was exported into Prism v6 (GraphPad), where Student's *t*-tests and two-sample Kolmogorov-Smirnov (KS) tests were performed and graphs including dot plot, box-and-whisker, and cumulative frequency distributions were generated.

For high-content screening (*Chapters 4 and 5*), genes that when silenced, induced a statistically significant change in cumulative frequency distributions according to KS tests (*p*-

value < 0.01) compared to si*GAPDH* negative controls were identified as putative human CIN genes. A *p*-value of 0.01 was utilized to create stringent conditions such that only the most promising genes inducing the strongest NA changes would be identified by the high-content screen. Conditions with < 40 interphase nuclei were excluded from subsequent analyses as they are predicted to induce death and/or cell cycle arrest. The cut-off value of 40 nuclei was determined through comparisons with conditions known to induce cell death, such as silencing of the essential gene Polo-like Kinase 1 (*PLK1*).

2.5.4. Quantification of Signal Intensities of Immunofluorescently Labelled Proteins

In addition to the standard nuclear DAPI labelling, cells that were immunofluorescently labelled for a protein of interest (*see Section 2.4.2*) were imaged using the DAPI filter in addition to the corresponding Alexa Fluor 488 and/or CY3 filters(s) as described above (*Section 2.5.1*). Following the generation of nuclear masks in Imaris (*Section 2.5.3*), the intensities of the Alexa Fluor 488 or CY3 channels overlapping with DAPI within the nuclear mask were automatically calculated. For assessing centromeric signals that do not overlap with the nucleus, the larger Pericentrin Alexa Fluor 488 centrosomal signal was used to generate the initial mask and the number of CY3 centriolar signal foci per centrosome was automatically calculated in Imaris. All signal intensities and focal counts for each nucleus or centrosome were exported into Prism for statistical analyses.

2.5.5. Micronucleus Enumeration Assay

The number of MNi in each condition was quantified using the Surfaces function in Imaris. MNi were operationally defined as small (< 1/3 the size of the nucleus), extra-nuclear, DAPI-stained bodies exhibiting no visible attachments with the primary nucleus[165]. Accordingly, area (1.25 μm^2 > 70 μm^2) and DAPI intensity center (> 1×10^4 au) inclusion/exclusion filters were

employed to exclude nuclei and apoptotic bodies. The total number of MNi in a given condition was normalized to the number of nuclei. MN data were imported into Prism where statistical analyses were performed and graphs were generated as above. To identify genes causing a significant increase in MN formation, an operational definition was employed based on a 95% confidence interval of the si*GAPDH* MN data. Genes causing an increase in MN formation > 2 standard deviations above the si*GAPDH* mean (beyond the 95% confidence interval) were deemed significant and identified as putative CIN genes. Conditions with < 40 nuclei were excluded from subsequent analyses.

2.6.0. Western Blot Analyses

Western blot analyses were employed to validate siRNA-based silencing for all genes of interest (*Chapters 3-5*). Additionally, western blotting was utilized to assess changes in the levels of downstream SCF complex target proteins (*e.g.* CCNE1) following *SKP1* silencing (*Chapter 6*).

2.6.1. Whole Cell Protein Extraction

Cells were seeded, silenced, and grown in 6-well tissue culture plates (Falcon; Corning) as described above (Table 2-2). To harvest whole cell protein lysates from siRNA-treated and negative control cells, cell culture media was aspirated from each well and cells were rinsed 3× with 4°C 1× PBS. Protein extraction buffer (200 µL) consisting of modified radioimmunoprecipitation assay (RIPA) buffer (Appendix A) and 25× protease inhibitor (cOmplete EDTA-free; Roche) (Appendix A) was added to each well and allowed to incubate at 4°C for 5 min. Using a cell scraper, cells remnants and protein lysates from each condition were collected and transferred to individual 1.5 mL microcentrifuge tubes. Samples were sonicated

twice in 3 second intervals using a Sonifer Cell Disrupter (Branson Sonic Power Co.) with a duty cycle of 50% and an output control setting of 6. Insoluble cellular debris was pelleted by centrifugation (Biofuge Fresco; Thermo Scientific) at 16,060 ×g for 2 min at 4ºC. The supernatant containing soluble proteins was carefully transferred into a sterile 1.5 mL microcentrifuge tube without disturbing the pellet and placed at -20ºC for short-term storage (< 2 weeks) or at -80ºC for long-term storage (> 2 weeks).

2.6.2. Protein Quantification via Bicinchoninic Acid Assay

A Pierce Bicinchoninic Acid (BCA) Assay kit (Thermo Scientific) was utilized according to manufacturer's instructions to quantify protein concentrations from each whole protein lysate sample. First, 200 µL of a 1:50 ratio of BCA-containing Reagent A and 4% cupric sulfate-containing Reagent B were dispensed into a 96-well plate (Corning). A set of 9 BSA protein standards of known concentrations ranging from 0 µg/mL to 2000 µg/mL were dispensed in duplicate (25 µL per well) and 5 µL of each unknown were dispensed along with 20 µL of RIPA diluent (25 µL volume) in triplicate. The BCA assay plate was incubated in the dark at 37°C for 1 h. Following incubation, the Cytation 3 (BioTek) plate reader function was employed to acquire 562 nm absorbance measurements for each well. The concentration of each diluted protein sample in the plate was determined by comparing the absorbance values to that of the standard curve generated from the BSA readings. Values from the 3 readings were averaged for each sample, and multiplied by 5 to calculate the final protein concentrations.

2.6.3. Electrophoresis and Immunoblotting

Following protein quantification, the appropriate volumes containing 20 µg protein for each sample were combined with 6× SDS Sample Loading Buffer (β-mercaptoethanol) (Appendix A) and RIPA diluent to a maximum volume of 25 µL. Samples were incubated at

95°C for 10 min with 1 min intervals of 700 rpm orbital mixing in a Thermomixer R (Eppendorf) to denature proteins. Denatured samples were allowed to cool to RT and were dispensed along with a Precision Plus Protein Dual Color Standards (BioRad) molecular weight ladder into pre-rinsed mini-Protean TGX gel wells (BioRad). A 4-20% mini-Protean TGX gel was utilized when assessing proteins of interest that were < 40 kDa in size, whereas a 7.5% gel was used for those > 40 kDa. Samples were electrophoresed in Miniprotean tank (BioRad) containing 1× Running Buffer (Appendix A) at a constant voltage (140 V) for 65 min at 4 °C using a PowerPac HC (BioRad) power supply. To prepare for transfer, polyvinylidene difluoride (PVDF) membranes (Millipore) were activated with methanol and rinsed 3× with Milli-Q water. For proteins < 40 kDa or > 40 kDa, PVDF membranes with 0.2 µm or 0.45 µm pore sizes were utilized, respectively. Proteins were electrophoretically transferred to the PVDF membrane at a constant voltage (14 V) for 45 min at RT in a TransBlot SD Semi-Dry Transfer Cell (Bio-Rad) containing 1× Transfer Buffer (Appendix A).

To assess protein transfer quality, PVDF membranes were stained with 5 mL of the total protein stain copper phthalocyanine 3,4',4'',4'''-tetrasulfonic acid tetrasodium salt (CPTS) (Appendix A) for 10 min at RT. Membranes were briefly de-stained with a 5 min wash in Tris-buffered saline solution containing 0.1% Tween 20 (TBST) (Appendix A) before visual inspection to ensure high quality protein transfer (even loading, no air bubbles, *etc.*). Membranes were blocked with 5% Non-fat Milk in 1× TBST (Appendix A) for 1 h at RT. Blocked membranes were transferred to ~5 mL of 5% Non-fat Milk containing primary antibody at the appropriate concentration (Table 2-3) overnight at 4°C with gentle rocking. Following incubation, primary antibody solution was removed and blots were rinsed 3× with 1× TBST (Appendix A) for 10 min each on a Belly Dancer (Stovall Life Science Inc.) set to medium

mixing speed. Membranes were incubated with appropriate secondary antibody conjugated to horse radish peroxidase (HRP) in ~5 mL of 5% Non-fat Milk for 1 h at RT with gentle rocking. Table 2-3 provides a complete list of the primary and secondary antibodies employed in this study including the working concentrations for western blot analyses.

2.6.4. Semi-Quantitative Immunoblot Analysis

To visualize the labelled proteins of interest, secondary antibody solution was removed and blots were washed 3× with 1× TBST. The SuperSignal West Dura Extended Duration Substrate (Thermo Scientific) was utilized as described by the manufacturer. Briefly, visualization solution was made by combining equal volumes of the Stable Peroxide Solution and the Luminol/Enhancer Solution, adding ~800 µL to the surface of the membrane, and incubating 5 min at RT. Excess visualization solution was removed and the membranes were placed into a clear sheet protector. Proteins of interest were visualized by standard chemiluminescence and 8-bit TIFF images were acquired with a MyECL imager (Thermo Scientific) using optimal exposure times (*i.e.* produce a strong signal without pixel saturation). Images were compiled in Photoshop CS6 and analyzed using MyImageAnalysis software. Local Background Corrected Density values were used to perform semi-quantification of protein expression levels. Band intensities were first normalized to the loading controls α-Tubulin or Cyclophilin B and compared to the normalized intensity of si*GAPDH* to evaluate siRNA silencing efficiency and determine whether protein expression differs between samples.

2.7.0. Identification of Candidate CIN Genes by Cross-species Approaches

Cross-species candidate gene approaches were employed to identify the most promising human candidate CIN genes to be subjected to screening by NA and MN assays described in

Sections 2.5.3 and 2.5.5 (*Chapter 4*). Recently, Stirling *et al*[65] performed a systematic screen in budding yeast (*S. cerevisiae*) and identified a comprehensive list of 692 CIN genes. Of those, 485 genes were found to have sequence-based and/or functional human orthologs. A total of 164 human genes with corresponding yeast orthologs reported to exhibit a strong meta-score (*i.e.* repeatedly demonstrated a strong CIN phenotype by at least one CIN assay[65]), but were not already well-established human CIN genes in the literature, were selected for screening.

2.8.0. Prioritization and Selection of Putative CIN Genes for Validation

Following high-content NA and MN screening in HT1080 and hTERT cells (*Chapter 4*), putative CIN genes were prioritized such that a manageable subset of 10 promising putative CIN genes could be pursued in validation. Prioritization was primarily based on the number of assays (NA HT1080, NA hTERT, MN HT1080, or MN hTERT) that identified the gene. Only genes that were identified in a minimum of 3/4 screens were deemed eligible for selection. Of the genes identified by both NA and MN assays in both HT1080 and hTERT cells (4/4 screens), the most promising putative CIN genes were defined as those inducing the strongest CIN phenotypes including the largest fold changes in median NA and greatest increases in MN formation. The top 5 highest ranked genes were selected for validation. As hTERT cells are typically more resistant to MN formation, 5 additional genes of interest were selected from the subset of genes identified by the NA assay in both cell types and the MN assay in HT1080 (3/4 screens). As these putative CIN genes displayed stronger CIN phenotypes in the cancer cell line, they were selected not only because they displayed extensive NA changes or MN formation but because they are frequency altered in a variety of cancer types according to available online databases (*e.g.* cBioPortal[155,156]) and may have important implications for oncogenesis.

2.9.0. Generation of Mitotic Chromosome Spreads and Chromosome Enumeration

To generate mitotic chromosome spreads, asynchronous cells were cultured and transfected on ethanol-sterilized coverslips in 6-well tissue culture plates and allowed to grow over 6 (hTERT) or 4 days (HCT116) as described above. Following incubation, cells were mitotically enriched using KaryoMAX colcemid (Gibco) at a dilution of 100 ng/mL (Appendix A) in complete media for 4 h (hTERT) or 2 h (HCT116) prior to harvesting. The colcemid-containing media was aspirated from each well and 2 mL of 75 mM KCl hypotonic solution (Appendix A) was added to each well for 8 (hTERT) or 16 min (HCT116). Cells were fixed with a 3:1 mixture of methanol:acetic acid (Appendix A) in three 10 min intervals. Fixative was aspirated and coverslips were placed on their side and allowed to air dry. Coverslips were mounted onto glass microscope slides with DAPI Mounting Media (Appendix A) and stored in the dark at 4 °C for at least 24 h prior to imaging. Mitotic chromosome spreads were visualized and imaged using an AxioImager Z1 microscope equipped with a 63× (1.4 numerical aperture) oil-immersion, plan apochromat lens and a Zeiss HRm CCD camera. A minimum of 100 spreads per condition were imaged and the 16-bit TIFFs were imported into FIJI software for manual chromosome enumeration and visual assessment. Chromosome spreads were classified as aberrant if they displayed small-scale (gained or lost fewer than 15 chromosomes), or large-scale numerical changes (gained or lost 15 chromosomes or more), structural abnormalities (*e.g.* chromosome breakages or decompaction), or cohesion defects (separation of sister chromatids). Mitotic chromosome spread analyses were performed once per condition per cell line (N = 1), for validation purposes. Statistical differences in the cumulative chromosome content frequency distributions between experimental conditions and the si*GAPDH* control were assessed using

two-sample KS tests (Prism) and a *p*-value of < 0.05 was deemed significant. Graphs were generated in Prism and figures assembled in Photoshop CS6.

2.10.0. Treatment with DNA Damage-Inducing Drugs

DNA damage-inducing drugs including Bleomycin (DNA DSBs) and Hydroxyurea (HU) (replication stress) were employed in Chapter 5 to serve as positive controls against which, the si*SKP1* HCT116 cells can be compared.

2.10.1. Treatment of HCT116 Cells with Hydroxyurea

HU-treated cells were utilized as a positive control for replication stress. A dilution of 20 mM HU in pre-warmed (37°C) complete media was prepared from the 100 mM stock. 1 mL of media from an untreated well containing 2 mL was removed and 1 mL of 20 mM HU (10 mM final) was added. Plates were gently rocked and returned to the incubator for 3 h to induce replication stress. Plates were fixed and immunofluorescently labelled for RPA, imaged and quantified as described in Section 2.4.2.

2.10.2. Treatment of HCT116 Cells with Bleomycin

Cells were treated with Bleomycin to serve as a positive control for DNA damage and to induce γH2AX foci that are a surrogate marker for DNA DSBs. A dilution of 0.2 μg/mL of Bleomycin in pre-warmed (37°C) complete media was prepared from the 1 mg/mL stock solution. 1 mL of media from an untreated well containing 2 mL of media was replaced with 1 mL of 0.2 μg/mL Bleomycin for a final concentration of 0.1 μg/mL. Plates were gently rocked and returned to the incubator for 2 h to allow for DNA damage to occur. Plates were fixed and immunofluorescently labelled for γH2AX as described in Section 2.4.2. The number of γH2AX foci per interphase nucleus, were manually assessed in Imaris. The standard definition of ≥ 5 γH2AX foci per nucleus[177,178] was employed as the cut-off value for positive nuclei.

2.11.0. Experimental Reproducibility and Statistical Analyses

Experiments presented in this thesis were performed at least 3 times ($N \geq 3$) to ensure experimental reproducibility with sample sizes of $n \geq 100$, unless otherwise stated. Data sets from one representative experimental replicate are presented. Prism v6 (GraphPad) was employed for all statistical analyses including linear regression analysis, Student's *t*-tests, and Kolmogorov-Smirnov tests. Linear regression was employed to determine whether there was a relationship described by a simple linear regression model between two data sets. The Student's *t*-test is a parametric statistical test employed to distinguish whether differences in population means (experimental vs. controls) that follow a normal distribution were statistically significant. Non-parametric Kolmogorov-Smirnov tests were utilized to evaluate whether differences in cumulative frequency distributions between values from a treated sample is statistically different from controls. For all tests, a *p*-value of < 0.05 was considered statistically significant, with exception of NA high-content screening where a *p*-value of < 0.01 was required. These highly stringent conditions were employed to ensure only the most promising putative CIN genes inducing the most extensive NA changes would be deemed significant and identified by the high-content screen.

CHAPTER 3

DEVELOPMENT OF MICROSCOPY-BASED ASSAYS TO DETECT THE PHENOTYPES UNDERLYING CHROMOSOME INSTABILITY IN HUMAN CELLS

3.1.0 Abstract

CIN is characterized by a progressive change in chromosome numbers or structures. It is a characteristic common to virtually all cancer types, and is commonly observed in highly aggressive and drug resistant tumors. Despite this, the majority of human CIN genes have yet to be elucidated. In this study, we developed and validated multiplexed assays capable of detecting two different phenotypes associated with CIN. Large-scale chromosome content changes were detected by quantifying changes in nuclear volumes and/or areas following RNAi-based gene silencing. MN enumeration was also performed, as an increase in MN formation is a classic hallmark of CIN. To validate the ability of each assay to detect phenotypes that underlie CIN, we silenced the established CIN gene, *SMC1A* in a human fibrosarcoma cell line (HT1080). Following silencing we detected increases in nuclear volumes and MN formation relative to controls (untreated and si*GAPDH*). Similar results were obtained in an unrelated human fibroblast cell line (hTERT). These findings indicate that each assay is capable of detecting CIN-associated phenotypes that correspond with chromosomal defects, and can be utilized in future experiments to uncover novel human CIN genes, which will provide critical insight into the pathogenesis of cancer.

3.2.0. Introduction

In order to develop superior cancer therapies, it is essential to gain a greater understanding of the etiologic origins and aberrant molecular mechanisms that drive oncogenesis. CIN, characterized by progressive numerical and/or structural chromosomal changes[1,47], serves as a driving force for cancer initiation and progression by increasing the rate at which oncogenes or tumor suppressor genes are gained or lost, respectively[2,179]. Although CIN is associated with highly aggressive cancers[61], multi-drug resistance[4,180], disease recurrence[60] and poor patient prognosis[181], the aberrant molecular origins underlying CIN remain largely unknown[47]. Therefore, identifying and characterizing the altered genes responsible for CIN is critical. This will not only provide a greater understanding of their potential role(s) in oncogenesis, but may also provide insight into how these altered CIN-associated genes and biological pathways can be exploited in therapeutic approaches designed to better combat cancers that exhibit CIN.

A significant challenge associated with CIN gene identification is that the CIN phenotype is heterogeneous and can arise from alterations involving numerous, distinct biological pathways, many of which still remain unknown. Defects associated with sister chromatid cohesion, centrosome homeostasis, cell cycle control/check-points, DNA replication, and DNA damage repair[68,179], have all been implicated in CIN. For example, sister chromatid cohesion is established following DNA replication[182] and is mediated by the cohesin complex and accessory proteins as described previously (*see Section 1.3.2*). Its main function is to prevent premature sister chromatid separation and ensure proper chromosome segregation and stability during mitosis[183]. Studies show that diminished expression of cohesion-related genes including the cohesin subunit, *SMC1A*, are associated with large-scale chromosome content changes characterized by an increase in the number of tri- and tetraploid cells[62,184-186]. More recently,

SMC1A and the cohesin complex have demonstrated additional roles in centrosome dynamics, mitotic spindle assembly, DNA damage-induced cell cycle checkpoints and DNA damage repair processes[187-189]. Thus, *SMC1A* alterations may not only result in large-scale numerical chromosome changes, but also smaller-scale changes involving individual chromosomes, or chromosomal fragments. Depending on the biological pathways impacted (*e.g.* large chromosome number changes due to chromosome missegregation vs. generation of an acentric chromosome fragment that cannot segregate properly), it is possible that altering a particular CIN gene could manifest as either large or small-scale DNA content changes or a combination of both. In order to assess candidate genes for a potential role in CIN, it is critical that assays capable of detecting both large and small-scale chromosomal changes be employed in a multiplexed approach to ensure variations of CIN phenotypes are readily detected.

Despite what is known about the pathways underlying CIN, relatively few human CIN genes have been identified. The gaps in our knowledge are attributed at least in part, to the lack of highly efficient methodologies capable of detecting CIN. Traditional cytogenetic approaches including chromosome enumeration within mitotic chromosome spreads are laborious, costly, and unsuitable for the high-throughput screening of hundreds to thousands of candidate genes[62-64]. These limiting aspects highlight the need for novel CIN detection methods that are amenable to rapid, high-content screening, in order to identify maximal numbers of novel CIN genes in humans. As described above (*Section 1.6.1*), the detection of nuclear size changes has begun to emerge as a surrogate marker for DNA content changes that underlie CIN. Conceptually, large increases in chromosome numbers will be reflected by corresponding increases in nuclear volume in order to contain the additional DNA. Indeed, studies evaluating the relationship between DNA content and nuclear size have generally revealed a positive correlation[160-163].

Although small-scale chromosome content changes may not have a significant impact on overall nuclear volume, lagging chromosomes or acentric chromosomal fragments that fail to incorporate into one of the daughter nuclei following division, may form MNi[166]. MNi are considered a hallmark of CIN and are frequently observed in cancer[165,167,168]. Thus, increases in the number of MNi, which can be easily detected using standard DNA counterstains such as DAPI or Hoechst[165,175], can be used as a surrogate marker for CIN. A screen capable of rapidly and simultaneously assessing these phenotypes would dramatically increase the speed at which novel human CIN genes are identified.

In this study, we developed and validated a multiplexed, image-based approach capable of detecting CIN phenotypes. The nuclear volume assay monitors changes in nuclear size as an indicator of large-scale chromosome content changes associated with CIN. Conversely, the micronucleus (MN) enumeration assay detects the loss of whole chromosomes or large chromosomal fragments derived from DNA DSBs and/or segregation defects. When utilized in combination, these approaches can rapidly distinguish whether a gene of interest has a potential role in CIN. Each assay was validated through the use of established positive (*SMC1A*) and negative (*GAPDH*) controls[62,182]. Following *SMC1A* silencing in a fibrosarcoma cell line (HT1080), significant increases in mean nuclear volume and MN formation were readily detected. When employed in a distinct, non-cancerous fibroblast cellular context (hTERT), similar results were obtained, and found to correlate with chromosomal defects indicative of CIN. These data validate the use of this multiplexed screen to identify phenotypes associated with CIN and represent a promising approach that can be adapted to and employed in high-content studies to identify novel CIN genes.

3.3.0. Results

3.3.1. Nuclear Volume Increases are Associated with Diminished Expression of a CIN Gene

Previous studies utilizing human tumor samples[160-163] have shown a positive correlation between increases in chromosome number and nuclear size. However, this concept has never been applied in the context of a screen in cell lines. To determine whether changes in nuclear volume may act as a surrogate marker of CIN (Figure 3-1A), the established CIN gene (*SMC1A*) was silenced, which can induce large increases in chromosome complements (*i.e.* ploidy)[62]. However, prior to volumetric analyses, the silencing efficiencies of the four individual siRNA (si*SMC1A*-1, -2, -3 and -4) and pooled (*SMC1A*-pool) duplexes were evaluated (Figure 3-1B). Having established that all siRNA conditions efficiently silence *SMC1A*, karyotypically stable HT1080 cells were transiently transfected using a pooled siRNA approach. Four days post-transfection, cells were fixed, counterstained with DAPI and subjected to 3D image acquisition and analysis as detailed within Materials and Methods (*Sections 2.5.1 and 2.5.3*). Briefly, the DAPI channel (which fluorescently labelled nuclei) was employed to generate surface renderings for each nucleus within each deconvolved image. Nuclear volumes were automatically determined for a minimum of 100 nuclei per condition, and statistical comparisons were made.

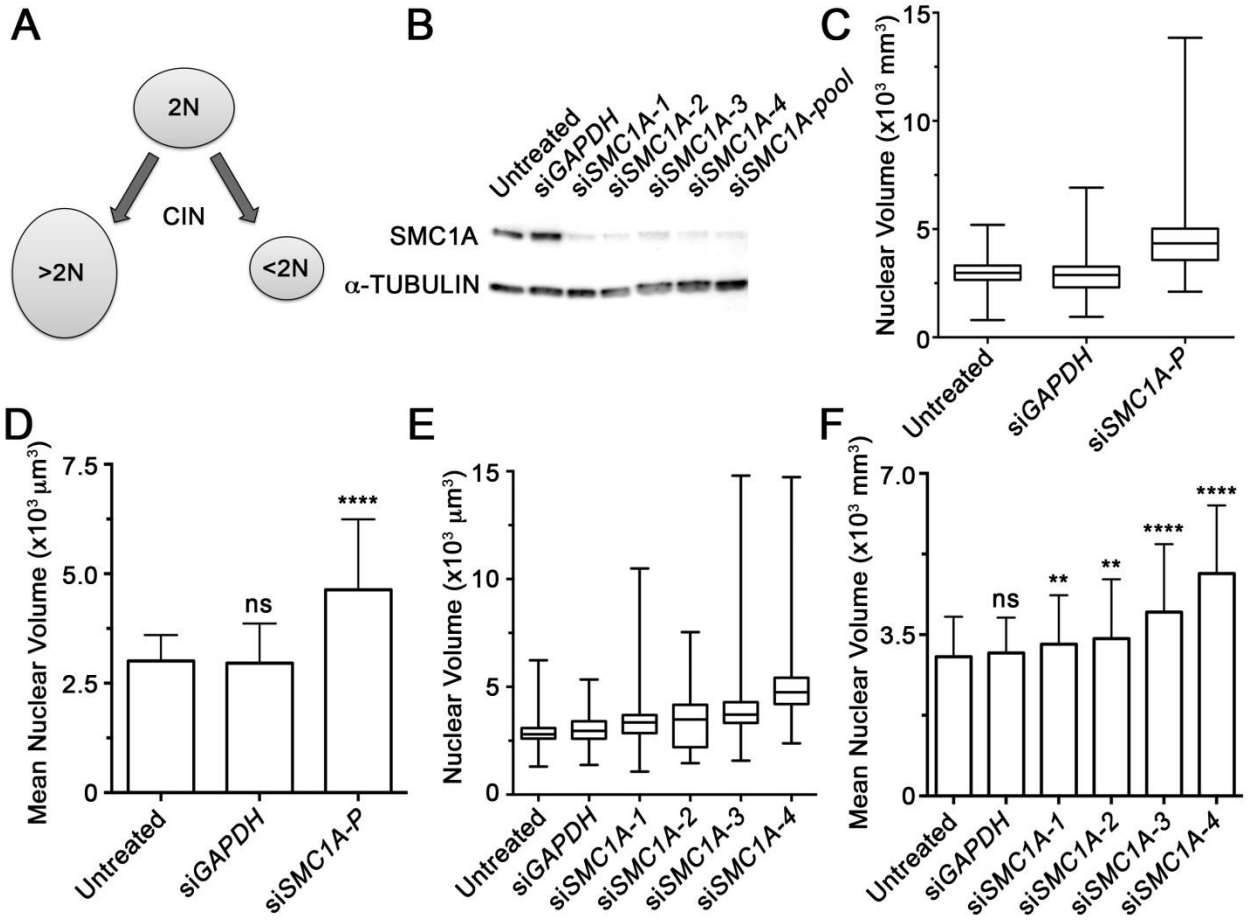

Figure 3-1. *SMC1A* Silencing Underlies Nuclear Volume Increases in HT1080
(A) Schematic depicting the relationship between nuclear volume changes (ovals) and DNA content (2N) that are predicted to occur as a result of chromosome missegregation events during cell division. ***(B)*** Western blot showing *SMC1A* silencing following treatment with individual (si*SMC1A-1*, *-2*, *-3* and *-4*) or pooled (si*SMC1A-P*) siRNA duplexes relative to controls (untreated and si*GAPDH*). α-TUBULIN serves as the loading control. ***(C)*** Box-and-whisker plot depicting the distribution range of nuclear volumes for each condition (x-axis). (N = 3). Whiskers delineate the entire distribution range, while the lower, middle and upper horizontal lines of the box identify the 25th, 50th and 75th percentiles, respectively. ***(D)*** Bar graph presenting the mean nuclear volumes ± standard deviation (SD) measured for the indicated conditions (x-axis). Statistically significant increases in mean nuclear volumes were observed following *SMC1A* silencing (*p*-value < 0.0001; ****) relative to the untreated controls that were not significant (*p*-value > 0.05; ns) following *GAPDH* silencing. ***(E)*** Box-and-whisker plot depicting the distribution range, 25th, 50th and 75th percentiles of nuclear volumes for each of the individual siRNA duplexes targeting *SMC1A* or controls. (N = 1). ***(F)*** Bar graph depicting the mean nuclear volume ± SD following silencing. Student's *t*-tests between untreated controls and each condition revealed statistically significant increases (*p*-value < 0.01; **: *p*-value < 0.0001; ****) in mean nuclear volumes following *SMC1A* silencing that were not significant (*p*-value > 0.05) in si*GAPDH* cells.

As predicted, decreased expression of *SMC1A* was accompanied by qualitative and quantitative changes in nuclear volume in HT1080 cells. More specifically, an increase in the total distribution range of the nuclear volumes (*i.e.* minimum to maximum) was observed within the *SMC1A*-silenced cells (total range = 11,735 μm^3) relative to untreated (4,397 μm^3) or *GAPDH*-silenced (5,967 μm^3) controls (Figure 3-1C). In addition, a 1.5-fold increase in mean nuclear volume occurred within the *SMC1A*-silenced cells (4,632.6 ± 1,608.7 μm^3 [SD]) relative to untreated (3,008.1 ± 592.6 μm^3) or *GAPDH*-silenced (2,955.9 ± 907.7 μm^3) controls (Figure 3-1D). Student's *t*-tests revealed this increase to be statistically significant compared to the untreated (*p*-value < 0.0001) (Figure 1D) or *GAPDH*-silenced (*p*-value < 0.0001) cells (SI Table S3-1).

To address potential off-target effects associated with the pooled siRNA approach, each individual duplex was also evaluated for its ability to induce changes in nuclear volume. Having established each individual siRNA duplex efficiently silences *SMC1A* (Figure 3-1B), volumetric analyses were performed as described above. In agreement with the pooled approach, silencing of *SMC1A* expression by each of the individual siRNA duplexes was associated with increases in the total distribution range of nuclear volumes (Figure 1E), increases in nuclear volumes, and statistically significant increases in the mean nuclear volumes relative to controls (Figure 3-1F and SI Table S3-2). Although differences were observed between each of the individual *SMC1A* duplexes, this was expected and may be attributed to the differences in silencing efficiency of each duplex, or more likely, the heterogeneous nature of the CIN phenotype itself. Collectively, the above data show that *SMC1A* silencing is accompanied by increases in nuclear volumes and therefore supports the use of nuclear volumes as surrogate markers for CIN in HT1080 cells.

To confirm the alterations in nuclear volumes observed above were not restricted to HT1080 cells, similar experiments were performed in hTERT, an immortalized and karyotypically stable, human fibroblast cell line. As above, western blots confirmed the silencing of *SMC1A* following transient transfection with siRNA duplexes (SI Figure S3-1A). In agreement with the HT1080 data, an overall increase in the total distribution range of the nuclear volumes was observed following *SMC1A* silencing (total range = 6,546 μm^3), relative to the untreated (4,301 μm^3) or *GAPDH*-silenced (5,096 μm^3) controls (SI Figure S3-1B). *SMC1A* silencing was also associated with a statistically significant, 1.3-fold increase in mean nuclear volume (3,539.5 ± 1225.0 μm^3) relative to untreated (2,640.7 ± 740.8 μm^3; *p*-value <0.0001) and *GAPDH*-silenced (2,720.1 ± 959.1 μm^3; *p*-value <0.0001) controls (SI Figure S3-1C and Table S3-3). These data indicate that the changes in nuclear volume following *SMC1A* silencing are conserved within an hTERT cellular context. Collectively, the above data show that silencing *SMC1A* induces statistically significant increases in nuclear volumes and validates the ability of the nuclear volume assay to detect changes that are indicative of CIN.

Having established changes in nuclear volume as an indicator for CIN, I sought to simplify and streamline the imaging process for future studies, making this assay more amenable to a rapid, high-content screen. Using 3D image projections acquired as described above, nuclear volumes were quantified for individual nuclei and compared to the NAs calculated from single 2D images through the focal plane of the same nuclei (*as described in Section 2.5.3*). Expectedly, linear regression analysis revealed that these values were highly correlated, (R = 0.92) (Figure 3-2). This confirms that NA and nuclear volume values are correlated and that changes in NAs calculated from 2D images can also be employed as an indicator for CIN in subsequent studies, which would dramatically reduce image acquisition and analysis times.

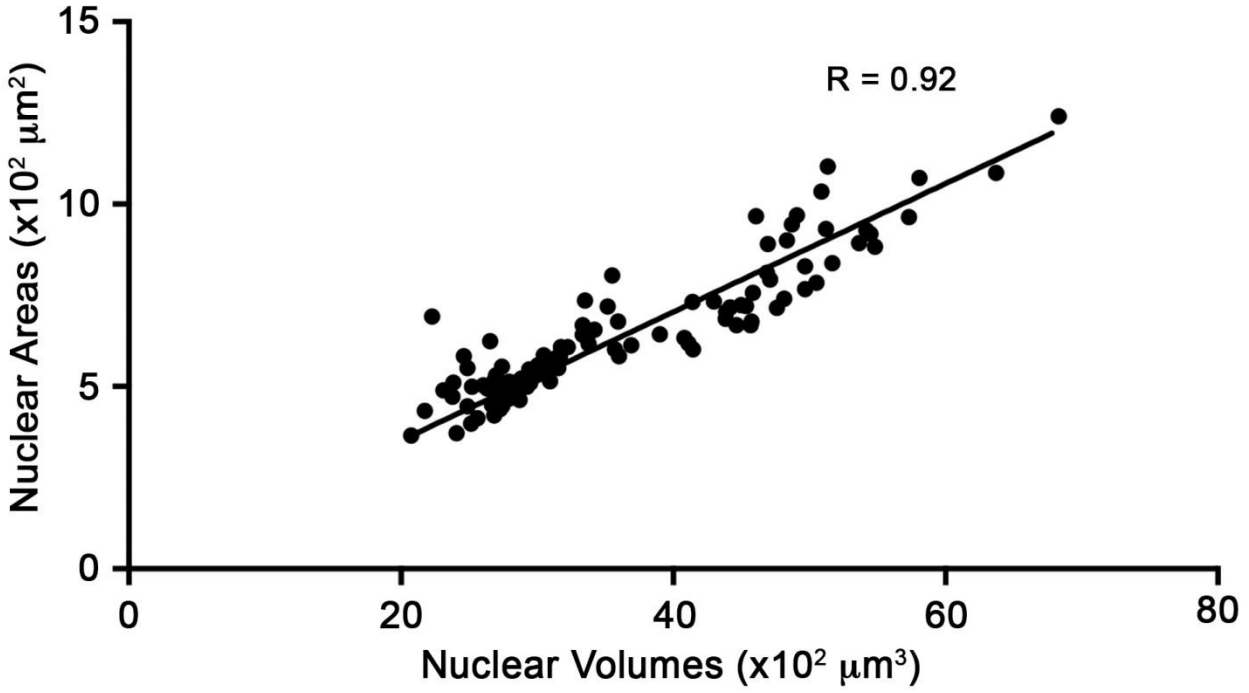

Figure 3-2. Nuclear Volume Increases Correlate with Nuclear Area Increases
Graph showing the strong positive correlation between nuclear volume and NA where each plotted point represents an individual nucleus. These data indicate that either nuclear volume or NA changes can be employed as an indicator for CIN. (N = 3, n > 100).

3.3.2. CIN Gene Silencing Causes Increases in Micronucleus Formation

I next sought to develop an image-based approach to evaluate the appearance of MNi, a hallmark of CIN (Figure 3-3A). To do so, we investigated whether increases in MN formation accompanied *SMC1A* silencing. HT1080 cells were transiently transfected as above with siRNA duplexes targeting either *SMC1A* or *GAPDH*, or left untreated. Following a four day incubation period, cells were fixed, counterstained, and imaged as above. The number of MNi in each condition was scored, and is expressed as a percentage of the total number of nuclei analyzed (Figure 3-3B). Overall, there was a 6.6-fold increase in the number of MNi observed within the *SMC1A*-silenced population (44.3%) relative to *GAPDH*-silenced (6.9%) or untreated (6.7%) controls. To ensure that the increase was not the result of off-target effects, MNi were enumerated following transfection with each of the four individual *SMC1A* siRNAs, as above. In agreement with the pooled approach, a marked increase in MN formation was observed following *SMC1A* silencing (24.9 – 39.0% MNi) compared to untreated (4.4%) or *GAPDH*-silenced (6.5%) cells (Figure 3-3C). As above, differences in MN formation occurred between the various *SMC1A* siRNAs that likely reflects the variability in silencing efficiency and/or the biological variation that is inherent within the CIN phenotype. Thus, these data validate the use of MN enumeration as a surrogate marker for CIN in HT1080 cells.

To verify that the increases in MN formation described above were not exclusive to the HT1080 cells, analogous experiments were performed in hTERT cells with similar, albeit less pronounced findings (SI Figure S3-1D). Overall, there was a 2.0-fold increase in MN formation following *SMC1A* silencing (5.4%) compared to untreated (2.7%) and *GAPDH*-silenced (3.0%) cells. Although beyond the scope of this study, the difference in MN formation observed between HT1080 and hTERT may reflect the different genetic contexts (*i.e.* gene alterations or

differential gene expression) inherent within the transformed cancerous cell line and the immortalized diploid cell line, respectively. Collectively, the above data show that increases in MN formation accompany the silencing of *SMC1A* in both HT1080 and hTERT cells, and provides strong evidence supporting the use of MN formation as a surrogate marker of CIN.

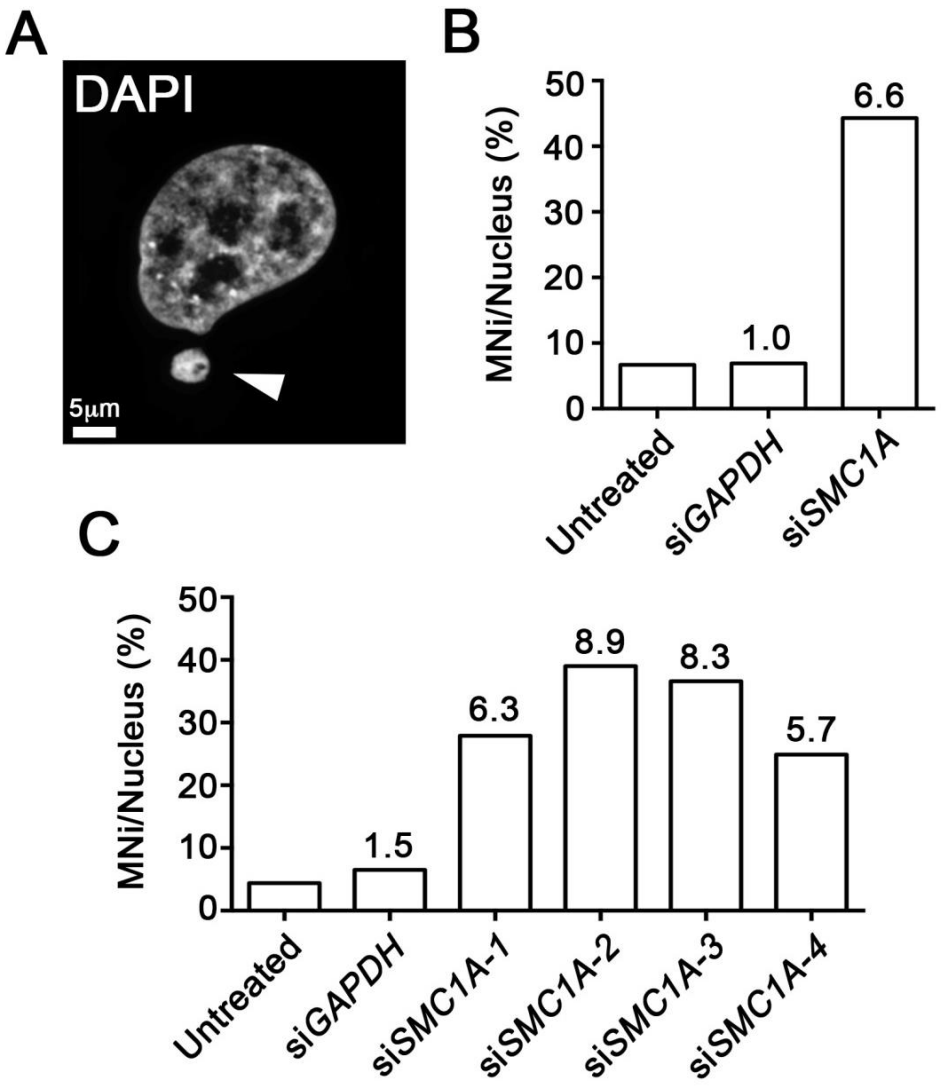

Figure 3-3. MN Formation is Induced Following *SMC1A* Silencing
(A) A representative high-resolution, 3D image highlighting a MN (arrowhead). ***(B)*** Bar graph presenting the average number of MNi in each condition (x-axis), expressed as a percentage of the total number nuclei analyzed. The fold-increase relative to the untreated control is indicated above each column. (N = 3). ***(C)*** Bar graph depicting the average number of MNi following *SMC1A* silencing with individual siRNA duplexes and controls (expressed as a percent). Fold-increases relative to untreated cells are indicated above each column. (N = 1).

3.3.3. Changes in Nuclear Volume and MN Formation are Associated with Chromosome Content Changes

To validate that the changes in nuclear volume and increases in MN formation observed following *SMC1A* silencing were associated with changes in chromosome content and CIN, traditional cytogenetic approaches were employed in hTERT cells. Chromosome enumeration was performed on 100 mitotic chromosome spreads generated within each condition. Following *SMC1A* silencing, 42% of mitotic spreads exhibited an abnormal chromosome number ($\neq 46$) representing a 3.8 to 4.7-fold increase compared to untreated (11%) or si*GAPDH*-treated (9%) hTERT cells (SI Table S3-4). The differences in the distribution of chromosome numbers following *SMC1A* silencing were deemed statistically significant by KS tests. These findings support the correlation between changes in nuclear volume or MN formation with changes in chromosome content, which is the defining characteristic of CIN. Overall, these findings support the use of nuclear size changes (*i.e.* volumes or areas) and MN formation as surrogate markers for CIN. Thus, these assays can be employed in combination to assess whether alteration of a gene of interest induces changes in CIN phenotypes that are indicative of CIN.

3.4.0. Discussion

In this chapter, I present a novel image-based approach capable of detecting phenotypes associated with CIN, namely changes in nuclear volume and MN formation. *SMC1A* was purposefully selected as the positive control, as it has a critical role in chromosome cohesion that is now known to impact chromosome segregation and DNA replication[187-189]. Evidence now suggests SMC1A may also play important roles in mitotic spindle assembly[189] and DNA DSB repair[187,188]. Thus, diminished SMC1A expression was predicted to produce multiple, aberrant phenotypes that are readily detected using epi-fluorescence imaging microscopy. Using an siRNA-based approach, statistically significant increases in nuclear volumes and increases in MN formation were observed following *SMC1A* silencing in HT1080 cells. Importantly, increases in nuclear volumes and MN formation were also observed in hTERT cells, highlighting the conserved nature of SMC1A function in chromosome stability in different cellular contexts. Collectively, the above data show that *SMC1A* silencing induces multiple CIN-related phenotypes that are detected through quantitative imaging microscopy. The results of this study validate the use of each individual assay to detect surrogate markers of CIN, and demonstrate the ability of this approach to screen for CIN phenotypes.

Intuitively, alterations in the physical space requirements associated with large increases in chromosome numbers (*i.e.* ploidy) will be reflected by corresponding changes in nuclear volume. The inter-relationship of DNA content and nuclear size has been known for decades[160-163,190,191], however the use of nuclear size changes (*i.e.* volumes or areas) as a screen for CIN is entirely novel. In CRC for example, up to 85% of all tumors exhibit CIN[192], with most late-stage tumors harboring large increases in chromosome numbers, typically in the triploid to tetraploid range (60-90 chromosomes)[193]. Due to the strong association of CIN and cancer, nuclear size can be

employed to provide diagnostic and/or prognostic information. For example, microscopy-based histomorphological assessment of lung cancer samples acquired through endoscopy or surgical resection, revealed that increases in NA correlate with ploidy, tumor grade and stage[162,190], likely because these NA changes are reflective of CIN. In support of the clinical associations highlighted above, our study demonstrates that significant increases in nuclear volumes accompany *SMC1A* silencing. The increases in nuclear volumes observed in HT1080 and hTERT cells likely reflect the large-scale increases in chromosome numbers previously observed using a similar siRNA-based approach in HCT116 cells[62]. Thus, I identify *SMC1A* as a CIN gene in both HT1080 and hTERT cells, and conclude SMC1A is normally required to maintain chromosome stability in mammalian cells.

In general, increases in nuclear sizes following *SMC1A* silencing were observed rather than decreases, which is contrary to the segregation model of CIN (Figure 3-1A) that suggests both increases and decreases should be apparent. Although unknown, the underlying reason(s) are likely to be biological in nature rather than technical. One possibility is that increases in chromosome numbers (and the hundreds to thousands of genes they contain) are better tolerated than chromosome losses, which will result in haploinsufficiencies (single chromosome loss) and homozygous losses (both chromosomes lost) of key genes. By definition, the loss of an essential gene will result in death and the removal of these cells from the population under study. Indeed, further scrutiny of the original images identified a small subset of cells exhibiting apoptotic hallmarks including chromatin compaction and nuclear blebbing (data not shown). A second possibility is that *SMC1A* silencing affects additional pathways that underlie increases in nuclear volumes, such as DNA replication or DSB repair[194]. While replication errors may amplify specific chromosomes and/or large chromosomal regions resulting in larger nuclei, DNA repair

defects may produce acentric chromosome fragments that are not accurately segregated. Presumably, if these acentric fragments are incorporated within a daughter nucleus it will result in a larger DNA complement. Alternatively, if the chromosomal fragments are not incorporated within daughter nuclei, MNi will be formed. Indeed, our MN analyses confirm that increases occurred following *SMC1A* silencing in both HT1080 and hTERT cells. However, it should be noted that MN formation occurred more readily within HT1080 cells than hTERT (6-fold versus 2-fold, respectively), which likely reflects the genetic differences between these cell types. While HT1080 cells are a cancer cell line with known defects in DNA repair genes (*e.g. ERCC5*, *FANCC*, *MSH3*, and *WRN*[195]), hTERT cells are a non-malignant cell line immortalized through integration and re-expression of human telomerase reverse transcriptase (TERT) that do not contain any known defects. Therefore, the HT1080 cells likely exhibit diminished repair capabilities relative to the hTERT cells that render them hypersensitive to *SMC1A* silencing, and thus produce elevated numbers of MNi.

The development of a quantitative, image-based approach for the detection of CIN phenotypes is an important advancement over traditional approaches such as flow cytometry. The current approach facilitates rapid, visual assessment of the cells under investigation, which allows for simultaneous assessment of multiple CIN phenotypes. Importantly, visual examination of the cells from each condition can provide further indications regarding the aberrant mechanisms that underlie the CIN phenotypes (multipolar spindle formation, lagging chromosomes *etc*.). Further, this approach offers significant time, cost and labor savings over conventional cytogenetic approaches (*e.g.* mitotic chromosome spreads, spectral karyotyping), particularly since it is scalable to 96- and 384-well assay formats. As nuclear volumes and NAs are strongly correlated, rapid 2D imaging can replace 3D image acquisition, which would reduce

the number of images acquired per condition, offering further time savings when performing a screen of hundreds to thousands of genes. Importantly, the current approach is performed on asynchronous cell populations, and in the absence of mitotic poisons including colcemid or nocodazole. Although these drugs are routinely employed by cytogeneticists to artificially increase mitotic indices, several studies have shown they can induce aneuploidy and MN formation[196,197]. In addition, because CIN phenotypes are evaluated within interphase cells, our analyses are not restricted to a minor fraction of the entire population, and thus larger sample sizes (hundreds to thousands of nuclei) are obtained. Accordingly, CIN phenotypes that specifically arise during interphase, such as increases in nuclear volumes associated with replication errors (*e.g.* endoreduplication), can also be quantified. In any case, it is not difficult to envision how similar approaches could be directed towards the mitotic cells contained within the images to quantitatively assess additional CIN phenotypes, including lagging chromosomes and multipolar spindles. Although this approach represents a significant advancement, I recognize that it does not replace the need and capabilities inherent within many classical cytogenetic approaches. Rather, I suggest that the multiplexed approach is highly amenable to screening siRNA/ short hairpin (sh)RNA or chemical libraries to identify putative CIN candidates that will require subsequent validation using traditional cytogenetic approaches.

An image-based assay that can simultaneously assess multiple phenotypes associated with CIN is important, particularly in the context of a screen. Multiplexing a nuclear size assay with MN enumeration assays will help ensure maximal numbers of putative CIN genes are identified. As shown by Yuen *et al*[66] in budding yeast, the use of complementary assays is critical, particularly since some genes display assay specificity while others are detected by multiple assays. Furthermore, knowing whether or not newly identified CIN genes exhibit assay

specificity will not only assist in prioritizing those candidates for subsequent study, but will also provide fundamental insight into the aberrant pathways implicated in CIN. This information will become particularly relevant as novel candidate CIN genes are identified, and their potential roles in the pathogenesis of human diseases such as cancer are explored. Thus, the identification of novel human CIN genes enabled with the current approach will provide critical insights into CIN and the aberrant biological mechanisms associated with highly aggressive, drug resistant, CIN-positive tumors. Ultimately, these insights may direct the future development of novel therapeutic strategies. Additionally, this new screening approach may hold prognostic or diagnostic value however its use in a clinical setting remains to be evaluated.

3.5.0 Supporting Information

3.5.1. Supporting Tables

Table S3-1. *SMC1A* Silencing Increases Mean Nuclear Volume in HT1080 Cells

	No. Nuclei	Mean Nuclear Volume (μm^3)	Standard Deviation	*p*-value[A]	*p*-value[B]	Fold Increase[C]
Untreated	223	3008.1	592.6	-	0.4602	1.0
si*GAPDH*	275	2955.9	907.7	0.4602	-	1.0
si*SMC1A*	273	4632.6	1608.7	< 0.0001	< 0.0001	1.5

[A]*p*-values obtained comparing mean nuclear volumes to untreated control (Student's t-test).
[B]*p*-values obtained comparing mean nuclear volume to si*GAPDH* control (Student's t-test).
[C]Fold increase values refer to the increase in mean nuclear volume relative to the untreated control.

Table S3-2. *SMC1A* Silencing by Individual siRNA Duplexes Increases Mean Nuclear Volume in HT1080 Cells

	No. Nuclei	Mean Nuclear Volume (μm^3)	Standard Deviation	*p*-value[A]	Fold Increase[B]
Untreated	207	3022.7	866.0	-	1.0
si*GAPDH*	191	3104.8	764.6	0.3184	1.0
si*SMC1A-1*	247	3292.2	1063.4	0.0036	1.1
si*SMC1A-2*	141	3412.9	1287.9	0.0008	1.1
si*SMC1A-3*	194	3991.2	1474.4	< 0.0001	1.3
si*SMC1A-4*	128	4828.0	1477.5	< 0.0001	1.6

[A]*p*-values obtained comparing mean nuclear volumes to untreated control (Student's t-test).
[B]Fold increase values refer to the increase in mean nuclear volume relative to the untreated control.

Table S3-3. *SMC1A* Silencing Increases Mean Nuclear Volume in hTERT Cells

	No. Nuclei	Mean Nuclear Volume (μm^3)	Standard Deviation	*p*-value[A]	*p*-value[B]	Fold Increase[C]
Untreated	157	2640.7	740.8	-	0.4558	1.0
si*GAPDH*	101	2720.1	959.1	0.4558	-	1.0
si*SMC1A*	60	3539.5	1225.0	< 0.0001	< 0.0001	1.3

[A]*p*-values obtained comparing mean nuclear volumes to untreated control (Student's t-test).
[B]*p*-values obtained comparing mean nuclear volumes to si*GAPDH* control (Student's t-test).
[C]Fold increase values refer to the increase in mean nuclear volume relative to the untreated control.

Table S3-4. *SMC1A* Silencing Induces Chromosome Content Changes in hTERT Cells

	No. Spreads	Spreads with Abnormal Chromosome Count (%)	Fold Increase[A]	*p*-value[B]
Untreated	100	11	-	-
si*GAPDH*	100	9	0.82	> 0.9999
si*SMC1A*	100	42	3.82	0.0112

[A]Fold increase values refer to the increase in the percentage of spreads harbouring an abnormal chromosome number ($\neq 46$) relative to the untreated negative control.
[B]*p*-values obtained using the Kolmogorov-Smirnov test to compare chromosome numbers from each condition with the untreated negative control where *p*-values < 0.05 are statistically significant. (N = 3).

3.5.2. Supporting Figures

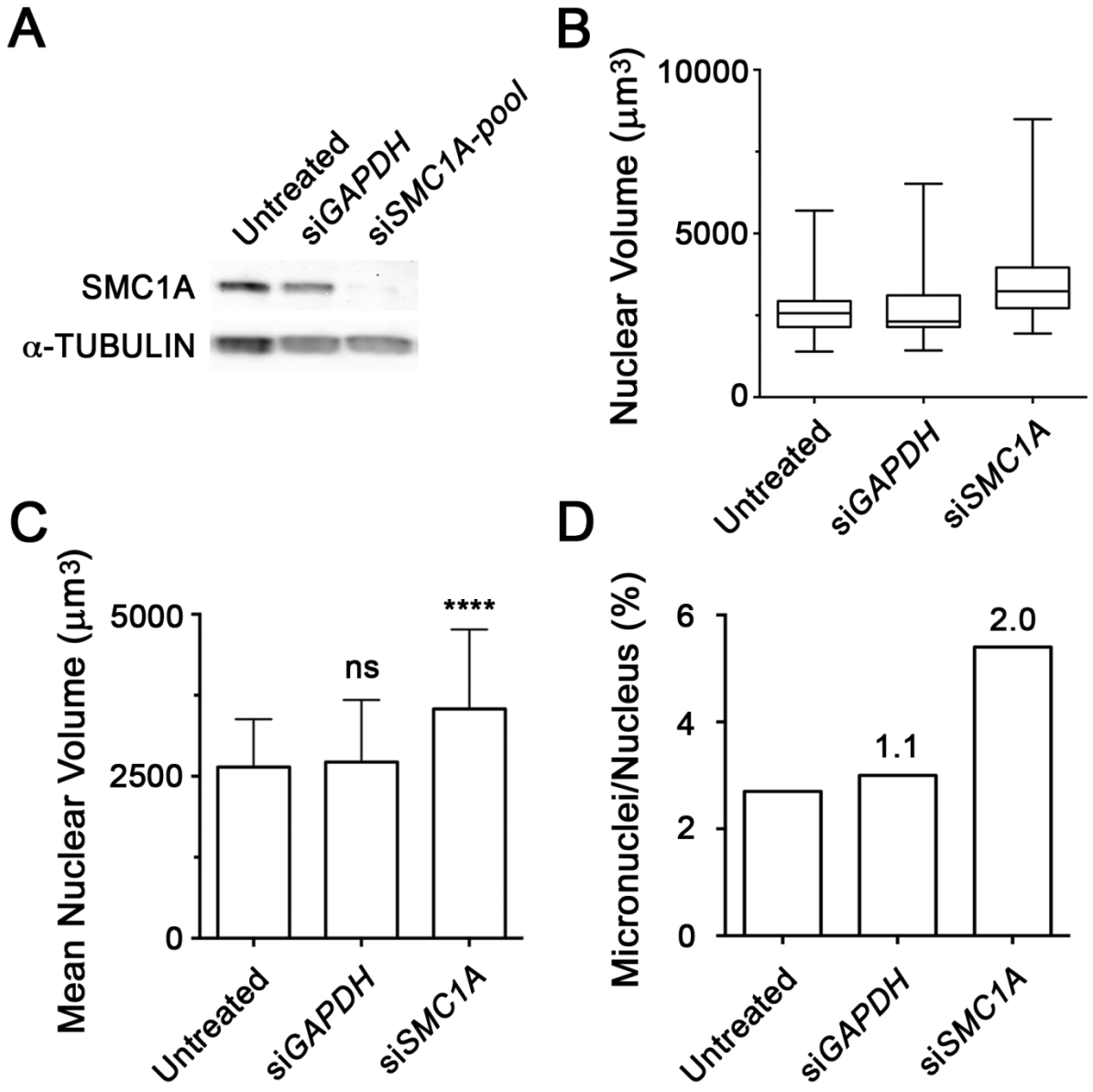

Figure S3-1. *SMC1A* Silencing in hTERT Induces Increases in CIN Phenotypes
(A) Western blot depicting SMC1A expression levels following silencing (si*SMC1A*-pool), with α-Tubulin as a loading control. ***(B)*** Box-and-whisker plot displaying the minimum, 25th percentile, median, 75th percentile and maximum nuclear volume values for each condition indicated on the x-axis. ***(C)*** Bar graph presents mean nuclear volumes (± SD). Student's *t*-tests were performed between the untreated hTERT cells and each of the conditions (si*GAPDH* and si*SMC1A*-pool). Statistically significant differences are identified by ****, ($p < 0.0001$), and ns, (not significant). ***(D)*** Bar graph displays the average number of MNi as a percentage of the total number nuclei analyzed for each condition. Fold increases in MN formation for the *GAPDH* and *SMC1A*-silenced cells (si*SMC1A*-pool) relative to the untreated condition are displayed above each column. (N = 3).

CHAPTER 4

A MULTIPLEXED SCREEN EXPEDITES IDENTIFICATION OF CHROMOSOME INSTABILITY GENES

4.1.0. Abstract

CIN is considered an enabling factor of oncogenesis, associated with aggressive tumors, multi-drug resistance, disease recurrence, and poor prognosis. Unfortunately, the altered genes that underlie CIN remain largely unknown, and traditional cytogenetic approaches for identifying CIN genes are laborious, expensive and unsuitable for large gene sets. Here, multiplexed NA and MN enumeration assays were employed in a high-content, RNAi-based screen to assess CIN-associated phenotypes following candidate gene silencing in two karyotypically stable human cell lines, HT1080 and hTERT. A total of 164 human candidate CIN genes identified through cross-species approaches were screened, and 148 putative CIN genes were identified. The list of putative CIN genes was prioritized based on the number of assays that identified the gene and the strength of the CIN phenotype, and a promising subset of putative CIN genes including *ARL2*, *BUB3*, *DSN1*, *GARS*, *GART*, *NUF2*, *PIGS*, *SHMT2*, *SPC24*, and *SKP1*, was selected for validation. Western blot and mitotic chromosome spread analyses were performed in hTERT and expanded into the karyotypically stable CRC cell line HCT116, which validated that gene silencing induces numerical and structural chromosome defects that are indicative of CIN. The human CIN genes identified in this study provide insight into the aberrant biological pathways that contribute to CIN in human cells and may represent novel cancer therapeutic targets.

4.2.0. Introduction

As stable inheritance of the genome is essential for the survival of all living organisms, many of the biological processes and genes/proteins that function to maintain chromosome stability are conserved across species. In humans, CIN promotes oncogenesis by increasing the rate at which key cancer genes including oncogenes, tumor suppressor genes, DNA repair genes, and apoptotic genes, are gained, lost, or altered[56]. Accordingly, CIN underlies cellular transformation, cancer progression, the acquisition of multi-drug resistance, and poor prognoses[2,3,60,61] (*see Section 1.2.2*). Although CIN is observed in > 80% of most cancers[198], the underlying genes that drive CIN in humans remain largely unknown[62,199]. Furthermore, traditional cytogenetic analyses commonly employed to identify CIN genes are prohibitive against rapid assessment of large gene sets[62-64]. Thus, approaches capable of rapidly assessing a large number of candidate genes are paramount to expedite the identification of human CIN genes and the biological pathways that drive oncogenesis. Characterization of novel CIN genes represents a critical first step towards the identification of new cancer therapeutic targets and the development of novel precision medicine strategies for improved treatment of aggressive, chromosomally unstable cancers. In this chapter, cross-species candidate gene approaches and the microscopy-based assays established in Chapter 3 were utilized to identify, prioritize and subsequently validate promising putative human CIN genes.

Recall from Section 1.3.0 that a comprehensive list of 692 CIN genes was established in *S. cerevisiae*[65,66]. As ~11.5% of *S. cerevisiae* genes are required to maintain chromosome stability in yeast, ~2,300 CIN genes are predicted to exist in humans (~11.5% of 20,000 total genes), provided similar frequencies are conserved across species. However, only a small fraction of human CIN genes have been identified to date[2,62,67,199]. As such, the budding yeast CIN gene list

serves as a valuable research resource that can be employed to rapidly identify orthologous candidates to test in human cells. Our findings from Chapter 3 serve as a proof of principle, as diminished expression of *SMC1A*, the human ortholog of the yeast CIN gene *smc1*, induced CIN-associated phenotypes including nuclear volume changes, nuclear size heterogeneity, MN formation and chromosomal aberrations[62,200].

Although ~40% of yeast CIN genes function in predictable biological pathways including mitosis, DNA replication or repair (*see Section 1.4.0*), the remaining CIN genes encode proteins that function in biological pathways with less established connections to CIN (*e.g.* RNA processing, proteasomal degradation, GPI-anchor or tRNA synthesis)[65]. Thus, cross-species approaches may prove especially valuable, as they may facilitate the identification of human genes and cellular pathways with less intuitive links to CIN. As the human orthologs of many yeast CIN genes (*e.g. SKP1*) are frequently altered in many cancer types including CRC[155,201], it is imperative they are assessed in appropriate human cell models. Regardless of the pathways impacted by gene alteration, the assays developed in Chapter 3 can effectively detect aberrant phenotypes associated with CIN[200]. Thus, we predict that coupling cross-species approaches with our newly developed microscopy-based assays, will dramatically expedite the identification of novel human CIN genes.

In this chapter, 164 candidate human CIN genes identified through cross-species approaches were screened via NA and MN enumeration assays following RNAi-based silencing in karyotypically-stable HT1080 fibrosarcoma and hTERT fibroblast cells. The 148 putative human CIN genes identified were subsequently prioritized based on the number of assays that identified the gene and the strength of the associated CIN phenotypes. A subset of 10 putative CIN genes were confirmed and shown to induce chromosomal aberrations following silencing

that are indicative of CIN. As CIN is observed in the majority (> 85%) of CRC tumors[1,54], validation was expanded into the karyotypically stable HCT116[202] CRC cell line and corroborated the CIN results. Overall, this multiplexed image-based screen allowed for rapid identification, validation and characterization of novel human CIN genes with potential pathogenic implications for CRC.

4.3.0 Results

4.3.1. NA Changes Reveal Putative Human CIN Genes

Cross-species candidate gene approaches were employed to identify human candidate CIN genes to evaluate using the NA and MN screen, as described in Section 2.7.0. From the 692 established yeast CIN genes[65], 164 genes with sequence or function-based human orthologs that exhibited a strong meta-score (*i.e.* repeatedly demonstrated a strong CIN phenotype by at least 1 CIN assay in yeast[65]) were selected for screening (Table 4-1). The 164 human candidate CIN genes and relevant controls (Table 4-2) were evaluated by combining reverse genetics, high-content microscopy, and the NA and MN enumeration assays. Briefly, HT1080 and hTERT cells were seeded into custom-arrayed reverse transfection plates, grown for 4 or 6 days, respectively, fixed, counterstained (*see Sections 2.2.2 and 2.3.2*) and imaged (*Section 2.5.2*). To identify potential changes in NAs and establish whether increases in NA heterogeneity (which is reflective of DNA content heterogeneity) were detected following silencing, cumulative NA frequency distributions for each of the 164 genes were compared to si*GAPDH* via KS tests to identify putative CIN genes (*as described in Section 2.5.3*).

Table 4-1. Cross-species Approaches Yield 164 Human Candidate CIN Genes

No.	Yeast Gene	Human Ortholog[A]	BLAST E-value[B]	No.	Yeast Gene	Human Ortholog	BLAST E-value
1	*ATM1*	*ABCB7*	0	**44**	*YHR122W*	*FAM96B*	-
2	*RLI1*	*ABCE1*	0	**45**	*FRS1*	*FARSB*	2.00E-172
3	*ACC1*	*ACACB*	0	**46**	*RAD27*	*FEN1*	2.00E-149
4	*ACO1*	*ACO2*	0	**47**	*MET7*	*FPGS*	3.00E-102
5	*ACT1*	*ACTB*	6.00E-58	**48**	*GRS1*	*GARS*	0
6	*DOC1*	*ANAPC10*	6.00E-26	**49**	*ADE5*	*GART*	-
7	*APC4*	*ANAPC4*	0.001	**50**	*FOL2*	*GCH1*	5.00E-72
8	*RET2*	*ARCN1*	1.00E-42	**51**	*PSF2*	*GINS2*	1.00E-13
9	*CIN4*	*ARL2*	2.00E-28	**52**	*PSF3*	*GINS3*	1.00E-05
10	*ASF1*	*ASF1A*	4.00E-61	**53**	*SLD5*	*GINS4*	1.00E-04
11	*YTA7*	*ATAD2B*	-	**54**	*YOR262W*	*GPN2*	-
12	*ELG1*	*ATAD5*	-	**55**	*SSL1*	*GTF2H2*	2.00E-27
13	*IPL1*	*AURKC*	3.00E-82	**56**	*HHF1*	*HIST2H4B*	-
14	*MOT1*	*BTAF1*	2.00E-16	**57**	*RAD5*	*HLTF*	7.00E-84
15	*BUB1*	*BUB1*	2.00E-43	**58**	*PSE1*	*IPO5*	1.00E-126
16	*BUB3*	*BUB3*	1.00E-33	**59**	*SPN1*	*IWS1*	2.00E-23
17	*AAR2*	*C20orf4*	1.00E-08	**60**	*CYC8*	*KDM6A*	2.00E-47
18	*CMD1*	*CALM2*	4.00E-62	**61**	*CIN8*	*KIF11*	2.00E-65
19	*CTK2*	*CCNK*	1.00E-10	**62**	*KAR3*	*KIFC1*	7.00E-93
20	*CDC7*	*CDC7*	4.00E-30	**63**	*SPC110*	*LAMA2*	2.00E-12
21	*CDC28*	*CDK3*	1.00E-135	**64**	*BIM1*	*MAPRE1*	2.00E-43
22	*MIF2*	*CENPC1*	-	**65**	*SCC4*	*MAU2*	-
23	*SWC5*	*CFDP1*	5.00E-12	**66**	*MCM10*	*MCM10*	1.00E-11
24	*RLF2*	*CHAF1A*	0.002	**67**	*MCM2*	*MCM2*	0
25	*CTF18*	*CHTF18*	6.00E-47	**68**	*MCM5*	*MCM5*	0
26	*CTF8*	*CHTF8*	-	**69**	*ETR1*	*MECR*	6.00E-57
27	*DRE2*	*CIAPIN1*	1.00E-09	**70**	*MRPL27*	*MRPL27*	2.00E-06
28	*CKS1*	*CKS2*	8.00E-23	**71**	*MUC1*	*MUC17 (MUC19)*	-
29	*CDC36*	*CNOT2*	2.00E-18	**72**	*KRE33*	*NAT10*	0
30	*CCR4*	*CNOT6*	4.00E-95	**73**	*SHP1*	*NSFL1C*	-
31	*POP2*	*CNOT8*	1.00E-59	**74**	*NUF2*	*NUF2*	8.00E-06
32	*CSE1*	*CSE1L*	0	**75**	*OMA1*	*OMA1*	3.00E-31
33	*RNA15*	*CSTF2*	2.00E-18	**76**	*ORC1*	*ORC1*	6.00E-56
34	*DBP6*	*DDX51*	4.00E-56	**77**	*KAE1*	*OSGEP*	5.00E-151
35	*IRC15*	*DLD*	4.00E-64	**78**	*ADE1*	*PAICS*	9.00E-07
36	*MDJ1*	*DNAJA3*	2.00E-20	**79**	*PCF11*	*PCF11*	2.00E-15
37	*DJP1*	*DNAJC10*	3.00E-19	**80**	*THP1*	*PCID2*	1.00E-11
38	*ZUO1*	*DNAJC2*	9.00E-52	**81**	*POL30*	*PCNA*	7.00E-61
39	*DCC1*	*DSCC1*	6.00E-09	**82**	*BUD16*	*PDXK*	3.00E-45
40	*DSN1*	*DSN1*	3.00E-138	**83**	*ADE6*	*PFAS*	0
41	*GCD1*	*EIF2B3*	7.00E-07	**84**	*GIM4*	*PFDN2*	3.00E-17
42	*GUS1*	*EPRS*	0	**85**	*PGK1*	*PGK1*	0
43	*RRP4*	*EXOSC2*	3.00E-67	**86**	*RRM3*	*PIF1*	1.00E-68

Table 4-1 *Continued*. Cross-species Approaches Yield 164 Human Candidate CIN Genes

No.	Yeast Gene	Human Ortholog[A]	BLAST E-value[B]	No.	Yeast Gene	Human Ortholog	BLAST E-value
87	*GPI17*	*PIGS*	7.00E-19	**126**	*RTN2*	*RTN4*	5.00E-08
88	*POL1*	*POLA1*	0	**127**	*RVB2*	*RUVBL2*	0
89	*POL3*	*POLD1*	0	**128**	*SNU66*	*SART1*	2.00E-06
90	*POL32*	*POLD3*	-	**129**	*SLY1*	*SCFD1*	1.00E-114
91	*RPC37*	*POLR3E*	7.00E-06	**130**	*MSL5*	*SF1*	1.00E-70
92	*RPC11*	*POLR3K*	3.00E-29	**131**	*SHM2*	*SHMT2*	0
93	*PIG1*	*PPP1R3C*	-	**132**	*SKP1*	*SKP1*	2.00E-49
94	*SDS22*	*PPP1R7*	9.00E-42	**133**	*VPS64*	*SLMAP*	-
95	*TPD3*	*PPP2R1B*	1.00E-163	**134**	*RSC8*	*SMARCC2*	9.00E-45
96	*RTS1*	*PPP2R5C*	2.00E-172	**135**	*SUB2*	*SNORD84 (DDX39B)*	0
97	*PRI1*	*PRIM1*	5.00E-76	**136**	*SNP1*	*SNRNP70*	2.00E-18
98	*PRI2*	*PRIM2*	1.00E-14	**137**	*SPC24*	*SPC24*	-
99	*PRE10*	*PSMA3*	9.00E-82	**138**	*SPC25*	*SPC25*	-
100	*PUP2*	*PSMA5*	6.00E-96	**139**	*MCM1*	*SRF*	6.00E-31
101	*SCL1*	*PSMA6*	3.00E-84	**140**	*SRP101*	*SRPR*	5.00E-82
102	*PRE6*	*PSMA7*	3.00E-96	**141**	*SSU72*	*SSU72*	4.00E-52
103	*RPN6*	*PSMD11*	1.00E-111	**142**	*IRR1*	*STAG1*	3.00E-22
104	*RPN5*	*PSMD12*	5.00E-115	**143**	*SGT1*	*SUGT1*	7.00E-25
105	*RPN1*	*PSMD2*	0	**144**	*TAF7*	*TAF7L*	1.00E-11
106	*RPN12*	*PSMD8*	4.00E-24	**145**	*TAF9*	*TAF9 (TAF9B)*	9.00E-23
107	*PWP1*	*PWP1*	0.002	**146**	*CSM3*	*TIPIN*	1.00E-08
108	*PRO3*	*PYCRL*	1.00E-29	**147**	*TOP3*	*TOP3A*	3.00E-148
109	*GLN4*	*QARS*	2.00E-174	**148**	*TPI1*	*TPI1*	-
110	*BET4*	*RABGGTA*	4.00E-37	**149**	*TRS130*	*TRAPPC10*	4.00E-05
111	*RAD17*	*RAD1*	0.16	**150**	*PSH1*	*TRIM25*	3.00E-07
112	*RAD18*	*RAD18*	3.00E-20	**151**	*TRM5*	*TRMT5*	3.00E-73
113	*RAD50*	*RAD50*	2.00E-68	**152**	*TUB1*	*TUBA4A*	0
114	*RAD51*	*RAD51*	4.00E-158	**153**	*TUB4*	*TUBG2*	1.00E-116
115	*RAD57*	*RAD51B*	5.00E-20	**154**	*SPC98*	*TUBGCP3*	2.00E-34
116	*RAD52*	*RAD52*	6.00E-48	**155**	*DIB1*	*TXNL4A*	3.00E-64
117	*RAD54*	*RAD54L*	0	**156**	*RAD6*	*UBE2A*	5.00E-77
118	*MSI1*	*RBBP4*	9.00E-51	**157**	*UBC9*	*UBE2I*	7.00E-63
119	*RFC4*	*RFC2*	9.00E-141	**158**	*UBR1*	*UBR2*	2.00E-28
120	*RFC2*	*RFC4*	5.00E-116	**159**	*UGP1*	*UGP2*	2.00E-178
121	*SLX8*	*RNF10*	1.00E-08	**160**	*CTF4*	*WDHD1*	4.00E-19
122	*RPL30*	*RPL30*	1.00E-38	**161**	*PFS2*	*WDR33*	1.00E-82
123	*RPL7*	*RPL7*	4.00E-27	**162**	*UTP5*	*WDR43*	8.00E-20
124	*RPL2B*	*RPL8*	2.00E-128	**163**	*SYF1*	*XAB2*	3.00E-59
125	*RTT103*	*RPRD1B*	2.00E-11	**164**	*YIP1*	*YIPF5*	5.00E-36

[A]Alphabetical list of 164 candidate human CIN genes identified using cross-species approaches. Genes in brackets are related genes selected for screening due to limited siRNA availability.
[B]Small E-values identify sequence orthologs; (-) = functional orthologs[65] with no sequence similarity.

Table 4-2. Controls Employed in High-Content Screen

No.	Pos. Control	Function	Reference
1	*SMC1A*	Sister chromatid cohesion	Barber, T.D., McManus, K.J. *et al*, 2008[62]
2	*FANCM*	ATPase for DNA repair	Gari, K. *et al*, 2008[203]
3	*RAD17*	DNA damage-induced cell cycle arrest	Wang, X. *et al*, 2003[204]
4	*CHEK2*	Cell-cycle regulation, DNA repair, Apoptosis	Stolz, A. *et al*, 2010[205]
5	*MRE11A*	Recombination, DNA repair, Telomere maintenance	Barber, T.D., McManus, K.J. *et al*, 2008[62]
6	*FBXW7*	Cell-cycle regulation	Barber, T.D., McManus, K.J. *et al*, 2008[62]
No.	**Neg. Control**	**Function**	**Reference**
7	*GAPDH*	Glycolysis	Barber, T.D., McManus, K.J. *et al*, 2008[62]
8	Non-targeting Pool #1	No gene target	McManus, K.J., unpublished observation
9	Non-targeting Pool #2	No gene target	McManus, K.J., unpublished observation
10	RISC-Free Control	No gene target	McManus, K.J., unpublished observation
No.	**Transfection Indicators**	**Function**	**Reference**
11	siGLO Green	No gene target	McManus, K.J., unpublished observation
12	siGLO RISC-Free	No gene target	McManus, K.J., unpublished observation
13	siGLO Lamin A/C (silencing control)	Components of the nuclear membrane/lamina	McManus, K.J., unpublished observation

SMC1A = Structural Maintenance of Chromosomes 1A, *FANCM* = Fanconi Anemia Complementation Group M, *RAD17* = Rad17 Homolog, *CHEK2* = Checkpoint Kinase 2, *MRE11A* = Meiotic Recombination 11 Homolog A, *FBXW7* = F-box and WD Repeat Domain Containing 7, *GAPDH* = Glyceraldehyde-3-Phosphate Dehydrogenase, RISC = RNA-Induced Silencing Complex. Protein function information was obtained from Gene Cards: http://www.genecards.org[149].

Of the 164 candidates screened by the NA assay in HT1080 cells, 88 genes (53.7% of candidates screened) induced statistically significant differences in cumulative NA frequency distributions (KS tests, *p*-value < 0.01) relative to controls (si*GAPDH*) (Figure 4-1A, SI Table S4-1). A total of 24 genes in which fewer than 40 nuclei were imaged (n < 40), were excluded from analysis as these presumably induce cell cycle arrest and/or death. Of the 88 genes identified, 35 induced decreases in median NAs, while 53 induced increases relative to controls (Figure 4-1A). Diminished expression of *SKP1* and *GART*, which encode proteins involved in ubiquitin-associated proteasomal degradation and *de novo* purine biosynthesis respectively, induced the greatest increases in median NA (~1.6-fold) relative to controls (Table 4-3). The hTERT NA screen identified 112 putative human CIN genes, representing 68.3% of the candidates analyzed (Figure 4-1A, SI Table S4-2). As above, 19 genes were excluded from analysis due to low cell numbers. In contrast to HT1080, the majority of putative CIN genes (76) identified in hTERT induced increases in median NA following silencing, while 36 genes induced decreases (Figure 4-1A). Diminished expression of *KIF11* (mitotic spindle motor protein-encoding gene[206]) induced the greatest increase in median NA (1.8-fold), while *SHMT2* (encodes regulator of mitochondrial thymidylate biosynthesis[207]) was among those inducing the greatest decreases (1.4-fold). *GART* and *SKP1* silencing in hTERT resulted in similar, albeit less extensive increases in median NAs compared to those observed in HT1080, inducing 1.4- (*GART*) and 1.3-fold (*SKP1*) increases (Table 4-4). Collectively, the NA assay identified 133 putative CIN genes (81.1% of candidates screened), with 67 genes (40.8%) identified in both cell lines (Figure 4-1B). Of those, *GART* and *SKP1* were ranked highest overall for inducing the greatest increases in median NAs (Table 4-5).

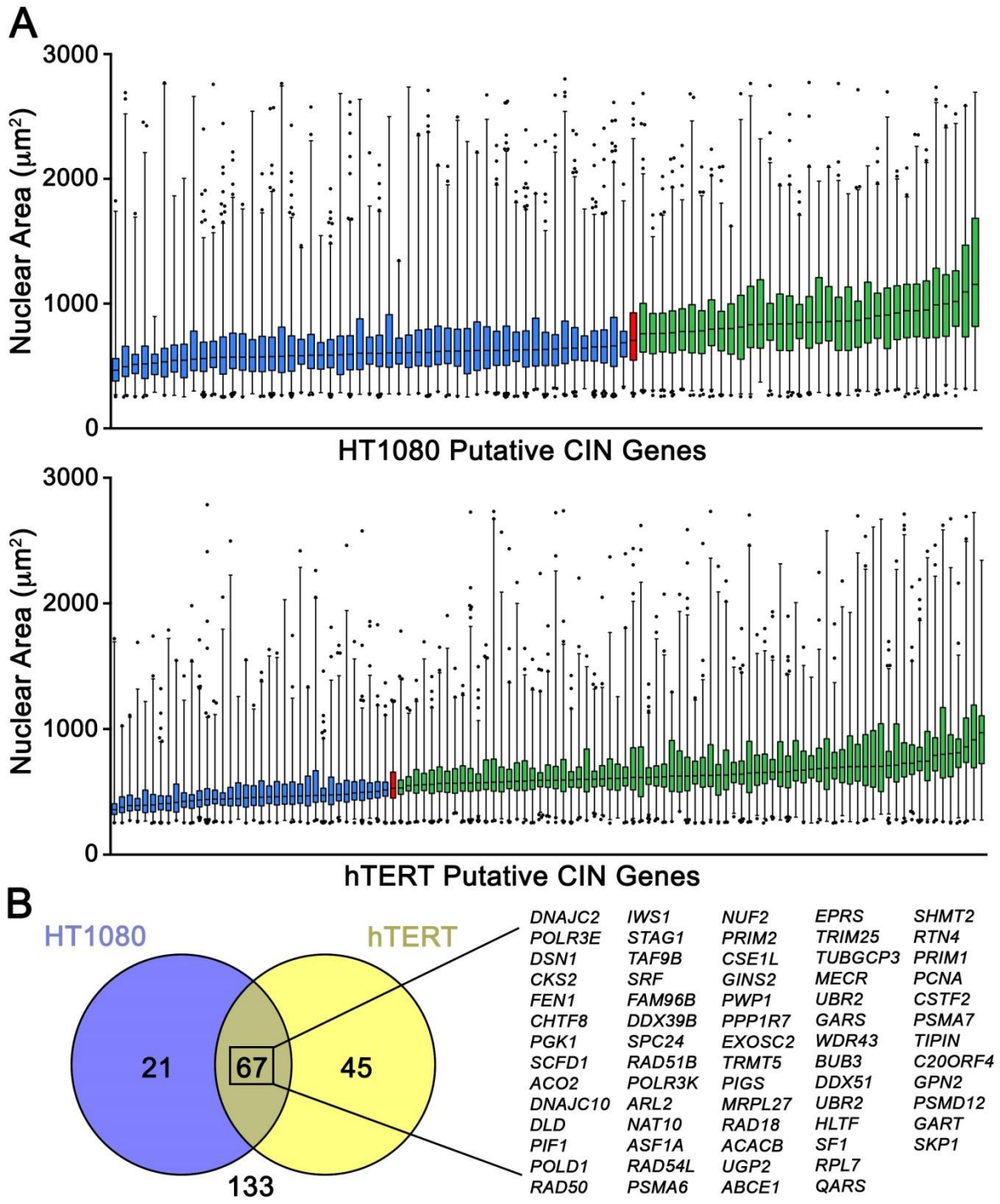

Figure 4-1. NA Assay Reveals Putative Human CIN Genes
(A) Box-and-whisker graphs displaying 1st – 99th percentiles (whiskers) and 25th, 50th, and 75th percentiles (box) of NA data for each putative CIN gene identified in HT1080 (top) and hTERT (bottom). Genes causing median NA increases or decreases relative to si*GAPDH* (red) are coloured green and blue, respectively. ***(B)*** Venn diagram displaying the numbers of putative CIN genes identified by the NA assay with the 67 genes identified in both HT1080 and hTERT listed by ascending fold change in median NA.

Table 4-3. Median NA Changes Induced Following Gene Silencing in HT1080

Gene[A]	*RNF10*	*QARS*	*RAD52*	*DDX51*	*RPL7*	*RTN4*	*RAD18*
N[B]	161	264	151	291	53	138	85
Median	466.5	493.7	512.8	517.9	523	532.1	544.2
FC[C]	1.51	1.43	1.37	1.36	1.35	1.32	1.29
Gene	*RABGGTA*	*TUBGCP3*	*POLR3K*	*SHMT2*	*MRPL27*	*EXOSC2*	*UBR2*
N	58	76	687	239	928	420	181
Median	546.5	554.4	559.1	567.9	569.1	570.6	571.5
FC	1.29	1.27	1.26	1.24	1.24	1.23	1.23
Gene	*CSE1L*	*DDX39B*	*ACACB*	*HLTF*	*RAD54L*	*WDR43*	*FAM96B*
N	72	247	633	188	763	107	244
Median	571.6	573.5	575.1	578.1	580.6	581.1	585.8
FC	1.23	1.23	1.22	1.22	1.21	1.21	1.20
Gene	*NAT10*	*UGP2*	*TRMT5*	*PPP1R7*	*CTF2H2*	*MECR*	*OSGEP*
N	53	736	95	747	86	178	444
Median	585.8	586.8	589.6	592.8	602.4	603.4	603.5
FC	1.20	1.20	1.19	1.19	1.17	1.17	1.17
Gene	*EPRS*	*AURKC*	*PSMA6*	*TAF9B*	*CNOT8*	*FPGS*	*RAD50*
N	88	122	52	102	401	118	214
Median	604.8	605.3	606.4	609.5	610.3	617.7	620
FC	1.16	1.16	1.16	1.16	1.15	1.14	1.14
Gene	*DNAJC10*	*MAU2*	*SPC24*	*DLD*	*PGK1*	*PIF1*	*SPC25*
N	141	76	109	122	480	784	254
Median	620.3	620.5	624.2	624.5	624.5	625.3	627.9
FC	1.14	1.13	1.13	1.13	1.13	1.13	1.12
Gene	*IWS1*	*RAD1*	*POLR3E*	*CKS2*	*STAG1*	*RBBP4*	*FARSB*
N	991	105	201	467	316	351	66
Median	628.9	629.7	629.8	632.9	634.1	641	641.1
FC	1.12	1.12	1.12	1.11	1.11	1.10	1.10
Gene	*DNAJC2*	*TRIM25*	*MCM5*	*ACO2*	*CHTF18*	*CHTF8*	*PYCRL*
N	659	59	68	667	242	504	86
Median	642.2	643.4	651.6	652.7	653.9	654.5	657.1
FC	1.10	1.09	1.08	1.08	1.08	1.08	1.07
Gene	*PFDN2*	*PRIM2*	*UBE2I*	*MUC17*	*GCH1*	*DSCC1*	*BUB1*
N	255	811	159	169	156	924	692
Median	660.9	661	662.9	663	663	663.7	665.3
FC	1.07	1.07	1.06	1.06	1.06	1.06	1.06
Gene	*SSU72*	*TOP3A*	*PFAS*	*TPI1*	*ANAPC10*	*ATAD2B*	*RPRD1B*
N	254	683	262	273	777	73	141
Median	666.3	667.7	667.9	674.9	680.1	681.2	685.1
FC	1.06	1.05	1.05	1.04	1.04	1.03	1.03
Gene	*PPP2R5C*	*ABCB7*	*RAD51*	*CDK3*	*RFC2*	*UBE2A*	*EIF2B3*
N	598	118	250	303	87	234	186
Median	685.8	686.9	687	688.2	690.8	697.4	698.4
FC	1.03	1.03	1.03	1.02	1.02	1.01	1.01

Table 4-3 *Continued*. Median NA Changes Induced Following Gene Silencing in HT1080

Gene[A]	*TRAPPC10*	*WDHD1*	*KDM6A*	*CDC7*	*PPP1R3C*	*GINS3*	*TUBG2*
N[B]	519	104	524	120	388	358	591
Median	700	701.5	701.9	702.1	702.1	702.3	702.4
FC[C]	1.01	1.00	1.00	1.00	1.00	1.00	1.00
Gene	*GINS4*	*ATAD5*	*NSFL1C*	*PDXK*	*OMA1*	*PCID2*	*KIFC1*
N	66	662	437	544	166	602	174
Median	709	710.8	711.2	711.4	713.1	713.7	715.4
FC	1.01	1.01	1.01	1.01	1.01	1.01	1.02
Gene	*CFDP1*	*TAF7L*	*HIST2H4B*	*IPO5*	*PSMA3*	*BTAF1*	*WDR33*
N	329	279	691	453	96	280	523
Median	720.3	723.6	730.4	737.4	744.5	746.3	748.5
FC	1.02	1.03	1.04	1.05	1.06	1.06	1.06
Gene	*CNOT6*	***SMARCC2***	***SCFD1***	***DSN1***	*PSMD2*	***ASF1A***	*RFC4*
N	210	559	248	491	156	421	68
Median	750	758.6	759.6	761.7	763.2	766.5	769.1
FC	1.07	1.08	1.08	1.08	1.08	1.09	1.09
Gene	***MCM2***	***ARL2***	***YIPF5***	*TUBA4A*	*CHAF1A*	*SNRNP70*	***POLD1***
N	343	281	337	102	74	140	342
Median	776.6	776.7	780.6	781.5	784.6	785.2	795.1
FC	1.10	1.10	1.11	1.11	1.11	1.12	1.13
Gene	***FEN1***	***ABCE1***	*CIAPIN1*	***NUF2***	***PSMA7***	***PSMD12***	***SF1***
N	372	102	66	172	134	90	354
Median	799.4	799.6	802.2	811	831.9	833.6	837.1
FC	1.14	1.14	1.14	1.15	1.18	1.18	1.19
Gene	***CSTF2***	***GINS2***	***GPN2***	***SRF***	***TIPIN***	***SLMAP***	***RAD51B***
N	104	405	343	342	61	104	349
Median	837.2	838.5	849.8	849.8	850.8	855.7	859.1
FC	1.19	1.19	1.21	1.21	1.21	1.22	1.22
Gene	***RUVBL2***	***C20orf4***	***MCM10***	***PWP1***	***POLD3***	***MAPRE1***	***PRIM1***
N	88	347	90	332	126	235	207
Median	859.2	866.8	882	900.9	907.4	924.6	942.3
FC	1.22	1.23	1.25	1.28	1.29	1.31	1.34
Gene	***PAICS***	***PIGS***	***BUB3***	***GARS***	***PCNA***	***GART***	***SKP1***
N	280	208	234	215	164	128	89
Median	942.4	948.2	989.1	998.3	1016	1091	1153
FC	1.34	1.35	1.40	1.42	1.44	1.55	1.64

[A]Genes arranged by ascending median NA, with putative CIN genes indicated in bold.
[B]N = Number of nuclei analyzed.
[C]FC = Fold change in median NA relative to si*GAPDH*.

Table 4-4. Median NA Changes Induced Following Gene Silencing in hTERT

Gene[A]	*KDM6A*	*SHMT2*	*MECR*	*UBE2I*	*DNAJA3*	*PYCRL*	*UBR2*
N[B]	115	121	119	154	88	215	514
Median	360.1	378	390.9	391	394.6	395.3	405.5
FC[C]	1.4707	1.4011	1.3548	1.3545	1.3421	1.3397	1.3060
Gene	*EPRS*	*RFC4*	*TUBGCP3*	*CENPC1*	*QARS*	*ACACB*	*DDX51*
N	138	100	186	203	509	621	262
Median	408.1	415.9	424	428.9	436.5	439.6	443.1
FC	1.2977	1.2734	1.2491	1.2348	1.2133	1.2047	1.1952
Gene	*TRMT5*	*SUGT1*	*PSMA5*	*CIAPIN1*	*STAG1*	*ACO2*	*RFC2*
N	153	126	51	133	142	218	113
Median	443.3	445.9	446.8	452.2	455.4	458.6	461.7
FC	1.1947	1.1877	1.1853	1.1712	1.1629	1.1548	1.1471
Gene	*FARSB*	*RPL8*	*CDK3*	*CSE1L*	*NAT10*	*PIF1*	*RAD54L*
N	191	84	264	143	114	208	639
Median	461.7	463.7	466	468.6	470.2	472	473.2
FC	1.1471	1.1421	1.1365	1.1302	1.1263	1.1220	1.1192
Gene	*DLD*	*GINS3*	*SART1*	*BTAF1*	*IPO5*	*DDX39B*	*EIF2B3*
N	276	390	175	182	594	355	171
Median	475.7	477.3	481.4	491.5	496.4	499.7	501.6
FC	1.1133	1.1096	1.1001	1.0775	1.0669	1.0598	1.0558
Gene	*FEN1*	*OSGEP*	*MCM5*	*RUVBL2*	*NSFL1C*	*TUBG2*	*MCM2*
N	303	767	118	153	199	283	185
Median	504.5	504.5	505.1	507.5	509.6	510.4	514
FC	1.0498	1.0498	1.0485	1.0435	1.0392	1.0376	1.0304
Gene	*ATAD2B*	*TPI1*	*RAD52*	*ABCB7*	*POLD3*	*KIFC1*	*DNAJC2*
N	302	189	86	133	76	186	304
Median	515.9	519.5	522.7	524.7	525.6	528.7	531.5
FC	1.0266	1.0194	1.0132	1.0093	1.0076	1.0017	1.0036
Gene	*PAICS*	*TRAPPC10*	*MAPRE1*	*CDC7*	*TUBA4A*	*PPP2R5C*	*YIPF5*
N	163	329	472	274	73	473	484
Median	536.8	538.4	538.8	540.6	540.9	542.6	544.9
FC	1.0136	1.0166	1.0174	1.0208	1.0213	1.0245	1.0289
Gene	*PFAS*	*PDXK*	*GINS4*	*POLR3E*	*CHTF18*	*CNOT8*	*SMARCC2*
N	256	841	221	291	230	512	395
Median	546.5	546.6	547	549.6	551.7	552.5	552.9
FC	1.0319	1.0321	1.0329	1.0378	1.0417	1.0432	1.0440
Gene	*SPC25*	*PIGS*	*GTF2H2*	*POLR3K*	*CKS2*	*SLMAP*	*CFDP1*
N	189	218	247	183	482	200	243
Median	553.3	554.5	555.1	557.3	559.2	559.9	567.4
FC	1.0448	1.0470	1.0481	1.0523	1.0559	1.0572	1.0714
Gene	*SRF*	*ACTB*	*AURKC*	*MUC17*	*RBBP4*	*FAM96B*	*PCID2*
N	245	172	132	211	179	292	679
Median	568.1	568.9	569.3	569.5	570	570.8	571.3
FC	1.0727	1.0742	1.0750	1.0753	1.0763	1.0778	1.0787

Table 4-4 *Continued*. Median NA Changes Induced Following Gene Silencing in hTERT

Gene[A]	***PGK1***	***DSN1***	*RAD51*	***RAD51B***	***OMA1***	*TXNL4A*	***PWP1***
N[B]	490	307	134	227	190	107	374
Median	573.4	574.6	575	577.5	578.1	578.7	582
FC[C]	1.0827	1.0850	1.0857	1.0904	1.0916	1.0927	1.0989
Gene	***DNAJC10***	***TOP3A***	***ANAPC10***	***CHTF8***	***RAD50***	***TAF9B***	***POLD1***
N	149	283	273	479	300	295	312
Median	585.3	586.7	591.1	592.1	592.1	593.1	594
FC	1.1052	1.1078	1.1161	1.1180	1.1180	1.1199	1.1216
Gene	***GARS***	***GCH1***	***SCFD1***	***RAD18***	***IWS1***	***BUB3***	***PSMA3***
N	309	282	168	344	260	195	59
Median	594.4	600.1	600.1	600.4	602.9	607.7	608.1
FC	1.1224	1.1331	1.1331	1.1337	1.1384	1.1475	1.1482
Gene	***EXOSC2***	***MRPL27***	***SPC24***	***HIST2H4B***	***UBE2A***	***RPRD18***	***PSMA6***
N	263	366	290	452	225	209	100
Median	611	615.8	616	616.4	618.1	619.2	625.6
FC	1.1537	1.1628	1.1631	1.1639	1.1671	1.1692	1.1813
Gene	***GINS2***	***PPP1R3C***	***PPP2R1B***	***BUB1***	***PPP1R7***	***CHAF1A***	***NUF2***
N	141	483	137	327	168	177	203
Median	625.7	626.3	627.9	630.7	631.6	634.1	635.1
FC	1.1815	1.1826	1.1856	1.1909	1.1926	1.1973	1.1992
Gene	***ARL2***	***ATAD5***	***SSU72***	***PCNA***	***TAF7L***	***ASF1A***	***RPL30***
N	150	401	204	165	237	322	90
Median	640.5	641.7	649	653	655.3	657.8	658.3
FC	1.2094	1.2117	1.2255	1.2330	1.2373	1.2421	1.2430
Gene	***UGP2***	***CALM2***	***WOR33***	***RPL7***	***PRIM2***	***SRPR***	***SNRNP70***
N	501	59	180	97	268	82	277
Median	660.8	670.7	672.2	679.9	684.3	690.1	691.4
FC	1.2477	1.2664	1.2693	1.2838	1.2921	1.3031	1.3055
Gene	***PRIM1***	***PSMD2***	***RTN4***	***SKP1***	***ABCE1***	***WDR43***	***DSCC1***
N	188	56	181	222	50	77	496
Median	695.8	700.7	700.9	701.1	702.5	703.5	710.3
FC	1.3138	1.3231	1.3235	1.3238	1.3265	1.3284	1.3412
Gene	***POLA1***	***HLTF***	***TRIM25***	***SF1***	***GART***	***CSTF2***	***PSMA7***
N	118	322	305	410	136	298	126
Median	712.1	727.3	728	743	744.1	791.3	799.9
FC	1.3446	1.3733	1.3746	1.4029	1.4050	1.4941	1.5104
Gene	***TIPIN***	***C20orf4***	***GPN2***	***PSMD12***	***KIF11***		
N	152	257	208	92	87		
Median	804.9	810.7	857.8	915	970.9		
FC	1.5198	1.5308	1.6197	1.7277	1.8333		

[A]Genes arranged by ascending median NA, with putative CIN genes in bold.
[B]N = Number of nuclei analyzed.
[C]FC = Fold change in median NA relative to si*GAPDH.*

Table 4-5. Rank Order of Putative CIN Genes Based on Fold Change in Median NA

Rank	Putative CIN Gene[A]	HT1080 FC[B]	hTERT FC[C]	FC[D]
1	*SKP1*	1.6373	1.3238	1.4806
2	*GART*	1.5493	1.4050	1.4771
3	*PSMD12*	1.1838	1.7277	1.4557
4	*GPN2*	1.2068	1.6197	1.4132
5	*C20orf4*	1.2309	1.5308	1.3808
6	*TIPIN*	1.2082	1.5198	1.3640
7	*PSMA7*	1.1813	1.5104	1.3459
8	*CSTF2*	1.1889	1.4941	1.3415
9	*PCNA*	1.4428	1.2330	1.3379
10	*PRIM1*	1.3138	1.3381	1.3260
11	*RTN4*	1.3234	1.3235	1.3234
12	*SHMT2*	1.2400	1.4011	1.3205
13	*QARS*	1.4264	1.2133	1.3198
14	*RPL7*	1.3465	1.2838	1.3151
15	*SF1*	1.1887	1.4029	1.2958
16	*HLTF*	1.2181	1.3733	1.2957
17	*DDX51*	1.3597	1.1952	1.2775
18	*BUB3*	1.4046	1.1475	1.2760
19	*WDR43*	1.2118	1.3284	1.2701
20	*GARS*	1.4176	1.1224	1.2700
21	*UBR2*	1.2322	1.3060	1.2691
22	*MECR*	1.1671	1.3548	1.2609
23	*TUBGCP3*	1.2702	1.2491	1.2596
24	*TRIM25*	1.0945	1.3746	1.2346
25	*EPRS*	1.1644	1.2977	1.2310
26	*ABCE1*	1.1355	1.3265	1.2310
27	*UGP2*	1.2001	1.2477	1.2239
28	*ACACB*	1.2245	1.2047	1.2146
29	*RAD18*	1.2940	1.1337	1.2138
30	*MRPL27*	1.2374	1.1628	1.2001
31	*PIGS*	1.3465	1.0470	1.1968
32	*TRMT5*	1.1944	1.1947	1.1945
33	*EXOSC2*	1.2341	1.1537	1.1939
34	*PPP1R7*	1.1879	1.1926	1.1903
35	*PWP1*	1.2793	1.0989	1.1891
36	*GINS2*	1.1907	1.1815	1.1861
37	*CSE1L*	1.2320	1.1302	1.1811
38	*PRIM2*	1.0654	1.2921	1.1787
39	*NUF2*	1.1517	1.1992	1.1754
40	*PSMA6*	1.1613	1.1813	1.1713
41	*RAD54L*	1.2129	1.1192	1.1660
42	*ASF1A*	1.0885	1.2421	1.1653
43	*NAT10*	1.2021	1.1263	1.1642

Table 4-5 *Continued.* Rank Order of Putative CIN Genes Based on Fold Change in Median NA

Rank	Putative CIN Gene[A]	HT1080 FC[B]	hTERT FC[C]	FC[D]
44	*ARL2*	1.1030	1.2094	1.1562
45	*POLR3K*	1.2595	1.0523	1.1559
46	*RAD51B*	1.2200	1.0904	1.1552
47	*SPC24*	1.1282	1.1631	1.1457
48	*DDX39B*	1.2279	1.0598	1.1439
49	*FAM96B*	1.2021	1.0778	1.1400
50	*SRF*	1.2068	1.0727	1.1397
51	*TAF9B*	1.1554	1.1199	1.1376
52	*STAG1*	1.1106	1.1629	1.1367
53	*IWS1*	1.1197	1.1384	1.1291
54	*RAD50*	1.1358	1.1180	1.1269
55	*POLD1*	1.1291	1.1216	1.1253
56	*PIF1*	1.1262	1.1220	1.1241
57	*DLD*	1.1276	1.1133	1.1205
58	*DNAJC10*	1.1353	1.1052	1.1202
59	*ACO2*	1.0789	1.1548	1.1169
60	*SCFD1*	1.0787	1.1331	1.1059
61	*PGK1*	1.1276	1.0827	1.1052
62	*CHTF8*	1.0759	1.1180	1.0970
63	*FEN1*	1.1352	1.0498	1.0925
64	*CKS2*	1.1127	1.0559	1.0843
65	*DSN1*	1.0817	1.0850	1.0833
66	*POLR3E*	1.1181	1.0378	1.0779
67	*DNAJC2*	1.0965	1.0036	1.0501

[A]Putative CIN genes identified in both cell types (67 genes) are displayed.
[B]FC = Fold change in median NA (vs. si*GAPDH*) in HT1080.
[C]FC = Fold change in median NA (vs. si*GAPDH*) in hTERT.
[D]FC = Average fold change from both cell lines.

4.3.2. Increases in MN Formation Identify Putative Human CIN Genes

To detect small-scale chromosome content changes that may arise due to DNA damage or mitotic defects, the MN enumeration assay was utilized to assess all 164 candidates in both HT1080 and hTERT. Putative CIN genes were defined as those inducing increases in MN formation that exceeded the mean MN formation plus 2 standard deviations calculated for the si*GAPDH* controls (*as described in Section 2.5.5*). In HT1080, 96 putative human CIN genes (58.5% of screened candidates) were identified (Figure 4-2A, SI Table S4-3) including *NUF2* and *SPC24*, which induced the largest increases at 13.0- and 12.8-fold, respectively (Figure 4-3). Only 19 genes (11.7%) surpassed the threshold in hTERT (Figure 4-2A). *SPC24* and *NUF2* were also strong MN inducers in hTERT, causing 5.7- and 5.3-fold increases in MN formation, respectively (SI Table S4-4). Interestingly, visual examination of *NUF2* and *SPC24* silenced cells not only confirmed these findings (Figure 4-3), but revealed increases in aberrant multinucleated cells in both cell lines, that are suggestive of cytokinesis defects, improper chromosome segregation and CIN (SI Table S4-5). Collectively, the MN enumeration assay identified 104 putative human CIN genes (63.4% of candidates screened) in HT1080 and hTERT, with 11 genes (6.7%) identified in both cell lines (Figure 4-2B). Of these, *SPC24*, *NUF2*, *DSN1* and *SHMT2* exhibited the highest levels of MN formation in both cell types, causing mean fold increases of 9.2, 9.2, 8.3, and 3.7, respectively (Figure 4-2B).

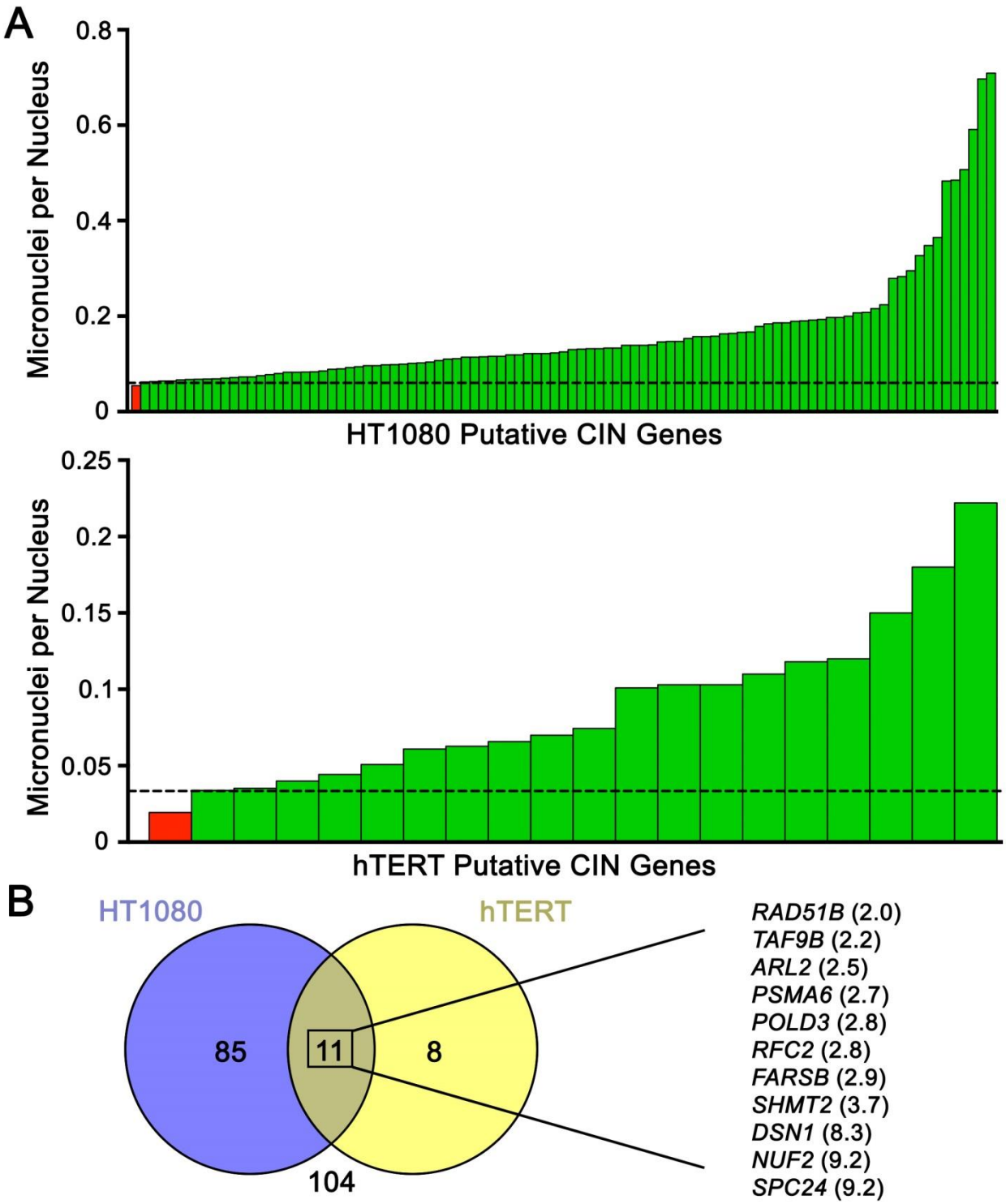

Figure 4-2. MN Enumeration Assay Identifies Putative Human CIN Genes
(A) Bar graph displaying normalized number of MNi per nucleus following silencing of putative CIN genes (green) identified in HT1080 (top) and hTERT (bottom). Dotted line represents 2× the standard deviation above the si*GAPDH* (red) mean. ***(B)*** Venn diagram displaying the total number of genes identified by the MN enumeration assay with 11 identified in both cell types listed with mean fold increases compared to the si*GAPDH* in brackets.

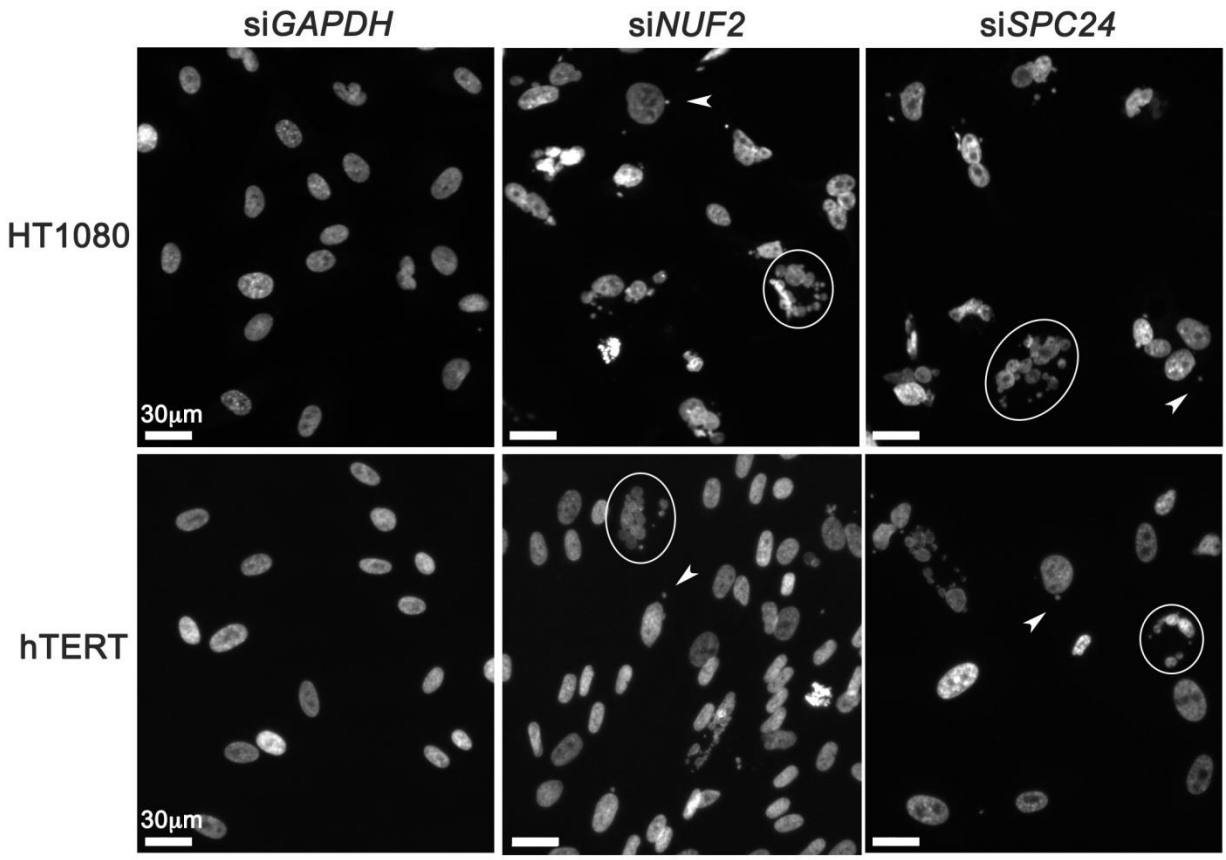

Figure 4-3. *NUF2* and *SPC24* Silencing Induces MN and Multinucleated Cell Formation
Representative 2D fluorescence microscopy images displaying increases in MN formation (arrow heads) and aberrant multinucleated cells (circled) in both si*NUF2* and si*SPC24* silenced HT1080 (top) and hTERT cells (bottom). Nuclei are counterstained with Hoechst.

4.3.3. Gene Silencing Induces CIN Phenotypes and Chromosomal Aberrations in hTERT and HCT116

Collectively, NA and MN high-content screens identified 148 putative CIN genes (90.2% of candidates) in both cell types (Figure 4-4). Of these, 47 were identified in at least 3 of 4 screens, suggesting they are strong putative CIN genes. Genes were subsequently prioritized and selected for validation as detailed in Section 2.8.0. Briefly, the 5 top ranked genes (*SHMT2*, *NUF2*, *SPC24*, *DSN1*, and *ARL2*) identified in 4/4 assays (SI Table S4-6), along with 5 additional genes of interest (*BUB3*, *SKP1*, *GART*, *GARS*, and *PIGS*) identified in 3/4 assays that induced strong CIN phenotypes were selected (Figure 4-4). These genes were purposefully selected to represent different gene ontology groups and biological pathways (*e.g.* proteasomal degradation or glycan anchor biosynthesis) (Table 4-6), many of which are not intuitively linked to CIN. Moreover, all 10 putative CIN genes (Table 4-6) are found altered in the 4 most common cancer types among Canadians and thus, were highly relevant to this study (Table 4-7).

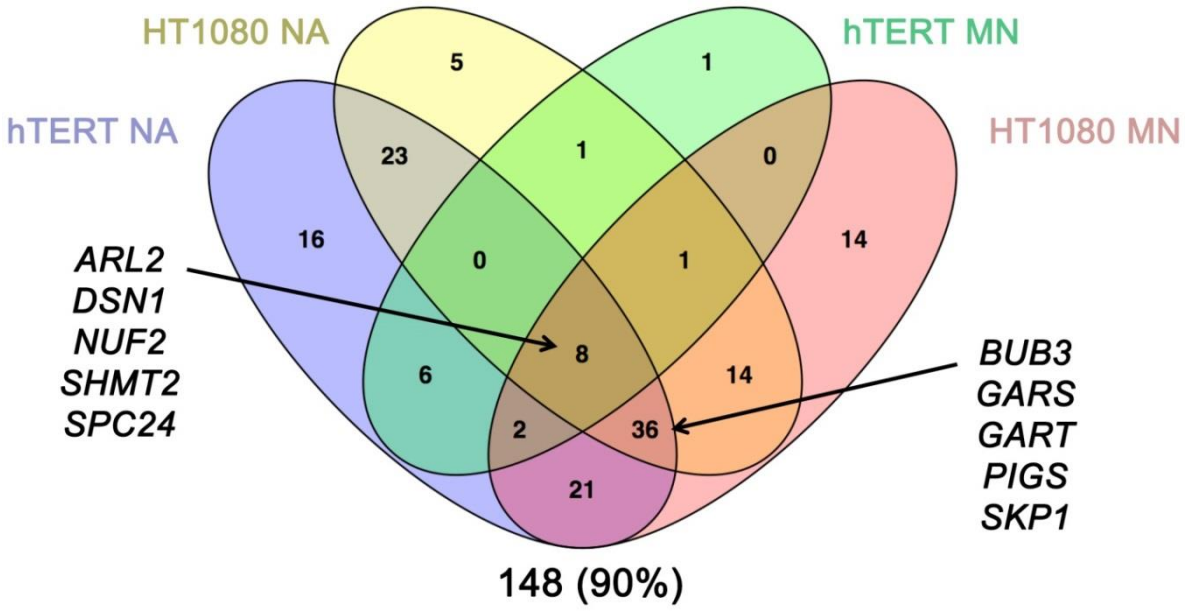

Figure 4-4. Multiplexed NA and MN Assays Identify Putative Human CIN Genes
Venn diagram summarizing NA and MN enumeration results from HT1080 and hTERT cells. A total of 148 putative CIN genes were identified. Listed genes identify those selected for subsequent validation.

Table 4-6. Biological Roles of Putative Human CIN Genes Pursued in Validation

Putative CIN Gene	Full Gene Name	Protein Function
ARL2	Adenosine Diphosphate (ADP)-Ribosylation Factor-Like 2	GTP-binding protein for microtubule formation and centrosome regulation
BUB3	Budding Uninhibited by Benzimidazoles 3 Homolog	Spindle-assembly checkpoint and kinetochore-microtubule attachments
DSN1	DSN1 homolog, MIS12 kinetochore complex component	Kinetochore assembly, cell cycle progression
GARS	Glycyl-tRNA Synthetase	Aminoacyl-tRNA synthetase that charges tRNAs with amino acids
GART	Phosphoribosylglycinamide Formyltransferase, Phosphoribosyl-glycinamide Synthetase, Phosphoribosylaminoimidazole Synthetase	*De novo* purine nucleotide biosynthesis
NUF2	NDC80 Kinetochore Complex Component	NDC80 complex component required for chromosome segregation and spindle checkpoint
PIGS	Phosphatidylinositol Glycan Anchor Biosynthesis Class S	Glycosylphosphatidylinositol-anchor transamidase activity
SHMT2	Serine Hydroxymethyltransferase 2 (Mitochondrial)	*De novo* mitochondrial thymidylate biosynthesis
SKP1	S-Phase Kinase-Associated Protein 1	Ubiquitin-dependent proteasomal degradation
SPC24	Spindle Pole Body Component 24 Homolog	NDC80 complex component required for chromosome segregation and spindle checkpoint

Protein function information obtained from Gene Cards: http://www.genecards.org[149].

Table 4-7. Alteration Frequencies of Putative CIN Genes in Cancer

Gene	Cancer Type				
	Colorectal (26,800)[A] %[B] / Cases[C]	Lung (28,600)[A] %[B] / Cases[C]	Breast (26,500)[A] %[B] / Cases[C]	Prostate (21,300)[A] %[B] / Cases[C]	Total Cases[D]
ARL2	13.0 / 3,484	15.0 / 4,290	18.0 / 4,770	9.0 / 1,917	14,461
BUB3	21.0 / 5,628	29.0 / 8,294	21.0 / 5,565	19.0 / 4,047	23,534
DSN1	31.0 / 8,308	17.0 / 4,862	14.0 / 3,710	12.0 / 2,556	19,436
GARS	14.0 / 3,752	10.0 / 2,860	11.0 / 2,915	11.0 / 2,343	11,870
GART	25.0 / 6,700	34.0 / 9,724	17.0 / 4,505	12.0 / 2,556	23,485
NUF2	10.0 / 2,680	15.0 / 4,290	14.0 / 3,710	9.0 / 1,917	12,597
PIGS	17.0 / 4,556	15.0 / 4,290	28.0 / 7,420	12.0 / 2,556	18,822
SHMT2	12.0 / 3,216	22.0 / 6,292	14.0 / 3,710	8.0 / 1,704	14,922
SKP1	19.0 / 5,092	41.0 / 11,726	16.0 / 4,240	16.0 / 3,408	24,466
SPC24	10.0 / 2,680	51.0 / 14,586	10.0 / 2,650	10.0 / 2,130	22,046

[A]Estimated number of Canadians diagnosed with the indicated cancer type in 2017[7].
[B]Frequency (%) of gene alterations.
[C]Number of new cases with altered gene, calculated by multiplying alteration frequency by the number of newly diagnosed individuals with the corresponding cancer type.
[D]Total cases for listed cancers with alterations in corresponding putative CIN gene.
Note: Only published data from The Cancer Genome Atlas (TCGA)[157,208-210] are included. Alteration frequencies include deletions (heterozygous or homozygous), amplifications, mutations, or mRNA expression changes (z-score threshold ± 2).

To validate the above NA and MN changes were not due to off-target effects, direct silencing tests were performed in hTERT using ON-TARGETplus siRNA duplexes (*see Section 2.3.1*). First, the silencing efficiency of siRNA duplexes targeting *ARL2*, *BUB3*, *DSN1*, *GARS*, *GART*, *NUF2*, *PIGS*, *SHMT2*, and *SPC24* was assessed in hTERT by western blot (Figure 4-5) (*see Section 2.6.0*). In agreement with the high-content screen, gene silencing induced significant changes in cumulative NA frequency distributions for each gene relative to controls (si*GAPDH*) (Table 4-8). In agreement with previous finding, *GARS* and *GART* silencing did not induce increases in MN beyond the 2-fold threshold. Interestingly, *BUB3* and *PIGS* silencing did induce MN increases that were not apparent in the initial hTERT MN screen, whereas *SHMT2* silencing failed to replicate the MN increases detected in the screen (Table 4-9). Silencing of *NUF2* and *SPC24* resulted in the most extensive increases in MN formation at 14.6- and 7.8-fold, respectively (Table 4-9), and as observed in the screen, generated aberrant multinucleated cells (Figure 4-6). Fluorescently tagged wheat germ agglutinin (WGA-Alexa Fluor 488) labelling of the plasma membrane allowed for confirmation of multinucleated cells (Figure 4-6). Interestingly, labelling these multinucleated cells with EdU (5-ethynyl-2'-deoxyuridine) Click-iT® Alexa Fluor 647, a thymidine nucleoside analog that is incorporated into DNA during active DNA synthesis, revealed that not all nuclei of the multinucleated cells are undergoing DNA replication concurrently (Figure 4-6), which can result in premature chromatin condensation and structural CIN[211,212].

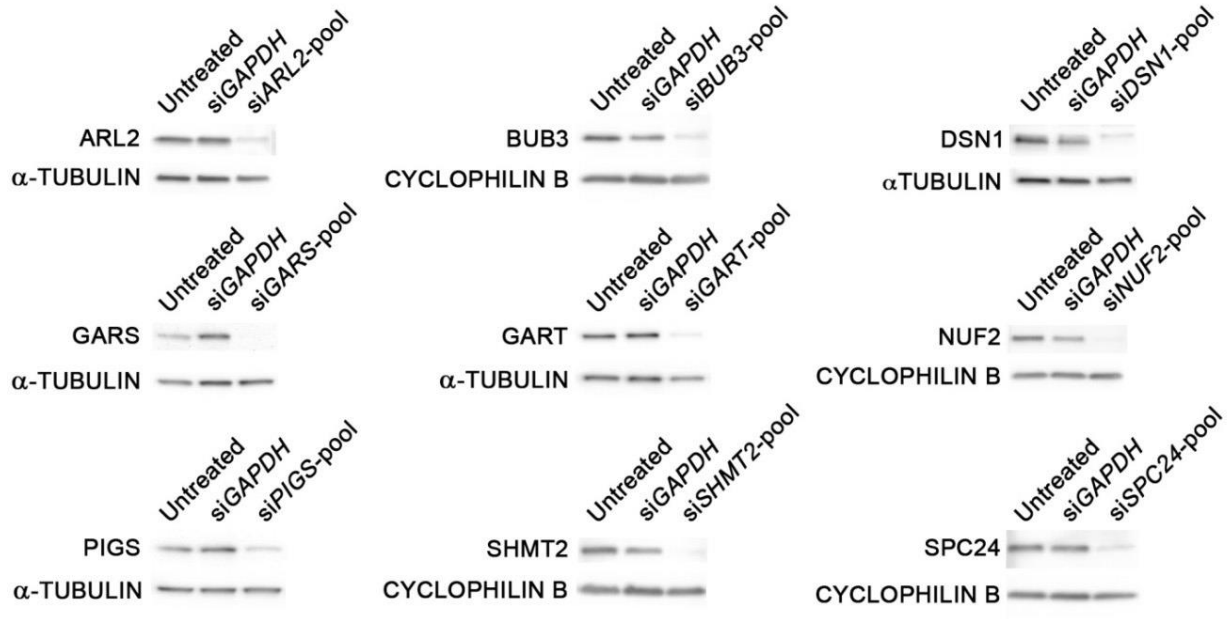

Figure 4-5. Putative CIN Gene Silencing in hTERT
Western blots displaying efficient silencing of 9 putative CIN genes relative to controls using ON-TARGETplus siRNA pools in hTERT cells.

Table 4-8. KS Tests Identify Significant Changes in NA Following Gene Silencing in hTERT

Condition[A]	*p*-value[B]	Significance[C]	*D*[D]
Untreated	0.1612	ns	0.1038
si*ARL2*	< 0.0001	****	0.5960
si*BUB3*	< 0.0001	****	0.4424
si*DSN1*	< 0.0001	****	0.6517
si*GARS*	< 0.0001	****	0.4441
si*GART*	< 0.0001	****	0.4978
si*NUF2*	< 0.0001	****	0.3120
si*PIGS*	0.0002	***	0.2477
si*SHMT2*	< 0.0001	****	0.2952
si*SPC24*	0.0003	***	0.1981

[A]Conditions in bold induce significant (*p*-value < 0.05) cumulative NA frequency distribution changes (vs. si*GAPDH*).
[B]*p*-values calculated from two-sample KS tests for the listed condition vs. si*GAPDH*.
[C]Significance level (ns = not significant, *** = *p*-value < 0.001, **** = *p*-value < 0.0001).
[D]*D*; *D*-statistic (maximum deviation between the two distribution curves).

Table 4-9. Gene Silencing Induces Increases in MN Formation in hTERT

Condition[A]	No. MNi[B]	No. Nuclei	MNi/Nucleus[C]	FI[D]
si*GAPDH*	17	922	0.0184	1.0
si*ARL2*	24	246	0.0976	5.3
si*BUB3*	56	994	0.0563	3.1
si*DSN1*	23	314	0.0732	4.0
si*GARS*	10	621	0.0161	0.9
si*GART*	17	596	0.0285	1.5
si*NUF2*	46	171	0.2690	14.6
si*PIGS*	24	510	0.0471	2.6
si*SHMT2*	3	1040	0.0029	0.2
si*SPC24*	117	818	0.1430	7.8

[A]Genes in bold induce MN increases greater than 2×standard deviation above the si*GAPDH* mean.
[B]Number of MNi.
[C]Number of MNi normalized to number of nuclei.
[D]Fold increase in MN formation (vs. si*GAPDH*).

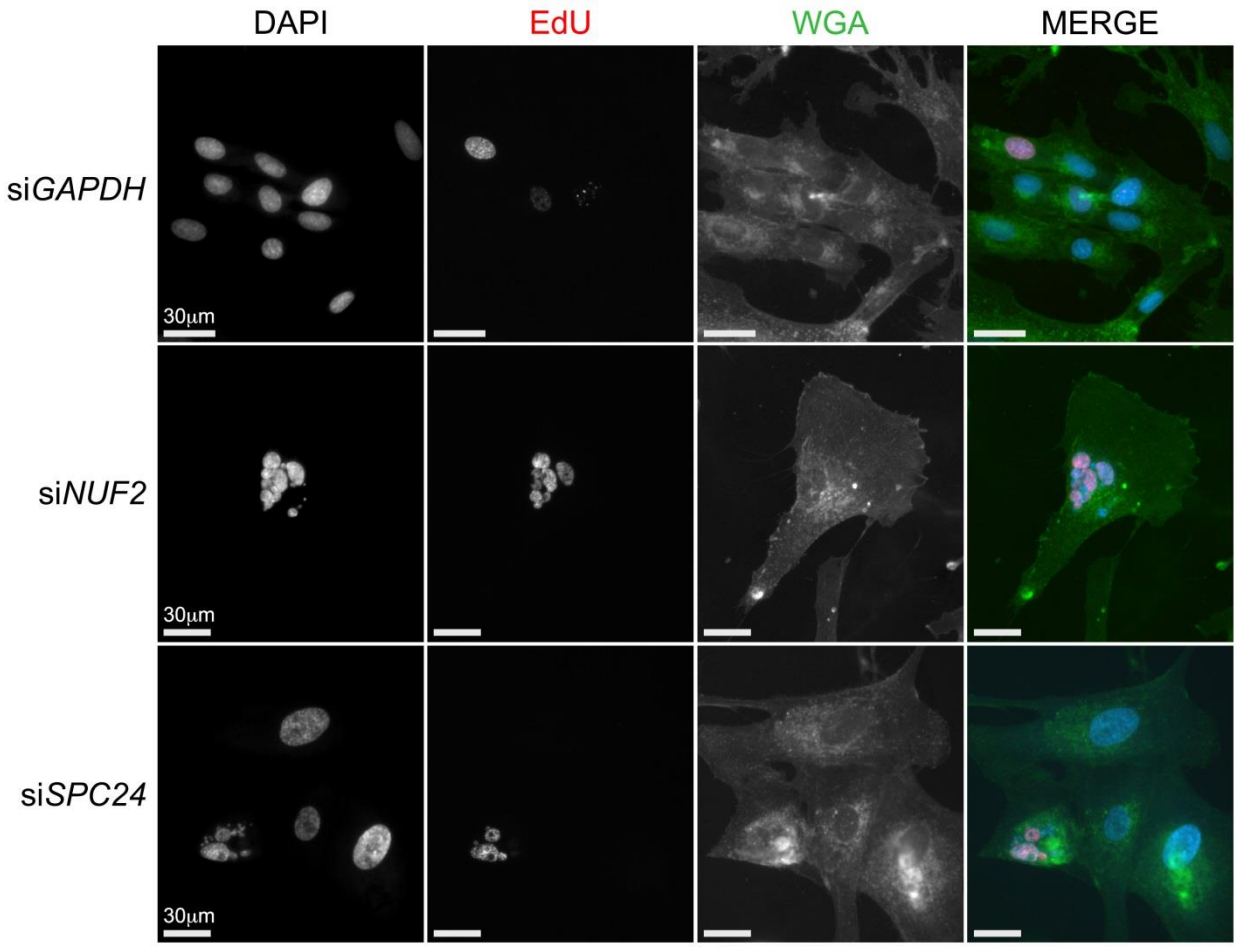

Figure 4-6. Validation of si*NUF2* and si*SPC24* Multinucleated Cells and CIN Phenotypes
Representative 2D fluorescence microscopy images following *NUF2* and *SPC24* silencing presenting multi-nucleated (DAPI, blue) cells (WGA, green), that does not occur in controls (si*GAPDH*). Not all nuclear bodies within a multinucleated cell label with the S-phase marker (EdU, red), indicating that multinucleated cell nuclei may not be undergoing DNA replication concurrently, which can induce CIN.

To determine whether the CIN-associated phenotypes identified above arise due to chromosomal defects, mitotic chromosome spreads were generated and assessed in hTERT cells (*as detailed in Section 2.9.0*). Briefly, CIN-associated aberrations including small-scale numerical (*i.e.* mitotic spreads that gained or lost < 15 chromosomes), large-scale numerical (*i.e.* mitotic spreads that gained > 15 chromosomes), structural (*e.g.* chromosome breakages or compaction defects) and cohesion defects were assessed following gene silencing (Figure 4-7). To determine whether changes in chromosome number distributions occur following silencing, KS tests were employed (*see Section 2.9.0*). Statistically significant changes in cumulative chromosome number frequency distributions were detected in *DSN1*, *GART*, *NUF2*, *PIGS*, *SHMT2* and *SPC24* silenced conditions relative to si*GAPDH* (KS tests, p-value < 0.05 [SI Table S4-7]) (Figure 4-8A). Although *ARL2*, *BUB3*, and *GARS* silencing induced increases in both small and large-scale numerical chromosome content changes, the overall impact on chromosome number distributions did not reach statistical significance according to KS tests. Despite this, > 3-fold increases in aberrant CIN phenotypes (Figure 4-8B and C) were observed for all 9 genes including *ARL2*, *BUB3*, and *GARS*. These data support *ARL2*, *BUB3*, *GARS*, *GART*, *DSN1*, *NUF2*, *PIGS*, *SHMT2* and *SPC24* as novel CIN genes, and further show that the CIN phenotypes are different between conditions.

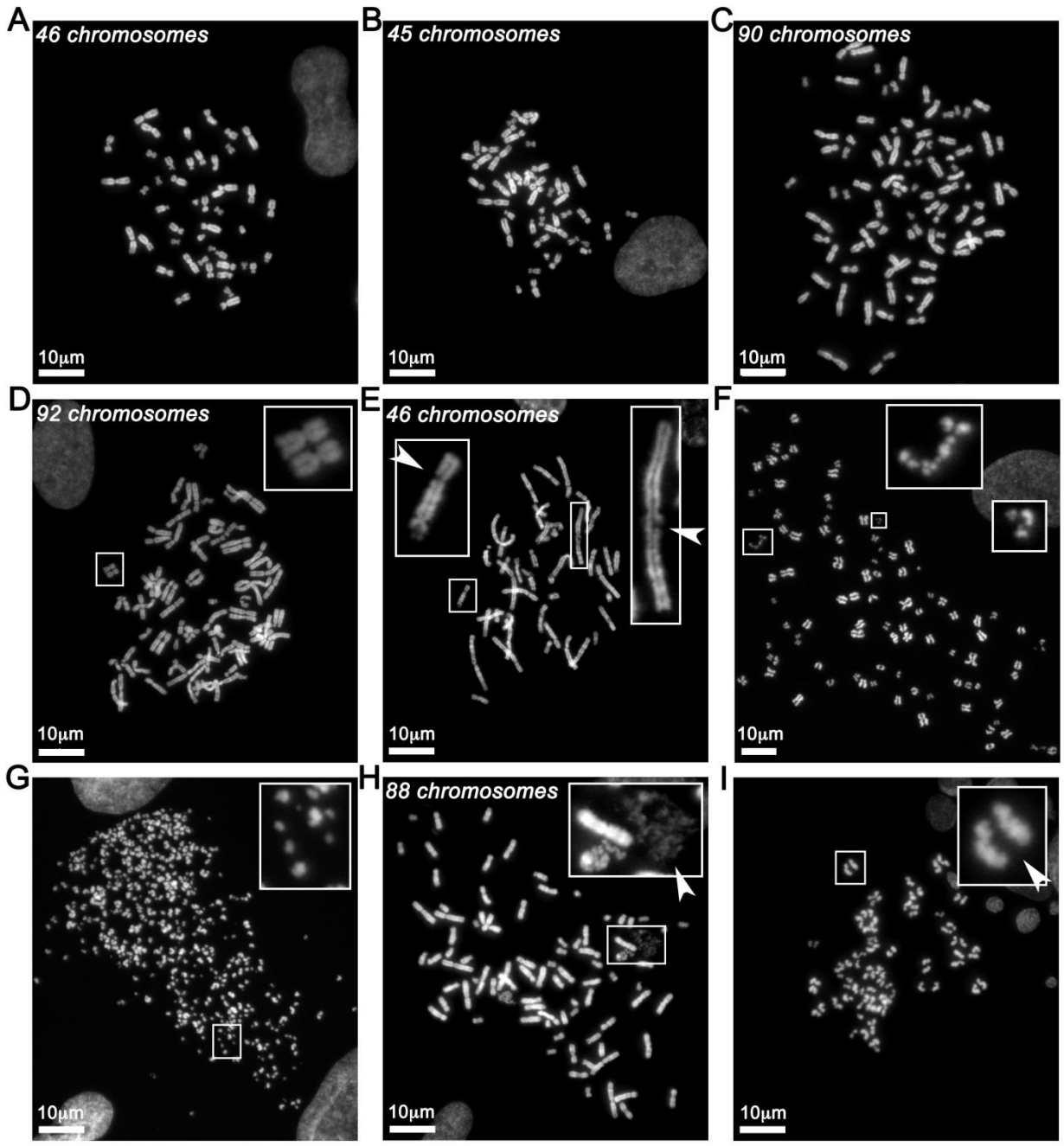

Figure 4-7. Numerical and Structural Phenotypes Observed Following Gene Silencing
(A) Typical mitotic chromosome spread harbouring the expected 46 chromosomes in hTERT. ***(B)*** Small-scale numerical defect. ***(C)*** Large-scale numerical defect. ***(D)*** Endoreduplication resulting in large-scale numerical gain. ***(E-G)*** Chromosome breakages (increasing in severity). ***(H)*** Chromosome decompaction ***(I)*** Sister chromatid cohesion defects.

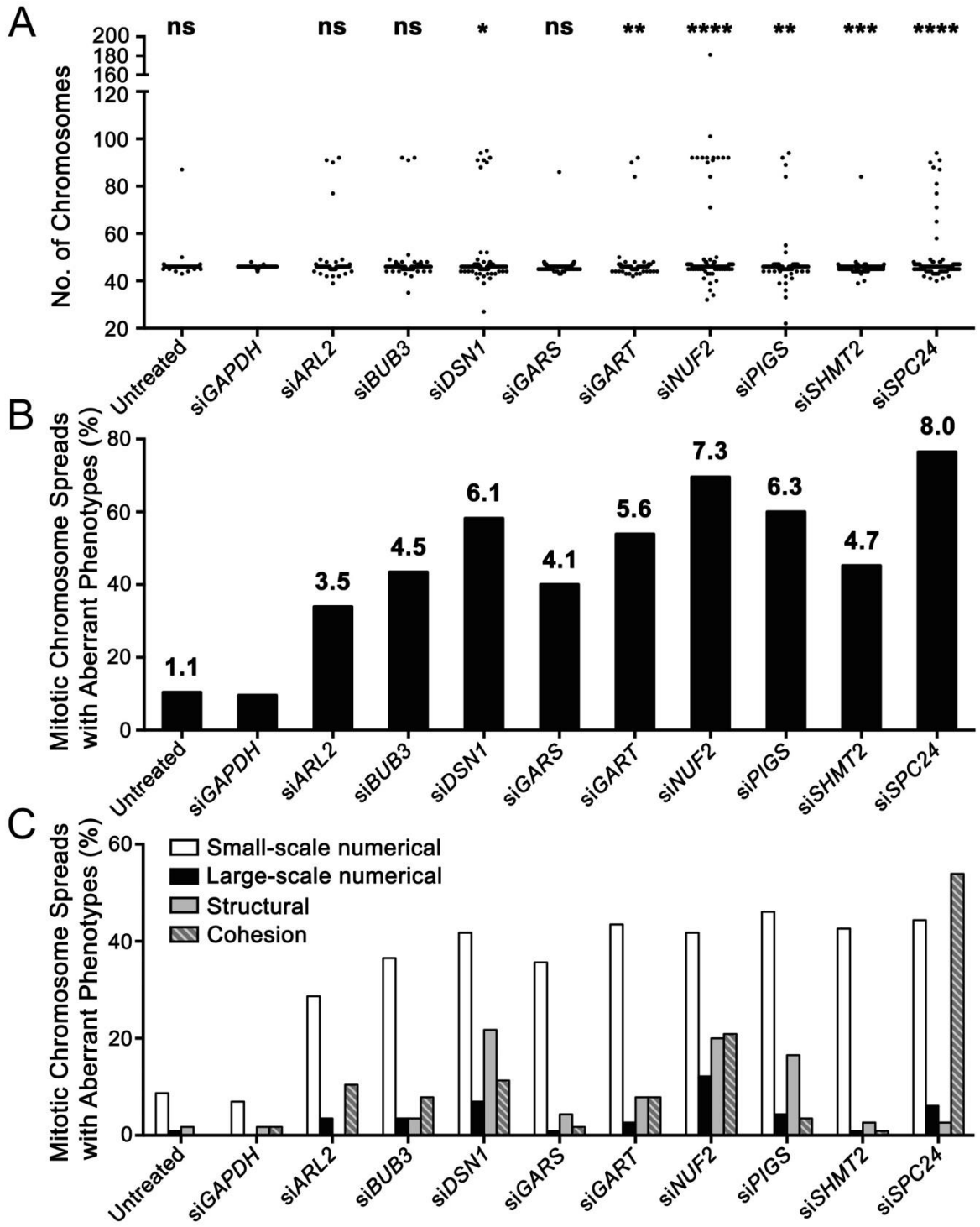

Figure 4-8. Gene Silencing Underlies Chromosomal Aberrations in hTERT

(A) Dot plot presenting the number of chromosomes enumerated from mitotic chromosome spreads for the indicated conditions (x-axis). Significant changes in chromosome number distributions (vs. si*GAPDH*) are displayed (KS tests, ns = not significant, * = p-value < 0.05, ** = p-value < 0.01, *** = p-value < 0.001, **** = p-value < 0.0001) (***B)*** Bar graph displaying the 3.5- to 8.0-fold increases in CIN phenotypes observed following gene silencing relative to si*GAPDH*. ***(C)*** Bar graph with percentages of specific chromosomal aberrations. (n = 115, N =1).

As CIN is frequently observed in CRC, we expanded our study into HCT116, a karyotypically stable CRC cell line. Similar to hTERT, silencing all 9 putative CIN genes in HCT116 (Figure 4-9) resulted in statistically significant differences in cumulative NA frequency distributions relative to controls (SI Table S4-8). Increases in MN formation beyond the established threshold were also detected for all genes, with exception of *GARS*, *GART*, and *SHMT2* (SI Table S4-9). *NUF2* and *SPC24* silencing induced the most extensive (~10-fold) MN increases (SI Table S4-9, Figure 4-10) and also generated multinucleated cells (Figure 4-10, SI Table S4-5), indicating these are not cell-type specific events. Mitotic chromosome spread analyses revealed similar, albeit more extensive numerical chromosome changes with all 9 genes inducing significant changes in chromosome number distributions (Figure 4-11A, SI Table S4-7). Similar trends were observed between cell types, as > 3-fold increases in aberrant CIN phenotypes were observed for all genes relative to controls, with si*SPC24*, si*NUF2* and si*DSN1* causing the largest increases overall (Figure 4-11B). Cell type specific results were also observed, as *SPC24* silencing typically induced small-scale numerical changes and cohesion defects in hTERT (Figure 4-11C), and small-scale numerical and structural aberrations in HCT116 (Figure 4-11C). Taken together, the above experiments provide convincing evidence to support the 9 genes as novel CIN genes, particularly within a CRC cellular context.

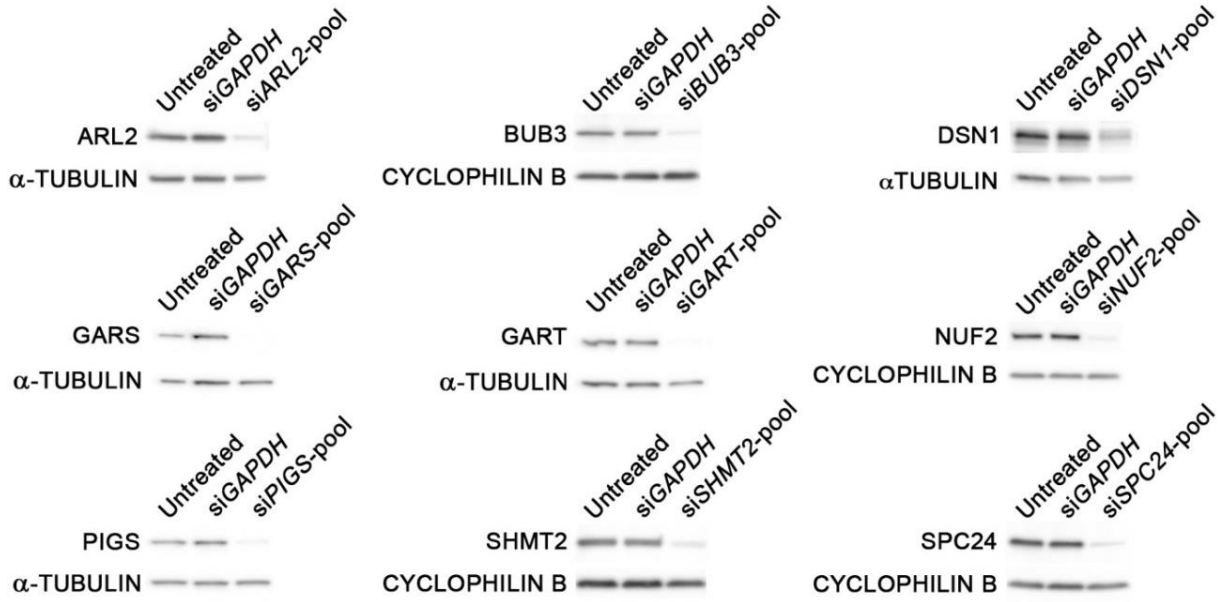

Figure 4-9. Putative CIN Gene Silencing in HCT116
Western blots displaying highly effective silencing of 9 putative CIN genes relative to controls in HCT116.

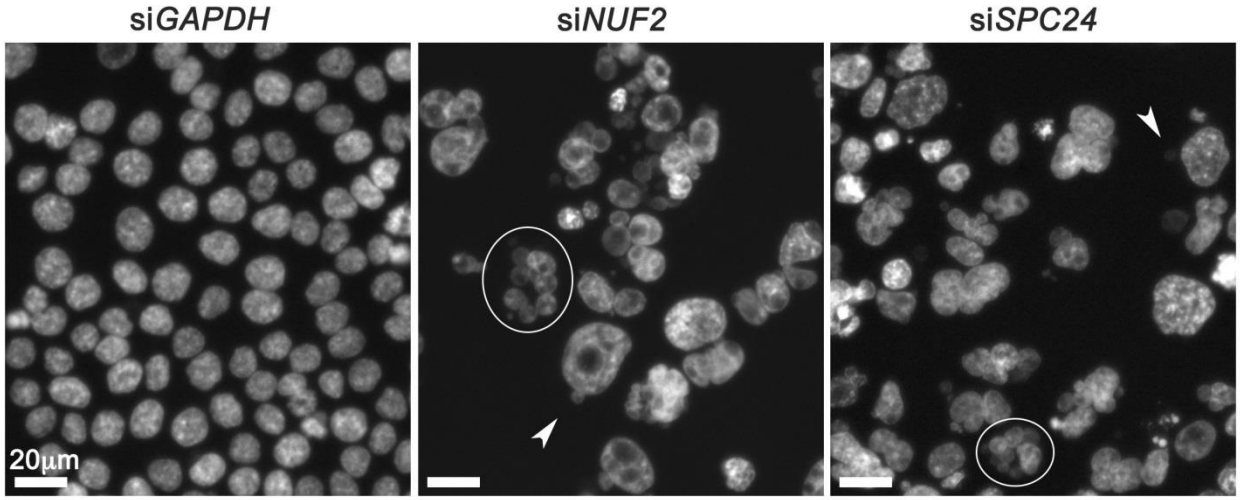

Figure 4-10. *NUF2* and *SPC24* Silencing Induces Increases in MN Formation and Multinucleated HCT116 Cells
2D fluorescence microscopy images presenting MN (arrowheads) and multinucleated cell formation (circled) in HCT116 following *NUF2* and *SPC24* silencing.

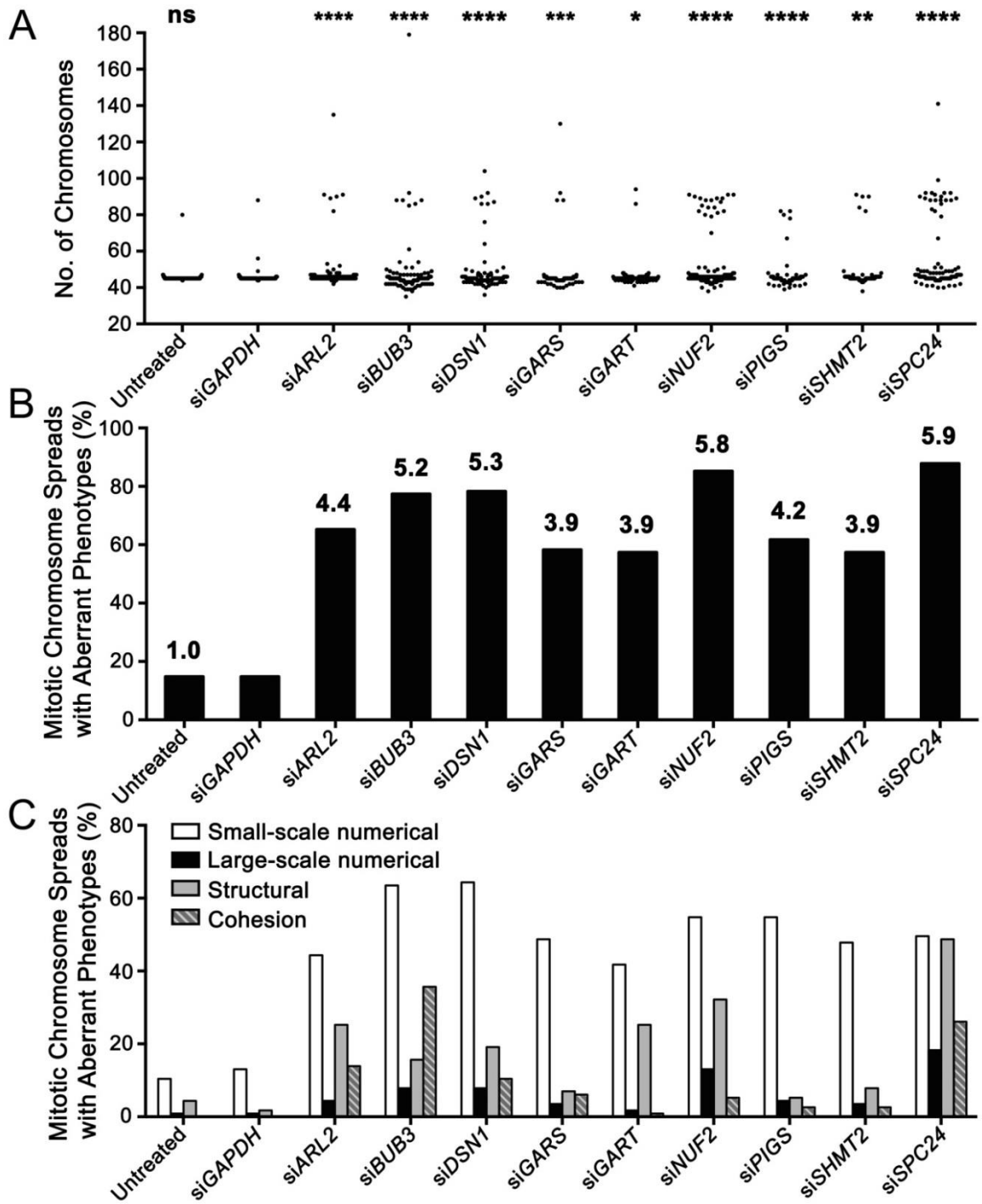

Figure 4-11. Gene Silencing Drives Chromosomal Changes in HCT116 Cells

(A) Dot plot presenting chromosome enumeration data acquired from the indicated conditions (x-axis). KS tests revealed significant changes in the cumulative chromosome number frequency distributions for all 9 genes relative to controls (si*GAPDH*) (ns = not significant, * = *p*-value < 0.05, ** = *p*-value < 0.01, *** = *p*-value < 0.001, **** = *p*-value < 0.0001). ***(B)*** Bar graph presenting the percentage of mitotic chromosome spreads displaying aberrant CIN phenotypes with the fold increase (vs. si*GAPDH*) presented above the bar. ***(C)*** Bar graph with percentages of specific aberrations. (n = 115, N = 1).

4.3.4. Diminished *SKP1* Expression Drives Chromosomal Changes in hTERT and HCT116

As SKP1 regulates degradation of numerous downstream substrates, *SKP1* alterations harbour potential broad spectrum implications for CIN and oncogenesis. Thus, *SKP1* validation and characterization (*see Chapter 5*) was pursued in the greatest detail. First, direct silencing tests (ON-TARGETplus siRNA-pool) (*see Section 2.3.1*) were performed in hTERT to confirm the high-content screen results. Indeed, *SKP1* silencing induced significant increases in mean NA (Student's *t*-test, p-value < 0.05) (Figure 4-12A and B) and significant cumulative NA frequency distribution changes (KS test, p-value < 0.05) relative to controls (Figure 4-12C). *SKP1* silencing also resulted in an ~2.5-fold increase in MN formation that was not apparent in the initial hTERT screen (Figure 4-12D). Mitotic chromosome spread analyses (*see Section 2.9.0*) revealed that silencing by the two most effective siRNAs (si*SKP1*-1 and -2) and the pool (Figure 4-13A), resulted in changes in chromosome numbers (Figure 4-13B) that were deemed statistically significant by KS tests (p-value < 0.05) (SI Table S4-7). *SKP1* silencing in all conditions induced > 5-fold increases in aberrant chromosome and CIN phenotypes (Figure 4-13C). The most frequently observed were small-scale numerical and structural aberrations followed by large-scale numerical and cohesion defects (Figure 4-13D and E). In HCT116, *SKP1* silencing (Figure 4-14A) corresponded with extensive NA increases (Figure 4-14B and C), cumulative NA frequency distribution changes (KS tests, p-value < 0.05) (Figure 4-14D) and > 3-fold MN increases relative to controls (Figure 4-14E). Significant chromosome number changes were also detected in si*SKP1*-1, -2, and pooled conditions (KS tests, p-value < 0.05 [SI Table S4-7]) (Figure 4-14F), each causing ~5-fold increases in CIN phenotypes relative to si*GAPDH* (Figure 4-14G). The trends for the most common CIN-phenotypes in HCT116 were similar to hTERT with small-scale numerical and structural abnormalities occurring most frequently, typically

followed by large-scale numerical and cohesion defects (Figure 4-14H). Overall, these data validate that *SKP1* silencing induces CIN phenotypes including large increases in NA as well as MN formation in both hTERT and HCT116, which correlate with CIN-associated chromosome aberrations.

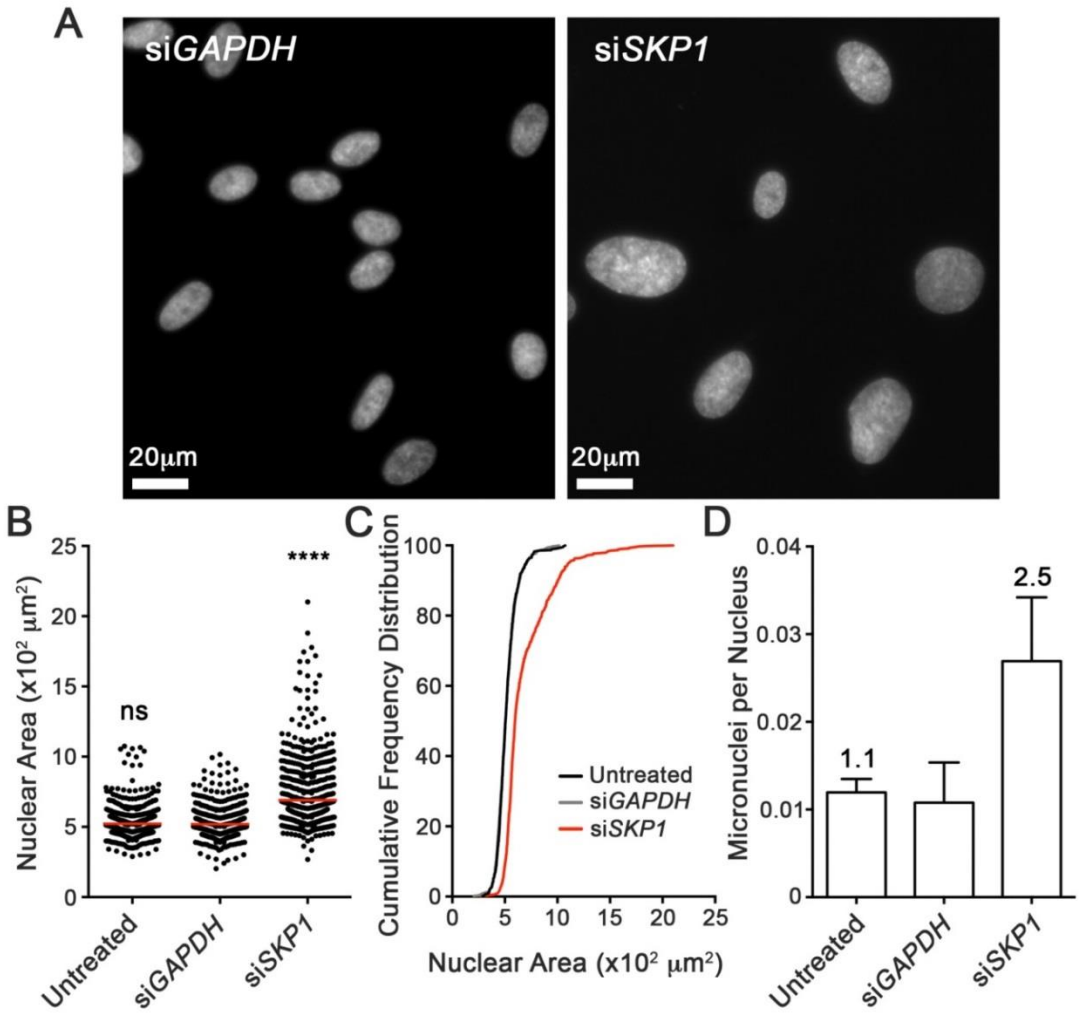

Figure 4-12. *SKP1* Silencing Induces CIN Phenotypes in hTERT Cells
(A) Fluorescence microscopy images displaying visual increases in NA following *SKP1* silencing. ***(B)*** Dot plot presenting NA values for each nucleus analyzed for the indicated conditions (x-axis). Note the statistically significant increase (Student's *t*-test, *p*-value < 0.0001) in mean NA (red line) in si*SKP1* cells (n > 650) relative to controls (si*GAPDH*). ***(C)*** Cumulative NA frequency distributions showing the significant increase (KS test, *p*-value < 0.0001) in NAs in si*SKP1* cells (red) relative to controls. Note the Untreated (black) and si*GAPDH* (gray) distributions are largely superimposable (n > 650). ***(D)*** Bar graph showing a statistically significant increase in MN formation following *SKP1* silencing relative to controls (Student's *t*-test, *p*-value < 0.05). Values above the bar represent the fold increase relative to control (si*GAPDH*) (n > 650). (N =3).

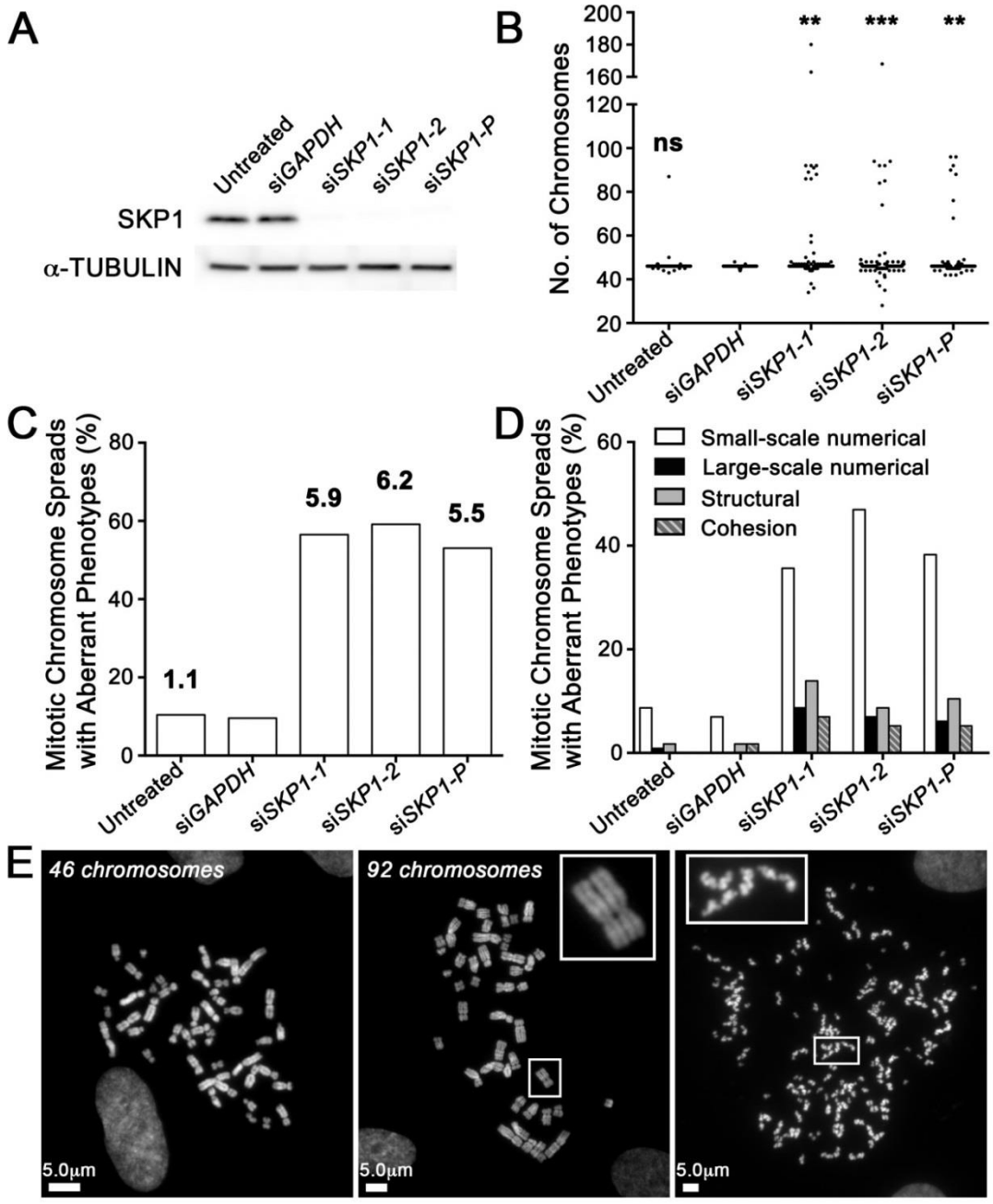

Figure 4-13. *SKP1* Silencing Drives Chromosomal Changes in hTERT Cells
(A) Western blot validates *SKP1* silencing by individual (si*SKP1*-1 and si*SKP1*-2) or pooled (si*SKP1*-P) siRNA duplexes. ***(B)*** Dot plot presenting number of chromosomes from 115 mitotic chromosome spreads. Significant chromosome number changes were observed following *SKP1* silencing compared to controls (KS tests, *p*-value < 0.05). ***(C)*** Bar graph with percentages of chromosome spreads displaying CIN phenotypes. Number above the bar represents fold increase relative to si*GAPDH*. ***(D)*** Bar graph displaying the aberrant chromosome phenotypes observed. ***(E)*** Representative mitotic chromosome spreads for si*GAPDH* displaying the expected number of 46 chromosomes (left), and the si*SKP1* condition displaying endoreduplication with large-scale chromosome content changes (middle) and sister chromatid cohesion defects with structural abnormalities (right). (N = 1).

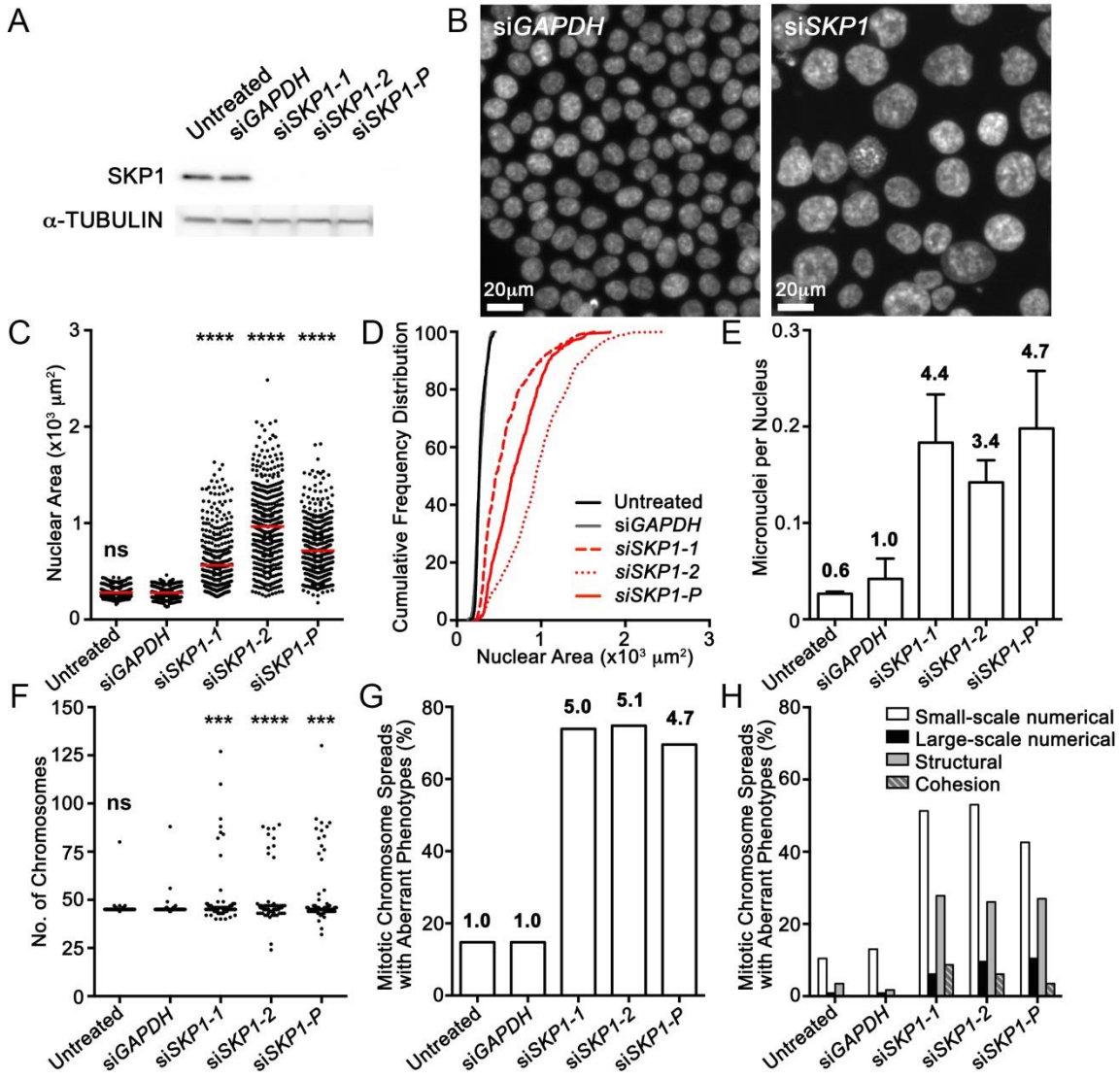

Figure 4-14. *SKP1* Silencing Induces CIN Phenotypes and Chromosome Aberrations in HCT116 Cells

(A) Western blot verifies *SKP1* silencing by si*SKP1*-1, -2, and -pool. ***(B)*** Representative fluorescence microscopy images of si*GAPDH* cells (left) and si*SKP1* cells displaying increased NA and MN formation (right). ***(C)*** Dot plot presenting NA data from each condition, displaying the significant mean NA (red) increases following *SKP1* silencing (**** = *p*-value < 0.0001, *n* = 450). ***(D)*** NA data presented as cumulative NA frequency distributions. Note the rightward shift (*i.e.* larger nuclei) following *SKP1* silencing (red lines) that were statistically significant (KS tests, *p*-value < 0.0001). ***(E)*** Bar graph presenting average number of MNi per nucleus from each condition (*n* = ~700). Fold increases relative to si*GAPDH* are presented above the bar. ***(F)*** Dot plot displaying the number of chromosomes enumerated from each chromosome spread analyzed from the *SKP1* silenced conditions (*n* = 115) and controls as presented previously. *SKP1* silencing induced significant changes in the relative frequency distribution of chromosome numbers relative to si*GAPDH* (KS tests, *p*-value < 0.001). ***(G)*** Bar graph with percentages of abnormal mitotic chromosome spreads. Fold increase relative to si*GAPDH* is presented above the bar. ***(H)*** Bar graph displaying the specific chromosome aberrations observed.

4.4.0. Discussion

In this study, NA and MN enumeration assays were utilized to identify 148 putative human CIN genes in HT1080 fibrosarcoma and hTERT fibroblast cells from a total of 164 candidate genes screened. A prioritized subset of 10 putative CIN genes was validated by cytogenetic approaches that confirmed gene silencing induced numerical and structural chromosome defects that are consistent with CIN. As CIN is a common feature of CRC, validation was expanded into HCT116 CRC cells, which provided similar, corroborating results. Overall, these findings validated *ARL2*, *BUB3*, *DSN1*, *GARS*, *GART*, *NUF2*, *PIGS*, *SHMT2*, *SPC24*, and *SKP1* as novel human CIN genes, and may have important implications for oncogenesis.

ARL2, BUB3, DSN1, NUF2, and SPC24 function in mitosis with roles in mitotic spindle assembly, microtubule dynamics, and kinetochore-microtubule attachment[213-215]. As misregulation of these pathways can result in chromosome missegregation, it was not unexpected for genes involved in these pathways to be identified and validated in our study. The phenotypic similarities between si*NUF2* and si*SPC24* (*e.g.* MN formation, multinucleated cells, extensive numerical and structural chromosome defects) were also anticipated, as the encoded proteins both function within the NDC80 kinetochore complex[213]. Alterations in NDC80 may prevent proper kinetochore-microtubule attachment causing chromosome missegregation and/or aberrant cytokinesis events leading to numerical CIN and multinucleated cells. Further, EdU labeling determined that the nuclei of si*NUF2* and si*SPC24* multinucleated cells may not be proceeding through the cell cycle in unison. Progression of a cell into mitosis before all nuclei have completed DNA replication can induce premature chromatin condensation[211], which may contribute to the structural defects observed in the mitotic chromosome spreads of si*NUF2* and si*SPC24* cells. Interestingly, *DSN1* silencing induced similar, albeit less pronounced CIN

phenotypes than si*NUF2* or si*SPC24*. DSN1 is a component of the MIS12 complex, which physically interacts with NDC80 to mediate kinetochore-microtubule attachment[213]. Phenotypic differences may be attributed to multiple factors, including differences in silencing efficiency, the heterogeneous nature of the CIN phenotype, proteins that functionally compensate for loss of DSN1, or perhaps, diminished DSN1 activity simply has less detrimental effects on MIS12-NDC80 or kinetochore-microtubule interactions than either NUF2 or SPC24.

The GTPase ARL2 functions within a chaperone complex to regulate soluble αβ-tubulin levels and support microtubule dynamics[214]. *ARL2* silencing may hinder mitotic spindle assembly or chromosome segregation leading to CIN. As si*ARL2*-associated chromosome changes were typically less extensive than those of si*NUF2*, si*SPC24* or si*DSN1*, the impact of reduced ARL2 on microtubule dynamics may not impede chromosome segregation as extensively as alterations that directly hinder kinetochore-microtubule attachment. *ARL2* silencing has also been shown to increase phosphorylated TP53 (TP53PhosS15) levels in breast cancer cells, causing TP53 to preferentially localize to the centrosome/mitotic spindle rather than undergoing nuclear translocation to mediate DNA damage repair[216]. This may explain the increase in chromosome breakages observed in si*ARL2* CRC cells. BUB3 also functions in mitosis as a component of the spindle assembly checkpoint, which ensures chromosomes are properly attached to the bi-oriented mitotic spindle prior to anaphase onset[217]. Diminished *BUB3* expression may result in checkpoint abrogation, allowing mitosis to proceed with chromosome malattachments, resulting in CIN. *BUB3* silencing also induced sister chromatid cohesion defects in HCT116 and hTERT, suggesting BUB3 may play an important role in cohesion. In fact, silencing each of *NUF2*, *SPC24*, *DSN1*, *ARL2*, and *BUB3* induced increases in cohesion defects in both cell lines, suggesting that kinetochore and mitotic spindle assembly are critical for proper

sister chromatid cohesion. *NUF2*, *SPC24*, *DSN1*, *ARL2* and *BUB3* are individually altered in 6%, 6%, 31%, 5% and 5% of all CRC cases respectively, or collectively altered in 42% of all CRC cases[209]. While diminished expression was investigated in this thesis, the most common alterations reported in CRC involving these genes are amplification and/or overexpression[209]. In combination with the above findings, this may indicate that kinetochore/mitotic spindle components must be maintained at specific cellular levels in order to prevent CIN and oncogenesis (*i.e.* induces CIN when under- or over-expressed). Conversely, overexpression may reflect rapid cellular proliferation, particularly for cancer cells with increased chromosome numbers due to CIN, which is permitted by overexpression of these genes. As *NUF2*, *SPC24*, *DSN1*, *ARL2* and *BUB3* are frequently amplified or overexpressed in CRC[209], their encoded proteins may represent potential targets in novel precision medicine therapies. However, inhibition of the above proteins as a therapeutic strategy must be investigated thoroughly, as diminished gene expression (akin to loss of function [inhibition]) induces CIN.

In contrast to the above genes, *GART*, *SHMT2*, *GARS*, *PIGS*, and *SKP1* encode proteins with functions that are less intuitively linked to CIN. GART functions in *de novo* purine biosynthesis[218], and gene silencing induces both small-scale numerical chromosomal changes and structural defects. Conceptually, reduced GART levels may diminish the pool of available purines required for DNA synthesis or DNA damage repair, thereby inducing CIN. Similarly, SHMT2 is a mitochondrial protein involved in *de novo* thymidylate biosynthesis[219], and diminished expression may hinder folate metabolism, thymidine nucleotide production[220] and induce CIN. In agreement with our findings, misregulation of nucleotide metabolism leading to an imbalance in the intracellular deoxyribonucleotide pool is a common mechanism contributing to cancer development and progression[221].

GARS normally functions to charge tRNAs with glycine[222] and diminished expression was typically associated with small-scale chromosome content changes that may arise indirectly from defective translation of proteins that normally function to maintain chromosome stability. While *GARS* is underexpressed in ~1% of CRCs, it is heterozygously deleted and underexpressed in ~27% of ovarian cancers[158], and therefore may have pathogenic implications. PIGS normally functions in GPI-anchor biosynthesis[223] and diminished expression was associated with small-scale numerical chromosome changes and DNA damage. Interestingly, Swanton *et al*[55] demonstrated that decreased levels of PIGN, which also mediates GPI-anchor biosynthesis[224], induces replication stress, anaphase bridges and CIN, and *PIGS* copy number loss is observed in 84% of aneuploid CRCs[55,209]. Although the link between altered GPI-anchor biosynthesis and replication stress has yet to be elucidated, it is not unexpected that *PIGS* silencing also induces CIN and may be important in CRC pathogenesis. Lastly, the altered mechanism(s) underlying CIN in *SKP1* silenced cells have yet to be characterized. However, the role of SKP1 in proteasomal degradation (*see Section 1.5.1*), suggests that alterations in SKP1 expression and function may indirectly impact a myriad of downstream substrates, CIN and oncogenic pathways, and will be further explored in Chapter 5. Overall, the above findings highlight the merit of screening for CIN phenotypes to expedite the identification of novel CIN genes from biological pathways with less intuitive links to CIN. Further, cancer cells with mutated and/or misexpressed CIN genes such as *ARL2*, *BUB3*, *DSN1*, *GARS*, *GART*, *NUF2*, *PIGS*, *SHMT2*, *SPC24* and *SKP1* may harbor vulnerabilities (*e.g.* mitotic defects or dysfunctional nucleotide biosynthesis) that can be exploited in novel precision medicine approaches to drive highly effective and specific killing of cancer cells, representing a promising avenue to explore in subsequent fundamental and translational studies.

4.5.0. Supporting Information

4.5.1. Supporting Tables

Table S4-1. KS Tests Reveal Significant Changes in NA Following Silencing in HT1080

Gene[A]	*OMA1*	*WDHD1*	*TAF7L*	*CFDP1*	*PPP1R3C*	*PDXK*	*KDM6A*
***p*-value**[B]	0.8689	0.8310	0.6266	0.6037	0.5729	0.5315	0.5304
Sig.[C]	ns	ns	ns	ns	ns	ns	ns
D[D]	0.0578	0.0711	0.0626	0.0612	0.0603	0.0583	0.0587
Gene	*CDC7*	*UBE2A*	*KIFC1*	*SSU72*	*TUBG2*	*PPP2R5C*	*GINS3*
***p*-value**	0.5228	0.5178	0.5019	0.3984	0.3840	0.3743	0.3647
Sig.	ns	ns	ns	ns	ns	ns	ns
D	0.0880	0.0714	0.0789	0.0766	0.0645	0.0649	0.0723
Gene	*EIF2B3*	*ATAD5*	*RPRD1B*	*RAD51*	*GINS4*	*NSFL1C*	*UBE2I*
***p*-value**	0.3454	0.3153	0.3042	0.3031	0.2812	0.2698	0.2275
Sig.	ns	ns	ns	ns	ns	ns	ns
D	0.0875	0.0671	0.0992	0.0833	0.1347	0.0752	0.1024
Gene	*PCID2*	*RFC2*	*RFC4*	*PFAS*	*TPI1*	*GCH1*	*MUC17*
***p*-value**	0.1940	0.1899	0.1882	0.1852	0.1380	0.1293	0.1175
Sig.	ns	ns	ns	ns	ns	ns	ns
D	0.0766	0.1322	0.1461	0.0924	0.0969	0.1157	0.1147
Gene	*HIST2H4B*	*TRAPPC10*	*CDK3*	*PYCRL*	*TOP3A*	*BUB1*	*CHAF1A*
***p*-value**	0.1156	0.1058	0.0928	0.0829	0.0720	0.0711	0.0640
Sig.	ns	ns	ns	ns	ns	ns	ns
D	0.0828	0.0882	0.1012	0.1545	0.0896	0.0896	0.1704
Gene	*IPO5*	*PSMA3*	*ATAD2B*	*ANAPC10*	*PSMD2*	*WDR33*	*FARSB*
***p*-value**	0.0590	0.0511	0.0508	0.0503	0.0491	0.0470	0.0401
Sig.	ns	ns	ns	ns	ns	ns	ns
D	0.0991	0.1590	0.1770	0.0926	0.1346	0.0995	0.1902
Gene	*MCM5*	*DSCC1*	*TUBA4A*	*CIAPIN1*	*PFDN2*	*RAD1*	*BTAF1*
***p*-value**	0.0379	0.0376	0.0359	0.0349	0.0317	0.0250	0.0185
Sig.	ns	ns	ns	ns	ns	ns	ns
D	0.1893	0.0940	0.1627	0.1936	0.1229	0.1681	0.1274
Gene	*CNOT6*	*CHTF18*	*SNRNP70*	***MAU2***	***DLD***	***SCFD1***	***DSN1***
***p*-value**	0.0169	0.0153	0.0101	0.0087	0.0082	0.0079	0.0059
Sig.	ns	ns	ns	**	**	**	**
D	0.1393	0.1351	0.1667	0.2120	0.1782	0.1431	0.1255
Gene	***PSMA6***	***CHTF8***	***PRIM2***	***PSMD12***	***TRIM25***	***RBBP4***	***EPRS***
***p*-value**	0.0052	0.0043	0.0039	0.0039	0.0035	0.0032	0.0028
Sig.	**	**	**	**	**	**	**
D	0.2595	0.1281	0.1198	0.2125	0.2542	0.1414	0.2201
Gene	***SPC24***	***POLR3E***	***ACO2***	***ABCB7***	***ASF1A***	***DNAJC10***	***ABCE1***
***p*-value**	0.0027	0.0024	0.0023	0.0021	0.0018	0.0016	0.0016
Sig.	**	**	**	**	**	**	**
D	0.2038	0.1675	0.1284	0.2016	0.1417	0.1928	0.2167

Table S4-1 *Continued*. KS Tests Reveal Significant Changes in NA Following Silencing in HT1080

Gene[A]	***YIPF5***	***TIPIN***	***FPGS***	***NUF2***	***SMARCC2***	***DNAJC2***	***CTF2H2***
***p*-value**[B]	0.0012	0.0012	0.0010	0.0009	0.0009	0.0008	0.0008
Sig.[C]	**	**	***	***	***	***	***
D[D]	0.1533	0.2715	0.2124	0.1881	0.1410	0.1383	0.2413
Gene	***TAF9B***	***MCM2***	***NAT10***	***STAG1***	***ARL2***	***SPC25***	***RUVBL2***
***p*-value**	0.0007	0.0007	0.0005	0.0004	0.0003	0.0001	0.0001
Sig	***	***	***	***	***	***	***
D	0.2289	0.1582	0.3048	0.1677	0.1757	0.1892	0.2685
Gene	***RAD50***	***PSMA7***	***IWS1***	***CKS2***	***PIF1***	***PGK1***	***FEN1***
***p*-value**	0.0001	0.0001	< 0.0001	< 0.0001	< 0.0001	< 0.0001	< 0.0001
Sig	***	***	****	****	****	****	****
D	0.1981	0.2279	0.1688	0.1733	0.1751	0.1790	0.1902
Gene	***CNOT8***	***POLD1***	***OSGEP***	***GINS2***	***FAM96B***	***AURKC***	***RAD51B***
***p*-value**	< 0.0001	< 0.0001	< 0.0001	< 0.0001	< 0.0001	< 0.0001	< 0.0001
Sig	****	****	****	****	****	****	****
D	0.2073	0.2178	0.2287	0.2435	0.2437	0.2479	0.2488
Gene	***PPP1R7***	***UGP2***	***CSTF2***	***SRF***	***C20orf4***	***MECR***	***RAD54L***
***p*-value**	< 0.0001	< 0.0001	< 0.0001	< 0.0001	< 0.0001	< 0.0001	< 0.0001
Sig	****	****	****	****	****	****	****
D	0.2492	0.2585	0.2599	0.2635	0.2637	0.2678	0.2703
Gene	***HLTF***	***EXOSC2***	***ACACB***	***SF1***	***DDX39B***	***MRPL27***	***TUBGCP3***
***p*-value**	< 0.0001	< 0.0001	< 0.0001	< 0.0001	< 0.0001	< 0.0001	< 0.0001
Sig	****	****	****	****	****	****	****
D	0.2787	0.2817	0.2861	0.2861	0.2867	0.2876	0.2974
Gene	***UBR2***	***WDR43***	***SHMT2***	***SLMAP***	***TRMT5***	***MCM10***	***POLD3***
***p*-value**	< 0.0001	< 0.0001	< 0.0001	< 0.0001	< 0.0001	< 0.0001	< 0.0001
Sig	****	****	****	****	****	****	****
D	0.2999	0.3014	0.3118	0.3143	0.3159	0.3162	0.3220
Gene	***GPN2***	***POLR3K***	***MAPRE1***	***CSE1L***	***PIGS***	***PRIM1***	***PWP1***
***p*-value**	< 0.0001	< 0.0001	< 0.0001	< 0.0001	< 0.0001	< 0.0001	< 0.0001
Sig	****	****	****	****	****	****	****
D	0.3228	0.3312	0.3424	0.3476	0.3575	0.3592	0.3621
Gene	***BUB3***	***RAD18***	***RABGGTA***	***PAICS***	***RTN4***	***GARS***	***DDX51***
***p*-value**	< 0.0001	< 0.0001	< 0.0001	< 0.0001	< 0.0001	< 0.0001	< 0.0001
Sig	****	****	****	****	****	****	****
D	0.3632	0.3692	0.3791	0.3879	0.3893	0.3910	0.4040
Gene	***GART***	***QARS***	***PCNA***	***SKP1***	***RAD52***	***RPL7***	***RNF10***
***p*-value**	< 0.0001	< 0.0001	< 0.0001	< 0.0001	< 0.0001	< 0.0001	< 0.0001
Sig	****	****	****	****	****	****	****
D	0.4184	0.4247	0.4537	0.4599	0.4949	0.5305	0.5420

[A]Genes in bold are putative CIN genes causing significant changes (*p*-value < 0.01) in cumulative NA frequency distributions relative to si*GAPDH*.

[B]*p*-values calculated from two-sample KS tests comparing listed gene to si*GAPDH*.

[C]Significance level where ns = not significant, ** = *p*-value < 0.01, *** = *p*-value < 0.001, **** = *p*-value < 0.0001.

[D]*D*; *D*-statistic (maximum deviation between the two distribution curves).

Table S4-2. KS Tests Reveal Significant Changes in NA Following Silencing in hTERT

Gene[A]	*ABCB7*	*TUBA4A*	*TPI1*	*PFAS*	*PPP2R5C*	*MCM5*	*MAPRE1*
***p*-value**[B]	0.5112	0.4888	0.3773	0.3407	0.2686	0.2215	0.1941
Sig.[C]	ns	ns	ns	ns	ns	ns	ns
D[D]	0.0865	0.1097	0.0859	0.0813	0.0756	0.1152	0.0815
Gene	*KIFC1*	*AURKC*	*POLD3*	*OSGEP*	*TUBG2*	*TRAPPC10*	*CHTF18*
***p*-value**	0.1792	0.1406	0.1378	0.1226	0.1136	0.1114	0.11
Sig.	ns	ns	ns	ns	ns	ns	ns
D	0.1039	0.1217	0.1496	0.0826	0.1010	0.0978	0.1072
Gene	*MCM2*	*GTF2H2*	*CDC7*	*GINS4*	*TXNL4A*	*EIF2B3*	*RBBP4*
***p*-value**	0.0937	0.0911	0.0812	0.0812	0.0667	0.0649	0.0606
Sig.	ns	ns	ns	ns	ns	ns	ns
D	0.1173	0.1086	0.1076	0.1140	0.1483	0.1271	0.1266
Gene	*PDXK*	*NSFL1C*	*SMARCC2*	*RUVBL2*	*RAD51*	*YIPF5*	*PAICS*
***p*-value**	0.0576	0.0555	0.0501	0.0456	0.0429	0.0316	0.0305
Sig.	ns	ns	ns	ns	ns	ns	ns
D	0.09201	0.1242	0.1062	0.1383	0.1457	0.1083	0.1426
Gene	*SPC25*	*RAD52*	*SLMAP*	*CFDP1*	*CNOT8*	***BTAF1***	***PSMA3***
***p*-value**	0.0253	0.0243	0.0169	0.0156	0.0118	0.0092	0.0046
Sig.	ns	ns	ns	ns	ns	**	**
D	0.1393	0.1832	0.1431	0.1367	0.1192	0.1563	0.2499
Gene	***IPO5***	***MUC17***	***DNAJC2***	***PSMA5***	***FEN1***	***NAT10***	***PIGS***
***p*-value**	0.0043	0.0041	0.0036	0.0032	0.0026	0.0026	0.0023
Sig.	**	**	**	**	**	**	**
D	0.1272	0.1604	0.1474	0.2732	0.1512	0.2024	0.1662
Gene	***CKS2***	***ACTB***	***SART1***	***CSE1L***	***DDX39B***	***RPL8***	***ATAD2B***
***p*-value**	0.0019	0.0018	0.0018	0.0015	0.001	0.0005	0.0004
Sig.	**	**	**	**	**	***	***
D	0.1402	0.1813	0.1806	0.1955	0.1556	0.2523	0.1703
Gene	***RFC2***	***PSMA6***	***OMA1***	***PIF1***	***GINS2***	***POLD1***	***PCID2***
***p*-value**	0.0003	0.0002	0.0002	0.0002	0.0001	< 0.0001	< 0.0001
Sig.	***	***	***	***	***	****	****
D	0.2324	0.2523	0.2011	0.1975	0.2293	0.1922	0.1922
Gene	***DLD***	***RAD51B***	***CDK3***	***GINS3***	***POLR3E***	***SRF***	***SCFD1***
***p*-value**	< 0.0001	< 0.0001	< 0.0001	< 0.0001	< 0.0001	< 0.0001	0.0001
Sig.	****	****	****	****	****	****	***
D	0.1946	0.2028	0.2076	0.2078	0.2090	0.2109	0.214
Gene	***TOP3A***	***PGK1***	***ACO2***	***POLR3K***	***FARSB***	***FAM96B***	***BUB3***
***p*-value**	< 0.0001	< 0.0001	< 0.0001	< 0.0001	< 0.0001	< 0.0001	< 0.0001
Sig.	****	****	****	****	****	****	****
D	0.2188	0.2211	0.2267	0.2271	0.2315	0.2345	0.2357
Gene	***SPC24***	***DNAJC10***	***DSN1***	***MRPL27***	***ANAPC10***	***PPP1R3C***	***CIAPIN1***
***p*-value**	< 0.0001	< 0.0001	< 0.0001	< 0.0001	< 0.0001	< 0.0001	< 0.0001
Sig.	****	****	****	****	****	****	****
D	0.2406	0.2407	0.2409	0.2422	0.2427	0.2441	0.2522

Table S4-2 *Continued*. KS Tests Reveal Significant Changes in NA Following Silencing in hTERT

Gene[A]	***CHAF1A***	***RAD54L***	***NUF2***	***TAF9B***	***GCH1***	***STAG1***	***RAD50***
***p*-value**[B]	< 0.0001	< 0.0001	< 0.0001	< 0.0001	< 0.0001	< 0.0001	< 0.0001
Sig.[C]	****	****	****	****	****	****	****
D[D]	0.2537	0.2564	0.2623	0.2699	0.2711	0.2719	0.2720
Gene	***PWP1***	***SSU72***	***GARS***	***BUB1***	***RPL30***	***SUGT1***	***UGP2***
***p*-value**	< 0.0001	< 0.0001	< 0.0001	< 0.0001	< 0.0001	< 0.0001	< 0.0001
Sig.	****	****	****	****	****	****	****
D	0.2831	0.2837	0.2865	0.2930	0.2989	0.3001	0.3003
Gene	***RPRD18***	***PPP1R7***	***RAD18***	***EXOSC2***	***CHTF8***	***ACACB***	***UBE2A***
***p*-value**	< 0.0001	< 0.0001	< 0.0001	< 0.0001	< 0.0001	< 0.0001	< 0.0001
Sig.	****	****	****	****	****	****	****
D	0.3008	0.3091	0.31	0.3132	0.318	0.3183	0.3229
Gene	***QARS***	***IWS1***	***SRPR***	***DDX51***	***RFC4***	***PCNA***	***WDR43***
***p*-value**	< 0.0001	< 0.0001	< 0.0001	< 0.0001	< 0.0001	< 0.0001	< 0.0001
Sig.	****	****	****	****	****	****	****
D	0.3318	0.3367	0.3367	0.3398	0.3434	0.3458	0.3515
Gene	***SKP1***	***ATAD5***	***HIST2H4B***	***TAF7L***	***ABCE1***	***TRMT5***	***TUBGCP3***
***p*-value**	< 0.0001	< 0.0001	< 0.0001	< 0.0001	< 0.0001	< 0.0001	< 0.0001
Sig.	****	****	****	****	****	****	****
D	0.3533	0.3547	0.3556	0.3606	0.3611	0.3751	0.3763
Gene	***PSMD2***	***WOR33***	***ARL2***	***POLA1***	***RTN4***	***PPP2R1B***	***PRIM2***
***p*-value**	< 0.0001	< 0.0001	< 0.0001	< 0.0001	< 0.0001	< 0.0001	< 0.0001
Sig.	****	****	****	****	****	****	****
D	0.3844	0.3934	0.4032	0.4033	0.4095	0.4109	0.4110
Gene	***GART***	***CENPC1***	***PRIM1***	***CALM2***	***PYCRL***	***ASF1A***	***DNAJA3***
***p*-value**	< 0.0001	< 0.0001	< 0.0001	< 0.0001	< 0.0001	< 0.0001	< 0.0001
Sig.	****	****	****	****	****	****	****
D	0.4149	0.4150	0.4174	0.4226	0.4243	0.4316	0.4321
Gene	***SNRNP70***	***RPL7***	***UBR2***	***DSCC1***	***EPRS***	***PSMA7***	***HLTF***
***p*-value**	< 0.0001	< 0.0001	< 0.0001	< 0.0001	< 0.0001	< 0.0001	< 0.0001
Sig.	****	****	****	****	****	****	****
D	0.4394	0.4560	0.4580	0.4581	0.4592	0.4603	0.4801
Gene	***TIPIN***	***MECR***	***TRIM25***	***SHMT2***	***UBE2I***	***CSTF2***	***SF1***
***p*-value**	< 0.0001	< 0.0001	< 0.0001	< 0.0001	< 0.0001	< 0.0001	< 0.0001
Sig.	****	****	****	****	****	****	****
D	0.4816	0.4933	0.5046	0.5072	0.5189	0.5403	0.5635
Gene	***C20orf4***	***PSMD12***	***KIF11***	***GPN2***	***KDM6A***		
***p*-value**	< 0.0001	< 0.0001	< 0.0001	< 0.0001	< 0.0001		
Sig.	****	****	****	****	****		
D	0.5649	0.5709	0.6245	0.6356	0.6386		

[A]Genes in bold are putative CIN genes causing significant changes (*p*-value < 0.01) in cumulative NA frequency distributions relative to si*GAPDH*.

[B]*p*-values calculated from two-sample KS tests comparing listed gene to si*GAPDH*.

[C]Significance level where ns = not significant, ** = *p*-value < 0.01, *** = *p*-value < 0.001, **** = *p*-value < 0.0001.

[D]*D*; *D*-statistic (maximum deviation between the two distribution curves).

Table S4-3. MN Enumeration Identifies Putative CIN Genes in HT1080

Gene[A]	*GAPDH*	*KIFC1*	*ACACB*	*OSGEP*	*QARS*	*TRMT5*
MNi[B]	-	3	11	8	5	2
N	-	174	633	444	264	95
MNi/N[C]	0.0544	0.0172	0.0174	0.0180	0.0189	0.0211
FI[D]	1.00	0.32	0.32	0.33	0.35	0.39
Gene	*PSMD12*	*SMARCC2*	*GTF2H2*	*ACO2*	*STAG1*	*HLTF*
MNi	2	13	2	16	8	5
N	90	559	86	667	316	188
MNi/N	0.0222	0.0233	0.0233	0.0240	0.0253	0.0266
FI	0.41	0.43	0.43	0.44	0.47	0.49
Gene	*PGK1*	*CNOT8*	*PPP1R37*	*IPO5*	*RTN4*	*RAD54L*
MNi	13	11	21	13	4	23
N	480	401	747	453	138	763
MNi/N	0.0271	0.0274	0.0281	0.0287	0.0290	0.0301
FI	0.50	0.50	0.52	0.53	0.53	0.55
Gene	*DSCC1*	*TUBG2*	*DDX51*	*POLR3K*	*DLD*	*MRPL27*
MNi	28	18	9	22	4	32
N	924	591	291	687	122	928
MNi/N	0.0303	0.0305	0.0309	0.0320	0.0328	0.0345
FI	0.56	0.56	0.57	0.59	0.60	0.63
Gene	*DNAJC10*	*ASF1A*	*FAM96B*	*IWS1*	*WDHD1*	*PFDN2*
MNi	5	15	9	37	4	10
N	141	421	244	991	104	255
MNi/N	0.0355	0.0356	0.0369	0.0373	0.0385	0.0392
FI	0.65	0.65	0.68	0.69	0.71	0.72
Gene	*TRAPPC10*	*PPP1R3C*	*ANAPC10*	*RBBP4*	*TPI1*	*CHTF18*
MNi	21	16	33	15	12	11
N	519	388	777	351	273	242
MNi/N	0.0405	0.0412	0.0425	0.0427	0.0440	0.0454
FI	0.74	0.76	0.78	0.78	0.81	0.83
Gene	*CIAPIN1*	*C20orf4*	*ATAD5*	*UBR2*	*PRIM2*	*BUB1*
MNi	3	16	31	9	41	37
N	66	347	662	181	811	692
MNi/N	0.0455	0.0461	0.0468	0.0497	0.0506	0.0535
FI	0.84	0.85	0.86	0.91	0.93	0.98
Gene	*GINS3*	*EXOSC2*	*MAPRE1*	***CKS2***	***SSU72***	***GPN2***
MNi	20	25	14	29	16	22
N	358	420	235	467	254	343
MNi/N	0.0559	0.0595	0.0596	0.0621	0.0630	0.0641
FI	1.03	1.09	1.10	**1.14**	**1.16**	**1.18**
Gene	***GINS2***	***RAD1***	***MECR***	***ABCB7***	***PCID2***	***WOR33***
MNi	26	7	12	8	41	36
N	405	105	178	118	602	523
MNi/N	0.0642	0.0667	0.0674	0.0678	0.0681	0.0688
FI	**1.18**	**1.23**	**1.24**	**1.25**	**1.25**	**1.26**

Table S4-3 *Continued*. MN Enumeration Identifies Putative CIN Genes in HT1080

Gene[A]	***EIF2B3***	***PIF1***	***PFAS***	***UBE2A***	***CHTF8***	***NSFL1C***
MNi[B]	13	56	19	17	38	34
N	186	784	262	234	504	437
MNi/N[C]	0.0699	0.0714	0.0725	0.0726	0.0754	0.0778
FI[D]	**1.28**	**1.31**	**1.33**	**1.33**	**1.39**	**1.43**
Gene	***POLR3E***	***TAF7L***	***PDXK***	***UGP2***	***TOP3A***	***DDX39B***
MNi	16	23	45	61	57	21
N	201	279	544	736	683	247
MNi/N	0.0796	0.0824	0.0827	0.0829	0.0835	0.0850
FI	**1.46**	**1.51**	**1.52**	**1.52**	**1.53**	**1.56**
Gene	***SCFD1***	***DNAJC2***	***RPRD1B***	***HIST2H4B***	***PSMA6***	***GCH1***
MNi	22	59	13	65	5	15
N	248	659	141	691	52	156
MNi/N	0.0887	0.0895	0.0922	0.0941	0.0962	0.0962
FI	**1.63**	**1.65**	**1.69**	**1.73**	**1.77**	**1.77**
Gene	***ABCE1***	***PPP2R5C***	***FEN1***	***SKP1***	***CDK3***	***PSMA7***
MNi	10	59	37	9	31	14
N	102	598	372	89	303	134
MNi/N	0.0980	0.0987	0.0995	0.1010	0.1020	0.1040
FI	**1.80**	**1.81**	**1.83**	**1.86**	**1.88**	**1.91**
Gene	***YIPF5***	***CNOT6***	***KDM6A***	***SRF***	***EPRS***	***RAD51B***
MNi	36	23	58	39	10	40
N	337	210	524	342	88	349
MNi/N	0.1070	0.1100	0.1110	0.1140	0.1140	0.1150
FI	**1.97**	**2.02**	**2.04**	**2.10**	**2.10**	**2.11**
Gene	***SF1***	***PYCRL***	***POLD3***	***TRIM25***	***PSMD2***	***PRIM1***
MNi	41	10	15	7	19	25
N	354	86	126	59	156	207
MNi/N	0.1160	0.1160	0.1190	0.1190	0.1210	0.1210
FI	**2.13**	**2.13**	**2.19**	**2.19**	**2.22**	**2.22**
Gene	***WDR43***	***POLD1***	***PAICS***	***GARS***	***TIPIN***	***RAD51***
MNi	13	42	35	28	8	33
N	107	342	280	215	61	250
MNi/N	0.1210	0.1230	0.1250	0.1300	0.1310	0.1320
FI	**2.22**	**2.26**	**2.30**	**2.39**	**2.41**	**2.43**
Gene	***BTAF1***	***CDC7***	***GART***	***CSE1L***	***AURKC***	***OMA1***
MNi	37	16	17	10	17	23
N	280	120	128	72	122	166
MNi/N	0.1320	0.1330	0.1330	0.1390	0.1390	0.1390
FI	**2.43**	**2.44**	**2.44**	**2.56**	**2.56**	**2.56**
Gene	***RAD50***	***RAD52***	***RFC4***	***TAF9B***	***RAD18***	***ARL2***
MNi	30	22	10	15	13	44
N	214	151	68	102	85	281
MNi/N	0.1400	0.1460	0.1470	0.1470	0.1530	0.1570
FI	**2.57**	**2.68**	**2.70**	**2.70**	**2.81**	**2.89**

Table S4-3 *Continued*. MN Enumeration Identifies Putative CIN Genes in HT1080

Gene[A]	***PWP1***	***MAU2***	***CSTF2***	***CFDP1***	***MUC17***	***PSMA3***
MNi[B]	52	12	17	54	28	16
N	332	76	104	329	169	96
MNi/N[C]	0.1570	0.1580	0.1630	0.1640	0.1660	0.1670
FI[D]	**2.89**	**2.90**	**3.00**	**3.01**	**3.05**	**3.07**
Gene	***MCM10***	***RFC2***	***TUBA4A***	***FPGS***	***RPL7***	***MCM2***
MNi	16	16	19	22	10	65
N	90	87	102	118	53	343
MNi/N	0.1780	0.1840	0.1860	0.1860	0.1890	0.1900
FI	**3.27**	**3.38**	**3.42**	**3.42**	**3.47**	**3.49**
Gene	***PIGS***	***RNF10***	***FARSB***	***SHMT2***	***SNRNP70***	***RABGGTA***
MNi	40	31	13	47	28	12
N	208	161	66	239	140	58
MNi/N	0.1920	0.1930	0.1970	0.1970	0.2000	0.2070
FI	**3.53**	**3.55**	**3.62**	**3.62**	**3.68**	**3.81**
Gene	***NAT10***	***RUVBL2***	***TUBGCP3***	***MCM5***	***UBE2I***	***SPC25***
MNi	11	19	17	19	45	75
N	53	88	76	68	159	254
MNi/N	0.2080	0.2160	0.2240	0.2790	0.2830	0.2950
FI	**3.82**	**3.97**	**4.12**	**5.13**	**5.20**	**5.42**
Gene	***SLMAP***	***GINS4***	***CHAF1A***	***BUB3***	***DSN1***	***ATAD2B***
MNi	34	23	27	113	238	37
N	104	66	74	234	491	73
MNi/N	0.3270	0.3480	0.3650	0.4830	0.4850	0.5070
FI	**6.01**	**6.40**	**6.71**	**8.88**	**8.92**	**9.32**
Gene	***PCNA***	***SPC24***	***NUF2***			
MNi	97	76	122			
N	164	109	172			
MNi/N	0.5910	0.6970	0.7090			
FI	**10.86**	**12.81**	**13.03**			

[A]Putative CIN genes causing MN increases > 2× standard deviation above the si*GAPDH* mean are presented in bold.
[B]Number of MNi.
[C]Number of MNi normalized to number of nuclei (N).
[D]Fold increase in MN formation (vs. si*GAPDH*). Note: Conditions with n < 40 were excluded.

Table S4-4. MN Enumeration Identifies Putative CIN Genes in hTERT

Gene[A]	*GAPDH*	*PSMA5*	*PSMD12*	*RAD51*	*STAG1*	*ATAD5*	*RTN4*
MNi[B]	-	0	0	0	0	0	0
N	-	51	92	134	142	401	181
MNi/N[C]	0.0194	0	0	0	0	0	0
FI[D]	1.00	0.00	0.00	0.00	0.00	0.00	0.00
Gene	*AURKC*	*ANAPC10*	*CDK3*	*PPP1R37*	*PPP2R1B*	*KDM6A*	*EIF2B3*
MNi	0	0	0	0	0	0	0
N	132	273	264	168	137	115	171
MNi/N	0	0	0	0	0	0	0
FI	0.00	0.00	0.00	0.00	0.00	0.00	0.00
Gene	*ABCE1*	*RPL7*	*WDR43*	*NAT10*	*ABCB7*	*OMA1*	*TXNL4A*
MNi	0	0	0	0	0	0	0
N	50	97	77	114	133	175	107
MNi/N	0	0	0	0	0	0	0
FI	0.00	0.00	0.00	0.00	0.00	0.00	0.00
Gene	*EXOSC2*	*SF1*	*GART*	*PFAS*	*DNAJC10*	*CALM2*	*SCFD1*
MNi	0	0	0	0	0	0	0
N	263	410	136	256	149	59	168
MNi/N	0	0	0	0	0	0	0
FI	0.00	0.00	0.00	0.00	0.00	0.00	0.00
Gene	*RAD54L*	*GARS*	*FEN1*	*DLD*	*UBR2*	*C20orf4*	*PPP1R3C*
MNi	1	1	1	1	2	1	2
N	639	309	303	276	514	257	483
MNi/N	0.00156	0.00324	0.0033	0.00362	0.00389	0.00389	0.00414
FI	0.08	0.17	0.17	0.19	0.20	0.20	0.21
Gene	*TAF7L*	*PCID2*	*ACO2*	*RPRD1B*	*SMARCC2*	*TPI1*	*PWP1*
MNi	1	3	1	1	2	1	2
N	237	679	218	209	395	189	374
MNi/N	0.00422	0.00442	0.00459	0.00478	0.00506	0.00529	0.00535
FI	0.22	0.23	0.24	0.25	0.26	0.27	0.28
Gene	*TUBGCP3*	*POLR3K*	*WOR33*	*CHAF1A*	*QARS*	*UGP2*	*PCNA*
MNi	1	1	1	1	3	3	1
N	186	183	180	177	509	501	165
MNi/N	0.00538	0.00546	0.00556	0.00565	0.00589	0.00599	0.00606
FI	0.28	0.28	0.29	0.29	0.30	0.31	0.31
Gene	*TRAPPC10*	*PAICS*	*YIPF5*	*HLTF*	*OSGEP*	*TIPIN*	*FAM96B*
MNi	2	1	3	2	5	1	2
N	329	163	484	322	767	152	292
MNi/N	0.00608	0.00613	0.0062	0.00621	0.00652	0.00658	0.00685
FI	0.31	0.32	0.32	0.32	0.34	0.34	0.35
Gene	*POLR3E*	*CSE1L*	*GINS2*	*DDX51*	*PSMA7*	*ACACB*	*CFDP1*
MNi	2	1	1	2	1	5	2
N	291	143	141	262	126	621	243
MNi/N	0.00687	0.00699	0.00709	0.00763	0.00794	0.00805	0.00823
FI	0.35	0.36	0.37	0.39	0.41	0.41	0.42

Table S4-4 *Continued.* MN Enumeration Identifies Putative CIN Genes in hTERT

Gene[A]	*CKS2*	*DDX39B*	*MCM5*	*MAPRE1*	*PIGS*	*ASF1A*	*MUC17*
MNi[B]	4	3	1	4	2	3	2
N	482	355	118	472	218	322	211
MNi/N[C]	0.0083	0.00845	0.00847	0.00847	0.00917	0.00932	0.00948
FI[D]	0.43	0.44	0.44	0.44	0.47	0.48	0.49
Gene	*GPN2*	*SLMAP*	*SPC25*	*TUBG2*	*GCH1*	*MCM2*	*SNRNP70*
MNi	2	2	2	3	3	2	3
N	208	200	189	283	282	185	277
MNi/N	0.00962	0.01	0.0106	0.0106	0.0106	0.0108	0.0108
FI	0.50	0.52	0.55	0.55	0.55	0.56	0.56
Gene	*CDC7*	*BTAF1*	*HIST2H4B*	*PRIM2*	*DNAJA3*	*RAD18*	*RAD52*
MNi	3	2	5	3	1	4	1
N	274	182	452	268	88	344	86
MNi/N	0.0109	0.011	0.0111	0.0112	0.0114	0.0116	0.0116
FI	0.56	0.57	0.57	0.58	0.59	0.60	0.60
Gene	*CNOT8*	*PPP2R5C*	*UBE2I*	*TRIM25*	*TRMT5*	*PDXK*	*RAD50*
MNi	6	6	2	4	2	11	4
N	512	473	154	305	153	841	300
MNi/N	0.0117	0.0127	0.013	0.0131	0.0131	0.0131	0.0133
FI	0.60	0.65	0.67	0.68	0.68	0.68	0.69
Gene	*IPO5*	*GINS4*	*TUBA4A*	*PYCRL*	*SSU72*	*CIAPIN1*	*NSFL1C*
MNi	8	3	1	3	3	2	3
N	594	221	73	215	204	133	199
MNi/N	0.0135	0.0136	0.0137	0.014	0.0147	0.015	0.0151
FI	0.70	0.70	0.71	0.72	0.76	0.77	0.78
Gene	*SUGT1*	*PRIM1*	*PGK1*	*ATAD2B*	*MECR*	*PSMA3*	*ACTB*
MNi	2	3	8	5	2	1	3
N	126	188	490	302	119	59	172
MNi/N	0.0159	0.016	0.0163	0.0166	0.0168	0.0169	0.0174
FI	0.82	0.82	0.84	0.86	0.87	0.87	0.90
Gene	*PSMD2*	*SKP1*	*IWS1*	*DNAJC2*	*RFC4*	*GTF2H2*	*BUB3*
MNi	1	4	5	6	2	5	4
N	56	222	260	304	100	247	195
MNi/N	0.0179	0.018	0.0192	0.0197	0.02	0.0202	0.0205
FI	0.92	0.93	0.99	1.02	1.03	1.04	1.06
Gene	*CHTF18*	*MRPL27*	*RPL8*	*DSCC1*	*CENPC1*	*TOP3A*	*CHTF8*
MNi	5	8	2	12	5	7	12
N	230	366	84	496	203	283	479
MNi/N	0.0217	0.0219	0.0238	0.0242	0.0246	0.0247	0.0251
FI	1.12	1.13	1.23	1.25	1.27	1.27	1.29
Gene	*GINS3*	*RUVBL2*	*UBE2A*	*SRF*	*POLD1*	*EPRS*	*CSTF2*
MNi	10	4	6	7	9	4	9
N	390	153	225	245	312	138	298
MNi/N	0.0256	0.0261	0.0267	0.0286	0.0288	0.029	0.0302
FI	1.32	1.35	1.38	1.47	1.48	1.49	1.56

Table S4-4 *Continued.* MN Enumeration Identifies Putative CIN Genes in hTERT

Gene[A]	***TAF9B***	***RAD51B***	***ARL2***	***RFC2***	***POLA1***	***SRPR***	***FARSB***
MNi[B]	10	8	6	5	6	5	12
N	295	227	150	113	118	82	191
MNi/N[C]	0.0339	0.0352	0.04	0.0442	0.0508	0.061	0.0628
FI[D]	**1.75**	**1.81**	**2.06**	**2.28**	**2.62**	**3.14**	**3.24**
Gene	***POLD3***	***PSMA6***	***SHMT2***	***RBBP4***	***NUF2***	***KIF11***	***SPC24***
MNi	5	7	9	18	21	9	32
N	76	100	121	179	203	87	290
MNi/N	0.0658	0.07	0.0744	0.101	0.103	0.103	0.11
FI	**3.39**	**3.61**	**3.84**	**5.21**	**5.31**	**5.31**	**5.67**
Gene	***KIFC1***	***SART1***	***DSN1***	***BUB1***	***RPL30***		
MNi	22	21	46	59	20		
N	186	175	307	327	90		
MNi/N	0.118	0.12	0.15	0.18	0.222		
FI	**6.08**	**6.19**	**7.73**	**9.28**	**11.44**		

[A]Putative CIN genes causing MN increases > 2× standard deviation above the si*GAPDH* mean are presented in bold.
[B]Number of MNi.
[C]Number of MNi normalized to number of nuclei (N).
[D]Fold increase in MN formation (vs. si*GAPDH*). Note: Conditions with n < 40 were excluded.

Table S4-5. Estimated Prevalence of Multinucleated Cells in *NUF2* and *SPC24* Silenced Cells

Cell Line	Condition	Mult N[A]	N[B]	Total Cells[C]	Multi N Cells (%)[D]
HT1080	si*GAPDH*	0	155	155	0.0
	si*NUF2*	63	63	126	50.0
	si*SPC24*	38	98	136	27.9
hTERT	si*GAPDH*	1	245	246	0.4
	si*NUF2*	21	92	113	18.6
	si*SPC24*	74	180	254	29.1
HCT116	si*GAPDH*	0	300	300	0.0
	si*NUF2*	75	74	149	50.3
	si*SPC24*	62	171	233	36.3

[A]Estimated number of cells with multiple nuclei.
[B]Number of cells with a single nucleus.
[C]Total number of cells.
[D]Percentage of multinucleated cells.

Table S4-6. Prioritization of 8 Putative CIN Genes Identified by all Assays based on Rank

		NA				MN			
	Gene[A]	HT1080 FC[B]	Rank	hTERT FC	Rank	HT1080 FI[C]	Rank	hTERT FI	Rank
1	***SHMT2***	1.24	1	1.40	1	3.62	4	3.84	4
2	***NUF2***	1.15	5	1.20	3	13.03	1	5.31	3
3	***SPC24***	1.13	6	1.16	5	12.81	2	5.67	2
4	***DSN1***	1.08	8	1.08	8	8.92	3	7.73	1
5	***ARL2***	1.10	7	1.21	2	2.89	5	2.06	6
6	*PSMA6*	1.16	3	1.18	4	1.77	8	3.61	5
7	*RAD51B*	1.22	2	1.09	7	2.11	7	1.81	7
8	*TAF9B*	1.16	4	1.12	6	2.70	6	1.75	8

[A]8 genes identified in 4/4 assays were prioritized on the strength of the CIN phenotype and the corresponding rankings in each assay, with the top 5 highest ranked (bold) selected for validation. *ARL2*, *DSN1*, and *PSMA6* tied for overall rank however visual assessment revealed greater cell viability in *ARL2* and *DSN1* silenced cells, which were selected.
[B]FC = Fold change in median NA (vs. si*GAPDH*).
[C]FI = Fold increase in MN formation (vs. si*GAPDH*).

Table S4-7. KS Tests Identify Significant Changes in Chromosome Number Distributions Following Silencing in hTERT and HCT116 Cells

Cell Line	Condition[A]	*p*-value[B]	Significance[C]	*D*[D]
hTERT	Untreated	> 0.9999	ns	0.0261
	si*ARL2*	0.0617	ns	0.1739
	si*BUB3*	0.0617	ns	0.1739
	si*DSN1*	0.0134	*	0.2087
	si*GARS*	0.0866	ns	0.1652
	si*GART*	0.0056	**	0.2261
	si*NUF2*	< 0.0001	****	0.3043
	si*PIGS*	0.0013	**	0.2522
	si*SHMT2*	0.0002	***	0.2870
	si*SKP1*-1	0.0013	**	0.2522
	si*SKP1*-2	0.0008	***	0.2609
	si*SKP1*-P	0.0087	**	0.2174
	si*SPC24*	< 0.0001	****	0.2957
HCT116	Untreated	> 0.9999	ns	0.0175
	si*ARL2*	< 0.0001	****	0.3246
	si*BUB3*	< 0.0001	****	0.4035
	si*DSN1*	< 0.0001	****	0.3246
	si*GARS*	0.0001	***	0.2895
	si*GART*	0.0287	*	0.1930
	si*NUF2*	< 0.0001	****	0.4123
	si*PIGS*	< 0.0001	****	0.3333
	si*SHMT2*	0.0013	**	0.2544
	si*SKP1*-1	0.0004	***	0.2719
	si*SKP1*-2	< 0.0001	****	0.3070
	si*SKP1*-P	0.0003	***	0.2807
	si*SPC24*	< 0.0001	****	0.4912

[A]Conditions in bold induce significant cumulative chromosome number frequency distribution changes (vs. si*GAPDH*) as determined by KS tests.
[B]*p*-values calculated from two-sample KS tests for the listed condition vs. si*GAPDH*.
[C]Significance level (ns = not significant, * = *p*-value < 0.05, ** = *p*-value < 0.01, *** = *p*-value < 0.001, **** = *p*-value < 0.0001).
[D]*D*; *D*-statistic (maximum deviation between the two distribution curves).

Table S4-8. KS Tests Identify Significant Changes in NA Following Silencing in HCT116

Condition[A]	*p*-value[B]	Significance[C]	*D*[D]
Untreated	0.4623	ns	0.1037
si*ARL2*	< 0.0001	****	0.2889
si*BUB3*	0.0397	*	0.1704
si*DSN1*	< 0.0001	****	0.4159
si*GARS*	0.0010	**	0.2370
si*GART*	< 0.0001	****	0.5185
si*NUF2*	< 0.0001	****	0.3556
si*PIGS*	0.0281	*	0.1778
si*SHMT2*	0.0195	*	0.1852
si*SPC24*	0.0006	***	0.2444

[A]Conditions in bold induce significant (*p*-value < 0.05) cumulative NA frequency distribution changes (vs. si*GAPDH*) as determined by KS tests.
[B]*p*-values calculated from two-sample KS tests for the listed condition vs. si*GAPDH*.
[C]Significance level (ns = not significant, * = *p*-value < 0.05, ** = *p*-value < 0.01, *** = *p*-value < 0.001, **** = *p*-value < 0.0001).
[D]*D*; *D*-statistic (maximum deviation between the two distribution curves).

Table S4-9. Putative CIN Gene Silencing Induces Increases in MN Formation in HCT116

Condition[A]	No. MNi[B]	No. Nuclei	MNi/Nucleus[C]	FI[D]
si*GAPDH*	8	1928	0.0041	1.0
si*ARL2*	4	402	0.0100	2.4
si*BUB3*	47	1754	0.0268	6.5
si*DSN1*	26	960	0.0271	6.5
si*GARS*	0	532	0.0000	0.0
si*GART*	1	808	0.0012	0.3
si*NUF2*	10	244	0.0410	9.9
si*PIGS*	9	731	0.0123	3.0
si*SHMT2*	9	1340	0.0067	1.6
si*SPC24*	13	307	0.0423	10.2

[A]Genes in bold induce MN increases > 2×standard deviation above si*GAPDH* mean.
[B]Number of MNi.
[C]Number of MNi normalized to number of nuclei.
[D]Fold increase in MN formation (vs. si*GAPDH*).

CHAPTER 5

CHARACTERIZING THE ABBERANT CELLULAR MECHANISMS THAT DRIVE CHROMOSOME INSTABILITY IN *SKP1*-SILENCED HCT116 CELLS

5.1.0. Abstract

The SCF complex adaptor protein, SKP1, binds upwards of 68 different substrate specific F-box proteins, which target a multitude of downstream substrates for polyubiquitination and proteasomal degradation. As many SCF substrates function in CIN and cancer-associated pathways, misexpression of SKP1 can potentially impact numerous pathways with implications for CIN and oncogenesis. In fact, *SKP1* silencing was shown to induce NA and MN increases, chromosome defects, and was validated as a human CIN gene in the preceding chapter. As *SKP1* is altered or misexpressed in a myriad of cancer types including CRC, a greater understanding of the mechanisms driving CIN in *SKP1* silenced cells is required. In this chapter, I outline how comprehensive NA and MN enumeration screening of all 68 F-box proteins was performed, identifying 53 genes including *EMI1 (FBXO5)*, *FBXL7*, and *SKP2 (FBXL1)* that induced CIN phenotypes following silencing. As F-box proteins function in a complex with SKP1, the screen revealed a subset of F-box proteins and SCF complexes (*e.g.* SCF^{EMI1}) that may contribute to CIN in *SKP1* silenced cells. Biochemical, immunofluorescence, and microscopy-based techniques were employed to further characterize the aberrations associated with *SKP1* silencing. *SKP1* and *EMI1* silencing induced replication stress, DNA damage, and CENPA mislocalization, suggesting that SCF^{EMI1} is critical for mediating these processes. Increases in the SCF^{FBXL7} and SCF^{SKP2} substrates, Survivin and CCNE1, were detected along with centrosomal aberrations, which are common in CCNE1 overexpressing cells. *SKP1* and *CCNE1* dual silencing confirmed that increased CCNE1 levels contribute in part, to si*SKP1*-associated CIN phenotypes. Overall these findings provide critical insights into the aberrant mechanisms contributing to CIN in *SKP1* silenced cells, and reveal potential cancer biomarkers and novel therapeutic targets to be explored in future studies.

5.2.0. Introduction

As detailed in the preceding chapters, CIN can arise from alterations in a number of biological pathways including DNA replication, mitotic spindle assembly, kinetochore-microtubule attachment, and centrosome regulation[67,68]. However, genes and pathways with less intuitive links to CIN, such as *SKP1* and ubiquitin-mediated proteasomal degradation, may also drive CIN and oncogenesis when misregulated (*see Chapter 4*)[65]. In fact, *SKP1* is somatically altered and/or misexpressed in a myriad of cancer types including both solid (colorectal[209], prostate[157], and ovarian[158]) and hematologic cancers (acute myelogenous leukemia[225]). In order to identify new therapeutic targets and reveal novel vulnerabilities to exploit for cancer treatment, a greater understanding of the aberrant biological mechanisms that contribute to CIN and oncogenesis in human cells is critical. In this chapter, the altered downstream substrates and biological pathways that underlie CIN in *SKP1* silenced CRC-derived HCT116 cells were investigated to gain insight into whether *SKP1* or the altered biology induced by altered *SKP1*, represent potential future therapeutic targets for improved treatment of aggressive, chromosomally unstable cancers.

SKP1 encodes the adaptor protein of the SCF E3 ubiquitin ligase complex, which consists of three core components including SKP1, RBX1, and CUL1[140]. Substrate specificity and targeting of the SCF complex is dictated by the variable substrate-recognition F-box protein subunit that binds SKP1[137]. F-box proteins recruit substrates to the core SCF complex for polyubiquitination and subsequent degradation by the 26S proteasome, thereby tightly regulating cellular substrate levels[141] (*see Section 1.5.0*). As there are 68 different F-box proteins encoded in the human genome, there are 68 predicted SCF complexes, each responsible for regulating a unique subset of target proteins[137]. Unfortunately, the substrates and functions for the majority of

human F-box-proteins, and thus SCF complexes, have yet to be elucidated. Of the F-box proteins characterized to date (*e.g.* SKP2 [FBXL1]), many regulate substrates involved in key CIN-associated processes such as cell cycle control[226], DNA replication[227], DNA damage repair[228,229], and centrosome biology[139,143,230,231]. Accordingly, aberrant expression and/or function of SCF complexes can indirectly induce CIN by misregulating downstream CIN-associated protein levels. For example, SCF^{SKP2} misregulation causes aberrant increases in cellular levels of substrate CCNE1[143]. *CCNE1* is an established onco- and CIN gene that is frequently amplified at the level of the genome and overexpressed in cancer. *In silico* queries of the cBioPortal database[155] reveal that *CCNE1* is amplified and/or overexpressed in ~5% of CRCs[209] and ~20% of ovarian serous cystadenocarcinomas[158], esophagus-stomach[232], neuroendocrine prostate[233], and bladder urothelial carcinomas[159]. Thus, proper regulation and turnover of SCF substrates including CCNE1 is critical to maintain chromosome stability and prevent oncogenesis. However, information regarding increases in CCNE1 or other downstream substrates resulting from aberrant SKP1 or SCF expression or function and proteasomal degradation is lacking. Accordingly, functional characterization of the remaining F-box proteins, SCF complexes, and downstream substrates to decipher their role in CIN and oncogenesis is warranted.

Although the functions and oncogenic potential of many SCF complexes remain unknown, alterations involving SCF subunits have been implicated in CIN and cancer. The F-box protein EMI1 (FBXO5), of SCF^{EMI1} was originally identified as an oncogene, as it is overexpressed in various cancers including lymphoma, ovarian, and hepatocellular carcinoma[234]. Overexpression of *EMI1* drives cellular proliferation[234-236], tetraploidization, CIN, and is predictive of advanced tumor grade and poor prognosis[234]. However, *EMI1* also exhibits tumor suppressive roles and is deleted in cancers including leukemia, head and neck, and pancreatic[155,237]. Diminished *EMI1*

expression in human cell lines including HCT116 and hTERT-RPE1 induces RPA foci[238] (an indicator of ssDNA intermediates that arise due to replication stress[239]), catenated DNA, γH2AX foci (a surrogate marker for DNA DSBs[128]), endoreduplication, and polyploidy[237,240]. The well-characterized F-box protein SKP2 that drives entry into S-phase, is also overexpressed in various cancer types including breast[241], Kaposi's sarcoma[242], T-cell lymphoma[243], and melanoma[244]. Increasing *SKP2* expression correlates with diminished levels of the cyclin-dependant kinase inhibitor P27 substrate, advanced cancer progression, and poor prognosis[245,246]. Conversely, *SKP2* KO mice exhibit CCNE1 and P27 overexpression, increases in nuclear size, polyploidy and centrosome defects[143]. These data suggest that the levels and activity of SCF components including EMI1 and SKP2 must be precisely regulated in a spatial and temporal manner to prevent CIN, cellular transformation, and cancer development. As alterations in individual F-box proteins are associated with CIN, cancer development and progression, alterations of the invariable SCF core component SKP1, may also be detrimental. Conceptually, diminished SKP1 expression or function could hinder SCF complex formation, F-box protein recruitment, polyubiquitination and substrate degradation, thereby impacting a number of key biological pathways like DNA replication and repair, or centromere and centrosome regulation (*see Section 1.4.0*) that underlie CIN and oncogenesis.

In this chapter, I describe how high-content NA and MN enumeration assays were employed to rapidly screen all 68 F-box protein-encoding genes. A total of 53 putative human CIN genes were identified, revealing a subset of F-box proteins including EMI1, FBXL7, and SKP2, that may induce CIN following diminished expression. As these F-box proteins function in a complex with SKP1, it is plausible that silencing the F-box proteins may phenocopy the defects observed following *SKP1* silencing (*see Chapter 4*) and reveal insights into the altered

SCF complexes and biological mechanisms driving CIN in *SKP1* silenced cells. *SKP1* and *EMI1* silencing were both associated with replication stress (RPA foci), DNA damage (γH2AX foci) and centromeric protein CENPA mislocalization, suggesting that SCF^{EMI1} is not only required for proper DNA replication, but is also critical for centromere maintenance. Increases in established downstream SCF substrates Survivin and CCNE1 levels and centrosomal aberrations were also observed in *SKP1* silenced cells. Dual *SKP1* and *CCNE1* silencing experiments revealed that increased CCNE1 levels contribute, in part to si*SKP1*-associated CIN phenotypes including NA increases, MN formation, and chromosomal aberrations. Overall these findings provide critical insights into the altered biology underlying the CIN phenotypes that result from diminished *SKP1* expression and offer important considerations for the development of novel treatment strategies in the future.

5.3.0. Results

5.3.1. Diminished Expression of F-box Proteins Induces CIN Phenotypes

To identify novel CIN genes and SCF complexes that may contribute to CIN, all 68 F-box protein encoding genes (Table 5-1) were screened for NA changes and MN formation following silencing in HCT116 in duplicate experiments[137]. Cells were seeded into a 96-well plate containing siGENOME siRNA duplexes (Dharmacon) targeting F-box genes or negative (si*GAPDH*, siNon-Targeting) and positive (si*SKP1*) controls. Cells were fixed, counter-stained (Hoechst) and subjected to high-content imaging and analysis as performed above (*see Sections 2.3.2, 2.5.2, 2.5.3 and 2.5.5*). The NA assay identified 49 and 58 putative CIN genes in the first and second screens respectively, with 44 (64.7% of candidates screened) identified in both experimental replicates (KS tests, p-value < 0.01) (Figure 5-1, SI Tables S5-1 and S5-2). NA

changes were consistent between replicates with an overall correlation coefficient of 0.87 (SI Figure S5-1). *SKP2* and *EMI1* silencing induced the largest median NA increases, ~1.3 and 2.4-fold, respectively (Figure 5-1, Table 5-2), with *EMI1* silenced cells (si*EMI1*) inducing NA increases most similar to those of si*SKP1* (Table 5-2). In fact, Student's *t*-tests (p-value < 0.05) revealed that si*SKP1* and si*EMI1* mean NAs are not statistically distinct in either screen (SI Table S5-3). These findings suggest that at least 44 different SCF complexes including SCF^{EM1} and SCF^{SKP2} could be impacted by *SKP1* silencing and contribute to the NA changes observed in *SKP1* silenced cells. It is possible that alterations involving SCF^{EM1} contribute to si*SKP1* CIN-associated NA changes to the greatest extent.

Table 5-1. F-box Candidate CIN Genes Subjected to NA and MN Enumeration Assays

No.	Gene Name[A]	No.	Gene Name	No.	Gene Name
1	*FBXW1 (BTRC)*	24	*FBXL15*	47	*FBXO20 (LMO7)*
2	*FBXW2*	25	*FBXL16*	48	*FBXO21*
3	*FBXW4 (SHFM3)*	26	*FBXL17*	49	*FBXO22*
4	*FBXW5*	27	*FBXL18*	50	*FBXO24*
5	*FBXW7*	28	*FBXL19*	51	*FBXO25*
6	*FBXW8*	29	*FBXL20*	52	*FBXO27*
7	*FBXW9*	30	*FBXL21*	53	*FBXO28*
8	*FBXW10*	31	*FBXL22*	54	*FBXO30*
9	*FBXW11 (β-TRCP2)*	32	*FBXO1 (CCNF)*	55	*FBXO31*
10	*FBXW12*	33	*FBXO2*	56	*FBXO32*
11	*FBXL1 (SKP2)*	34	*FBXO3*	57	*FBXO33*
12	*FBXL2*	35	*FBXO4*	58	*FBXO34*
13	*FBXL3*	36	*FBXO5 (EMI1)*	59	*FBXO36*
14	*FBXL4*	37	*FBXO6*	60	*FBXO38*
15	*FBXL5*	38	*FBXO7*	61	*FBXO39*
16	*FBXL6*	39	*FBXO8*	62	*FBXO40*
17	*FBXL7*	40	*FBXO9*	63	*FBXO41*
18	*FBXL8*	41	*FBXO10*	64	*FBXO42*
19	*FBXL10*	42	*FBXO11*	65	*FBXO43*
20	*FBXL11 (KDM2A)*	43	*FBXO15*	66	*FBXO44*
21	*FBXL12*	44	*FBXO16*	67	*FBXO45*
22	*FBXL13*	45	*FBXO17*	68	*FBXO46*
23	*FBXL14*	46	*FBXO18*		

[A]Gene names presented in brackets are commonly used aliases

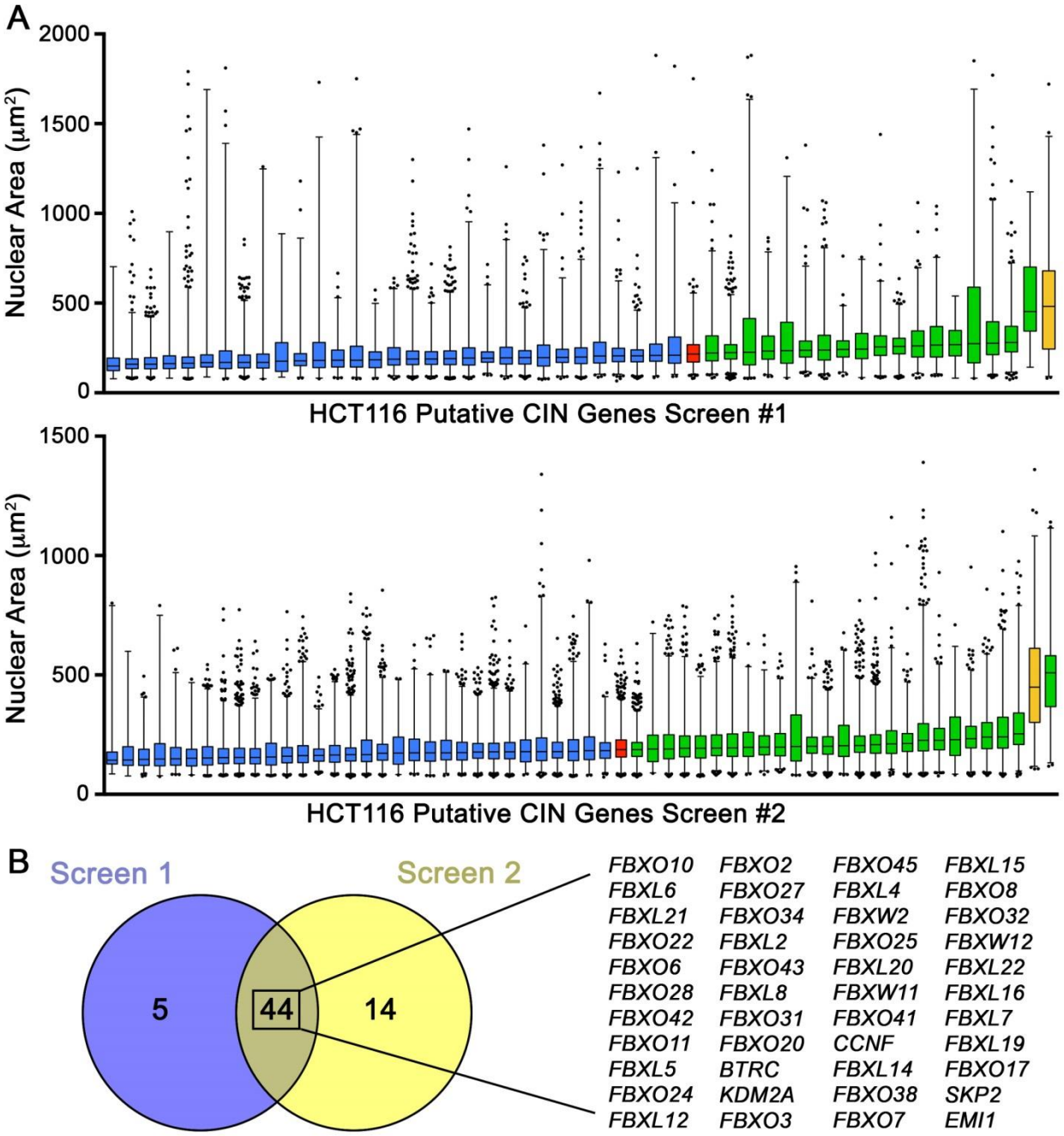

Figure 5-1. Silencing 44 F-box Genes Induces NA Changes that are Indicative of CIN
(A) Box-and-whisker graph displaying 1st – 99th percentiles (whiskers) and 25th, 50th, and 75th percentiles (box) of NA data for each putative CIN gene identified in HCT116 from the first (top) and second (bottom) screens. Genes causing median NA increases or decreases relative to si*GAPDH* (red) are coloured green and blue, respectively, with *SKP1* in yellow for comparison. ***(B)*** Venn diagram displaying the numbers of putative CIN genes identified by the NA assay, with the 44 genes identified in both replicates listed by ascending median NA (N = 2).

Table 5-2. Median NA Changes Following F-box Gene Silencing in HCT116

Gene[A]	*FBXO10*	*FBXL6*	*FBXL21*	*FBXO22*	*FBXO6*	*FBXO28*	*FBXO42*
Med 1[B]	150	160	159	163	170	178	170
Med 2[B]	144	154	155	151	149	146	155
Avg.[C]	147	157	157	157	159.5	162	162.5
FC[D]	1.37	1.28	1.28	1.28	1.26	1.24	1.24
Gene	*FBXO11*	*FBXL5*	*FBXO24*	*FBXL12*	*FBXO2*	*FBXO27*	*FBXO34*
Med 1	169	165	182	180.5	188	176	209
Med 2	156	166	152	162	160	173	143
Avg.	162.5	165.5	167	171.25	174	174.5	176
FC	1.24	1.22	1.21	1.18	1.16	1.15	1.14
Gene	*FBXL2*	*FBXO43*	*FBXL8*	*FBXO31*	*FBXO20*	*BTRC*	*KDM2A*
Med 1	182	193	184	187	195.5	188	196
Med 2	173.5	163	174	172	165	178	179
Avg.	177.75	178	179	179.5	180.25	183	187.5
FC	1.13	1.13	1.13	1.12	1.12	1.10	1.07
Gene	*FBXO3*	*FBXO45*	*FBXL4*	*FBXW2*	*FBXO25*	*FBXL20*	*FBXW11*
Med 1	196	206	205	210	206	222	233
Med 2	180	177	183	179	187	194	193
Avg.	188	191.5	194	194.5	196.5	208	213
FC	1.07	1.05	1.04	1.04	1.03	1.03	1.06
Gene	*FBXO41*	*CCNF*	*FBXL14*	*FBXO38*	*FBXO7*	*FBXL15*	*FBXO8*
Med 1	226.5	238	224	237	244	235.5	274.5
Med 2	200.5	190	205	198	193	204	166
Avg.	213.5	214	214.5	217.5	218.5	219.75	220.25
FC	1.06	1.06	1.06	1.08	1.08	1.09	1.09
Gene	*FBXO32*	*FBXW12*	*FBXL22*	*FBXL16*	*FBXL7*	*FBXL19*	*FBXO17*
Med 1	241.5	259	256.5	268	276	262	266
Med 2	213	208	233	226	226	240	240
Avg.	227.25	233.5	244.75	247	251	251	253
FC	1.13	1.16	1.21	1.23	1.25	1.25	1.26
Gene	*SKP2*	*EMI1*	-	***SKP1***			
Med 1	281	453	-	482			
Med 2	253	509	-	449			
Avg.	267	481	-	465.5			
FC	1.33	2.39	-	2.32			

[A]List of 44 F-box putative CIN genes identified by NA assays in HCT116 high-content screens 1 and 2, arranged by ascending median NA. *SKP1* (bold) listed for comparison.
[B]Median NA for each gene in Screens 1 and 2.
[C]Average median NA from Screens 1 and 2.
[D]Fold increase or decrease in median NA (vs. si*GAPDH* – Median NA: 201.5μm^2).

Following gene silencing, the MN enumeration assay performed in duplicate identified 32 and 44 genes causing increases in MN formation greater than 2-times the standard deviation above the si*GAPDH* mean (SI Table S5-4 and S5-5), for a total of 25 putative CIN genes identified in both replicates (36.8% of candidates) (Figure 5-2). Diminished expression of these 25 genes induced mean fold increases in MN formation from 2.0- (*FBXL17*) to 9.5-fold (*FBXO10*) compared to si*GAPDH*. Interestingly, the top 5 genes, *FBXO7* (5.8), *FBXL18* (6.0), *FBXO8* (6.0), *FBXL8* (7.6), *FBXO10* (9.5), induced MN increases that exceeded the increase observed following *SKP1* (5.7) silencing (Figure 5-2). *EMI1* silencing, which caused the largest NA increases, was not identified by the MN enumeration assay, forming the fewest MNi overall (0.2-fold change relative to controls) (SI Tables S5-4 and S5-5). These data indicate that the misregulation of at least 25 different SCF complexes (*e.g.* SCF^{FBXO10} and SCF^{FBXL8}) and their downstream substrates, may contribute to the increases in MN formation observed following *SKP1* silencing.

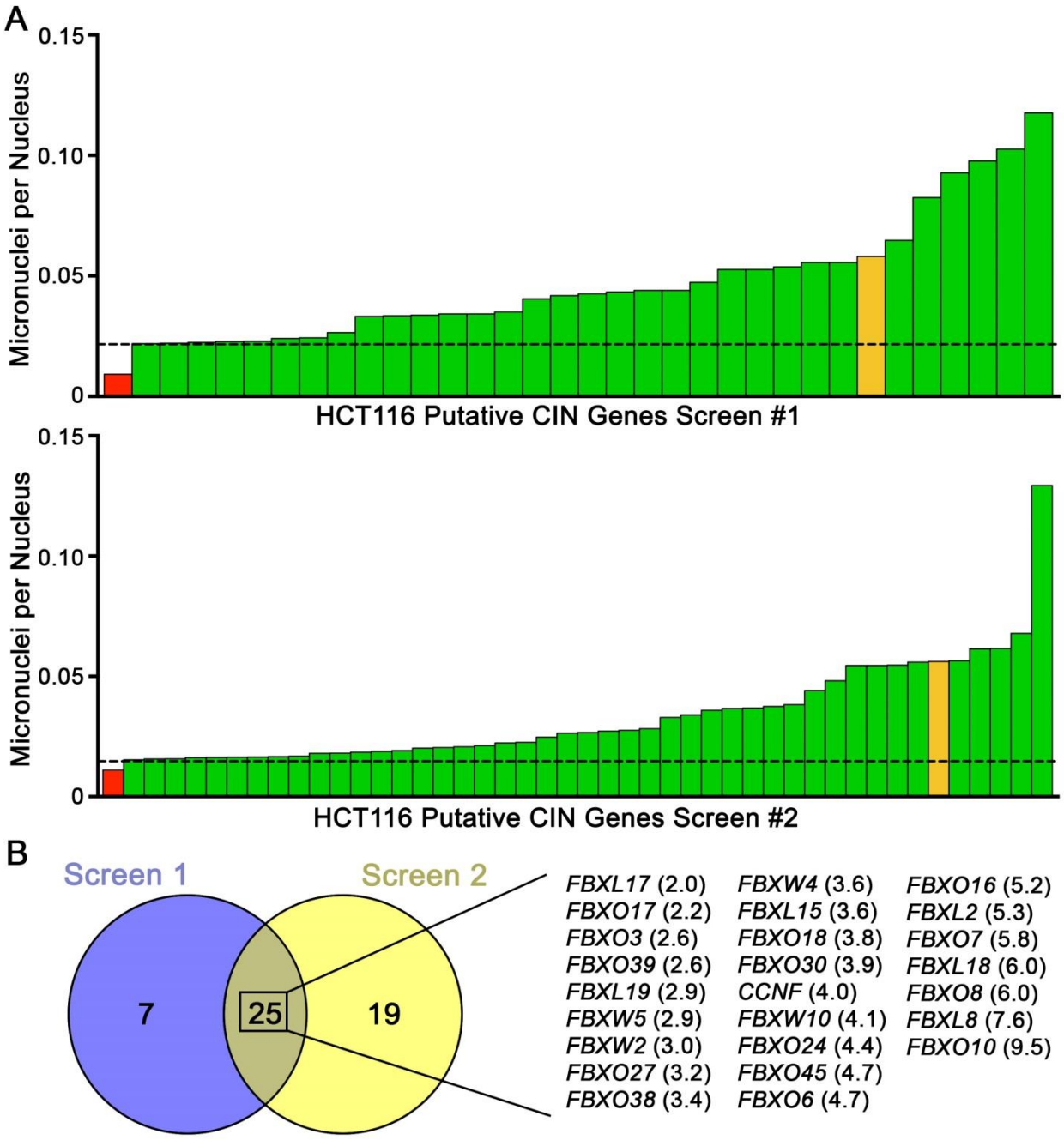

Figure 5-2. Silencing 25 F-box Genes Induces MN Increases that are Indicative of CIN
(A) Bar graph displaying normalized number of MNi per nucleus following silencing of putative CIN genes (green) identified in HCT116 in the first (top) and second (bottom) screens. Dotted line represents 2-times the standard deviation above the si*GAPDH* (red) mean. *SKP1* is shown in yellow for comparison purposes. ***(B)*** Venn diagram displaying the number of genes identified by the MN enumeration assay. The 25 genes presented (right hand side) are those identified in both experimental replicates with the corresponding mean MN fold increases in brackets relative to si*GAPDH* (N = 2).

Collectively, the NA and MN enumeration assays identified 53 putative CIN genes of the 68 F-box genes screened (77.9%) (Figure 5-3). Thus, these 53 F-box proteins, their corresponding SCF complexes, and downstream substrates, are implicated in chromosome stability in human cells. Accordingly, misregulation of these SCF complexes may contribute to the CIN phenotypes observed following *SKP1* silencing in HCT116 cells (*see Chapter 4*). Furthermore, a total of 16 genes were identified by both NA and MN assays and are promising putative CIN genes (Figure 5-3 and SI Table S5-6) to pursue further in future studies.

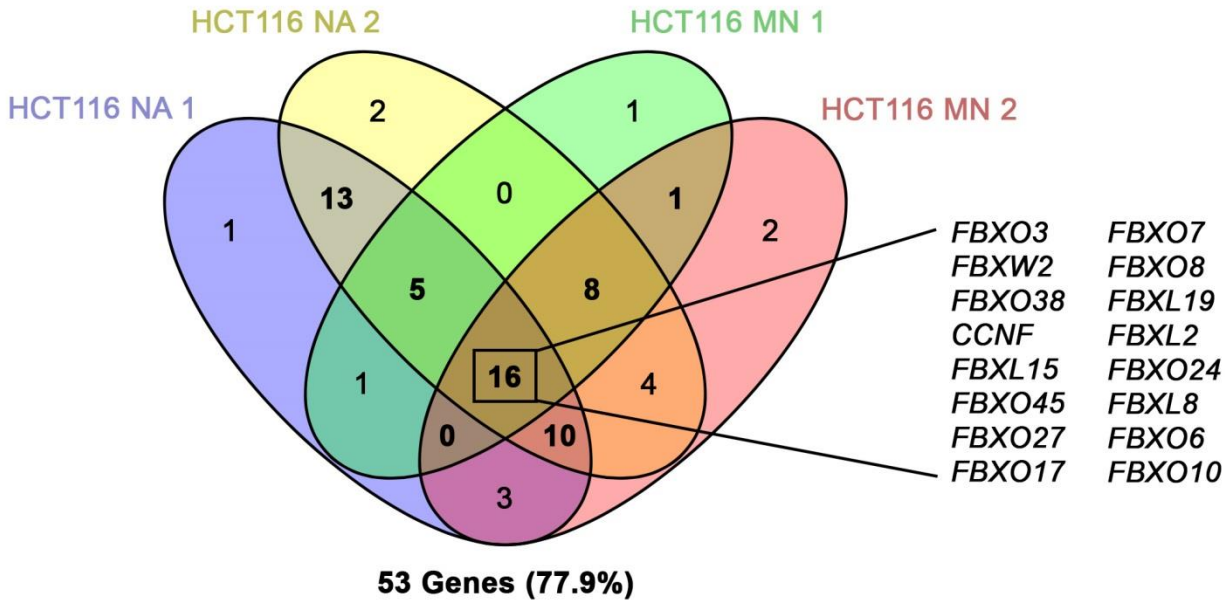

Figure 5-3. NA and MN Assays Reveal Putative F-box CIN Genes
Venn diagram displaying 53 genes (bold) identified by either assay in both experimental replicates. The 16 genes presented (right hand side) are those identified by both NA and MN assays in both replicates.

5.3.2. *SKP1* Silencing Induces Increases in RPA Foci Indicative of DNA Replication Stress

As *EMI1* silencing induces large increases in NAs, which is the predominant CIN phenotype observed following *SKP1* silencing, misregulation of the SCF^{EMI1} complex may contribute to CIN in *SKP1* silenced cells. High-content screening results were validated by direct silencing tests (ON-TARGETplus siRNA-pool) and CIN assays, which confirmed that *EMI1* silencing (Figure 5-4A) induced significant increases in mean NA (Figure 5-4B and C) and NA frequency distributions (Figure 5-4D), with no evidence for corresponding increases in MN formation (Figure 5-4E). As detailed in Chapter 4, *SKP1* silencing induces chromosomal aberrations that are characteristic of replication defects including endoreduplication and chromosome breakages. Diminished *EMI1* expression is known to induce endoreduplication and replication stress[237,238,240] as indicated by increases in RPA foci[247]. To assess whether *SKP1* silencing induces similar replication stress, *SKP1* and *EMI1* were silenced in HCT116 cells, immunofluorescently labeled for RPA, and imaging microscopy was employed to quantitatively assess changes in RPA foci (*see Sections 2.2.2, 2.3.1, 2.4.2*), with HU (10mM) used as a positive control (*see Section 2.10.1*). Statistically significant increases (Student's *t*-test, *p*-value < 0.0001) in mean RPA signal intensity were detected in si*SKP1* cells, similar to the positive control (Figure 5-5). In agreement with Machida *et al*[240], *EMI1* silencing induced extensive, statistically significant (Student's *t*-test, *p*-value < 0.0001) RPA signal increases (Figure 5-5)[247]. These results show that *SKP1* silencing induces RPA foci indicative of replication stress, which may contribute to CIN through diminished function of the SCF^{EMI1} complex.

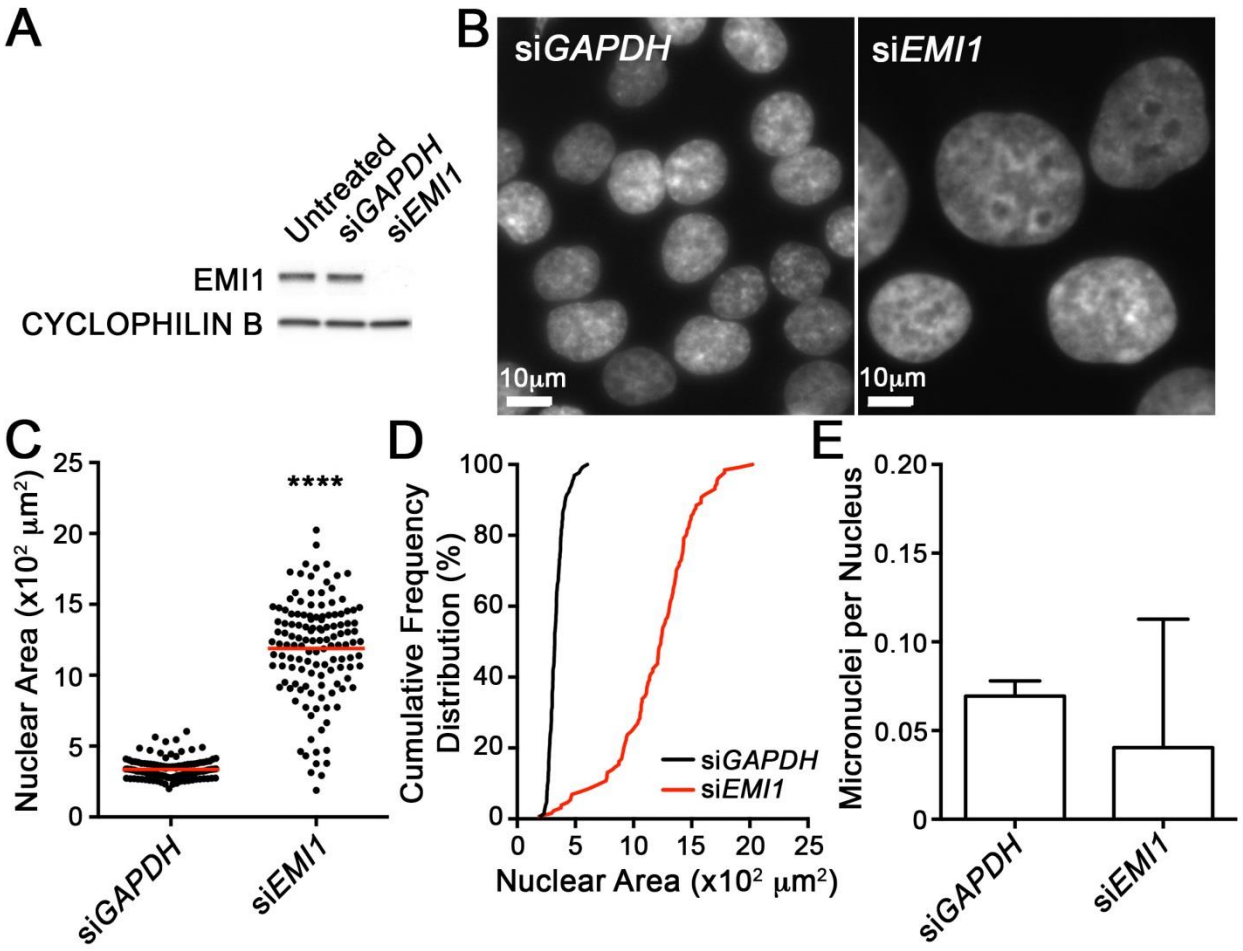

Figure 5-4. *EMI1* Silencing Induces Large NA Increases in HCT116
(A) Western blot displaying *EMI1* silencing in HCT116 with Cyclophilin B employed as the loading control. ***(B)*** Representative 2D fluorescence microscopy images at equivalent magnification showing large NA increases in si*EMI1* cells. ***(C)*** Dot plot presenting NA data and the statistically significant increase in mean NA (red line) following *EMI1* silencing (Student's *t*-test, **** = *p*-value < 0.0001). ***(D)*** Cumulative NA frequency distributions presenting the statistically significant, rightward shift towards larger NAs in si*EMI1* (KS tests, *p*-value < 0.0001) relative to controls. ***(E)*** Bar graph presenting the number of micronuclei per nucleus analyzed in each condition. Note: *EMI1* silencing does not induce statistically significant changes in MN formation relative to si*GAPDH*. (n > 100, N = 3).

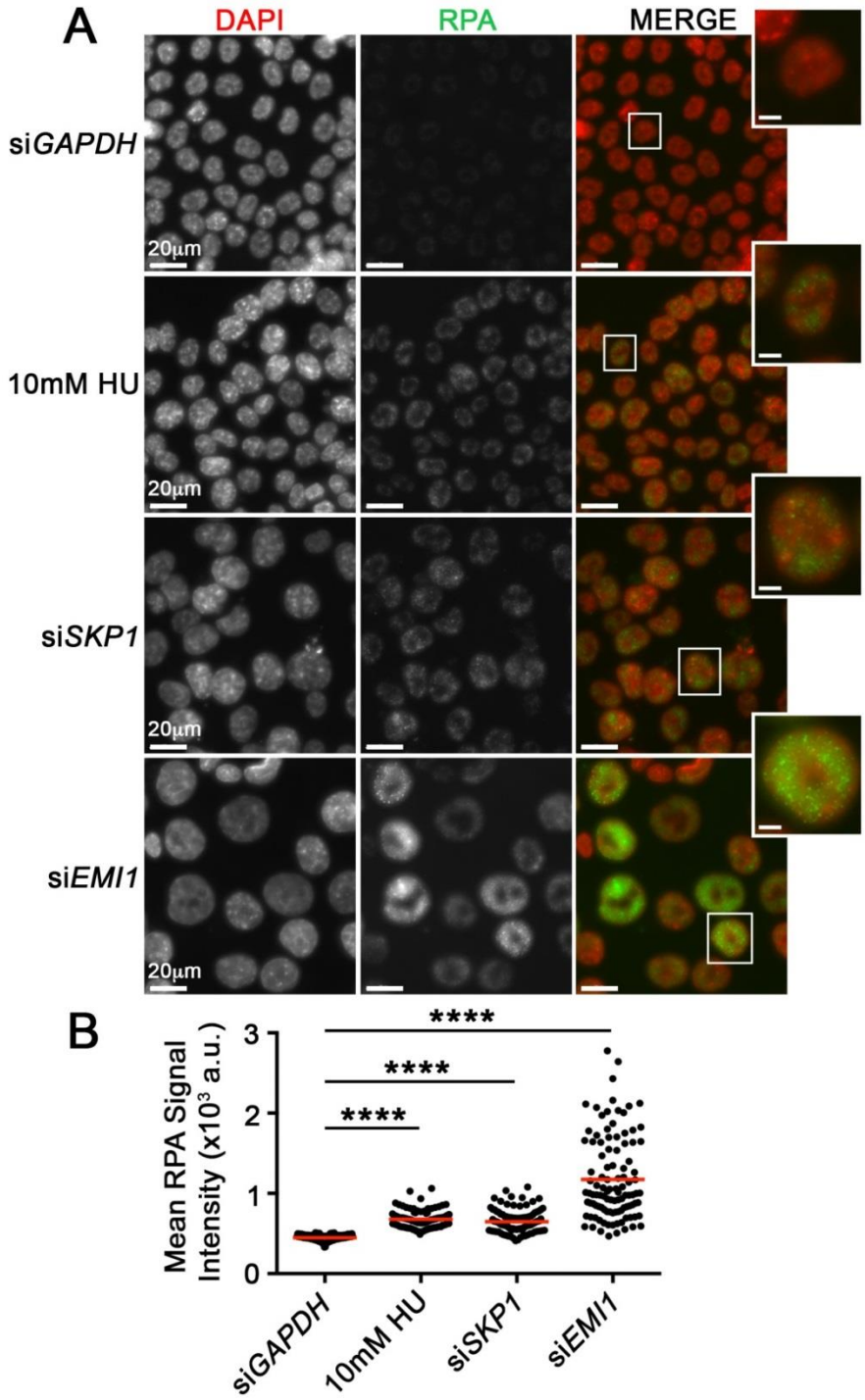

Figure 5-5. *SKP1* Silencing Induces Increases in RPA Foci Indicative of Replication Stress
(A) Representative 3D image projections of interphase nuclei (red) acquired using identical exposure times. Note the RPA signal (green) increases in HU-treated (positive control), *SKP1* and *EMI1* silenced HCT116 cells relative to controls. For illustrative purposes, an individual nucleus (white bounding box) from each condition is presented magnified within the inlay. ***(B)*** Dot plot presenting the statistically significant increase in mean RPA signal intensity (red line) observed in HU, si*SKP1* and si*EMI1* treatment conditions relative to si*GAPDH*. (Student's *t*-tests; **** = *p*-value < 0.0001) (n > 100, N = 3).

5.3.3. *SKP1* Silencing Induces Increases in γH2AX Foci Indicative of Increases in DNA Double Strand Breaks

Aberrant DNA replication attributed to depleted EMI1 is known to generate DNA DSBs that are revealed by increases in γH2AX foci[240]. To assess whether *SKP1* silencing induces similar increases in DNA DSBs, immunofluorescent labeling, quantitative fluorescent microscopy and γH2AX focus enumeration was performed following *SKP1* and *EMI1* silencing in HCT116, and compared to negative (si*GAPDH*) and positive (bleomycin-treated [0.1mg/ml]) controls (*see Sections 2.5.1 and 2.10.2*). *SKP1* silencing induced an increase in the percentage of cells harbouring ≥ 5 γH2AX foci (33.5%) relative to controls (si*GAPDH*; 10.4%), which approached that of the positive control (Bleomycin; 40.3%) (Figure 5-6). In agreement with the RPA foci, *EMI1* silencing induced more extensive increases in interphase nuclei with ≥ 5 foci (85.8%) than those observed in either si*SKP1* or bleomycin-treated cells (Figure 5-6). In support of mitotic chromosome spread results detailed in Chapter 4 that show extensive chromosomal breakages following *SKP1* silencing, the current γH2AX results show that DNA DSBs occur following *SKP1* silencing, which may be attributed to diminished SCF^{EMI1} activity.

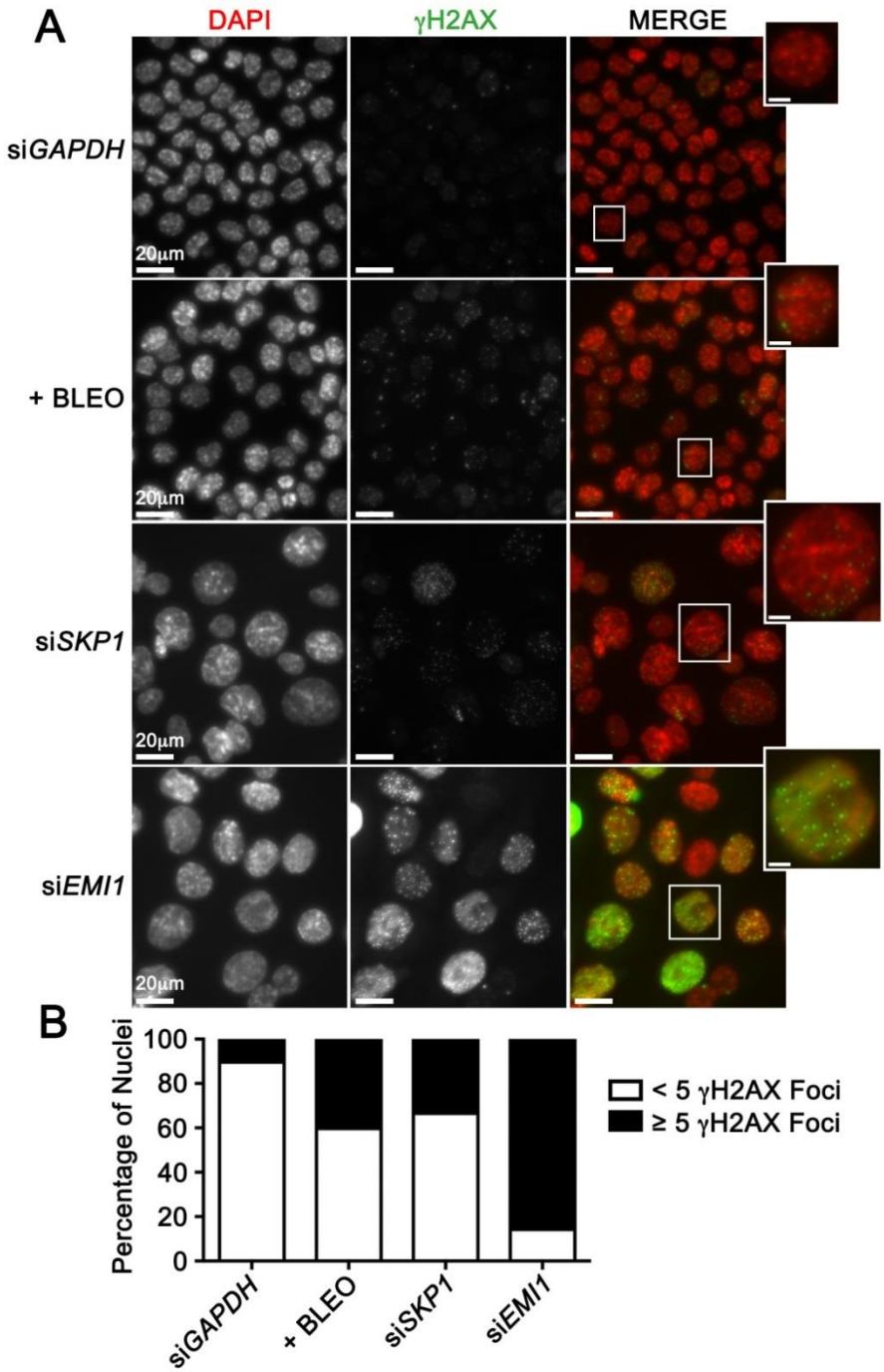

Figure 5-6. *SKP1* and *EMI1* Silencing Induce Increases in γH2AX Foci and DNA Double Strand Breaks

(A) Representative 3D image projections of interphase HCT116 nuclei (red) showing increases in γH2AX (green) following *SKP1* and *EMI1* silencing relative to si*GAPDH* control (scale bars = 20μM). Note that all images were acquired with identical exposure times. For illustrative purposes, an individual nucleus (white bounding box) from each condition is presented magnified within the inlay (scale bars = 5 μm). ***(B)*** Bar graph displaying the increase in the percentage of nuclei with ≥ 5 γH2AX foci (black) in the bleomycin (40.3%), si*SKP1* (33.5%) and si*EMI1* (85.8%) treatments relative to si*GAPDH* (10.4%) (N = 1, n > 100).

5.3.4. *SKP1* Silencing Induces Centromeric Defects

As described above, SCF^{EMI1} alterations may underlie large-scale numerical and structural chromosome changes due to DNA replication defects. However, the high-content screen identified numerous SCF complexes involved in additional downstream pathways that may also be impacted by *SKP1* silencing and induce CIN. As centromere/kinetochore defects leading to mitotic aberrations are known to cause CIN (*see Chapter 4*), centromeric changes were assessed following *SKP1* silencing. To do so, si*GAPDH* and si*SKP1* cells were immunofluorescently labelled for centromeric marker CENPA (*see Section 2.4.2*), which forms the foundation for centromeric and kinetochore complex assembly, and were imaged via quantitative fluorescence microscopy (*see Section 2.5.1*). Unlike the expected focal CENPA labeling pattern observed within 100% of control (si*GAPDH*) cells (Figure 5-7A), *SKP1* silencing resulted in a diffuse, nuclear labeling in ~50.5% (Figure 5-7B) of interphase cells examined. Quantitative image analysis (*see Section 2.5.4*) also revealed a significant 1.5-fold increase in mean CENPA signal intensity following *SKP1* silencing relative to controls (Student's *t*-test, *p*-value < 0.0001) (Figure 5-7C).

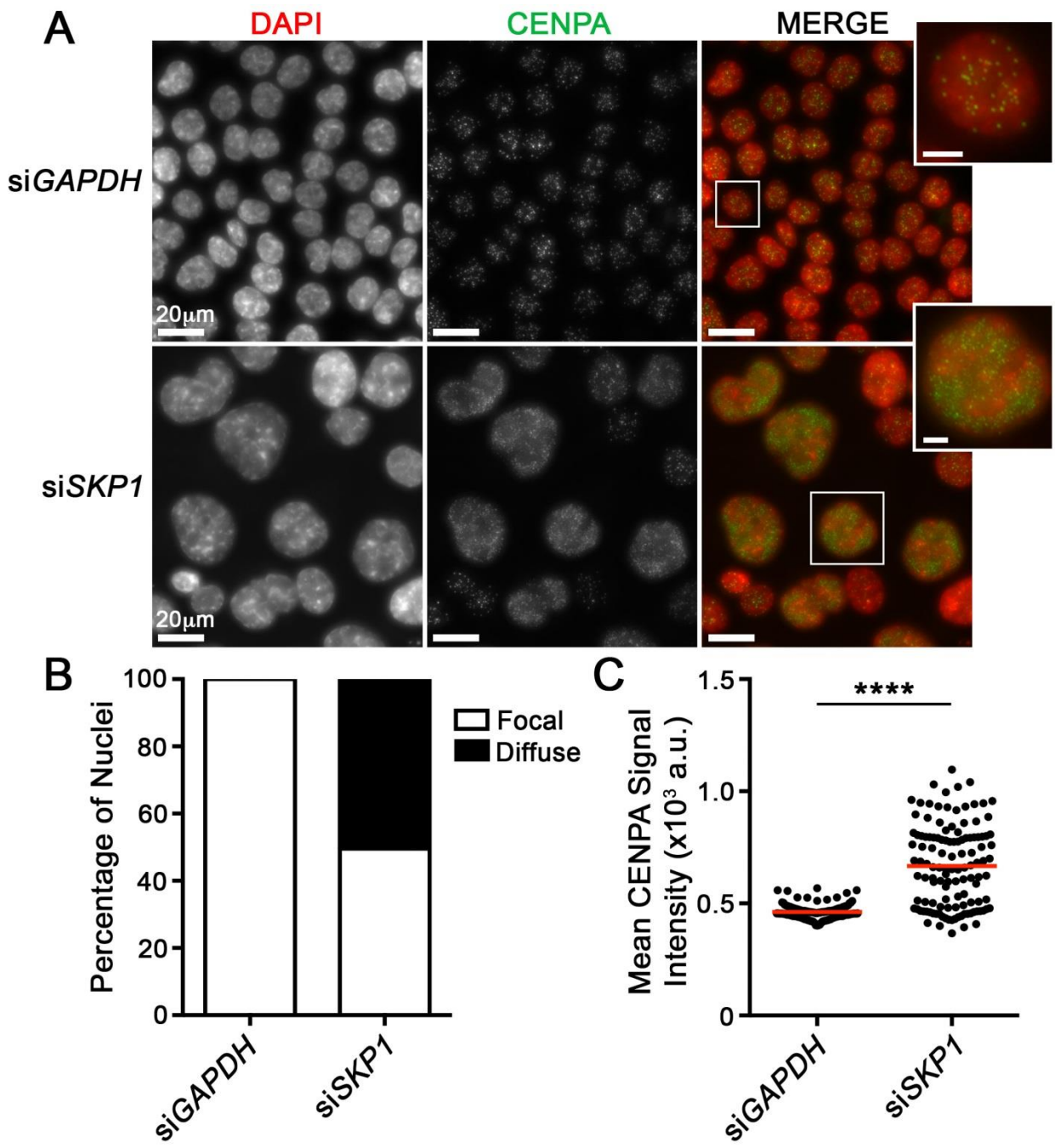

Figure 5-7. *SKP1* Silencing Alters CENPA Localization and Expression Levels in HCT116
(A) Representative 3D image projections of interphase HCT116 nuclei (red) showing a diffuse CENPA (green) labelling pattern in si*SKP1* cells relative to focal CENPA labelling in siGAPDH control cells. For illustrative purposes, an individual nucleus (white bounding box) from each condition is presented magnified within the inlay (scale bars = 5 μm). ***(B)*** Bar graph displaying the increase in the percentage of nuclei with diffuse CENPA labeling (black) relative to normal, focal labeling (white). ***(C)*** Dot plot displaying the significant increase (Student's *t*-test, *p*-value < 0.0001) in mean CENPA signal intensity (red line) following *SKP1* silencing relative to control (n > 100, N = 3).

Centromeric CENPA localization is predicted to be regulated by ubiquitin-associated proteasomal degradation that removes and degrades ectopically integrated CENPA[73]; however, the specific SCF complex(es) that perform this function in human cells remain unknown. To identify SCF complex(es) that regulate CENPA levels and localization, immunofluorescent labeling and assessment of CENPA signal following F-box gene silencing was performed in a high-content screen. Of the 68 F-box protein-encoding genes evaluated, only *EMI1* silencing induced a similar diffuse CENPA localization pattern (Figure 5-8). To assess whether centromeric structure was compromised in *SKP1* or *EMI1* silenced cells, CENPA was co-immunofluorescently labelled with the α-satellite DNA sequence-specific centromeric marker CENPB, which produced a focal staining pattern in all conditions, indicating the centromeres remained intact (Figure 5-8A). *SKP1* and *EMI1* silencing induced increases in the percentages of interphase nuclei with a diffuse CENPA labeling pattern (48.2% and 62.0%, respectively) (Figure 5-8B). Further, both *SKP1* and *EMI1* silencing induced statistically significant 1.7- and 1.6-fold increases, respectively, in mean CENPA signal intensities (Figure 5-8C). Additionally, subsequent experiments demonstrated that *SKP1* and *EMI1* silencing was associated with increases in HJURP levels, the chaperone assembly factor responsible for CENPA integration (Figure 5-9). These findings show that SKP1 and EMI1 are both critical for maintaining proper CENPA levels and localization within the nucleus, perhaps directly or indirectly, through an SCF^{EMI1}-associated mechanism.

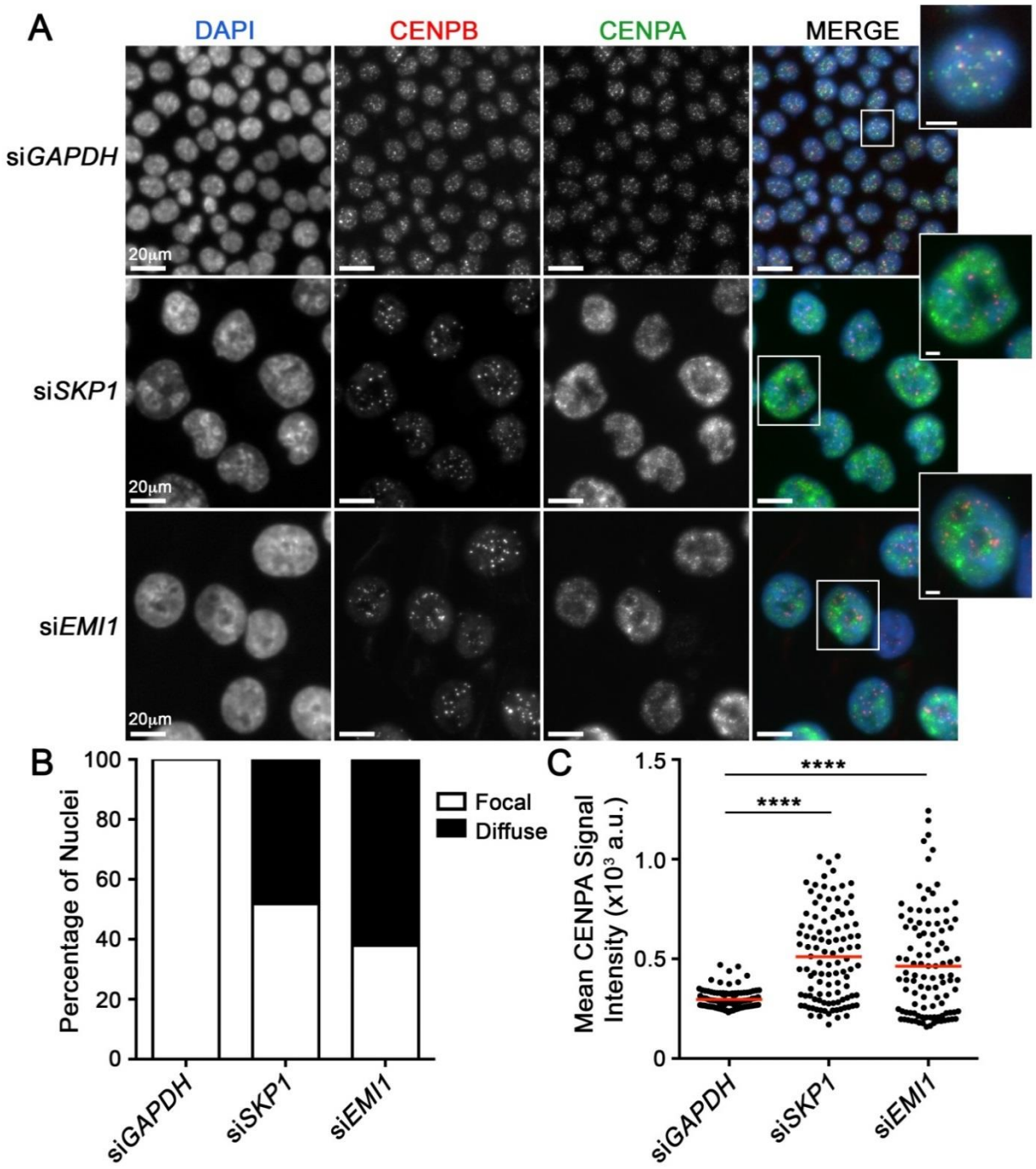

Figure 5-8. Diffuse CENPA Labeling in *SKP1* and *EMI1* Silenced HCT116 Cells
(A) Representative 3D fluorescent microscopy images depicting changes in CENPA localization (green) from a focal staining pattern corresponding with centromeric CENPB foci (red) in si*GAPDH*, to diffuse labelling in si*SKP1* or si*EMI1*. For illustrative purposes, an individual nucleus (white bounding box) from each condition is presented magnified within the inlay (scale bars = 5 µm). ***(B)*** Bar graph showing increases in the percentage of nuclei with diffuse CENPA labeling (black) relative to normal, focal labeling (white) (n > 100). ***(C)*** Dot plot displaying the statistically significant (Student's *t*-tests, *p*-value < 0.0001) increases in mean CENPA signal intensities (red lines) in si*SKP1* and si*EMI1* cells relative to control (n > 100, N = 3).

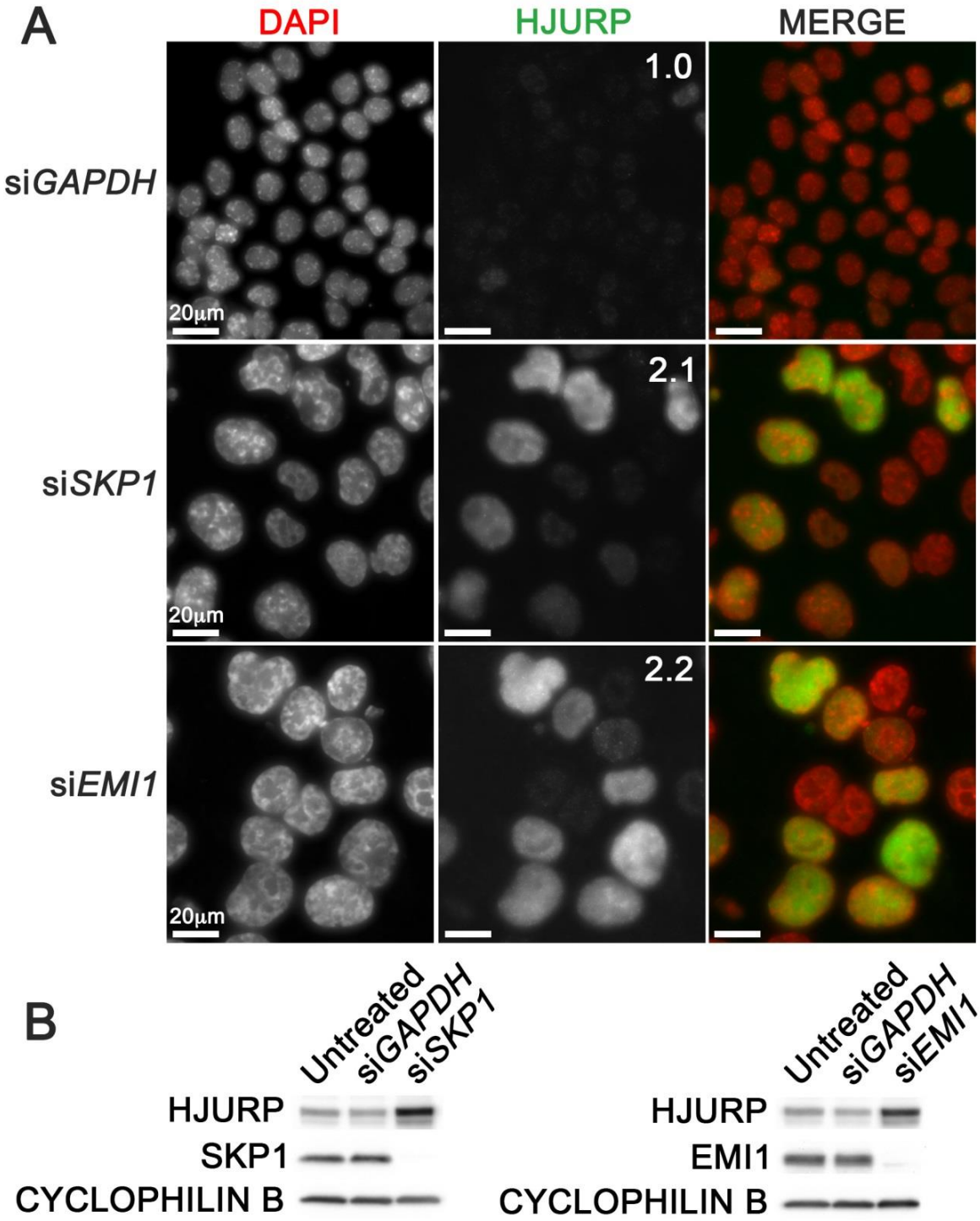

Figure 5-9. *SKP1* and *EMI1* Silencing Induce Aberrant Increases in HJURP Levels
(A) Representative 3D fluorescence microscopy images displaying increases in HJURP (green) fluorescence signal intensities in si*SKP1* and si*EMI1* nuclei (red) relative to si*GAPDH* HCT116 cells. Numbers displayed in HJURP panels (middle) represent the fold increase in mean HJURP signal intensity relative to the si*GAPDH* control ($n > 100$, $N = 2$). Note that images are acquired with identical exposure times. ***(B)*** Western blots confirming HJURP levels increase following *SKP1* (left) and *EMI1* (right) silencing ($N = 2$).

5.3.5. *SKP1* Silencing Underlies Increases in Survivin, an Anti-apoptotic Protein

As described above, *SKP1* silencing presumably impacts numerous SCF complexes beyond SCF^{EMI1}. In fact, the pro-apoptotic gene *FBXL7* induced NA increases and was identified as a putative CIN gene following silencing in the above high-content screen (Table 5-2). FBXL7 functions within the SCF^{FBXL7} complex to regulate degradation of the anti-apoptotic protein Survivin[248]. Interestingly, *SKP1* silencing induced aberrant increases in Survivin levels according to both immunofluorescent (Figure 5-10A) and western blot analyses (Figure 5-10B) (*see Sections 2.4.2, 2.5.1, 2.5.4, and 2.6.0*), while *EMI1* silencing failed to increase Survivin levels (Figure 5-10). This further demonstrates that the altered biology that arises following *SKP1* silencing is likely a culmination of multiple misregulated SCF complexes, including SCF^{FBXL7}. These data further suggest that *SKP1* silenced cells may be resistant to apoptosis and may therefore exhibit enhanced drug resistance due to diminished SCF^{FBXL7} activity and increased Survivin levels, whereas cells with diminished *EMI1* expression and potentially reduced Survivin levels may be more prone to apoptosis.

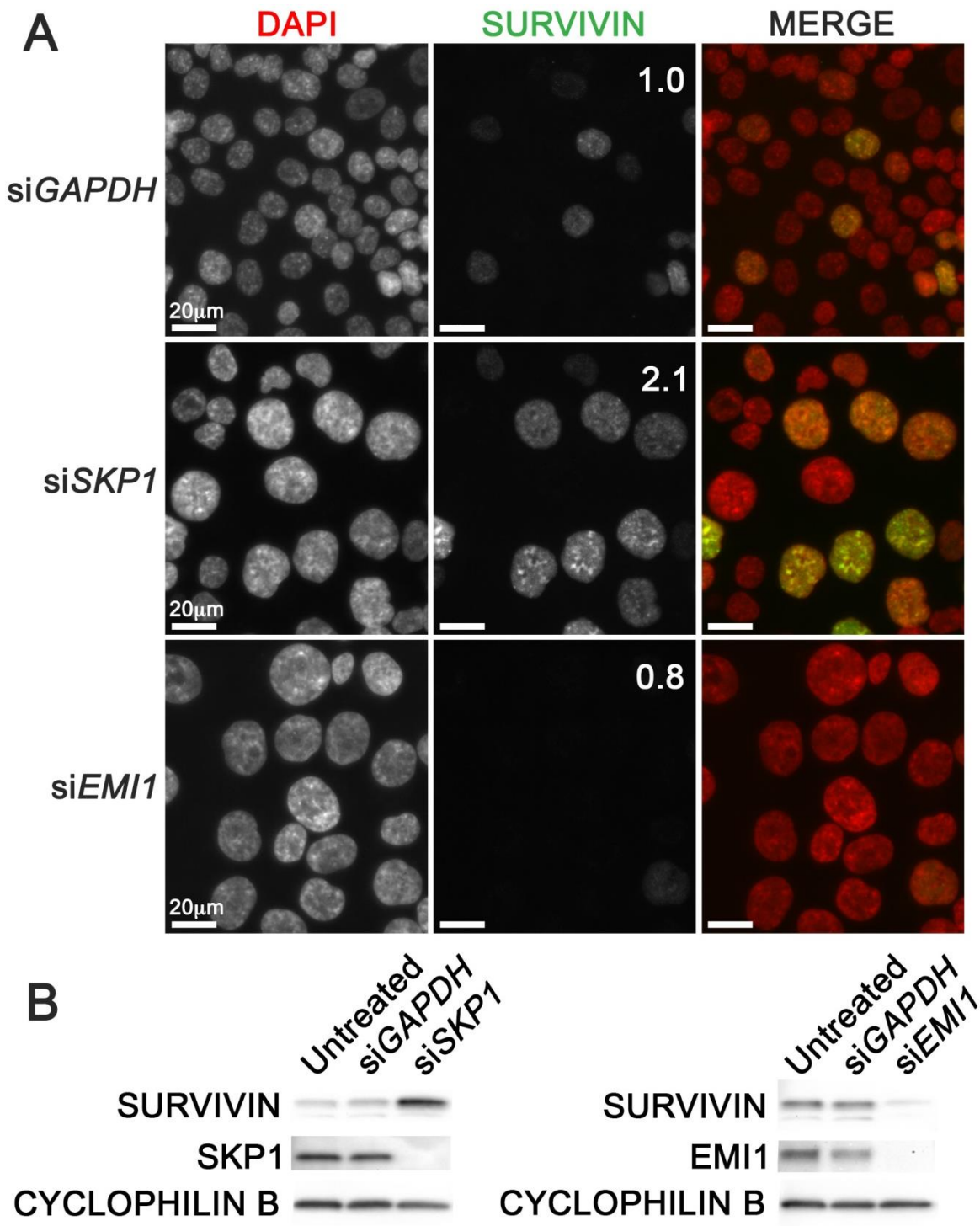

Figure 5-10. *SKP1* Silencing Induces Aberrant Increases in Survivin Levels
(A) Representative 2D fluorescence microscopy images showing Survivin (green) levels increase in si*SKP1* nuclei (red) and decrease slightly in si*EMI1* nuclei. Number in Survivin panel (middle) represents the fold change in mean Survivin signal intensities relative to si*GAPDH*. (N = 1, n > 100). Note images are acquired with identical exposure times. ***(B)*** Western blots confirm Survivin levels increase in si*SKP1* cells (left) and decrease in si*EMI1* cells (right) (N = 2).

5.3.6. Abnormal Increases in CCNE1 Levels Drive CIN Following *SKP1*-Silencing

SKP2 induced the second largest increases in median NA following silencing within the high-content screen (Table 5-2). As SCF^{SKP2} is known to mediate the polyubiquination and degradation of the established CIN- and onco-protein CCNE1, we next sought to investigate whether *SKP1* silencing alters cellular CCNE1 levels. Quantitative microscopy approaches revealed statistically significant increases (Student's *t*-tests, p-value < 0.05) in mean CCNE1 signal intensity following *SKP1* silencing relative to controls (Figure 5-11A and B) and were confirmed by western blots (Figure 5-11C). These data suggest that diminished *SKP1* expression and/or function can impair proper CCNE1 turnover by the SCF^{SKP2} complex.

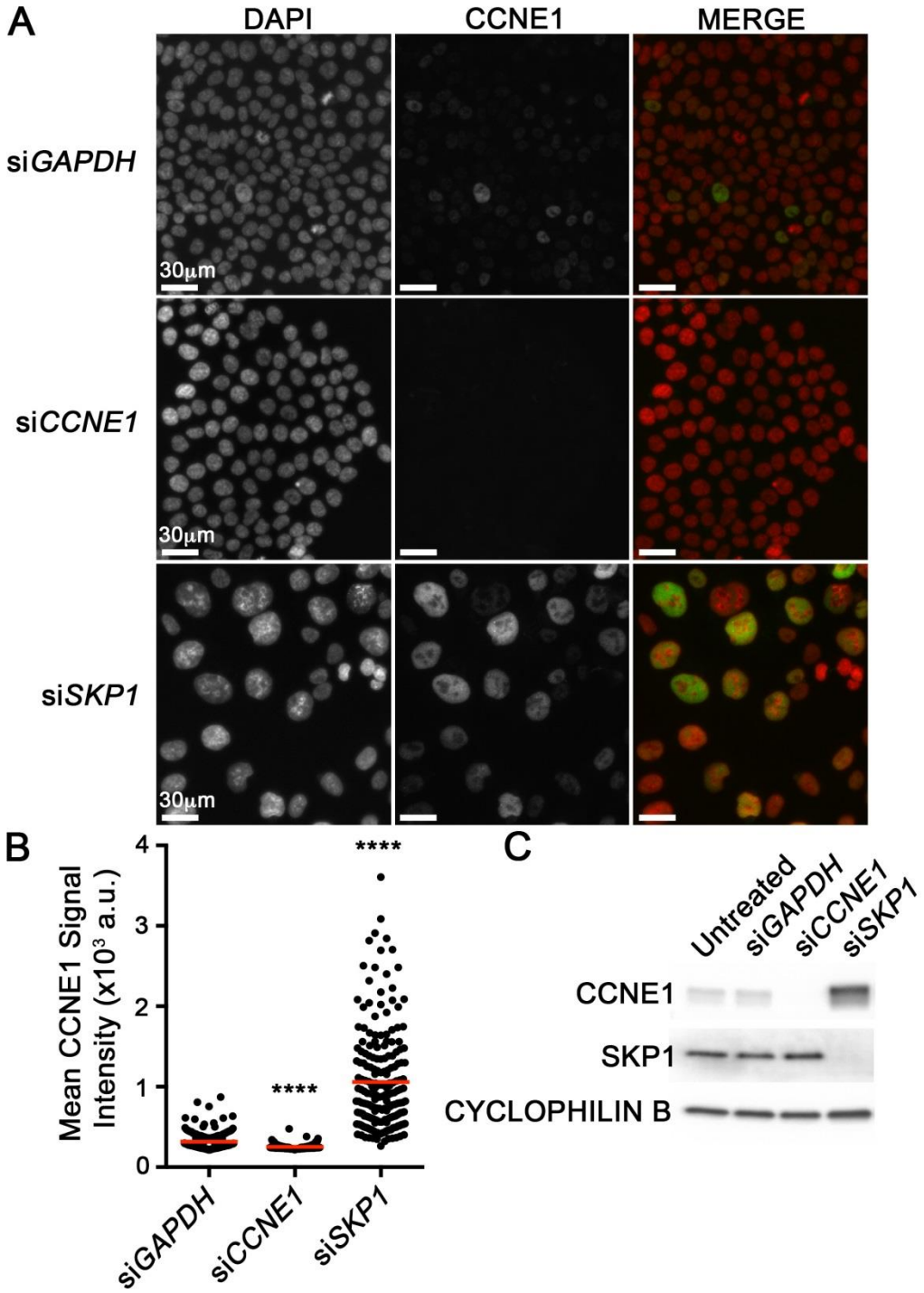

Figure 5-11. *SKP1* Silencing Underlies Increases in CCNE1 Levels in HCT116 Cells
(A) Quantitative fluorescence microscopy images depicting increases in CCNE1 (green) levels in interphase nuclei (red) following *SKP1* silencing relative to si*GAPDH* controls. All images are acquired with identical exposure times. Note the loss of visually detectable signal in the si*CCNE1* control. ***(B)*** Dot plot presenting the statistically significant (Student's t- test, **** = *p*-value < 0.0001) increase in mean CCNE1 signal intensity (red line) in si*SKP1* cells relative to the si*GAPDH* control (n = 200). ***(C)*** Western blots confirming increases in CCNE1 levels following *SKP1* silencing (N =3).

To assess whether increases in CCNE1 levels contribute to the si*SKP1*-associated CIN phenotypes observed above, *SKP1* and *CCNE1* co-silencing experiments (*i.e.* phenotypic rescue) were performed. First, western blot analyses were employed to validate that *SKP1* and *CCNE1* were effectively co-silenced in the same condition (Figure 5-12A). NA analyses were performed on *SKP1*, *SKP1* + *GAPDH*, and *SKP1* + *CCNE1* silenced cells and associated controls. In agreement with our previous findings, significant increases in mean NAs (Student's *t*-tests, *p*-value < 0.05) as well as in cumulative NA frequency distributions (KS tests, *p*-value < 0.05) were observed for si*SKP1* and si*SKP1* + si*GAPDH* conditions relative to controls. As predicted, a statistically significant decrease in mean NA (Student's *t*-test, *p*-value < 0.05) was detected in the si*SKP1* + si*CCNE1* dual silenced condition compared to the si*SKP1* + si*GAPDH* dual silenced control (Figure 5-12B and C). KS tests (*p*-value < 0.001) also revealed a significant decrease in the cumulative NA frequency distribution towards smaller nuclei relative to si*SKP1* + si*GAPDH* or si*SKP1* conditions (Figure 5-12D). Further assessment of CIN phenotypes revealed ~2.0-fold decreases in the number of MN formed (Figure 5-12E) and the number of mitotic chromosome spreads that displayed aberrant CIN-associated phenotypes (Figure 5-12F) in si*SKP1* + si*CCNE1* dual silenced cells compared to the si*SKP1* + si*GAPDH* condition. These observations suggest that increases in CCNE1 levels, contribute at least in part, to the CIN phenotypes observed following *SKP1* silencing in HCT116 cells.

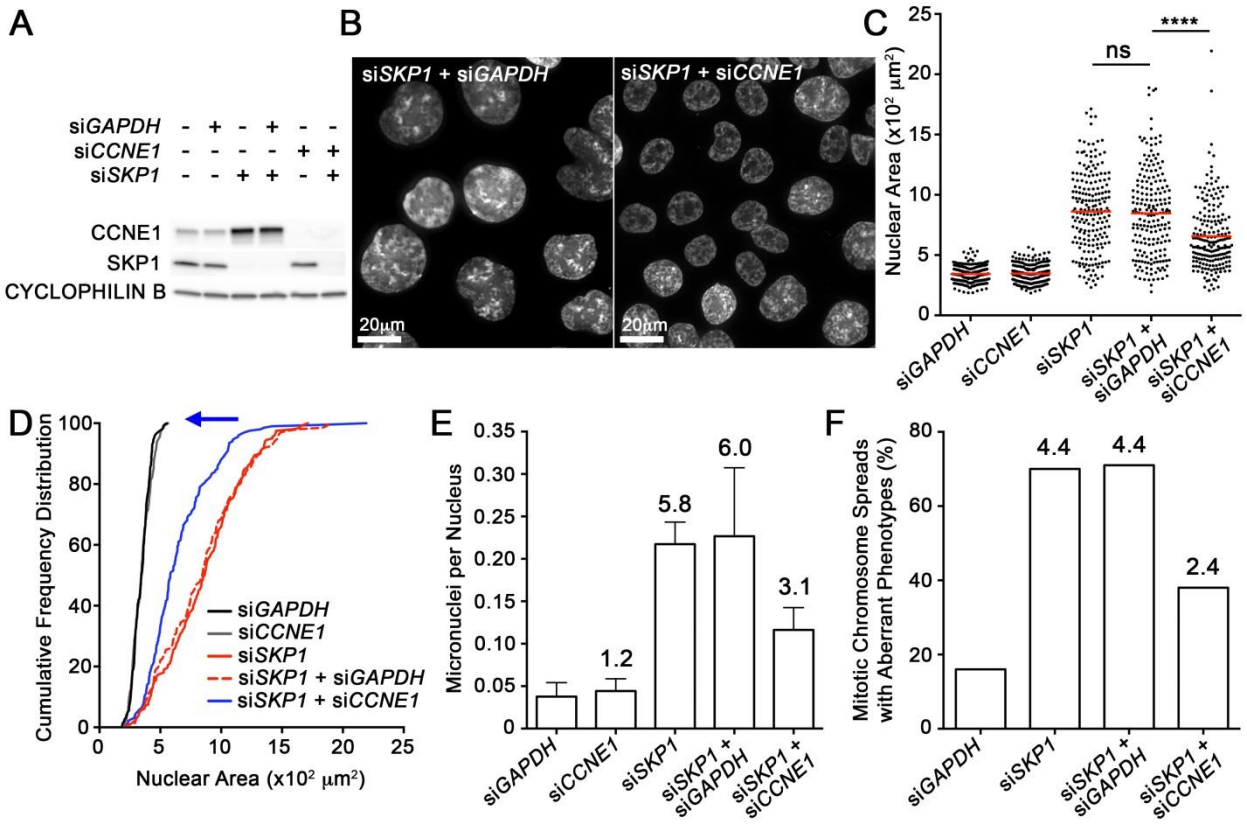

Figure 5-12. *CCNE1* Silencing Rescues the CIN Phenotypes Associated with *SKP1* Silencing in HCT116 Cells

(A) Western blot showing CCNE1 increases in *SKP1* and *SKP1* + *GAPDH* silenced cells relative to controls, as well as effective *SKP1* and *CCNE1* dual-silencing (far right). ***(B)*** Representative fluorescence microscopy images at equal magnification showing NA decreases in *SKP1* + *CCNE1* dual silenced cells compared to the si*SKP1* + si*GAPDH* condition. ***(C)*** Dot plots of NA values showing a significant decrease mean NA (red line) in si*SKP1* + si*CCNE1* cells compared to si*SKP1* or si*SKP1* + si*GAPDH* conditions. (Student's *t*-test, *p*-value < 0.0001; n = 200, N = 3). Note the differences in mean NA of negative controls si*GAPDH* and si*CCNE1* are not significantly different. ***(D)*** Cumulative NA frequency distributions showing a statistically significant shift towards smaller NA in si*SKP1* + si*CCNE1* cells compared to si*SKP1* or si*SKP1* + si*GAPDH*. (KS-test, *p*-value < 0.0001, n = 200, N = 3). Note the NA frequency distributions for si*GAPDH* and si*CCNE1* conditions are virtually superimposable. ***(E)*** Bar graph showing a ~2.0-fold decrease in MN formation following *SKP1* + *CCNE1* dual-silencing relative to *SKP1* or *SKP1* + *GAPDH* silenced conditions. Numbers above the bar represent the fold increase relative to the si*GAPDH* negative control. (n = > 200, N = 3) ***(F)*** Bar graph showing the ~2.0-fold decrease in the percentage of aberrant mitotic chromosome spreads in the si*SKP1* + si*CCNE1* condition compared to si*SKP1* + si*GAPDH* conditions (n = 100, N = 1). Previous findings for si*GAPDH* and si*SKP1* are presented for comparison purposes. Numbers above the bar represent the fold increase relative to si*GAPDH*.

5.3.7. *SKP1* Silencing Induces Centrosomal Aberrations

As CCNE1 overexpression is associated with centrosome defects[106,143,249,250], we sought to determine whether centrosome biology was altered in *SKP1* silenced HCT116 cells. Co-immunofluorescent labelling of the centrosomal marker Pericentrin[251] was performed in conjunction with the centriolar marker Cenexin (Figure 5-13A). Quantitative 3D fluorescence microscopy imaging and image deconvolution was performed as described in Materials and Methods (*see Section 2.5.1*) enabling high-resolution centrosome analysis. Quantitative analysis of pericentrin labeling revealed a statistically significant increase in mean centrosome volume (Student's *t*-test, *p*-value < 0.0001) compared to controls (Figure 5-13B). Further, a significant ~3-fold increase in the mean number of Cenexin foci/centrosome occurred in si*SKP1* cells compared to the expected 1 Cenexin focus/centrosome in controls (Figure 5-13C and SI Table S5-7). Analogous co-immunofluorescent labelling experiments were performed utilizing Centrin and CCP110 as additional centriolar markers in combination with Pericentrin labelling and similar increases in centrosome volume and the number of centriolar signals were observed (SI Table S5-7 and Figure S5-2). Overall these findings indicate that *SKP1* silencing results in aberrant centrosome biology, a known driver of CIN.

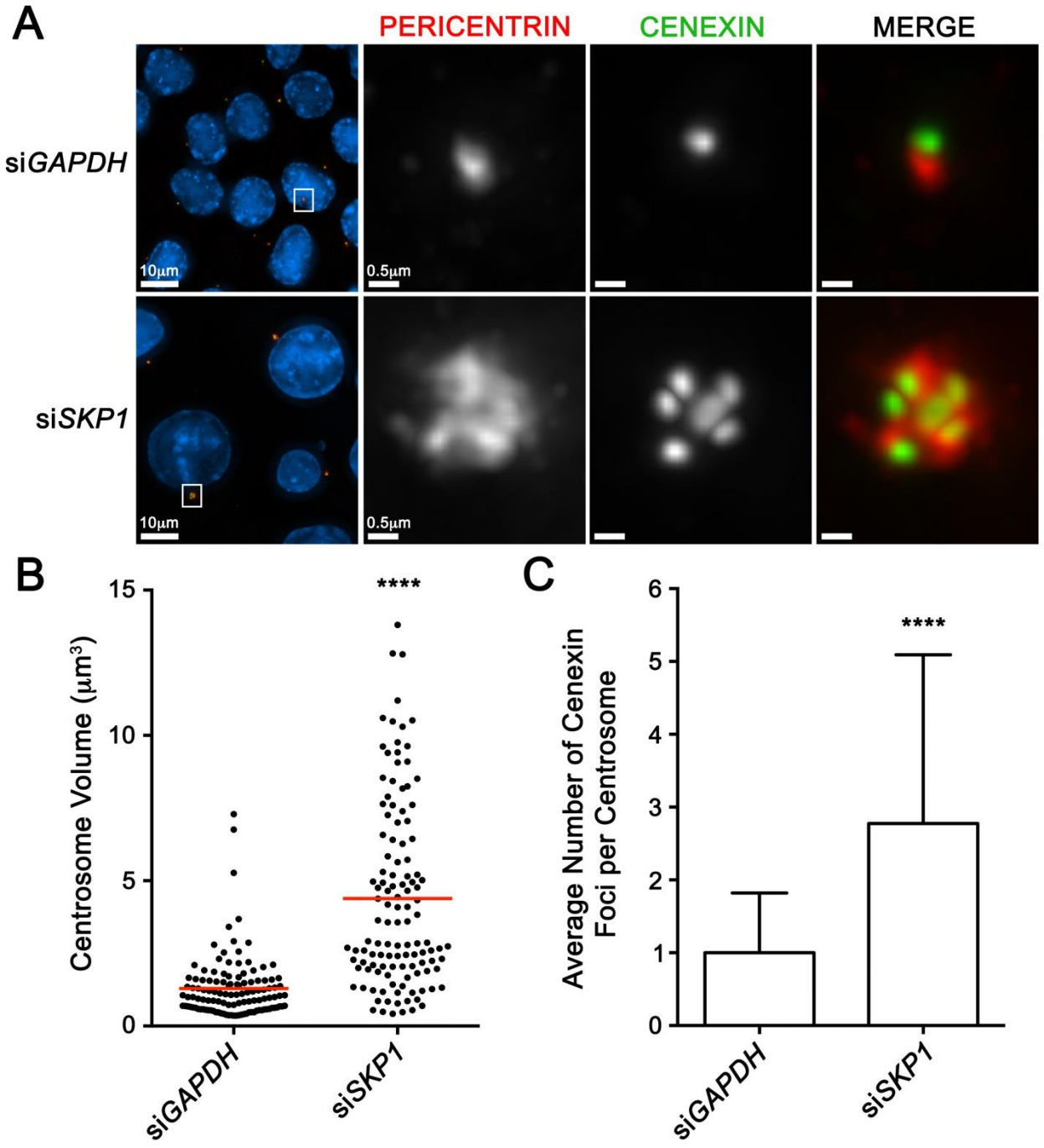

Figure 5-13. *SKP1* Silencing Induces Aberrant Centrosome Biology in HCT116
(A) Deconvolved 3D fluorescence microscopy images (left) showing *GAPDH* and *SKP1* silenced interphase nuclei (blue) and centrosome markers Pericentrin (red) and Cenexin (green). Centrosomes in white bounding boxes are magnified to show increases in centrosome size (Pericentrin) as well as amplification of centriolar signals (Cenexin) following *SKP1* silencing. ***(B)*** Dot plot showing the statistically significant increase in mean centrosome volume in si*SKP1* cells (Student's *t*-test, *p*-value < 0.0001). ***(C)*** Bar graph presenting significant increase in the number of Cenexin foci in si*SKP1* cells compared to the expected 1 Cenexin focus per centrosome in si*GAPDH* cells (Student's *t*-test; *p*-value < 0.0001). (n > 100, N = 3).

5.4.0. Discussion

In this study, 68 F-box protein-encoding genes were subjected to NA and MN enumeration screens. A total of 53 putative CIN genes were identified, 16 of which, were identified by both assays in both experimental replicates. As each of the corresponding SCF complexes could be impacted by *SKP1* silencing, upwards of 53 distinct SCF complexes and the misregulation of their downstream substrates may contribute to the si*SKP1*-associated CIN phenotypes presented in Chapter 4. *EMI1* silencing was found to induce similar increases in NA as those observed following *SKP1* silencing. *SKP1* and *EMI1* silencing both induced replication stress and aberrant localization of centromeric proteins (CENPA and HJURP), suggesting these processes are regulated by SCF^{EMI1}. Increased levels of Survivin and CCNE1, substrates of SCF^{FBXL7} and SCF^{SKP2}, respectively, were also observed in *SKP1* silenced cells. CIN phenotypes including NA increases, MN formation, and chromosomal aberrations were reduced when *SKP1* and *CCNE1* were co-silenced, implicating increased CCNE1 as an underlying cause of the CIN phenotypes. *SKP1* silencing was also found to induce centrosomal aberrations, which are commonly observed in *CCNE1* overexpressing cancer cells[249,250].

Although *SKP1* is somatically altered and/or misexpressed in cancer[157,158,209,225], the pathogenic implications of aberrant SKP1 expression or function are not clearly delineated. This study has provided critical insight into the CIN-inducing oncogenic mechanisms that are misregulated in *SKP1* silenced CRC-derived HCT116 cells. The above data indicate that the si*SKP1*-associated CIN phenotypes are likely culmination of multiple misregulated SCF complexes. This concept is exemplified by *SKP1* and *CCNE1* dual silencing experiments that failed to achieve a complete phenotypic rescue, indicating that increased CCNE1 levels only partially contribute to the CIN phenotypes. Confounding factors including failure to achieve

sufficient silencing of both *SKP1* and *CCNE1* within the same cell may also influence the extent of phenotypic rescue. Regardless, increased CCNE1 levels were found to contribute to CIN and are in agreement with previous studies[143,250,252-254]. While there is a wealth of knowledge regarding *CCNE1* amplification and overexpression in the pathogenesis of breast[254], non-small cell lung[255], and high-grade serous ovarian cancer[253], few studies have investigated the link between SKP1, CCNE1 and CRC. The above findings demonstrate that increased CCNE1 levels drive CIN in *SKP1* silenced CRC cells. Thus, alterations in SKP1, SCF activity, and/or CCNE1 levels may represent initiating events in the development of CRC. Further, increased CCNE1 levels in a CRC tumor may induce CIN and promote ITH, tumor adaptability, drug resistance, and disease progression[4,59,60]. *In silico* cBioPortal[155,156] searches reveal that copy number loss or underexpression of *SKP1* and *SKP2*, or copy number gains or overexpression of *CCNE1* occur in ~31% of CRC[209], and thus may represent a novel pathway that can be therapeutically exploited in CRC cells. Moreover, if extrapolated to additional cancer types where the oncogenic role of CCNE1 is better established (*e.g.* ovarian[158] or lung cancer[208]), a larger proportion of patients (51% and 72%, respectively) may therapeutically benefit from such targeted therapies.

The observed increases in SCF^{FBXL7} substrate Survivin in si*SKP1* HCT116 cells are particularly relevant in terms of cancer development and progression, as Survivin is a proposed driver of CRC oncogenesis. Survivin expression increases with transition from an adenoma with low dysplasia, to CRC with high dysplasia, and correlates with increased cellular proliferation, apoptotic resistance, and angiogenesis[256]. Survivin is frequently overexpressed in CRC, and increases with TNM stage, lymph node involvement, and metastatic progression[257]. In fact, specific Survivin polymorphisms (31G>C) confer an increased risk to CRC[258]. In addition to CRC, Survivin is overexpressed in numerous cancer types including urothelial[259], ovarian[260],

lung[261], cervical[262], and breast[263], correlating with increased tumor grade, cancer recurrence, disease progression and drug resistance, indicating that increases in Survivin are highly pathogenic and may likely drive oncogenesis in cells with diminished SKP1 activity. Additionally, Survivin is an established component of the Chromosome Passenger Complex (*see Section 1.4.4*), which mediates kinetochore microtubule attachment and cytokinesis[114]. Survivin overexpression has been shown through centromeric FISH probe analysis to contribute to CIN in breast cancer[263]. Thus, cancers with altered SCF function due to mutation or diminished expression of *SKP1* or *FBXL7* may exhibit increased levels of Survivin, which drives CIN, cancer development, disease progression and drug resistance.

While *EMI1* silencing induced similar NA changes to those observed in si*SKP1* cells, phenotypic differences were apparent. *EMI1* silencing induced increases in DNA replication defects (RPA foci) and DNA damage (γH2AX foci) well beyond those observed following *SKP1* silencing, as well as opposing changes in Survivin levels, and a failure to increase MN formation. Presumably, the effect of SCF^{EMI1} alteration is diluted in si*SKP1* cells that display aberrant phenotypes derived from additional misregulated SCF complexes. In comparison to *SKP1* silenced cells, the si*EMI1* condition required twice the number of HCT116 cells to be seeded in order to obtain comparable cell numbers at the end of the experiment. Thus, diminished EMI1 may adversely impact cell cycle progression or cell division, corresponding with previous studies that characterized *EMI1* as an oncogene[234-236]. However, EMI1 can also function as a tumor suppressor[237], and unfortunately, few studies have examined the impact of diminished EMI1 expression/function in CRC. Despite initial decreases in cell numbers, *EMI1* silencing in a CRC context could generate a subpopulation of cells within the tumor that exhibit aberrant DNA replication, increased DNA damage, centromeric aberrations and CIN, thereby

promoting cancer cell evolution and the development of a highly aggressive, drug resistant cancer. The above findings also suggest that SCF^{EMI1} is the previously unidentified SCF complex responsible for removing and degrading ectopically integrated and/or soluble nuclear CENPA to maintain chromosome stability in human cells. Whether SCF^{EMI1} functions directly in CENPA polyubiquitination and proteasomal degradation, or indirectly through interaction with CENPA regulatory proteins such as HJURP, remains to be determined. *HJURP* is overexpressed in numerous cancer types including non-small cell lung[83], glioblastoma[84], astrocytoma[85], and breast cancers[86]. Similarly, CENPA is a known CIN and oncogenic driver and is increased in lung[87], osteosarcoma[88], and colorectal[89] tumor samples relative to adjacent normal tissue. Overexpression of either HJURP or CENPA correlates with poorer patient outcomes[85-88]. Interestingly, siRNA-based *HJURP* silencing in glioblastoma cells that overexpress *HJURP* induces cancer cell-specific killing, suggesting that centromeric components may represent novel therapeutic targets in cancers with aberrant centromere biology and altered SCF activity[85].

In this chapter, the high-content NA and MN enumeration screen was expanded into an additional gene set (F-box proteins), where the biological functions for the majority of encoded proteins have yet to be characterized. While previously characterized CIN genes such as *CCNF* (*FBXO1*)[227,230], *β-TRCP2* (*FBXW11*)[264], *EMI1* (*FBXO5*)[237,238], and *SKP2* (*FBXL1*)[143] were detected in the screen, the majority of putative CIN genes identified have no established links to CIN. As such, the list of F-box protein-encoding putative CIN genes identified above serves as a valuable resource that can be exploited in additional studies beyond the scope of this thesis, to validate (*see Chapter 4*) and characterize the altered F-box proteins, SCF complexes, and downstream substrates that may underlie CIN and oncogenesis. The investigation of SCF

complexes in future studies may reveal novel CIN-associated pathways, prognostic or diagnostic indicators, and novel cancer therapeutic targets.

5.5.0. Supporting Information

5.5.1. Supporting Tables

Table S5-1. KS Tests Reveal Significant Changes in NA Frequency Distributions in HCT116 High-Content Screen #1

Gene[A]	*FBXO30*	*FBXW4*	*FBXO46*	*FBXO39*	*FBXO9*	*FBXL13*	*FBXW5*
***p*-value**[B]	0.6678	0.3872	0.2675	0.1930	0.1334	0.0954	0.0798
Sig.[C]	ns	ns	ns	ns	ns	ns	ns
D[D]	0.0718	0.0670	0.0600	0.1481	0.0638	0.0525	0.0837
Gene	*FBXO36*	*FBXO18*	*FBXW8*	*FBXL18*	*FBXL17*	*FBXO16*	*FBXW10*
***p*-value**	0.0710	0.0693	0.0601	0.0252	0.0215	0.0185	0.0100
Sig.	ns	ns	ns	ns	ns	ns	ns
D	0.0954	0.0954	0.0590	0.1358	0.1094	0.1071	0.1438
Gene	***FBXO34***	***FBXL4***	***FBXO7***	***FBXW2***	***FBXO20***	***FBXL16***	***FBXL14***
***p*-value**	0.0100	0.0013	0.0010	0.0010	0.0003	0.0001	< 0.0001
Sig.	**	**	**	***	***	***	****
D	0.1251	0.1113	0.1762	0.1372	0.1281	0.2637	0.1031
Gene	***FBXW9***	***FBXO45***	***FBXO3***	***FBXL3***	***FBXO40***	***FBXO25***	***FBXL20***
***p*-value**	< 0.0001	< 0.0001	< 0.0001	< 0.0001	< 0.0001	< 0.0001	< 0.0001
Sig.	****	****	****	****	****	****	****
D	0.1180	0.1190	0.1290	0.1300	0.1416	0.1461	0.1498
Gene	***KDM2A***	***FBXW11***	***FBXW7***	***FBXO38***	***CCNF***	***BTRC***	***FBXO32***
***p*-value**	< 0.0001	< 0.0001	< 0.0001	< 0.0001	< 0.0001	< 0.0001	< 0.0001
Sig.	****	****	****	****	****	****	****
D	0.1538	0.1675	0.1680	0.1698	0.1729	0.1791	0.1819
Gene	***FBXO31***	***FBXO2***	***FBXL8***	***FBXO43***	***FBXL2***	***FBXO24***	***FBXL12***
***p*-value**	< 0.0001	< 0.0001	< 0.0001	< 0.0001	< 0.0001	< 0.0001	< 0.0001
Sig.	****	****	****	****	****	****	****
D	0.1842	0.1894	0.1970	0.2005	0.2047	0.2053	0.2086
Gene	***FBXL22***	***FBXO17***	***FBXO41***	***FBXL19***	***FBXL15***	***FBXW12***	***FBXO28***
***p*-value**	< 0.0001	< 0.0001	< 0.0001	< 0.0001	< 0.0001	< 0.0001	< 0.0001
Sig.	****	****	****	****	****	****	****
D	0.2253	0.2537	0.2554	0.2619	0.2665	0.2690	0.2704
Gene	***FBXO11***	***FBXO42***	***FBXL7***	***FBXO6***	***FBXO27***	***FBXL10***	***SKP2***
***p*-value**	< 0.0001	< 0.0001	< 0.0001	< 0.0001	< 0.0001	< 0.0001	< 0.0001
Sig.	****	****	****	****	****	****	****
D	0.2817	0.2924	0.2941	0.3136	0.3192	0.3213	0.3330
Gene	***FBXL5***	***FBXO22***	***FBXO8***	***FBXL6***	***FBXL21***	***FBXO10***	***EMI1***
***p*-value**	< 0.0001	< 0.0001	< 0.0001	< 0.0001	< 0.0001	< 0.0001	< 0.0001
Sig.	****	****	****	****	****	****	****
D	0.3458	0.3489	0.3586	0.3659	0.3948	0.4296	0.7324

[A]Putative CIN genes (bold) induce significant (*p*-value < 0.01) cumulative NA frequency distribution changes (vs. si*GAPDH*).
[B]*p*-values calculated from two-sample KS tests for listed condition relative to si*GAPDH*.
[C]Significance level (ns = not significant, ** = *p*-value < 0.01, *** = *p*-value < 0.001, **** = *p*-value < 0.0001).
[D]*D*; *D*-statistic (maximum deviation between the two distribution curves).

Table S5-2. KS Tests Reveal Significant Changes in NA Frequency Distributions in HCT116 High-Content Screen #2

Gene[A]	*FBXO40*	*FBXL10*	*FBXW9*	*FBXO39*	*FBXW7*	*FBXL3*	*FBXO33*
***p*-value**[B]	0.3491	0.2289	0.1642	0.0901	0.0308	0.0251	0.0219
Sig.[C]	ns	ns	ns	ns	ns	ns	ns
D[D]	0.0319	0.0541	0.0279	0.1570	0.0383	0.0682	0.1264
Gene	*FBXW8*	***FBXW5***	***FBXW10***	***FBXO15***	***FBXL2***	***FBXO38***	***FBXO30***
***p*-value**	0.0129	0.0086	0.0047	0.0019	0.0013	0.0002	0.0001
Sig.	ns	**	**	**	**	***	***
D	0.0496	0.0983	0.1465	0.1264	0.1129	0.1209	0.1432
Gene	***KDM2A***	***FBXO25***	***FBXL17***	***FBXW11***	***BTRC***	***FBXO7***	***CCNF***
***p*-value**	< 0.0001	< 0.0001	< 0.0001	< 0.0001	< 0.0001	< 0.0001	< 0.0001
Sig.	****	****	****	****	****	****	****
D	0.0613	0.0715	0.0777	0.0789	0.0840	0.0860	0.0978
Gene	***FBXO45***	***FBXL13***	***FBXL20***	***FBXO9***	***FBXO46***	***FBXO3***	***FBXW2***
***p*-value**	< 0.0001	< 0.0001	< 0.0001	< 0.0001	< 0.0001	< 0.0001	< 0.0001
Sig.	****	****	****	****	****	****	****
D	0.0984	0.1046	0.1049	0.1084	0.1128	0.1172	0.1198
Gene	***FBXO16***	***FBXO31***	***FBXO18***	***FBXL8***	***FBXL4***	***FBXW4***	***FBXW12***
***p*-value**	< 0.0001	< 0.0001	< 0.0001	< 0.0001	< 0.0001	< 0.0001	< 0.0001
Sig.	****	****	****	****	****	****	****
D	0.1211	0.1230	0.1386	0.1400	0.1436	0.1621	0.1622
Gene	***FBXL18***	***FBXL14***	***FBXO8***	***FBXL5***	***FBXO20***	***FBXL15***	***FBXO27***
***p*-value**	< 0.0001	< 0.0001	< 0.0001	< 0.0001	< 0.0001	< 0.0001	< 0.0001
Sig.	****	****	****	****	****	****	****
D	0.1630	0.1711	0.1799	0.1909	0.1920	0.1962	0.1974
Gene	***FBXL12***	***FBXO32***	***FBXO43***	***FBXO2***	***FBXL7***	***FBXL16***	***FBXO41***
***p*-value**	< 0.0001	< 0.0001	< 0.0001	< 0.0001	< 0.0001	< 0.0001	< 0.0001
Sig.	****	****	****	****	****	****	****
D	0.2087	0.2245	0.2255	0.2337	0.2489	0.2572	0.2602
Gene	***FBXO42***	***FBXO11***	***FBXL6***	***FBXL21***	***FBXO44***	***FBXO24***	***FBXO22***
***p*-value**	< 0.0001	< 0.0001	< 0.0001	< 0.0001	< 0.0001	< 0.0001	< 0.0001
Sig.	****	****	****	****	****	****	****
D	0.2719	0.2722	0.2748	0.2827	0.2929	0.3038	0.3122
Gene	***FBXL19***	***FBXO17***	***FBXO6***	***FBXL22***	***FBXO4***	***FBXO10***	***FBXO28***
***p*-value**	< 0.0001	< 0.0001	< 0.0001	< 0.0001	< 0.0001	< 0.0001	< 0.0001
Sig.	****	****	****	****	****	****	****
D	0.3149	0.3209	0.3240	0.3288	0.3348	0.3480	0.3506
Gene	***FBXO34***	***SKP2***	***EMI1***				
***p*-value**	< 0.0001	< 0.0001	< 0.0001				
Sig.	****	****	****				
D	0.3928	0.4107	0.8492				

[A]Putative CIN genes (bold) induce significant (*p*-value < 0.01) cumulative NA frequency distribution changes (vs. si*GAPDH*).

[B]*p*-values calculated from two-sample KS tests for listed condition relative to si*GAPDH*.

[C]Significance level (ns = not significant, ** = *p*-value < 0.01, *** = *p*-value < 0.001, **** = *p*-value < 0.0001).

[D]*D*; *D*-statistic (maximum deviation between the two distribution curves).

Table S5-3. *EMI1* and *SKP1* Silencing Induces Similar Increases in Mean NAs in HCT116 Cells

Screen	Condition	N[A]	Mean	SD[B]	*p*-value[C]	Significance[D]
1	si*SKP1*	241	504.64	292.86	-	-
	si*EMI1*	62	523.18	237.77	0.6454	ns
2	si*SKP1*	374	475.47	214.98	-	-
	si*EMI1*	221	497.28	176.11	0.2025	ns

[A]N = Number of nuclei analyzed
[B]SD = Standard deviation
[C]Student's *t*-test comparing mean si*SKP1* and si*EMI1* NA values (*p*-value < 0.05 considered significant)
[D]ns = Not significant

Table S5-4. MN Enumeration Reveals F-box Putative CIN Genes in HCT116 Screen #1

Gene[A]	*EMI1*	*FBXO28*	*BTRC*	*FBXL4*	*FBXO46*	*FBXL6*	*FBXL21*
MNi[B]	0	0	6	1	1	6	5
N	62	270	2819	465	426	1931	1352
MNi/N[C]	0.0000	0.0000	0.0021	0.0022	0.0023	0.0031	0.0037
FI[D]	0.00	0.00	0.23	0.23	0.26	0.34	0.40
Gene	*FBXW7*	*FBXL5*	*FBXO42*	*FBXO34*	*FBXW8*	*FBXO31*	*KDM2A*
MNi	9	12	10	1	7	3	11
N	2183	2825	2297	214	1328	532	1321
MNi/N	0.0041	0.0042	0.0044	0.0047	0.0053	0.0056	0.0083
FI	0.45	0.46	0.47	0.51	0.57	0.61	0.91
Gene	*FBXL13*	*FBXL7*	*FBXO25*	*SKP2*	*FBXW12*	*FBXL10*	*FBX043*
MNi	15	7	12	9	9	1	4
N	1723	801	1327	986	825	82	320
MNi/N	0.0087	0.0087	0.0090	0.0091	0.0109	0.0122	0.0125
FI	0.95	0.95	0.99	0.99	1.19	1.33	1.36
Gene	*FBX041*	*FBXO22*	*FBXL14*	*FBXL20*	*FBXO40*	*FBXO20*	*FBXL22*
MNi	6	1	27	9	8	7	10
N	470	75	2000	636	557	402	534
MNi/N	0.0128	0.0133	0.0135	0.0142	0.0144	0.0174	0.0187
FI	1.39	1.45	1.47	1.54	1.56	1.90	2.04
Gene	*FBXO32*	*FBXO9*	*FBXL3*	***FBXO2***	***FBXO17***	***FBXO38***	***FBXL19***
MNi	6	11	10	15	11	15	12
N	318	564	499	685	499	670	528
MNi/N	0.0189	0.0195	0.0200	0.0219	0.0220	0.0224	0.0227
FI	2.06	2.12	2.18	2.39	2.40	2.44	2.48
Gene	***FBXO11***	***FBXW9***	***FBXL17***	***FBXW11***	***FBXW2***	***FBXO3***	***FBXO36***
MNi	8	23	6	10	9	23	8
N	349	955	247	378	271	687	237
MNi/N	0.0229	0.0241	0.0243	0.0265	0.0332	0.0335	0.0338
FI	2.50	2.62	2.65	2.88	3.62	3.65	3.68
Gene	***FBXO30***	***FBXO24***	***FBXO39***	***FBXW5***	***FBXO18***	***FBXW4***	***CCNF***
MNi	4	17	2	13	10	10	43
N	117	497	57	321	239	235	993
MNi/N	0.0342	0.0342	0.0351	0.0405	0.0418	0.0426	0.0433
FI	3.72	3.73	3.82	4.41	4.56	4.64	4.72
Gene	***FBXO27***	***FBXO16***	***FBXL15***	***FBXW10***	***FBXL2***	***FBXO45***	***FBXO7***
MNi	4	12	7	8	17	40	8
N	91	273	148	152	323	744	144
MNi/N	0.0440	0.0440	0.0473	0.0526	0.0526	0.0538	0.0556
FI	4.79	4.79	5.15	5.73	5.73	5.86	6.05
Gene	***FBXO6***	***FBXL18***	***FBXL12***	***FBXL8***	***FBXO8***	***FBXL16***	***FBXO10***
MNi	9	9	16	23	17	8	6
N	162	139	194	248	174	78	51
MNi/N	0.0556	0.0647	0.0825	0.0927	0.0977	0.1026	0.1176
FI	6.05	7.05	8.98	10.10	10.64	11.17	12.82

[A]Putative CIN genes (bold) increase MN formation > 2× the standard deviation above si*GAPDH*.
[B]Number of MNi.
[C]Number of MNi normalized to number of nuclei (N).
[D]Fold increase in MNi/N (vs. si*GAPDH* (0.0092 MNi/N)).

Table S5-5. MN Enumeration Reveals F-box Putative CIN Genes in HCT116 Screen #2

Gene[A]	*FBXO22*	*EMI1*	*BTRC*	*FBXO43*	*FBXO11*	*FBXL21*	*FBXO15*
MNi[B]	0	1	17	5	4	15	2
N	133	221	3506	854	654	1894	232
MNi/N[C]	0.0000	0.0045	0.0048	0.0059	0.0061	0.0079	0.0086
FI[D]	0.00	0.41	0.44	0.53	0.55	0.72	0.78
Gene	*FBXO34*	*FBXL6*	*FBXW9*	*FBXL10*	*FBXO31*	*FBXL5*	*FBXL12*
MNi	1	15	28	4	16	46	20
N	114	1614	2928	412	1646	4136	1664
MNi/N	0.0088	0.0093	0.0096	0.0097	0.0097	0.0111	0.0120
FI	0.79	0.84	0.87	0.88	0.88	1.01	1.09
Gene	*FBXW11*	*FBXL16*	*FBXO42*	*FBXO41*	*FBXL4*	*FBXO2*	*FBXO46*
MNi	18	10	52	4	7	27	29
N	1494	823	4120	316	541	1914	2049
MNi/N	0.0120	0.0122	0.0126	0.0127	0.0129	0.0141	0.0142
FI	1.09	1.10	1.14	1.15	1.17	1.28	1.28
Gene	*KDM2A*	***FBXL17***	***FBXO39***	***FBXO8***	***FBXO25***	***FBXW5***	***FBXO3***
MNi	45	25	1	19	54	5	27
N	3136	1632	64	1210	3328	306	1652
MNi/N	0.0143	0.0153	0.0156	0.0157	0.0162	0.0163	0.0163
FI	1.30	1.39	1.41	1.42	1.47	1.48	1.48
Gene	***FBXO28***	***FBXL3***	***FBXL20***	***FBXO20***	***FBXW8***	***FBXL22***	***FBXO27***
MNi	7	9	25	19	26	19	4
N	425	541	1494	1055	1440	1031	213
MNi/N	0.0165	0.0166	0.0167	0.0180	0.0181	0.0184	0.0188
FI	1.49	1.51	1.51	1.63	1.63	1.67	1.70
Gene	***FBXL14***	***FBXO4***	***FBXO33***	***FBXL13***	***FBXW7***	***FBXL15***	***FBXO17***
MNi	62	4	3	43	50	8	32
N	3241	199	147	2077	2352	359	1418
MNi/N	0.0191	0.0201	0.0204	0.0207	0.0213	0.0223	0.0226
FI	1.73	1.82	1.85	1.87	1.92	2.02	2.04
Gene	***FBXL7***	***FBXO9***	***FBXW2***	***FBXW10***	***FBXW4***	***FBXO32***	***FBXW12***
MNi	60	39	22	4	6	26	102
N	2427	1476	827	147	218	920	3102
MNi/N	0.0247	0.0264	0.0266	0.0272	0.0275	0.0283	0.0329
FI	2.24	2.39	2.41	2.46	2.49	2.56	2.98
Gene	***FBXO18***	***FBXO44***	***FBXO6***	***CCNF***	***FBXL19***	***FBXO45***	***FBXO30***
MNi	29	6	13	58	36	69	11
N	853	167	355	1577	960	1806	249
MNi/N	0.0340	0.0359	0.0366	0.0368	0.0375	0.0382	0.0442
FI	3.08	3.25	3.31	3.33	3.39	3.46	4.00

Supporting Table S5-5 *Continued*. MN Enumeration Reveals F-box Putative CIN Genes in HCT116 Screen #2

Gene	*FBXO38*	*FBXL2*	*FBXL18*	*SKP2*	*FBXL8*	*FBXO24*	*FBXO16*
MNi	17	17	29	34	33	65	39
N	353	312	532	622	590	1150	635
MNi/N	0.0482	0.0545	0.0545	0.0547	0.0559	0.0565	0.0614
FI	4.36	4.93	4.93	4.95	5.06	5.11	5.56
Gene	***FBXO7***	***FBXO10***	***FBXO40***				
MNi	55	4	19				
N	893	59	147				
MNi/N	0.0616	0.0678	0.1293				
FI	5.57	6.13	11.70				

[A]Putative CIN genes (bold) increase MN formation > 2× the standard deviation above si*GAPDH*.
[B]Number of MNi.
[C]Number of MNi normalized to number of nuclei (N).
[D]Fold increase in MNi/N (vs. si*GAPDH* (0.0111 MNi/N)). Note: Conditions with fewer than 40 nuclei were excluded.

Table S5-6. Prioritized List of 16 F-box Putative CIN Genes

Ranking[A]	Putative CIN Gene	High-Content Screen #1		High-Content Screen #2	
		NA Assay[B]	MN Assay[C]	NA Assay[B]	MN Assay[C]
1	*FBXO10*	2/49 (1.44)	1/32 (12.82)	4/58 (1.30)	2/44 (6.13)
2	*FBXO6*	12/49 (1.27)	8/32 (6.05)	9/58 (1.26)	15/44 (3.31)
3	*FBXL8*	24/49 (1.17)	4/32 (10.10)	37/58 (1.07)	6/44 (5.06)
4	*FBXO24*	22/49 (1.19)	20/32 (3.73)	12/58 (1.23)	5/44 (5.11)
5	*FBXL2*	23/49 (1.19)	11/32 (5.73)	33/58 (1.08)	9/44 (4.93)
6	*FBXL19*	18/49 (1.21)	29/32 (2.48)	6/58 (1.28)	13/44 (3.39)
7	*FBXO8*	11/49 (1.27)	3/32 (10.64)	26/58 (1.13)	42/44 (1.42)
8	*FBXO7*	29/49 (1.13)	7/32 (6.05)	52/58 (1.03)	3/44 (5.57)
9	*FBXO17*	15/49 (1.23)	31/32 (2.40)	5/58 (1.28)	25/44 (5.11)
10	*FBXO27*	16/49 (1.23)	13/32 (4.79)	32/58 (1.08)	32/44 (1.70)
11	*FBXO45*	45/49 (1.05)	9/32 (5.86)	42/58 (1.06)	12/44 (3.46)
12	*FBXL15*	39/49 (1.09)	12/32 (5.15)	30/58 (1.09)	26/44 (2.02)
13	*CCNF*	36/49 (1.10)	15/32 (4.72)	56/58 (1.02)	14/44 (3.33)
14	*FBXO38*	37/49 (1.10)	30/32 (2.44)	41/58 (1.06)	10/44 (4.36)
15	*FBXW2*	48/49 (1.03)	24/32 (3.62)	48/58 (1.04)	22/44 (2.41)
16	*FBXO3*	34/49 (1.10)	23/32 (3.65)	50/58 (1.04)	39/44 (1.48)

[A]Overall ranking of 16 F-box putative CIN genes.
[B]Putative CIN gene rank based on median NA changes in either screen with fold change (vs. si*GAPDH*) in brackets.
[C]Putative CIN gene rank based on MN increases in either screen with fold change (vs. si*GAPDH*) in brackets.

Table S5-7. *SKP1* Silencing Induces Increases in Mean Centrosome Volumes and the Number of Centriolar Foci per Centrosome

Experiment	Features	Conditions		FI[A]
		si*GAPDH*	si*SKP1*	
1	Mean CV[B]	1.29	4.39	3.4
	No. Cenexin Foci[C]	1.00	2.78	2.8
2	Mean CV	1.26	4.96	3.9
	No. CCP110 Foci[D]	1.68	7.02	4.2
3	Mean CV	1.36	4.18	3.1
	No. Centrin Foci[E]	2.34	7.83	3.3

[A]Fold increases in centrosome volume or centriolar foci number in si*SKP1* cells (vs. si*GAPDH*).
[B]Mean centrosome volume (CV).
[C]Mean number of Cenexin foci/centrosome.
[C]Mean number of CCP110 foci/centrosome.
[C]Mean number of Centrin foci/centrosome.

5.5.2. Supporting Figures

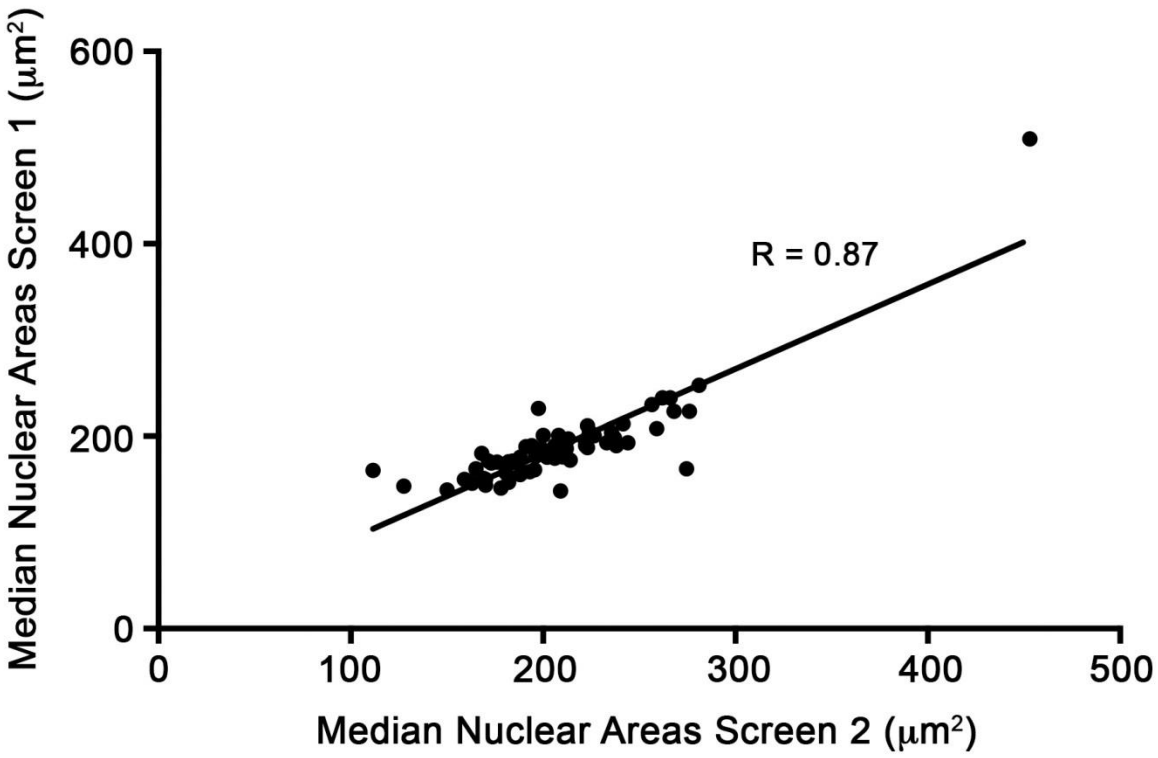

Figure S5-1. NA Screens Exhibit High Reproducibility and are Highly Correlated
Dot plot displaying the strong positive correlation between median NA values from the high-content screening replicates in HCT116. Each point represents the median NA calculated for each of the 68 F-box protein encoding genes in Screen 1 and 2.

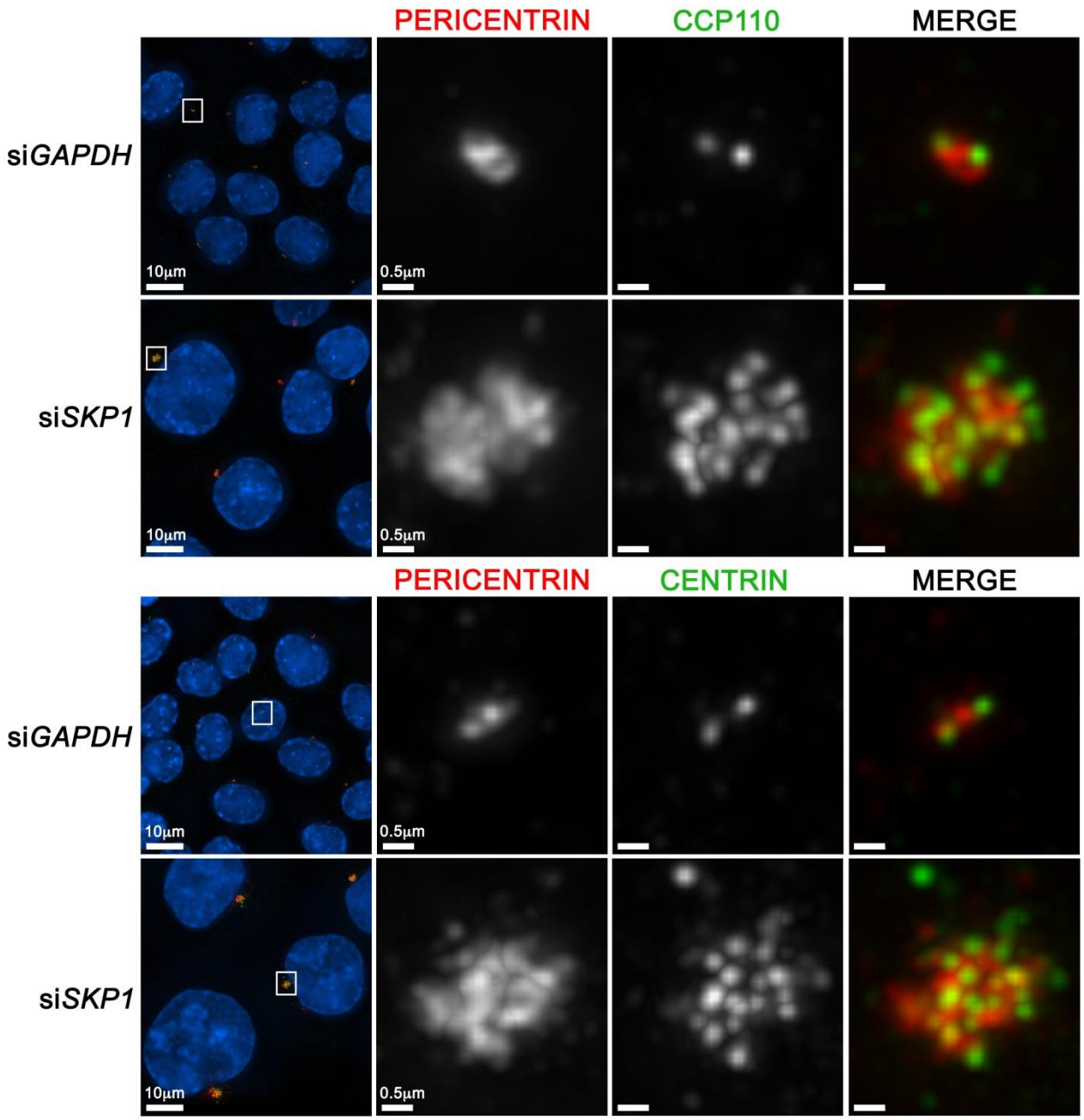

Figure S5-2. *SKP1* Silencing Increases Centrosome Volume and Centriole Foci Number in HCT116

Deconvolved 3D fluorescence microscopy images (left) showing *GAPDH* and *SKP1* silenced interphase nuclei (blue) and centrosome markers Pericentrin (red) and either CCP110 (green, top) or Centrin (green, bottom). Centrosomes in white bounding boxes are magnified to show increases in centrosome size (Pericentrin) as well as amplification of centriolar signals (CCP110 and Centrin) following *SKP1* silencing relative to controls.

CHAPTER 6: DISCUSSION

6.1.0. Summary and Conclusions

This thesis discusses the development and utilization of a novel high-content, image-based screen to detect CIN-associated phenotypes for the purpose of identifying genes that normally function to maintain chromosome stability (*i.e.* CIN genes). This approach permits the rapid assessment of large gene sets and expedites the identification of novel human CIN genes that may have important implications for oncogenesis. In Chapter 3, nuclear volume/NA changes and increases in MN formation were explored as surrogate markers for chromosomal changes that are indicative of CIN. Through direct silencing tests of the established human CIN gene *SMC1A*, significant changes in nuclear volumes and MN formation were detected and found to correspond with si*SMC1A*-associated chromosomal defects. As NA changes correlate with nuclear volume changes, NA and MN enumeration assays were employed (as they are amenable to automated 2D image acquisition and analysis in high-content screens) to simultaneously assess a large number of genes for a potential role in CIN (*Chapters 4 and 5*).

In Chapter 4, NA and MN enumeration assays were multiplexed in a high-content, microscopy-based screen of 164 human CIN candidate genes identified via cross-species approaches. Screening in two karyotypically stable cell lines (hTERT and HT1080), identified 148 putative human CIN genes. A subset of 10 prioritized putative CIN genes, *ARL2*, *BUB3*, *DSN1*, *GARS*, *GART*, *NUF2*, *PIGS*, *SHMT2*, *SPC24*, and *SKP1* were validated by traditional cytogenetic approaches and gene silencing was associated with increases in chromosomal aberrations, including numerical, structural and cohesion defects in hTERT and HCT116 cells. As CIN is a known driver of oncogenesis, diminished expression or function of each of the above 10 genes can potentially contribute to neoplastic transformation and cancer

development/progression in humans. Due to the extensive CIN phenotypes observed in *SKP1* silenced cells and the role of SKP1 in SCF-mediated proteasomal degradation of numerous downstream substrates, the mechanisms underlying CIN in *SKP1* silenced HCT116 cells were further investigated (*Chapter 5*).

As described in Chapter 5, the newly developed high-content screening approach was employed against a distinct gene library to determine which F-box protein encoding genes (and by extension which SCF complexes), phenocopy si*SKP1*-associated CIN phenotypes when silenced. As 53 F-box protein encoding putative CIN genes, including *EMI1* (*FBXO5*), *FBXL7*, and *SKP2* (*FBXL1*), induced NA changes or MN increases following silencing, misregulation of 53 different SCF complexes including SCF^{EMI1}, SCF^{FBXL7}, and SCF^{SKP2}, may contribute to the CIN phenotypes observed in *SKP1* silenced cells. Indeed, the genetic/phenotypic rescue experiment determined that co-silencing *SKP1* and the gene encoding the SCF^{SKP2} substrate, CCNE1 (that is increased in *SKP1* silenced cells), reduced si*SKP1*-associated CIN phenotypes including NA, MN, and chromosomal changes, indicating that increased CCNE1 levels contribute to CIN. *SKP1* and *EMI1* silencing both resulted in increases in CENPA and HJURP levels, suggesting that SCF^{EMI1} may exhibit a previously uncharacterized role in centromeric protein regulation. The SCF^{FBXL7} complex substrate and anti-apoptotic protein, Survivin, was also aberrantly increased in *SKP1* silenced cells. CCNE1, CENPA, HJURP, and Survivin are all considered oncogenic drivers that are frequently overexpressed in cancer and correlate with CIN, drug resistance, disease recurrence and poor patient outcomes[86,87,248,260,265,266]. SKP1 silencing also induced replication stress (RPA foci), DNA damage (γH2AX foci), and centrosomal defects, which are mechanisms known to underlie CIN (*see Sections 1.4.0-6*) that are implicated in cancer development and progression[124,250].

It is apparent from the results presented in this thesis, that a high-content screen designed to detect phenotypes associated with CIN (*i.e.* NA and MN changes) dramatically expedites the identification and characterization of novel human CIN genes, by providing a means by which to rapidly screen large numbers of candidate or suspected CIN genes. As CIN is an enabling feature of cancer, characterizing aberrant CIN genes and pathways is critical for better understanding the molecular mechanisms that underlie CIN and oncogenesis, which may provide insights into disease development, progression and treatment options. CIN genes and pathways may represent novel therapeutic targets that can be exploited in superior treatment approaches to help offset the devastating morbidity and mortality rates associated with cancer.

6.2.0. Benefits and Future Applications of a Multiplexed High-Content Image-Based Screen

The results presented in Chapters 4 and 5 highlight the utility of an image-based approach capable of simultaneously assessing a large number of genes. An image-based platform is beneficial as it allows for direct assessment of the phenotypic outcomes of gene silencing. For example, multinucleated cells were not originally evaluated in the high-content screen, but were subsequently detected and quantified within *NUF2* and *SPC24* silenced conditions, providing additional evidence for chromosome missegregation, cytokinesis defects, and CIN. Furthermore, image-based screening enables classification/prioritization of genes by CIN phenotype and severity (*e.g.* fold increase in MN formation) that may provide insight into protein function and the altered pathway(s) that underlie CIN within each condition. For example, large NA increases in the absence of MN formation may indicate endoreduplication, while extensive MN formation may be suggestive of chromosome breaks due to inadequate DNA damage repair. However, mechanism cannot be determined from phenotype alone, as numerical and structural CIN are

intricately linked, frequently occur within the same tumor cell, and often exhibit a causal relationship[55,267]. For example, DNA DSB (structural CIN) can occur as a result of forces acting on missegregated chromosomes (numerical CIN) that remain "trapped" within the cleavage furrow (*i.e.* intercellular bridge[268]) during cytokinesis[267]. Thus, subsequent validation experiments are needed to fully elucidate the altered pathways responsible for CIN.

In future studies, this image-based CIN screen can easily be adapted to address specific experimental questions. For example, Hoechst (DNA counterstain) can be multiplexed with fluorescence-based labeling (*e.g.* CENPA, RPA, γH2AX, or WGA) to glean additional mechanistic information. In Chapter 5, immunofluorescent CENPA labelling was performed to assess centromeric protein aberrations following F-box gene silencing. In future experiments, immunofluorescent CENPA signal could be further examined by assessing the presence or absence of CENPA foci within MNi. MNi that harbour centromeric CENPA foci are indicative of whole chromosome missegregation and numerical CIN. Conversely, MNi that lack centromeres are suggestive of acentric chromosome fragments derived from chromosome breakages and/or DNA replication or damage repair defects. Co-immunofluorescent RPA or γH2AX labeling would also provide insights into whether DNA replication or DNA damage repair defects promote CIN in each condition. Labeling of the cell membrane using fluorescently tagged WGA, would also allow for rapid, automated detection of multinucleated cells in a high-content screen, as was performed above in *NUF2* and *SPC24* silenced conditions. These multiplexed approaches would provide additional insights into the altered mechanisms underlying CIN in each condition. Additionally, cells expressing a fluorescently tagged histone could be utilized in live-cell imaging to evaluate NA changes, MN increases, or mitotic defects as they occur over the time-course of the experiment. If alterations in a specific protein or

pathway are suspected, stable cell lines expressing a fluorescently tagged protein (*e.g.* RPA) could be generated to monitor changes in real time. Importantly, this screen can easily be expanded into a variety of adherent cell types as was performed above (*e.g.* HT1080, hTERT and HCT116) to investigate the cell- or cancer-specific impact of gene silencing. It is also possible to expand the screen beyond an siRNA-based system to assess Clustered Regularly Interspaced Short Palindromic Repeats (CRISPR)/CRISPR-associated Protein 9 (Cas9) knockouts (homozygous or heterozygous), mutated or overexpressed genes, and chemical libraries, to evaluate the impact that numerous different conditions/treatments have on chromosome stability. Overall, the screening results of Chapters 4 and 5 serve as proof-of-principle that this approach detects CIN phenotypes and is amenable to a myriad of gene sets, cell lines, and experimental applications. In the future, analogous experiments can be scaled-up to genome-wide screens, which will be instrumental in identifying a comprehensive list of human CIN genes, predicted to consist of up to 2,300 genes (*see Section 1.3.0*).

The assays established in this thesis serve as valuable tools that can be multiplexed with techniques, including FISH, to glean additional insights into CIN, in a variety of cancer contexts and samples. For example, the NA assay has since been multiplexed with interphase centromeric FISH probe enumeration by Penner-Goeke *et al*[269] to assess the temporal dynamics of CIN in primary epithelial ovarian cancer patient samples acquired from ascites (*i.e.* cancer cells collected by paracentesis from fluid that can accumulate within the peritoneal cavity[270]). This combinatorial approach revealed that CIN, as measured by changes in NAs and in the number of FISH probe signals per nucleus, is both present and dynamic in serial patient samples and increases in women with drug resistant disease[269]. This enables researchers to monitor CIN phenotypes over the disease course and assess changes that occur with patient treatment and

response, or disease progression/relapse. This approach could be adapted in future studies to assess CIN in both solid and liquid cancer biopsies or in circulating tumor cells collected from peripheral blood. Changes in CIN detected by these assays may ultimately be employed as a novel biomarker of disease progression, treatment response, and/or patient prognosis. Thus, the assays developed in this thesis have enabled and will continue to expedite future CIN studies in cell lines and patient samples.

The putative CIN genes identified in Chapters 4 and 5, serve as valuable resources that can be referenced in future studies to expedite the identification and characterization of CIN genes, beyond those discussed in this study. For example, in Chapter 4, *KIF11* (encodes a microtubule motor protein required for spindle pole dynamics during mitosis[271]) was identified as a strong putative CIN gene in hTERT that induced a large 1.8-fold increase in median NA, a significant change in NA frequency distribution, and a 5-fold increase in MN formation following silencing. *KIF11* is altered (*i.e.* copy number alterations, somatic mutations or misexpression) in numerous cancer types[155,156], suggesting that KIF11 misregulation or aberrant spindle pole dynamics may contribute to cancer development and progression. Based on these findings, Asbaghi *et al*[206] pursued validation of *KIF11* as a CIN gene in hTERT and HCT116. Both *KIF11* silencing and inhibition by Monastrol induced increases in NAs, MNi, DNA content, and chromosome numbers in both cell types, validating *KIF11* as a human CIN gene that may be implicated in oncogenesis[206]. In the past, KIF11 inhibitors have been explored as a novel cancer treatment strategy, with modest therapeutic success[272,273]. As diminished KIF11 expression and function induces CIN (an oncogenic driver) this may potentially explain the limited efficacy of Monastrol and other KIF11 inhibitors in the clinic. Thus, this study highlights the value of identifying and characterizing CIN genes, as discussed below, to better understand the fundamental mechanisms

that can contribute to CIN and oncogenesis, and to translate this information into clinically relevant contexts to inform treatment decisions.

6.3.0. Aberrant Biological Pathways that Underlie CIN in *SKP1* Silenced Cells

As hypomorphic expression or function of the invariable SCF adaptor protein SKP1, has the potential to impact numerous downstream CIN- and cancer-associated proteins and pathways, the biological implications of *SKP1* silencing was a major focus of this thesis. The high-content screen (*Chapter 5*) identified 53 F-box genes, including *EMI1 FBXL7*, and *SKP2*, that induced CIN phenotypes following silencing. Thus, the corresponding SCF complexes (Figure 6-1A) may be misregulated and contribute to CIN (Figure 6-1B). Although the substrates and functions of SCF^{SKP2} are generally well characterized, much less is known about SCF^{FBXL7} and SCF^{EMI1} (Table 6-1), emphasizing the need to further investigate the role of F-box proteins/SCF complexes in CIN and oncogenesis. *SKP1* silencing induced mislocalization and aberrant increases in the levels of centromeric proteins CENPA and HJURP (*Section 6.2.1*), increases in SCF^{FBXL7} and SCF^{SKP2} substrates Survivin and CCNE1, as well as DNA replication stress (*Section 6.2.2*), DNA damage (*Section 6.2.3*), and centrosome misregulation (*Section 6.2.4*) (Figure 6-1B), as discussed below. Thus, the CIN phenotypes observed in *SKP1* silenced cells are likely an accumulation of multiple misregulated SCF complexes that normally function by regulating substrates involved in key biological pathways that maintain chromosome stability.

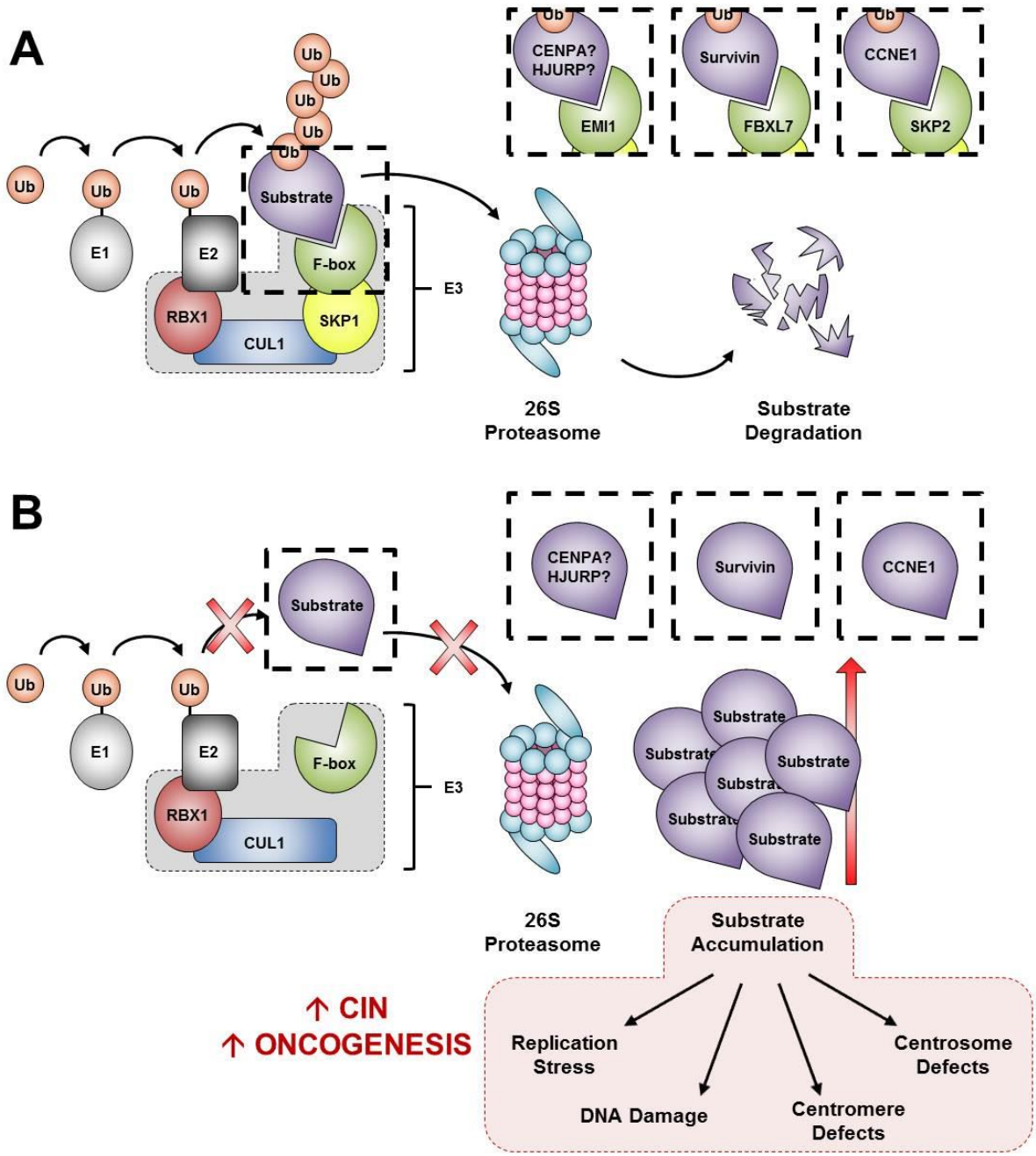

Figure 6-1. Regulation of Substrate Turnover by the SCF Complex

(A) Schematic illustrating SCF-mediated polyubiquitination and proteasomal degradation of downstream substrates. Bounding boxes provide examples of F-box proteins that normally function to maintain chromosome stability by regulating the indicated substrates (*discussed in text*). ***(B)*** Model illustrating how *SKP1* silencing can impair SCF-mediated protein turnover leading to substrate (bounding boxes) accumulation, misregulation of key biological pathways, CIN and oncogenesis. E1, E1 ubiquitin-activating enzyme; E2, E2 ubiquitin-conjugating enzyme; E3, E3 ubiquitin-protein ligase; Ub, Ubiquitin; EMI1, Early Mitotic Inhibitor 1; CENPA, Centromeric Protein A; HJURP, Holliday Junction Recognition Protein; FBXL7, F-Box and Leucine Rich Repeat Protein 7; SKP2, S-Phase Kinase Associated Protein 2; CCNE1, Cyclin E1; RBX1, Ring-Box 1; CUL1, Cullin 1; SKP1, S-Phase Kinase Associated Protein 1.

Table 6-1. Substrates and Functions of SCF^{SKP2}, SCF^{FBXL7}, and SCF^{EMI1}

F-box Protein	Substrates	Biological Functions of Substrates
SKP2 (FBXL1)[274]	BRCA2	DNA Repair
	CDK9	Kinase, Transcription Elongation
	CDT1	pre-RC, DNA Replication
	CCNA	Cyclin, Cell Cycle
	CCND1	Cyclin, Cell Cycle
	CCNE1	Cyclin, Cell Cycle, DNA and Centrosome Replication
	E2A	Transcription Factor, T- and B-cell Development
	E2F1	Transcription Factor, Cell Cycle
	FOXO1	Transcription Factor, Cell Growth/Proliferation
	MEF	Transcription Factor, Cell Growth/Proliferation
	MKP1	Phosphatase, ERK Signaling
	KMT2A	Histone Methyltransferase
	MYBL2	Transcription Factor, Cell Growth/Proliferation
	MYC	Transcription Factor, Cell Growth/Proliferation
	ORC1	DNA Replication
	P21	CDK Inhibitor, Cell Cycle
	P27	CDK Inhibitor, Cell Cycle
	P57	CDK Inhibitor, Cell Cycle
	RAG2	Recombination
	RASSF1	Microtubule Dynamics
	P130	Transcription Repressor, Cell Cycle
	SMAD4	Transcription Factor, BMP/TGF Signaling
	TAL1	Transcription Factor, Erythroid Differentiation
	TOB1	Transcription Factor, Cell Growth/Proliferation
	USP18	de-Ubiquinating Enzyme, Interferon signaling
FBXL7[248,275]	AURKA	Mitotic Spindle
	Survivin	Apoptosis
EMI1 (FBXO5)[240]	*Unknown*	APC/C Inhibitor

[A]BRCA2, Breast Cancer 2; CDK9, Cyclin Dependent Kinase 9; CCNA, Cyclin A; CCND1, Cyclin D1; E2A, Transcription Factor 3; E2F, Transcription Factor 1; FOXO1, Forkhead Box O1; MEF, Myeloid Elf-1-Like Factor; MKP1, Mitogen-Activated Protein Kinase Phosphatase 1; KMT2A, Lysine Methyltransferase 2A; MYBL2, MYB Proto-Oncogene Like 2; MYC, MYC Proto-Oncogene; P21, Cyclin Dependent Kinase Inhibitor 1A; P27, Cyclin Dependent Kinase Inhibitor 1B; P57, Cyclin Dependent Kinase Inhibitor 1C; RAG2, Recombination Activating 2; RASSF1, Ras Association Domain Family Member 1; P130, RB Transcriptional Corepressor Like 2; SMAD4, SMAD Family Member 4; TAL1, T-Cell Acute Lymphocytic Leukemia 1; TOB1, Transducer of ERBB2 1; USP18, Ubiquitin Specific Peptidase 18; AURKA, Aurora Kinase A; ERK, Mitogen-Activated Protein Kinase 1; BMP/TGF, Bone Morphogenetic Protein/Transforming Growth Factor. (Table adapted from Skaar *et al*[274]).

6.3.1. *SKP1* and *EMI1* Silencing Induce Centromeric Protein Aberrations

Assembly of a mature kinetochore complex is critical for proper kinetochore-microtubule attachment and chromosome alignment/segregation. Histone octamers containing the histone H3 variant, CENPA, epigenetically define the centromere and form the foundation for assembly of the inner (*e.g.* CCAN) and outer (*e.g.* KMN) kinetochore complexes[75] (*see Section 1.4.2* [Figure 1-2]). CENPA-containing histones can be integrated ectopically throughout the genome, but are readily removed and degraded by an SCF complex that has yet to be identified in humans[73]. In this study, both *SKP1* and *EMI1* silencing increased CENPA levels and induced diffuse CENPA labeling in interphase nuclei. Thus, SCF^{EMI1} likely plays an important role in CENPA turnover and centromeric localization. It remains to be determined whether SCF^{EMI1} regulates CENPA directly or indirectly by regulating CENPA-interacting proteins like HJURP (also increased in *SKP1* and *EMI1* silenced cells). Future co-immunoprecipitation experiments could determine whether CENPA or HJURP directly interacts with EMI1. CENPA overexpression drives ectopic, non-centromeric integration events[75], which could also be validated in *SKP1* silenced cells using chromatin immunoprecipitation assays. Ectopic CENPA can sequester centromere/kinetochore proteins and prevent mature kinetochore complex assembly at the centromere[75]. As CENPA is critical for recruitment of the SAC protein, BUBR1, cells with mislocalized or aberrant CENPA may also exhibit SAC defects that permit cells with microtubule mal-attachments to proceed through mitosis[276]. Understandably, overexpression of HJURP and/or CENPA drives CIN and oncogenesis[83-89] (*see Section 1.4.2*). Thus, further characterizing the regulation of cancer-relevant proteins like CENPA and HJURP by the SCF complex is critical, as it may reveal novel biomarkers or therapeutic vulnerabilities. For example, breast cancers that overexpress HJURP

are more responsive to radiotherapy[86], which may also apply to cancers with misregulated CENPA, SKP1, EMI1 or other SCF components (*e.g.* CUL1 or RBX1).

6.3.2. *SKP1* and *EMI1* Silencing Induce DNA Replication Stress and DNA Damage

As many of the proteins involved in DNA replication are SCF substrates (*e.g.* ORC1[277], CDT1[278], CDH1[279], CCNE1[280]), it is not unexpected that diminished *SKP1* expression negatively impacts DNA replication and induces numerical and structural CIN. Both *SKP1* and *EMI1* silencing result in replication stress (RPA foci) and DNA damage (γH2AX foci), thus, misregulation of SCF^{EMI1} likely contributes to replication defects. However, the substrates regulated by SCF^{EMI1} are currently unknown (Table 6-1), and the role of SCF^{EMI1} in DNA replication is poorly understood. Subsequent studies designed to identify and characterize the downstream substrates of SCF^{EMI1} (*e.g.* co-immunoprecipitation studies) will be critical for better understanding SCF^{EMI1} function. Regardless, diminished *EMI1* expression is known to drive DNA re-replication/endoreduplication (increasing the number of cells that harbour > 4C DNA content) and induce DNA damage in various cell types including HCT116[240]. Extensive endoreduplication can result in nucleotide deficiency, replication fork stalling (*i.e.* replication stress), DNA damage and CIN, which may also account for the increases in RPA and γH2AX foci in *SKP1* silenced cells. Interestingly, structural CIN derived from replication stress in CRC cells has also been shown to induce chromosome missegregation in mitosis (*i.e.* numerical CIN)[55]. In fact, CRC cells exhibiting replication stress or stalled replication forks that are supplemented with nucleosides, show reduced DNA damage and chromosome missegregation[55], although the underlying mechanism by which replication stress causes numerical CIN is poorly understood. In subsequent experiments, *SKP1* and *EMI1* silenced cells could be supplemented with nucleosides to assess whether replication stress, DNA damage (*i.e.* ssDNA [RPA foci] and

DSB [γH2AX foci]), or structural and numerical CIN defects are alleviated. This would further delineate the proportion of structural and numerical CIN defects in *SKP1* and *EMI1* silenced cells that are attributed to replication stress.

The replication defects observed in *SKP1* silenced cells are unlikely attributed solely to SCF^{EMI1}, as numerous DNA replication proteins are regulated by SCF complexes[277-280]. For example, overexpression of the SCF^{SKP2} substrate CCNE1 aberrantly accelerates the G1/S transition and impairs DNA replication[252]. CCNE1 overexpression is reported to have dual, contradictory effects on replication, by both reducing DNA origin licensing and increasing origin firing[124]. More specifically, CCNE1 overexpression reduces MCM2-7 recruitment to replication origins during G1 (*see Section 1.4.5* [Figure 1-5]), impairing origin licensing. Thus, fewer replication origins are activated in S-phase, resulting in longer DNA replication tracks, increased fork stalling, abnormal ssDNA intermediates, and chromosome breakages[239,252]. Additionally, there are fewer licensed dormant origins available to fire in response to stalled or collapsed replication forks, further exacerbating replication stress and DNA damage[252]. CCNE1 overexpression in S-phase also drives replication origin firing and causes increased collisions between transcription and replication machinery, to induce replication stress and DNA damage[125]. Thus, misregulation of SCF^{SKP2} may also contribute to replication stress and DNA damage observed in *SKP1* silenced cells. Subsequent studies designed to assess how SCF misregulation contributes to replication stress, DNA damage, CIN, and oncogenesis may reveal novel vulnerabilities in cancer cells that can be therapeutically exploited (reviewed in Kitao *et al*[281]).

6.3.3. *SKP1* Silencing Drives Centrosomal Aberrations

Centrosome aberrations are frequently observed in cancer and are associated with CIN, disease recurrence, metastatic progression, and poor prognoses[108]. *SKP1* silencing induces increases in centrosome size, as indicated by increased volume of the PCM (*i.e.* immunofluorescent Pericentrin signal), as well as increases in the number of centriolar signals per centrosome (*i.e.* Cenexin, CCP110, and Centrin). In general, centrosome defects are typically classified as either numerical or structural[109] (*see Section 1.4.3*); however, distinguishing between the two categories can be challenging. Cancer cells often demonstrate adaptation to supernumerary (> 2) centrosomes (numerical defect) through centrosomal clustering, in order to generate a pseudo-bipolar mitotic spindle[275,276]. Centrosome clusters can increase PCM size, which may be erroneously classified as a structural defect. Co-immunofluorescent labeling of centrosomal and centriolar markers can help to mitigate this issue. For example, Cenexin is a sub-distal appendage protein of the mother centriole (*see Section 1.4.3* [Figure 1-3]) that produces a single focus per centrosome following immunofluorescent labelling[98]. As *SKP1* silencing induced increases in the number of Cenexin foci (as well as CCP110 and Centrin centriolar foci), in addition to increases in centrosome size, *SKP1* silencing likely induces a numerical centrosome defect. Numerical defects can arise from misregulation of the centrosome/centriole duplication cycle or regulatory factors (*e.g.* CCNE1[106]), *de novo* centriole assembly, mitotic slippage, or cytokinesis errors[109]. However, the numerical defects observed in si*SKP1* cells do not negate the possibility for concurrent structural defects, including changes in PCM structure or centriolar length.

Interestingly, human cells with supernumerary centrosomes exhibit CIN, but do not frequently undergo multipolar mitoses. In fact, live cell imaging of MCF7 (breast cancer cells)

and HT29 (CRC cells), revealed that cells with supernumerary centrosomes frequently missegregated chromosomes (every 2-5 divisions), but underwent multipolar mitoses only once every 50 or more divisions[277,278]. Indeed, cancer cells often cluster supernumerary centrosomes to maintain a pseudo-bipolar spindle[282,283] and minimize large-scale chromosome losses that may adversely impact cancer cell viability (*discussed in Section 6.6.0*). Cells with supernumerary centrosomes experience transient multipolar intermediates that promote merotelic attachments (*i.e.* one kinetochore is aberrantly attached to microtubules emanating from opposite poles). Merotelic attachments are not detected by the SAC, allowing cell division to proceed with lagging and missegregated chromosomes. As centromeric clustering appears to favor cancer cell viability[284,285], cancers with clustered centrosomes may be therapeutically susceptible to centrosome de-clustering compounds. In fact, *in vitro* studies in breast cancer cell lines have shown that treatment with the centrosome de-clustering compound 5-Nitro-N-(3-pyridinylmethyl)-2-furancarboxamide (CCCI-01), induces multipolar spindle formation, extensive CIN, and apoptosis[286]. Thus, treatment with CCCI-01 may help improve cancer specificity and reduce off-target toxicities, by killing cancer cells with diminished *SKP1* expression, defective SCF activity, and supernumerary centrosomes.

6.3.4. Defective SKP1/SCF Activity in Biological Pathways that are Indirectly Linked to CIN

This thesis primarily considers the role of the SCF complex in proteasomal degradation of downstream substrates by examining increases in the levels of known (*e.g.* CCNE1) and potential (*e.g.* CENPA) SCF substrates following *SKP1* silencing. However, emerging evidence indicates that the SCF complex can function in biological pathways beyond proteasomal degradation[287]. For example, the SCF^{FBXO28} serves as a transcriptional co-activator that

polyubiquitinates MYC and positively regulates the expression of MYC target genes[287]. *FBXO28* was identified as a putative CIN gene in this study, inducing significant NA increases following silencing (*see Chapter 5*). Conceptually, *SKP1* silencing can induce changes in downstream protein levels by interrupting SCF complexes that regulate both proteasomal degradation and gene transcription, adding a level of complexity to deciphering the biological impact of *SKP1* misregulation. This is further confounded by functional overlap between the various SCF complexes. For instance, SCF^{SKP2} regulates proteasomal degradation of MYC. Thus, SCF^{SKP2} misregulation due to *SKP1* silencing, may also impact MYC-driven gene expression profiles[288]. Future experiments characterizing changes in global gene expression and proteomic changes by microarray and mass spectrometry, respectively, would allow for a more exhaustive characterization of the impact that *SKP1* silencing has on CIN and oncogenesis, which may reveal novel pathways to exploit therapeutically in cancers harbouring altered SCF activity. As SKP1 is a component of the SCF complex, defects not only in specific F-box proteins, but in either of the remaining core SCF components, RBX1 and CUL1, are predicted to phenocopy the aberrant biology associated with *SKP1* silencing. Thus, future experiments analogous to those described above for *SKP1* should be performed for *RBX1* and *CUL1* to delineate their collective and specific roles in cell biology, CIN, and oncogenesis.

6.4.0. Misexpression of CIN Genes in Cancer

In Chapter 4, a large proportion of candidate genes (90%) were identified as putative CIN genes by at least one of the NA or MN enumeration assays. This high hit-rate was expected, given that the human candidates were initially identified from a biased list of budding yeast CIN genes[65]. *ARL2*, *BUB3*, *DSN1*, *GARS*, *GART*, *NUF2*, *PIGS*, *SHMT2*, *SPC24* and *SKP1* were

validated as CIN genes in HCT116 cells (*i.e.* induced numerical or structural chromosome changes following silencing). As CIN promotes the gain and loss of key cancer genes (*e.g.* apoptotic or DNA damage repair genes, oncogenes or tumor suppressors) and is a known driver of neoplastic transformation, CRC progression, and drug resistance[2-4], hypomorphic expression/function of the above genes is predicted to contribute to the development and progression of CRC. Indeed, data gleaned from cBioPortal[155,156] indicate that collectively, these 10 genes exhibit hypomorphic alterations (*e.g.* mutation, deletion, underexpression) in > 50% of CRCs, with *ARL2* (10%), *BUB3* (17%), *GART* (21%), *PIGS* (10%), and *SKP1* (14%) exhibiting the most frequent alterations (Table 6-2)[209]. Beyond CRC, these genes are also frequently altered in additional cancer types including lung[208], breast[210], prostate[157] and ovarian cancers[158] (Table 6-2). Thus, validation and characterization of the above genes must be expanded into additional, relevant cell lines, to assess the context-specific effects of gene silencing and investigate how hypomorphic alterations can promote CIN and oncogenesis in different cell/tissue types (*see Section 6.4.1*). For example, assessing diminished expression of the 10 CIN genes in fallopian tube secretory epithelial cells (the precursor to serous ovarian cancer[289,290]) would be valuable, as collectively, these genes are deleted and/or underexpressed in > 95% of ovarian cancers[158]. This would provide critical insights into the mechanisms underlying neoplastic transformation and progression of high-grade serous ovarian cancer.

Table 6-2. Deletion and Diminished Expression Frequencies of CIN Genes in Cancer

	Alteration Frequency in Cancer (%)[A]				
Gene	**Colorectal**	**Lung**	**Breast**	**Prostate**	**Ovarian**
ARL2	10.0	15.0	15.0	1.4	19.0
BUB3	17.0	28.0	18.0	15.0	34.0
DSN1	0.5	14.0	5.0	4.0	9.0
GARS	2.6	7.0	5.0	1.0	27.0
GART	21.0	33.0	9.0	6.0	33.0
NUF2	6.0	5.0	2.6	4.0	5.0
PIGS	10.0	13.0	22.0	9.0	79.0
SHMT2	5.0	17.0	8.0	5.0	18.0
SKP1	14.0	41.0	16.0	11.0	47.0
SPC24	5.0	51.0	9.0	6.0	37.0
Total[B]	**51.0**	**84.0**	**57.0**	**36.0**	**97.0**

[A]Alterations include DNA mutations or deletions (heterozygous and homozygous), or mRNA underexpression (z-score threshold < -2) according to published TCGA study data[157,158,208-210].
[B]Total values do not equal sum of individual alterations as some tumors exhibit alterations in multiple genes

As CIN genes function in biological pathways that must be precisely regulated to maintain chromosome stability in human cells (*see Sections 1.4.0-7*), it is possible that overexpression of the 10 CIN genes identified in this thesis, may also deregulate these biological mechanisms and induce CIN and oncogenesis. In fact, cBioPortal data[155,156] show that the above CIN genes are also amplified (DNA) and overexpressed (mRNA) in colorectal[209], lung[208], breast[210], prostate[157] and ovarian cancers[158] (Table 6-3). Hypermorphic high-content screens of candidate genes of interest will be critical for assessing whether gene overexpression (*e.g.* achieved by transfection of an overexpression plasmid), can also induce CIN and transformation/oncogenesis using the assays described below (*see Section 6.4.1*).

Table 6-3. Amplification and Overexpression Frequencies of CIN Genes in Cancer

	Alteration Frequency (%)[A]				
Gene	**Colorectal**	**Lung**	**Breast**	**Prostate**	**Ovarian**
ARL2	4.0	0.0	3.0	8.0	4.0
BUB3	4.0	0.9	4.0	4.0	4.0
DSN1	30.0	3.0	9.0	8.0	8.0
GARS	11.0	3.0	6.0	11.0	6.0
GART	4.5	1.3	8.0	6.0	2.5
NUF2	4.0	10.0	11.0	5.0	4.0
PIGS	7.0	2.2	6.0	2.8	1.6
SHMT2	8.0	5.0	6.0	2.8	4.0
SKP1	5.0	0.0	0.0	4.0	1.3
SPC24	5.0	0.0	1.3	4.0	10.0
Total[B]	**52.0**	**22.0**	**37.0**	**31.0**	**37.0**

[A]Alterations include DNA-level gene amplification and mRNA overexpression (z-score threshold > 2) from published TCGA study data[157,158,208-210].
[B]Total values do not equal sum of individual alterations as some tumors exhibit alterations in multiple genes

6.4.1. Future Studies to Evaluate Hypomorphic CIN Gene Expression in Oncogenesis

As CIN is considered an early event in oncogenesis[253,291-293], models of early disease development are needed to determine whether hypomorphic expression/function of *ARL2*, *BUB3*, *DSN1*, *GARS*, *GART*, *NUF2*, *PIGS*, *SHMT2*, *SPC24*, and *SKP1* can promote neoplastic transformation. For example, immortalized, non-transformed *TP53*-deficient fallopian tube or *TP53/APC*-deficient colonic epithelial cells could be employed in future studies as precursor cell models (to serous ovarian and CRC, respectively) to assess whether alteration of the genes of interest can synergize with the aberrant genetics of these cell lines, to induce transformation. Further, the effects of hypomorphic expression/function on classical cancer hallmarks including

increased proliferation, invasion, or migration in *in vitro* cellular models can be evaluated using the assays described below.

Short hairpin (sh)RNAs or homozygous and/or heterozygous gene knockouts (*e.g.* generated by CRISPR/Cas9 system) can be employed to evaluate the long-term effects of hypomorphic CIN gene expression on various phenotypes associated with oncogenesis. For example, changes in cellular proliferation rates could be assessed using real-time cellular analysis (RTCA). RTCA is a technique that measures electrical impedance from cells attached to the bottom of a microelectrode sensor array-coated plate. Electrical impedance increases proportionally as cells proliferate (and remain attached to the plate), which can be used to calculate proliferation rates/doubling times and assess viability[294]. Increases in cellular invasion and migration capacity can be quantified by a variety of assays including the transwell cell migration and invasion assay[295]. Cells that underexpress the gene of interest would be plated on top of a filter, and the rate and extent at which cells directionally migrate towards a chemoattractant across a filter (migration) or through a 3D matrix of extracellular components (*e.g.* fibronectin or collagen) can be measured using CIM (cell invasion/migration) plates on the RTCA instrument[295]. The proliferative and self-renewal capacity of genetically altered cells can also be assessed using ultra-low attachment plates, for the ability of these cells to form tumor spheres *in vitro*[296].

The above assays are limited in that they assess increases in oncogenic cell properties in an *in vitro* system. To more accurately assess the tumor-generating potential of the genetically altered cells *in vivo*, analyses must be transitioned to mouse models. For example, *SKP1* is heterozygously deleted in 47% of serous ovarian cancers[158]. Thus, an appropriate strategy would be to generate heterozygous *SKP1* knockout cells (*e.g.* in *TP53*-compromised fallopian tube

epithelial cells) using CRISPR/Cas9 techniques and injecting these cells into the intraperitoneal cavity of immunocompromised non-obese diabetic (NOD)/severe combined immunodeficient (SCID) mice. The ability of these cells to transform and generate tumors could be determined by surgical dissection and assessment of tumor formation (number and size), along with extent of tumor invasion, and degree of metastatic spread[296,297]. Overall, the above studies are critical for delineating the impact that misexpression of CIN genes has in a variety of cellular contexts and in the pathogenesis of cancer.

6.4.2. Immunohistochemical Assessment of CIN Gene Expression in Patient Samples

DNA sequencing and mRNA expression data from cBioPortal[155,156] indicate that *ARL2*, *BUB3*, *DSN1*, *GARS*, *GART*, *NUF2*, *PIGS*, *SHMT2*, *SPC24*, and *SKP1* exhibit copy number alterations (DNA) and are misexpressed (mRNA) in numerous cancer types (Tables 6-2 and 6-3 above). However, there is a paucity of information regarding alterations at the level of the protein. Evaluating whether the encoded proteins are misexpressed and/or mislocalized (suggestive of aberrant function), in patient tumor samples by immunohistochemistry (IHC), may provide insight into the functional or clinical relevance of these alterations. For example, *GART*, *BUB3*, and *SKP1* are deleted or underexpressed in 14-21% of CRCs[209]. IHC analyses would determine whether the encoded proteins are correspondingly altered in patient samples and potentially contribute to the pathogenesis of CRC. Ideally, microarrays would be generated with samples from normal tissue, precancerous lesions, and various stages of disease (*e.g.* Stages I-IV CRC), to evaluate changes in the protein of interest throughout disease progression and potentially identify pathogenic events in early versus late stage disease. Correlating expression/localization IHC data with clinical features (*e.g.* CIN status [determined by

centromeric FISH probe enumeration], tumor grade/stage, treatment response, or overall patient survival) may reveal valuable fundamental, diagnostic/prognostic, or therapeutic information.

Interestingly, genomic amplification and overexpression of *CCNE1* mRNA is an established mechanism known to drive CIN and malignant transformation of certain tumor types, including high-grade serous ovarian cancer, in which amplification/overexpression occurs in ~20% of cases[158]. The data presented in this thesis suggest that *SKP1* silencing and SCF misregulation (*i.e.* lack of protein degradation) underlie increases in CCNE1 that are predicted to phenocopy genomic *CCNE1* amplification. Thus, misregulation of CCNE1 at the level of the protein may be a novel pathogenic event leading to increased levels of CCNE1 in ovarian cancers that do not exhibit genomic *CCNE1* amplification. However, increases in CCNE1 protein levels as a result of defects in SKP1 or SCF-mediated proteasomal degradation, have not yet been explored. IHC analyses of SKP1 and CCNE1 in ovarian cancer patient samples would further define the relationship between SKP1 and CCNE1 in oncogenesis and in correlation with clinical features or CIN status, as described above. For example, IHC analyses could ascertain whether cancers with diminished SKP1 and increased CCNE1 constitute a particularly aggressive, chromosomally unstable cancer subtype. Other aberrations associated with diminished SKP1 or increased CCNE1 expression including centromeric, DNA replication, or centrosomal defects could also be assessed by IHC to further characterize the mechanisms that contribute to oncogenesis in patient samples. As more cancer- and CIN-associated SCF components (*e.g.* F-box proteins) and substrates are identified, IHC can be expanded to investigate the clinical relevance of these altered proteins in oncogenesis. Ultimately, IHC analyses will be essential to identify cancer biomarkers and/or therapeutic vulnerabilities that can be exploited in novel cancer treatments.

6.5.0. Strategies to Therapeutically Target CIN Genes and Pathways

6.5.1. Exploiting Synthetic Lethal Relationships for Cancer Treatment

Novel precision medicine approaches that specifically target cancer cells are needed to mitigate the potential for off-target toxicities associated with systemic chemotherapeutic regimens (*e.g.* FOLFOX or FOLFIRI for CRC treatment). Synthetic lethal (SL) approaches specifically exploit the genetic aberrations of cancer cells to induce highly-specific cancer cell killing[298]. Synthetic lethality occurs when two independently viable, loss-of-function protein or pathway alterations, induce cell death when they occur within the same cell[299]. The genetic defects of cancer cells (*e.g.* diminished CIN gene expression and/or encoded function), can therefore be exploited by downregulating or inhibiting a SL interactor (*i.e.* drug target) to induce cell death. This treatment strategy is best exemplified by the SL targeting of *BRCA1/2*-deficient HRR-defective ovarian cancers using inhibitors of the DNA repair protein poly(ADP-ribose) polymerase (PARP)[300] (*e.g.* Olaparib) to exacerbate DNA damage and induce cell death. Synthetic lethality offers the significant advantage that deletion or loss-of-function alterations involving tumor suppressors or genes involved in DNA damage repair, apoptosis, and chromosome stability can be therapeutically exploited. As CIN is a driver of neoplastic transformation and metastatic progression, CIN genes represent promising therapeutic targets that can be exploited in SL approaches to specifically target both primary and metastatic disease. SL therapies are also expected to reduce adverse side-effects and the development of secondary cancers, as they are inherently restricted to targeting cancer cells with defects in CIN genes. As the 10 CIN genes identified above are often underexpressed in cancer (Tables 6-2), they represent ideal candidates to exploit using SL approaches.

6.5.2. Targeting Diminished *SKP1* Expression in Novel Synthetic Lethal Approaches

SKP1 is deleted (heterozygous or homozygous) and/or underexpressed in various cancer types including 11-47% of colorectal, lung, breast, prostate and ovarian cancers (Table 6-4), and may be therapeutically actionable in SL approaches. This equates to > 20,000 CRC patients per year in Canada and the United States (Table 6-4) that may benefit from a *SKP1*-targeted SL therapy. These numbers increase dramatically when additional cancer types are included like lung, breast, prostate, and ovarian (Table 6-4), suggesting that SL targeting of *SKP1* may be an effective broad spectrum, precision medicine strategy for a myriad of cancer types.

Much of our current understanding of SL relationships is derived from genetic interaction studies in model organisms including *S. cerevisiae*. As many biological and CIN-associated pathways are evolutionarily conserved, SL interactors identified in yeast are often maintained and many have been validated in human cellular contexts[176,202,301]. *In silico* queries of the online genetic interaction database, BioGrid3.4[302], revealed that *CDC53*, *HSC82/HSP82*, *MAD2*, *MET22*, *PLC1*, and *SMC2* are SL interactors with *SKP1* in *S. cerevisiae*[302] (Table 6-5). Accordingly, an siRNA-based SL screen of the human orthologs and associated pathways of the SL interactors identified in yeast (Table 6-5) using approaches already established in the McManus laboratory[176,202,303], would be a valuable step towards identifying novel *SKP1* SL interactors in humans. As an alternate strategy, cancers that harbor hypomorphic defects in SL interactors of SKP1 can conceivably be therapeutically targeted in cancers with unaltered or overexpressed *SKP1,* using SKP1 or SCF inhibitors (*see Section 6.5.4*) in the future.

Table 6-4. Frequencies of *SKP1* Deletion and Underexpression in Cancer Cases

Cancer Type	Alteration Frequency (%)[A]	New Cases (Canada)[B]	New Cases (USA)[C]	Cases with *SKP1* Alt. (Canada)[D]	Cases with *SKP1* Alt. (USA)[E]
Colorectal	14.0	26,800	135,430	3,752	18,960
Lung	41.0	28,600	222,500	11,726	91,225
Breast	16.0	26,500	255,180	4,240	40,829
Prostate	11.0	21,300	161,360	2,343	17,750
Ovarian	47.0	2,800	22,440	1,316	10,547

[A]Frequency (%) of *SKP1* deletion (homozygous or heterozygous) and/or underexpression.
[B]Estimated number of Canadians diagnosed with the indicated cancer type in 2017[7].
[C]Estimated number of Americans diagnosed with the indicated cancer type in 2017[304].
[D]Number of newly diagnosed Canadian patients with tumors that harbour *SKP1* alterations.
[E]Number of newly diagnosed American patients with tumors that harbour *SKP1* alterations.
Note: Only published TCGA study data are included[157,158,209-211].

Table 6-5. Human Orthologs of *SKP1* SL Interactors Identified in Yeast

Yeast Gene[A]	Human Ortholog[B]	Protein Function[C]
CDC53[305]	*CUL1*	Scaffold component of the SCF complex required for ubiquitination and degradation of proteins
HSC82/HSP82[306]	*HSP90B*	Molecular chaperone regulates protein folding
MAD2[307]	*MAD2L1*	SAC component
MET22[298]	*BPNT1*	Metabolism: Production of adenosine 5-phosphosulfate and adenosine 5'-monophosphate
PLC1[308]	*PLC1*	Metabolism: Production of second messenger molecules diacylglycerol and inositol 1,4,5-trisphosphate
SMC2[309]	*SMC2*	Central component of the Condensin complex required for DNA compaction

[A]SL interactors of *SKP1* identified using BioGrid[302].
[B]Human orthologs identified using NCBI Protein Blast[310].
[C]Protein function information collected from GeneCards[149].

Screening genes involved in the heat shock response, SAC, or chromatin condensation (Table 6-5) for SL interactions with *SKP1*, may identify novel SL relationships and therapeutic avenues to pursue in subsequent studies. In this regard, Zaarur *et al*[311] showed that inhibition of the heat shock response by silencing Heat Shock Transcription Factor 1 (*HSF1*) sensitized cancer cell lines, including HCT116, to proteasomal inhibition by Bortezomib and induced synergistic cancer cell killing, which supports that the SL relationship between *HSC90* and *SKP1* observed in yeast, may be conserved in humans.

Importantly, genes/proteins within the same biological pathway often share SL interactors[176,202,301]. Thus, therapies that exploit one defective complex/pathway member are likely to be effective against additional defective members of the same complex/pathway. For example, PARP inhibitors that target the *BRCA1/2* defects underlying HRR-deficiencies (*see Section 1.4.6*) are also effective at killing cancer cells harboring defects in additional HRR genes, like *RAD51*, *ATM*, *ATR*, *CHEK1*, and *RAD54B*[312-319]. Thus, an ideal therapeutic strategy would be to identify targets and pathways that are SL with aberrant SKP1, SCF components (*e.g. CUL1*, *RBX1*, and F-box genes) and substrate turnover, to increase the potential number of patients that can therapeutically benefit from this approach. In Chapter 5, a total of 16 F-box genes were identified by both NA and MN enumeration screens in both experimental replicates, providing strong evidence to support these as CIN genes. According to cBioPortal[155,156], colorectal (59%)[209], lung (89%)[208], breast (90%)[210], prostate (54%)[157], and ovarian (99%)[158] cancers harbour alterations in at least one of these 16 F-box genes, suggesting that aberrant SCF activity is a common feature of cancer. Identifying novel SL interactors that are shared by core components of the SCF complex (*i.e. SKP1*, *CUL1*, and *RBX1*) and a subset of CIN-associated F-box proteins, would dramatically increase the proportion of cancer patients that may therapeutically benefit from novel SCF-exploiting SL approaches.

6.5.3. Chemical Inhibitors of SKP1

Currently, there are no small molecule inhibitors for SKP1 that are approved for clinical use in humans. Recently, > 21,000 compounds were screened using structure-based high-throughput virtual screening, and the 3 natural compounds liriodenine, evodiamine, and 6-O-angeloylplenolin (6-OAP) demonstrated significant binding energy affinities for SKP1[320]. Indeed, 6-OAP, isolated from the medicinal herb *Centipeda minima* could bind and sequester

SKP1, causing dissociation and degradation of specific F-box proteins including SKP2 and β-TRCP[320]. SKP1 inhibition induced anti-proliferative effects in murine lung cancer models, with minimal adverse effects, supporting SKP1 inhibition as a promising treatment strategy for lung cancers that overexpress SKP1 or oncogenic F-box proteins[320]. Importantly, 6-OAP did not induce increases in CCNE1, which may explain the anti-cancer activity and therapeutic benefit observed in lung cancer mouse models. However, the biological/mechanistic basis for this distinction between 6-OAP-treated and *SKP1* silenced cells remains unknown. Perhaps SKP1 inhibition simply reduced hypermorphic SKP1 activity back to basal, non-pathogenic levels. Despite the potential therapeutic applications of 6-OAP in cancer, these studies were performed recently and high-quality 6-OAP extracts (purity > 99.5%[320]) are not yet commercially available. In fact, despite repeated attempts, I was unable to successfully procure 6-OAP for testing purposes. This will presumably change in the future, as 6-OAP becomes more widely recognized, and increasingly employed in fundamental and translational studies.

Based on the findings of this thesis, SKP1 inhibitors must be employed with caution, as our data show that *SKP1* silencing (akin to inhibition) in CRC cells is associated with increased protein levels of oncogenes like CCNE1, Survivin, and CENPA, and underlies CIN. Thus, SKP1 inhibitors may cause off-target effects, induce CIN in non-cancerous cells (resulting in secondary cancers), or increase the rate of CIN in cancer cells, creating a more highly aggressive, drug resistant cancer. In fact, transgenic mouse models with hypomorphic SKP1 function in the T-cell lineage, show an initial proliferation lag, but exhibit extensive CIN, CCNE1 overexpression, neoplastic transformation, and ultimately, > 80% of mice succumb to T-cell lymphoma[154]. Thus, further fundamental studies are required to determine the genetic and cancer contexts in which SKP1 inhibition may be therapeutically beneficial (*e.g.* cancers that overexpress *SKP1*).

6.5.4. Emerging Therapeutic Strategies to Exploit the SCF Complex and Proteasomal Degradation

An emerging therapeutic strategy designed to exploit proteasomal degradation and the SCF complex is termed Targeted Protein Degradation. This approach enables targeting of the classically "untargetable" proteome (*e.g.* transcription factors such as MYC, scaffolding proteins and non-enzymatic proteins) through the use of Proteolysis Targeting Chimeras (PROTACs). PROTACs are heterobifunctional fusion proteins with two recruiting ligands connected by a linker[321] (Figure 6-2). PROTACs effectively commandeer the proteasomal degradation system by specifically recruiting a disease-associated protein to an E3 ubiquitin ligase (*e.g.* SCF complex) for polyubiquitination and selective degradation (Figure 6-2). This enables conditional and/or tissue-specific degradation of proteins that drive CIN and oncogenesis when overexpressed. Conceptually, PROTACs could be developed for all proteins to which a specific binding molecule could be developed, regardless of whether it is classically "targetable," (*i.e.* harbours an enzymatic binding pocket). Sakamoto *et al*[321] showed as proof-of-principle that a novel PROTAC can recruit the pro-angiogenic Methionine Aminopeptidase-2 (METAP2), which is not a substrate of any known SCF complex, to $SCF^{\beta TRCP}$ and induce its polyubiquitination and degradation. In mouse xenograft models, PROTACs targeting the apoptotic suppressor Phosphatidylinositol-3-Kinase (PI3K), for ubiquitination and proteasomal degradation, resulted in a 40% reduction in tumor size[322], supporting PROTACs as a promising treatment strategy.

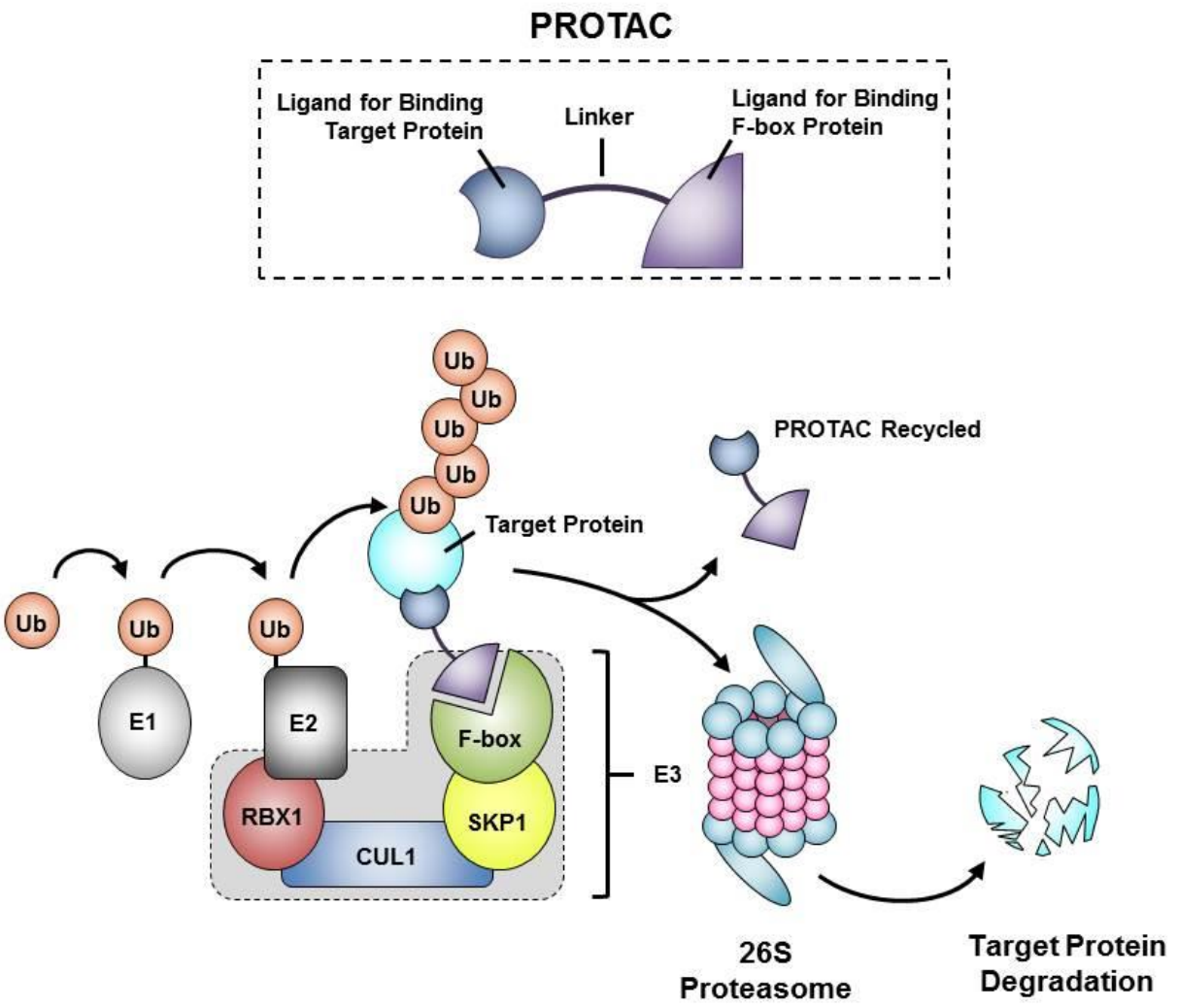

Figure 6-2. Targeted Protein Degradation as a Therapeutic Strategy
Schematic showing PROTAC-mediated protein recruitment to the SCF complex, allowing for polyubiquitination and degradation of cancer-promoting proteins that are not typically regulated by the SCF complex (*see text for details*). PROTAC, Proteolysis Targeting Chimera; E1, E1 ubiquitin-activating enzyme; E2, E2 ubiquitin-conjugating enzyme; E3, E3 ubiquitin-protein ligase; Ub, Ubiquitin; RBX1, Ring-Box 1; CUL1, Cullin 1; SKP1, S-Phase Kinase Associated Protein 1.

PROTACs could be employed to target specific F-box proteins for degradation in order to prevent ubiquitination and degradation of tumor suppressor substrates. Additionally, overexpressed SCF-regulated oncoproteins (*e.g.* CCNE1), proteins not typically regulated by the SCF complex, mutated/dominant-negative proteins, or oncoproteins that have lost binding affinity for their F-box proteins, could now be targeted for proteasomal degradation by novel interactions with a specified SCF complex. As PROTACs can initiate multiple cycles of protein degradation and the targeted proteins must be resynthesized in order to recover from treatment[323], concentrations lower than that of a small molecule inhibitor, would have similar therapeutic effects. Although PROTACs are not currently a viable treatment option due to their large size (700-1000 Da vs. 300-500 Da for traditional small molecules[324]) and limited bioavailability, fundamental research that seeks to improve PROTAC delivery mechanisms, is actively being pursued[321] in order to make PROTACs a feasible cancer treatment option in the future.

6.6.0. Strategies to Exploit CIN as a Cancer Therapeutic Target

Two fundamental strategies can be employed to directly exploit CIN for cancer treatment, namely, CIN-reducing or CIN-inducing therapies[67,68,325] (reviewed in Thompson *et al*[326]). Although CIN is generally considered an oncogenic driver[2-4], there is a paradoxical relationship reported between extensive CIN (measured by FISH probe enumeration) and improved patient outcome in some cancer types, including breast, ovarian, gastric, and lung[327,328]. In these studies, the poorest patient outcomes are associated with intermediate, rather than extreme levels of CIN[328]. This suggests that a CIN threshold exists and if it is exceeded by the cell, it is deleterious

and induces cell cytotoxicity[326]. Accordingly, treatment strategies that either reduce CIN or drive extreme levels of CIN may both be therapeutically beneficial.

Conceptually, CIN-reducing approaches aim to slow the rate of CIN by inhibiting the abnormal processes leading to chromosome missegregation or structural defects in CIN-positive cancer cells. This strategy seeks to prevent the acquisition of further chromosomal alterations, minimizing ITH and tumor adaptability, and impeding cancer progression or the acquisition of drug resistance. For example, PROTACs designed to specifically target a pathogenic protein that deregulates chromosome stability pathways, represents a novel CIN-reducing therapeutic strategy. Several *in vitro* studies have successfully employed chemical or genetic CIN-reducing approaches and identified promising targets[329-333], however, few have been translated to the clinic[332,334]. Conversely, CIN-inducing therapies exploit the paradoxical relationship observed between extensive CIN and improved patient outcomes[327,328] and aim to exacerbate CIN, generating extreme levels of chromosome missegregation and/or DNA damage, to induce cell death[67,335-337]. For example, treatment with the centrosome de-clustering compound CCCI-01 induces multipolar mitoses and extensive, large-scale numerical CIN and apoptosis in cancer cells with supernumerary centrosomes[286]. Thus, identifying and characterizing CIN genes is critical, as it may identify novel CIN-associated pathways that can be exploited in broad-spectrum therapies.

Although *SKP1* is frequently heterozygously deleted in CRC (Table 6-2), *SKP1* is rarely homozygously deleted according to cBioPortal data[209]. This may suggest that while reduced levels of SKP1 promote CIN and oncogenesis, a complete abrogation of SKP1 and SCF complex activity may be detrimental to CRC cell viability *in vivo*. This is supported by the observation that hypomorphic defects in both *SKP1* and *CUL1* are SL in budding yeast (*see Section 6.5.2*

[Table 6-5]). Additionally, in the above experiments, a larger number of cells were seeded for the *SKP1* silenced condition compared to controls, in order to obtain similar cellular confluencies at the experimental endpoint (*see Section 2.2.2* [Table 2-2]). Perhaps in certain cellular/genetic contexts, loss of SKP1 and SCF activity induces excessive replication stress, DNA damage, mitotic spindle defects and CIN (*see Sections 6.3.0-4*) that are incompatible with cancer cell viability. Accordingly, cancers with centromeric, centrosomal, DNA replication or damage repair defects and CIN, may potentially benefit from treatment with SKP1 or SCF inhibitors, as this could potentially exacerbate CIN beyond a critical threshold to induce cancer cell-specific killing. This concept of CIN gene inhibition to induce cell death may also apply to other CIN genes identified in this thesis such as *DSN1*, which is rarely deleted or underexpressed in CRC (0.5%), but induces CIN phenotypes in CRC-derived cells *in vitro* (*see Chapter 4*). Investigating this strategy of inhibiting/exploiting CIN genes and pathways to induce extensive CIN and cell death is a promising future direction.

6.7.0. Future Directions of Fundamental and Translational CIN Studies

Cancer therapies that seek to exploit the genetic/biological aberrations associated with CIN represent an innovative treatment strategy with great therapeutic potential and broad-spectrum applicability for a myriad of cancer types and stages. As we gain a greater understanding of the aberrant genes and biological pathways that underlie CIN, our ability to identify and develop novel therapeutics that exploit those aberrations, will continue to evolve and expand. Overall, this thesis has provided a novel screening approach that dramatically expedites the identification and characterization of human CIN genes, like *SKP1*, which may have important implications for oncogenesis. Executing the future studies proposed and discussed throughout Chapter 6 will be

instrumental for determining whether CIN genes harbor prognostic, diagnostic, or therapeutic significance. Performing SL screens in different cellular contexts are needed to identify novel precision medicine strategies. Therapeutic targeting of CIN genes by chemical inhibition requires extensive fundamental and translational research, as gene silencing (akin to inhibition) was shown to induce CIN. Investigating whether inhibition of CIN genes can effectively drive CIN beyond a critical threshold that induces cancer cell death in specific cancer contexts is another promising treatment strategy to be explored further. Combinatorial treatment approaches will be instrumental to help mitigate the risk for side effects, drug resistance, and tumor recurrence. For example, molecularly-targeted SL therapies could be combined with general (non-specific) cytotoxic DNA damaging agents to induce robust cancer cell death, while reducing the risk for drug resistance by cancer cells that acquired mutations in the target gene or activated compensatory pathways. In conclusion, characterizing novel human CIN genes provides fundamental insight into the cellular pathways normally required to maintain chromosome stability and genome integrity in human cells. Exploring and exploiting CIN has tremendous therapeutic potential in cancer, and may represent a critical vulnerability that can be targeted to treat aggressive, drug resistant cancers, to ultimately improve the quality of life and outcomes for individuals living with cancer.

CHAPTER 7: REFERENCES

1. Lengauer, C., Kinzler, K.W. & Vogelstein, B. Genetic instability in colorectal cancers. *Nature* **386**, 623-7 (1997).
2. Nowak, M.A. *et al.* The role of chromosomal instability in tumor initiation. *Proc Natl Acad Sci U S A* **99**, 16226-31 (2002).
3. Gao, C. *et al.* Chromosome instability drives phenotypic switching to metastasis. *Proc Natl Acad Sci U S A* **113**, 14793-14798 (2016).
4. Lee, A.J. *et al.* Chromosomal instability confers intrinsic multidrug resistance. *Cancer Res* **71**, 1858-70 (2011).
5. Society, A.C. Global Cancer Facts & Figures. 3rd edn (American Cancer Society, Atlanta, 2015).
6. Torre, L.A., Siegel, R.L., Ward, E.M. & Jemal, A. Global Cancer Incidence and Mortality Rates and Trends--An Update. *Cancer Epidemiol Biomarkers Prev* **25**, 16-27 (2016).
7. Statistics, C.C.S.s.A.C.o.C. Canadian Cancer Statistics (Canadian Cancer Society, Toronto, Ontario, 2017).
8. Xie, L., Semenciw, R. & Mery, L. Cancer incidence in Canada: trends and projections (1983-2032). *Health Promot Chronic Dis Prev Can* **35 Suppl 1**, 2-186 (2015).
9. Favoriti, P. *et al.* Worldwide burden of colorectal cancer: a review. *Updates Surg* **68**, 7-11 (2016).
10. Gonzalez, E.C., Roetzheim, R.G., Ferrante, J.M. & Campbell, R. Predictors of proximal vs. distal colorectal cancers. *Dis Colon Rectum* **44**, 251-8 (2001).
11. Binefa, G., Rodríguez-Moranta, F., Teule, À. & Medina-Hayas, M. Colorectal cancer: From prevention to personalized medicine. *World J Gastroenterol* **20**, 6786-808 (2014).
12. Staarmann, J., Kotb, W.F. & Petersen, I. DNA ploidy and morphology of colon tumors in the adenoma-carcinoma sequence. *Folia Histochem Cytobiol* **53**, 11-8 (2015).
13. Vogelstein, B. *et al.* Genetic alterations during colorectal-tumor development. *N Engl J Med* **319**, 525-32 (1988).
14. Janjua, H.G., Hogdall, E. & Linnemann, D. Hyperplastic polyps of the colon and rectum - reclassification, BRAF and KRAS status in index polyps and subsequent colorectal carcinoma. *APMIS* **123**, 298-304 (2015).
15. Snover, D.C. Update on the serrated pathway to colorectal carcinoma. *Hum Pathol* **42**, 1-10 (2011).
16. Bufill, J.A. Colorectal cancer: evidence for distinct genetic categories based on proximal or distal tumor location. *Ann Intern Med* **113**, 779-88 (1990).
17. Nishihara, R. *et al.* Biomarker correlation network in colorectal carcinoma by tumor anatomic location. *BMC Bioinformatics* **18**(2017).
18. Ahmed, S., Johnson, K., Ahmed, O. & Iqbal, N. Advances in the management of colorectal cancer: from biology to treatment. *Int J Colorectal Dis* **29**, 1031-42 (2014).
19. Recommendations on screening for colorectal cancer in primary care. *CMAJ* **188**, 340-8 (2016).
20. Young, G.P. *et al.* Advances in Fecal Occult Blood Tests: The FIT Revolution. *Dig Dis Sci* **60**, 609-22 (2015).
21. Ontario, H.Q. Fecal Occult Blood Test for Colorectal Cancer Screening: An Evidence-Based Analysis. *Ont Health Technol Assess Ser* **9**, 1-40 (2009).

22. Paterson, W.G. *et al.* Canadian consensus on medically acceptable wait times for digestive health care. *Can J Gastroenterol* **20**, 411-23 (2006).
23. Del Giudice, M.E. *et al.* Guideline for referral of patients with suspected colorectal cancer by family physicians and other primary care providers. *Can Fam Physician* **60**, 717-23 (2014).
24. Rabeneck, L. *et al.* Ontario's ColonCancerCheck: results from canada's first province-wide colorectal cancer screening program. *Cancer Epidemiol Biomarkers Prev* **23**, 508-15 (2014).
25. Lieberman, D.A. *et al.* Guidelines for colonoscopy surveillance after screening and polypectomy: a consensus update by the US Multi-Society Task Force on Colorectal Cancer. *Gastroenterology* **143**, 844-857 (2012).
26. Walter, F.M. *et al.* Symptoms and patient factors associated with longer time to diagnosis for colorectal cancer: results from a prospective cohort study. *Br J Cancer* **115**, 533-41 (2016).
27. Miyoshi, N. *et al.* Clinicopathological characteristics and prognosis of stage IV colorectal cancer. *Mol Clin Oncol* **3**, 1093-1098 (2015).
28. Bruin, S.C. *et al.* Molecular alterations associated with liver metastases development in colorectal cancer patients. *Br J Cancer* **105**, 281-7 (2011).
29. Wingfield, S.A. & Heflin, M.T. Cancer Screening in Older Adults. *Clin Geriatr Med* **32**, 17-33 (2016).
30. Obuch, J.C. & Ahnen, D.J. Colorectal Cancer: Genetics is Changing Everything. *Gastroenterol Clin North Am* **45**, 459-76 (2016).
31. Schreuders, E.H. *et al.* Colorectal cancer screening: a global overview of existing programmes. *Gut* **64**, 1637-49 (2015).
32. Alecu, M., Simion, L., Straja, N. & Bratucu, E. Multiple polyps and colorectal cancer. *Chirurgia (Bucur)* **109**, 342-6 (2014).
33. Kolligs, F.T. Diagnostics and Epidemiology of Colorectal Cancer. *Visc Med* **32**, 158-64 (2016).
34. van Duijvendijk, P., Slors, J.F.M., Taat, C.W., Oosterveld, P. & Vasen, H.F.A. Functional Outcome After Colectomy and Ileorectal Anastomosis Compared With Proctocolectomy and Ileal Pouch–Anal Anastomosis in Familial Adenomatous Polyposis. *Ann Surg* **230**, 648 (1999).
35. Song, Y.X. *et al.* Can the tumor deposits be counted as metastatic lymph nodes in the UICC TNM staging system for colorectal cancer? *PLoS One* **7**, e34087 (2012).
36. Watanabe, T. *et al.* Japanese Society for Cancer of the Colon and Rectum (JSCCR) Guidelines 2014 for treatment of colorectal cancer. *Int J Clin Oncol* **20**, 207-39 (2015).
37. Sridharan, M., Hubbard, J.M. & Grothey, A. Colorectal cancer: how emerging molecular understanding affects treatment decisions. *Oncology (Williston Park)* **28**, 110-8 (2014).
38. Zheng, Y., Zhou, J. & Tong, Y. Gene signatures of drug resistance predict patient survival in colorectal cancer. *Pharmacogenomics J* **15**, 135-43 (2015).
39. Hammond, W.A., Swaika, A. & Mody, K. Pharmacologic resistance in colorectal cancer: a review. *Ther Adv Med Oncol* **8**, 57-84 (2016).
40. Longley, D.B. & Johnston, P.G. Molecular mechanisms of drug resistance. *J Pathol* **205**, 275-92 (2005).

41. Al-Sukhni, W., Aronson, M. & Gallinger, S. Hereditary colorectal cancer syndromes: familial adenomatous polyposis and lynch syndrome. *Surg Clin North Am* **88**, 819-44, vii (2008).
42. Fearon, E.R. Molecular genetics of colorectal cancer. *Annu Rev Pathol* **6**, 479-507 (2011).
43. Stoffel, E.M. & Kastrinos, F. Familial colorectal cancer, beyond Lynch syndrome. *Clin Gastroenterol Hepatol* **12**, 1059-68 (2014).
44. Short, E., Thomas, L.E., Hurley, J., Jose, S. & Sampson, J.R. Inherited predisposition to colorectal cancer: towards a more complete picture. *J Med Genet* **52**, 791-6 (2015).
45. Armaghany, T., Wilson, J.D., Chu, Q. & Mills, G. Genetic Alterations in Colorectal Cancer. *Gastrointest Cancer Res* **5**, 19-27 (2012).
46. Ogino, S. & Goel, A. Molecular Classification and Correlates in Colorectal Cancer. *J Mol Diagn* **10**, 13-27 (2008).
47. Geigl, J.B., Obenauf, A.C., Schwarzbraun, T. & Speicher, M.R. Defining 'chromosomal instability'. *Trends Genet* **24**, 64-9 (2008).
48. Hanahan, D. & Weinberg, R.A. Hallmarks of cancer: the next generation. *Cell* **144**, 646-74 (2011).
49. Ziadi, S. *et al.* Clinicopathologic characteristics of colorectal cancer with microsatellite instability. *Pathol Res Pract* **210**, 98-104 (2014).
50. Kavakiotis, I. *et al.* Pattern discovery for microsatellite genome analysis. *Comput Biol Med* **46**, 71-8 (2014).
51. Alhopuro, P. *et al.* Candidate driver genes in microsatellite-unstable colorectal cancer. *Int J Cancer* **130**, 1558-66 (2012).
52. Mahon, S.M. Microsatellite testing in colon cancer. *Oncol Nurs Forum* **41**, 331-3 (2014).
53. Toyota, M. *et al.* CpG island methylator phenotype in colorectal cancer. *Proc Natl Acad Sci U S A* **96**, 8681-6 (1999).
54. Cisyk, A.L. *et al.* Characterizing the prevalence of chromosome instability in interval colorectal cancer. *Neoplasia* **17**, 306-16 (2015).
55. Burrell, R.A. *et al.* Replication stress links structural and numerical cancer chromosomal instability. *Nature* **494**, 492-6 (2013).
56. Kaufmann, W.K. *et al.* Mechanisms of chromosomal instability in melanoma. *Environ Mol Mutagen* **55**, 457-71 (2014).
57. Burrell, R.A. & Swanton, C. Tumour heterogeneity and the evolution of polyclonal drug resistance. *Mol Oncol* **8**, 1095-111 (2014).
58. Miura, M. *et al.* Accumulated chromosomal instability in murine bone marrow mesenchymal stem cells leads to malignant transformation. *Stem Cells* **24**, 1095-103 (2006).
59. Burrell, R.A. *et al.* Targeting chromosomal instability and tumour heterogeneity in HER2-positive breast cancer. *Journal of cellular biochemistry* **111**, 782-790 (2010).
60. Sotillo, R., Schvartzman, J.M., Socci, N.D. & Benezra, R. Mad2-induced chromosome instability leads to lung tumour relapse after oncogene withdrawal. *Nature* **464**, 436-40 (2010).
61. Carter, S.L., Eklund, A.C., Kohane, I.S., Harris, L.N. & Szallasi, Z. A signature of chromosomal instability inferred from gene expression profiles predicts clinical outcome in multiple human cancers. *Nat Genet* **38**, 1043-8 (2006).
62. Barber, T.D. *et al.* Chromatid cohesion defects may underlie chromosome instability in human colorectal cancers. *Proc Natl Acad Sci U S A* **105**, 3443-8 (2008).

63. Leonard, J.M., Ye, H., Wetmore, C. & Karnitz, L.M. Sonic Hedgehog signaling impairs ionizing radiation-induced checkpoint activation and induces genomic instability. *J Cell Biol* **183**, 385-91 (2008).
64. Pantazi, E. *et al.* GLI2 induces genomic instability in human keratinocytes by inhibiting apoptosis. *Cell Death Dis* **5**, e1028 (2014).
65. Stirling, P.C. *et al.* The complete spectrum of yeast chromosome instability genes identifies candidate CIN cancer genes and functional roles for ASTRA complex components. *PLoS Genet* **7**, e1002057 (2011).
66. Yuen, K.W.Y. *et al.* Systematic genome instability screens in yeast and their potential relevance to cancer. *Proceedings of the National Academy of Sciences of the United States of America* **104**, 3925-3930 (2007).
67. Bakhoum, S.F. & Compton, D.A. Chromosomal instability and cancer: a complex relationship with therapeutic potential. *J Clin Invest* **122**, 1138-43 (2012).
68. Thompson, S.L., Bakhoum, S.F. & Compton, D.A. Mechanisms of chromosomal instability. *Curr Biol* **20**, R285-95 (2010).
69. Losada, A. Cohesin in cancer: chromosome segregation and beyond. *Nat Rev Cancer* **14**, 389-93 (2014).
70. Canudas, S. & Smith, S. Differential regulation of telomere and centromere cohesion by the Scc3 homologues SA1 and SA2, respectively, in human cells. *J Cell Biol* **187**, 165-73 (2009).
71. Mirkovic, M. & Oliveira, R.A. Centromeric Cohesin: Molecular Glue and Much More. *Prog Mol Subcell Biol* **56**, 485-513 (2017).
72. Litwin, I. & Wysocki, R. New insights into cohesin loading. *Curr Genet* (2017).
73. Stellfox, M.E., Bailey, A.O. & Foltz, D.R. Putting CENP-A in its place. *Cell Mol Life Sci* **70**, 387-406 (2013).
74. Zafar, F. *et al.* Regulation of mitotic recombination between DNA repeats in centromeres. *Nucleic Acids Res* (2017).
75. Van Hooser, A.A. *et al.* Specification of kinetochore-forming chromatin by the histone H3 variant CENP-A. *J Cell Sci* **114**, 3529-42 (2001).
76. Black, B.E. *et al.* Structural determinants for generating centromeric chromatin. *Nature* **430**, 578-82 (2004).
77. Falk, S.J. & Black, B.E. Centromeric Chromatin and the Pathway that Drives Its Propagation. *Biochim Biophys Acta* **1819**, 313-21 (2012).
78. Dunleavy, E.M. *et al.* HJURP is a cell-cycle-dependent maintenance and deposition factor of CENP-A at centromeres. *Cell* **137**, 485-97 (2009).
79. Thakur, J. & Henikoff, S. CENPT bridges adjacent CENPA nucleosomes on young human α-satellite dimers. *Genome Res* **26**, 1178-87 (2016).
80. Tschernyschkow, S. *et al.* Rule-based modeling and simulations of the inner kinetochore structure. *Prog Biophys Mol Biol* **113**, 33-45 (2013).
81. Ranjitkar, P. *et al.* An E3 ubiquitin ligase prevents ectopic localization of the centromeric histone H3 variant via the centromere targeting domain. *Mol Cell* **40**, 455-64 (2010).
82. Mishra, P.K. *et al.* Misregulation of Scm3p/HJURP causes chromosome instability in Saccharomyces cerevisiae and human cells. *PLoS Genet* **7**, e1002303 (2011).
83. Kato, T. *et al.* Activation of Holliday junction recognizing protein involved in the chromosomal stability and immortality of cancer cells. *Cancer Res* **67**, 8544-53 (2007).

84. Valente, V. *et al.* Selection of suitable housekeeping genes for expression analysis in glioblastoma using quantitative RT-PCR. *BMC Mol Biol* **10**, 17 (2009).
85. Valente, V. *et al.* Modulation of HJURP (Holliday Junction-Recognizing Protein) Levels Is Correlated with Glioblastoma Cells Survival. *PLoS One* **8**(2013).
86. Hu, Z. *et al.* The expression level of HJURP has an independent prognostic impact and predicts the sensitivity to radiotherapy in breast cancer. *Breast Cancer Res* **12**, R18 (2010).
87. Wu, Q. *et al.* Expression and prognostic significance of centromere protein A in human lung adenocarcinoma. *Lung Cancer* **77**, 407-14 (2012).
88. Gu, X.M. *et al.* Expression and prognostic relevance of centromere protein A in primary osteosarcoma. *Pathol Res Pract* **210**, 228-33 (2014).
89. Tomonaga, T. *et al.* Overexpression and mistargeting of centromere protein-A in human primary colorectal cancer. *Cancer Res* **63**, 3511-6 (2003).
90. Amato, A., Schillaci, T., Lentini, L. & Di Leonardo, A. CENPA overexpression promotes genome instability in pRb-depleted human cells. *Mol Cancer* **8**, 119 (2009).
91. Masumoto, H., Masukata, H., Muro, Y., Nozaki, N. & Okazaki, T. A human centromere antigen (CENP-B) interacts with a short specific sequence in alphoid DNA, a human centromeric satellite. *J Cell Biol* **109**, 1963-73 (1989).
92. Røe, O.D. *et al.* Molecular Resistance Fingerprint of Pemetrexed and Platinum in a Long-Term Survivor of Mesothelioma. *PLoS One* **7**(2012).
93. Friedman, S. & Freitag, M. Chapter One - Evolving Centromeres and Kinetochores. in *Advances in Genetics*, Vol. 98 (eds. Friedmann, T., Dunlap, J.C. & Goodwin, S.F.) 1-41 (Academic Press, 2017).
94. Fukasawa, K. Centrosome amplification, chromosome instability and cancer development. *Cancer Lett* **230**, 6-19 (2005).
95. Inanc, B. *et al.* Abnormal centrosomal structure and duplication in Cep135-deficient vertebrate cells. *Mol Biol Cell* **24**, 2645-54 (2013).
96. Alushin, G.M. *et al.* High-resolution microtubule structures reveal the structural transitions in alphabeta-tubulin upon GTP hydrolysis. *Cell* **157**, 1117-29 (2014).
97. Meunier, S. & Vernos, I. Microtubule assembly during mitosis - from distinct origins to distinct functions? *J Cell Sci* **125**, 2805-14 (2012).
98. Hung, H.F., Hehnly, H. & Doxsey, S. The Mother Centriole Appendage Protein Cenexin Modulates Lumen Formation through Spindle Orientation. *Curr Biol* **26**, 1248 (2016).
99. Lange, B.M. & Gull, K. A molecular marker for centriole maturation in the mammalian cell cycle. *J Cell Biol* **130**, 919-27 (1995).
100. Moritz, M., Braunfeld, M.B., Sedat, J.W., Alberts, B. & Agard, D.A. Microtubule nucleation by gamma-tubulin-containing rings in the centrosome. *Nature* **378**, 638-40 (1995).
101. Fu, J., Hagan, I.M. & Glover, D.M. The centrosome and its duplication cycle. *Cold Spring Harb Perspect Biol* **7**, a015800 (2015).
102. Lee, M., Seo, M.Y., Chang, J., Hwang, D.S. & Rhee, K. PLK4 phosphorylation of CP110 is required for efficient centriole assembly. *Cell Cycle* **16**, 1225-1234 (2017).
103. Habedanck, R., Stierhof, Y.D., Wilkinson, C.J. & Nigg, E.A. The Polo kinase Plk4 functions in centriole duplication. *Nat Cell Biol* **7**, 1140-6 (2005).
104. Bettencourt-Dias, M. *et al.* SAK/PLK4 is required for centriole duplication and flagella development. *Curr Biol* **15**, 2199-207 (2005).

105. Chen, Z., Indjeian, V.B., McManus, M., Wang, L. & Dynlacht, B.D. CP110, a cell cycle-dependent CDK substrate, regulates centrosome duplication in human cells. *Dev Cell* **3**, 339-50 (2002).
106. Ferguson, R.L. & Maller, J.L. Cyclin E-dependent localization of MCM5 regulates centrosome duplication. *J Cell Sci* **121**, 3224-32 (2008).
107. Vora, S.M. & Phillips, B.T. The benefits of local depletion: The centrosome as a scaffold for ubiquitin-proteasome-mediated degradation. *Cell Cycle* **15**, 2124-34 (2016).
108. Chan, J.Y. A Clinical Overview of Centrosome Amplification in Human Cancers. *Int J Biol Sci* **7**, 1122-44 (2011).
109. Godinho, S.A. & Pellman, D. Causes and consequences of centrosome abnormalities in cancer. *Philos Trans R Soc Lond B Biol Sci* **369**(2014).
110. Pihan, G.A. *et al.* Centrosome defects and genetic instability in malignant tumors. *Cancer Res* **58**, 3974-85 (1998).
111. Lara-Gonzalez, P., Westhorpe, F.G. & Taylor, S.S. The spindle assembly checkpoint. *Curr Biol* **22**, R966-80 (2012).
112. Chen, J. & Liu, J. Spatial-temporal model for silencing of the mitotic spindle assembly checkpoint. *Nat Commun* **5**, 4795 (2014).
113. Kuijt, T.E., Omerzu, M., Saurin, A.T. & Kops, G.J. Conditional targeting of MAD1 to kinetochores is sufficient to reactivate the spindle assembly checkpoint in metaphase. *Chromosoma* **123**, 471-80 (2014).
114. van der Waal, M.S., Hengeveld, R.C., van der Horst, A. & Lens, S.M. Cell division control by the Chromosomal Passenger Complex. *Exp Cell Res* **318**, 1407-20 (2012).
115. Sotillo, R. *et al.* Mad2 overexpression promotes aneuploidy and tumorigenesis in mice. *Cancer Cell* **11**, 9-23 (2007).
116. Hernando, E. *et al.* Rb inactivation promotes genomic instability by uncoupling cell cycle progression from mitotic control. *Nature* **430**, 797-802 (2004).
117. Cahill, D.P. *et al.* Mutations of mitotic checkpoint genes in human cancers. *Nature* **392**, 300-3 (1998).
118. Heaney, A.P. *et al.* Expression of pituitary-tumour transforming gene in colorectal tumours. *Lancet* **355**, 716-9 (2000).
119. Kim, D.S. *et al.* Securin induces genetic instability in colorectal cancer by inhibiting double-stranded DNA repair activity. *Carcinogenesis* **28**, 749-59 (2007).
120. Fragkos, M., Ganier, O., Coulombe, P. & Mechali, M. DNA replication origin activation in space and time. *Nat Rev Mol Cell Biol* **16**, 360-74 (2015).
121. Chao, T.C. *et al.* Thymosin beta-4 knockdown in IEC-6 normal intestinal epithelial cells induces DNA re-replication via downregulating Emi1. *J Cell Physiol* **229**, 1639-46 (2014).
122. Zeman, M.K. & Cimprich, K.A. Causes and consequences of replication stress. *Nat Cell Biol* **16**, 2-9 (2014).
123. Masai, H., Matsumoto, S., You, Z., Yoshizawa-Sugata, N. & Oda, M. Eukaryotic chromosome DNA replication: where, when, and how? *Annu Rev Biochem* **79**, 89-130 (2010).
124. Hills, S.A. & Diffley, J.F. DNA replication and oncogene-induced replicative stress. *Curr Biol* **24**, R435-44 (2014).
125. Jones, R.M. *et al.* Increased replication initiation and conflicts with transcription underlie Cyclin E-induced replication stress. *Oncogene* **32**, 3744-53 (2013).

126. Hosoya, N. & Miyagawa, K. Targeting DNA damage response in cancer therapy. *Cancer Sci* **105**, 370-88 (2014).
127. Lee, J.H. & Paull, T.T. ATM activation by DNA double-strand breaks through the Mre11-Rad50-Nbs1 complex. *Science* **308**, 551-4 (2005).
128. Matsumoto, M. *et al.* Perturbed gap-filling synthesis in nucleotide excision repair causes histone H2AX phosphorylation in human quiescent cells. *J Cell Sci* **120**, 1104-12 (2007).
129. Nam, E.A. & Cortez, D. ATR signalling: more than meeting at the fork. *Biochem J* **436**, 527-36 (2011).
130. Takayama, T., Miyanishi, K., Hayashi, T., Sato, Y. & Niitsu, Y. Colorectal cancer: genetics of development and metastasis. *J Gastroenterol* **41**, 185-92 (2006).
131. Kandoth, C. *et al.* Mutational landscape and significance across 12 major cancer types. *Nature* **502**, 333-339 (2013).
132. Ben-Aroya, S. *et al.* Proteasome nuclear activity affects chromosome stability by controlling the turnover of Mms22, a protein important for DNA repair. *PLoS Genet* **6**, e1000852 (2010).
133. Kleiger, G. & Mayor, T. Perilous journey: a tour of the ubiquitin–proteasome system. *Trends Cell Biol* **24**, 352-9 (2014).
134. Pack, C.G. *et al.* Quantitative live-cell imaging reveals spatio-temporal dynamics and cytoplasmic assembly of the 26S proteasome. *Nat Commun* **5**, 3396 (2014).
135. Thrower, J.S., Hoffman, L., Rechsteiner, M. & Pickart, C.M. Recognition of the polyubiquitin proteolytic signal. *EMBO J* **19**, 94-102 (2000).
136. Deshaies, R.J. & Joazeiro, C.A. RING domain E3 ubiquitin ligases. *Annu Rev Biochem* **78**, 399-434 (2009).
137. Jin, J. *et al.* Systematic analysis and nomenclature of mammalian F-box proteins. *Genes Dev* **18**, 2573-80 (2004).
138. Chandra Dantu, S., Nathubhai Kachariya, N. & Kumar, A. Molecular dynamics simulations elucidate the mode of protein recognition by Skp1 and the F-box domain in the SCF complex. *Proteins* **84**, 159-71 (2016).
139. Hussain, M. *et al.* Skp1: Implications in cancer and SCF-oriented anti-cancer drug discovery. *Pharmacol Res* **111**, 34-42 (2016).
140. Yoshida, Y., Murakami, A. & Tanaka, K. Skp1 stabilizes the conformation of F-box proteins. *Biochem Biophys Res Commun* **410**, 24-8 (2011).
141. Kulathu, Y. & Komander, D. Atypical ubiquitylation - the unexplored world of polyubiquitin beyond Lys48 and Lys63 linkages. *Nat Rev Mol Cell Biol* **13**, 508-23 (2012).
142. Dias, D.C., Dolios, G., Wang, R. & Pan, Z.Q. CUL7: A DOC domain-containing cullin selectively binds Skp1·Fbx29 to form an SCF-like complex. *Proc Natl Acad Sci U S A* **99**, 16601-6 (2002).
143. Nakayama, K. *et al.* Targeted disruption of Skp2 results in accumulation of cyclin E and p27(Kip1), polyploidy and centrosome overduplication. *EMBO J* **19**, 2069-81 (2000).
144. Walter, D. *et al.* SCF(Cyclin F)-dependent degradation of CDC6 suppresses DNA re-replication. *Nat Commun* **7**, 10530 (2016).
145. Cunha-Ferreira, I. *et al.* Regulation of autophosphorylation controls PLK4 self-destruction and centriole number. *Curr Biol* **23**, 2245-54 (2013).
146. Mandel, S.A., Fishman-Jacob, T. & Youdim, M.B. Targeting SKP1, an ubiquitin E3 ligase component found decreased in sporadic Parkinson's disease. *Neurodegener Dis* **10**, 220-3 (2012).

147. Sandhya, P. & Danda, D. Role of vacuolar ATPase and Skp1 in Sjogren's syndrome. *Med Hypotheses* **82**, 319-25 (2014).
148. Silverman, J.S., Skaar, J.R. & Pagano, M. SCF ubiquitin ligases in the maintenance of genome stability. *Trends Biochem Sci* **37**, 66-73 (2012).
149. GeneCards. The GeneCards Human Gene Database. 1996-2015 edn (Crown Human Genome Center, Department of Molecular Genetics, the Weizmann Institute of Science, 2017).
150. Schulman, B.A. *et al.* Insights into SCF ubiquitin ligases from the structure of the Skp1-Skp2 complex. *Nature* **408**, 381-6 (2000).
151. Yamanaka, A. *et al.* Multiple Skp1-related proteins in Caenorhabditis elegans: diverse patterns of interaction with Cullins and F-box proteins. *Curr Biol* **12**, 267-75 (2002).
152. Kong, H., Leebens-Mack, J., Ni, W., dePamphilis, C.W. & Ma, H. Highly heterogeneous rates of evolution in the SKP1 gene family in plants and animals: functional and evolutionary implications. *Mol Biol Evol* **21**, 117-28 (2004).
153. Ng, R.W. *et al.* Characterization of the cullin and F-box protein partner Skp1. *FEBS Lett* **438**, 183-9 (1998).
154. Piva, R. *et al.* In vivo interference with Skp1 function leads to genetic instability and neoplastic transformation. *Mol Cell Biol* **22**, 8375-87 (2002).
155. Cerami, E. *et al.* The cBio cancer genomics portal: an open platform for exploring multidimensional cancer genomics data. *Cancer Discov* **2**, 401-4 (2012).
156. Gao, J. *et al.* Integrative analysis of complex cancer genomics and clinical profiles using the cBioPortal. *Sci Signal* **6**, pl1 (2013).
157. Network, C.G.A.R. The Molecular Taxonomy of Primary Prostate Cancer. *Cell* **163**, 1011-25 (2015).
158. Network, C.G.A.R. Integrated genomic analyses of ovarian carcinoma. *Nature* **474**, 609-15 (2011).
159. Network, C.G.A.R. Comprehensive molecular characterization of urothelial bladder carcinoma. *Nature* **507**, 315-22 (2014).
160. Podgornova, M.N., Dubova, E.A. & Shchyogolev, A.I. Comparative characteristics of nuclear ploidy of cells in endocrine and solid pseudopapillary tumors of the pancreas. *Bull Exp Biol Med* **148**, 643-5 (2009).
161. Zeimet, A.G. *et al.* DNA ploidy, nuclear size, proliferation index and DNA-hypomethylation in ovarian cancer. *Gynecol Oncol* **121**, 24-31 (2011).
162. Petersen, I. *et al.* Core classification of lung cancer: correlating nuclear size and mitoses with ploidy and clinicopathological parameters. *Lung Cancer* **65**, 312-8 (2009).
163. Nielsen, K., Petersen, S.E. & Orntoft, T. A comparison between stereological estimates of mean nuclear volume and DNA flow cytometry in bladder tumours. *APMIS* **97**, 949-56 (1989).
164. Kudo, T. *et al.* Classification of nuclear morphology in endocytoscopy of colorectal neoplasms. *Gastrointest Endosc* **85**, 628-638 (2017).
165. Bhatia, A. & Kumar, Y. Cancer cell micronucleus: an update on clinical and diagnostic applications. *Apmis* **121**, 569-581 (2013).
166. Fenech, M. Chromosomal biomarkers of genomic instability relevant to cancer. *Drug Discov Today* **7**, 1128-37 (2002).
167. Stopper, H. & Muller, S.O. Micronuclei as a biological endpoint for genotoxicity: A minireview. *Toxicology in Vitro* **11**, 661-667 (1997).

168. Fliedner, T.M., Andrews, G.A., Cronkite, E.P. & Bond, V.P. Early and late cytologic effects of whole body irradiation on human marrow. *Blood* **23**, 471-87 (1964).
169. Maffei, F. *et al.* Micronucleus frequency in human peripheral blood lymphocytes as a biomarker for the early detection of colorectal cancer risk. *Mutagenesis* **29**, 221-5 (2014).
170. El-Zein, R.A. *et al.* Cytokinesis-blocked micronucleus assay as a novel biomarker for lung cancer risk. *Cancer Res* **66**, 6449-56 (2006).
171. Bonassi, S. *et al.* An increased micronucleus frequency in peripheral blood lymphocytes predicts the risk of cancer in humans. *Carcinogenesis* **28**, 625-31 (2007).
172. Arora, S.K., Dey, P. & Saikia, U.N. Micronucleus in atypical urothelial cells. *Diagn Cytopathol* **38**, 811-3 (2010).
173. Jadhav, K., Gupta, N. & Ahmed, M.B. Micronuclei: An essential biomarker in oral exfoliated cells for grading of oral squamous cell carcinoma. *J Cytol* **28**, 7-12 (2011).
174. Hogstedt, B., Nilsson, P.G. & Mitelman, F. Micronuclei in erythropoietic bone marrow cells: relation to cytogenetic pattern and prognosis in acute nonlymphocytic leukemia. *Cancer Genet Cytogenet* **3**, 185-93 (1981).
175. Fenech, M. Cytokinesis-block micronucleus cytome assay. *Nat Protoc* **2**, 1084-104 (2007).
176. Sajesh, B.V., Bailey, M., Lichtensztejn, Z., Hieter, P. & McManus, K.J. Synthetic lethal targeting of superoxide dismutase 1 selectively kills RAD54B-deficient colorectal cancer cells. *Genetics* **195**, 757-67 (2013).
177. Nepomuceno, T.C. *et al.* BRCA1 recruitment to damaged DNA sites is dependent on CDK9. *Cell Cycle* **16**, 665-672 (2017).
178. Tu, W.Z. *et al.* gammaH2AX foci formation in the absence of DNA damage: mitotic H2AX phosphorylation is mediated by the DNA-PKcs/CHK2 pathway. *FEBS Lett* **587**, 3437-43 (2013).
179. Orr, B. & Compton, D.A. A double-edged sword: how oncogenes and tumor suppressor genes can contribute to chromosomal instability. *Front Oncol* **3**, 164 (2013).
180. McClelland, S.E., Burrell, R.A. & Swanton, C. Chromosomal instability: a composite phenotype that influences sensitivity to chemotherapy. *Cell Cycle* **8**, 3262-6 (2009).
181. Heilig, C.E. *et al.* Chromosomal instability correlates with poor outcome in patients with myelodysplastic syndromes irrespectively of the cytogenetic risk group. *J Cell Mol Med* **14**, 895-902 (2010).
182. Mannini, L., Menga, S. & Musio, A. The expanding universe of cohesin functions: a new genome stability caretaker involved in human disease and cancer. *Hum Mutat* **31**, 623-30 (2010).
183. Solomon, D.A., Kim, J.S. & Waldman, T. Cohesin gene mutations in tumorigenesis: from discovery to clinical significance. *BMB Rep* **47**, 299-310 (2014).
184. Sajesh, B.V., Lichtensztejn, Z. & McManus, K.J. Sister chromatid cohesion defects are associated with chromosome instability in Hodgkin lymphoma cells. *BMC Cancer* **13**, 391 (2013).
185. Iwaizumi, M. *et al.* Human Sgo1 downregulation leads to chromosomal instability in colorectal cancer. *Gut* **58**, 249-60 (2009).
186. Wirth, K.G. *et al.* Separase: a universal trigger for sister chromatid disjunction but not chromosome cycle progression. *J Cell Biol* **172**, 847-60 (2006).
187. Bauerschmidt, C. *et al.* Cohesin phosphorylation and mobility of SMC1 at ionizing radiation-induced DNA double-strand breaks in human cells. *Experimental Cell Research* **317**, 330-337 (2011).

188. Bauerschmidt, C. *et al.* Cohesin promotes the repair of ionizing radiation-induced DNA double-strand breaks in replicated chromatin. *Nucleic Acids Res* **38**, 477-87 (2010).
189. Kong, X. *et al.* Cohesin associates with spindle poles in a mitosis-specific manner and functions in spindle assembly in vertebrate cells. *Mol Biol Cell* **20**, 1289-301 (2009).
190. Fischer, A.H. The diagnostic pathology of the nuclear envelope in human cancers. *Adv Exp Med Biol* **773**, 49-75 (2014).
191. Webster, M., Witkin, K.L. & Cohen-Fix, O. Sizing up the nucleus: nuclear shape, size and nuclear-envelope assembly. *J Cell Sci* **122**, 1477-86 (2009).
192. Markowitz, S.D. & Bertagnolli, M.M. Molecular origins of cancer: Molecular basis of colorectal cancer. *N Engl J Med* **361**, 2449-60 (2009).
193. Rajagopalan, H., Nowak, M.A., Vogelstein, B. & Lengauer, C. The significance of unstable chromosomes in colorectal cancer. *Nat Rev Cancer* **3**, 695-701 (2003).
194. Dorsett, D. & Strom, L. The ancient and evolving roles of cohesin in gene expression and DNA repair. *Curr Biol* **22**, R240-50 (2012).
195. Barretina, J. *et al.* The Cancer Cell Line Encyclopedia enables predictive modelling of anticancer drug sensitivity. *Nature* **483**, 603-7 (2012).
196. Cox, D.M. A quantitative analysis of colcemid-induced chromosomal nondisjunction in Chinese hamster cells in vitro. *Cytogenet Cell Genet* **12**, 165-74 (1973).
197. Rudd, N.L., Williams, S.E., Evans, M., Hennig, U.G. & Hoar, D.I. Kinetochore analysis of micronuclei allows insights into the actions of colcemid and mitomycin C. *Mutat Res* **261**, 57-68 (1991).
198. Weaver, B.A.A. & Cleveland, D.W. Does aneuploidy cause cancer? [Current Opinion in Cell Biology 2006, 18:658–667]. *Current Opinion in Cell Biology* **19**, 246 (2007).
199. Wang, Z. *et al.* Three classes of genes mutated in colorectal cancers with chromosomal instability. *Cancer Res* **64**, 2998-3001 (2004).
200. Thompson, L.L. & McManus, K.J. A novel multiplexed, image-based approach to detect phenotypes that underlie chromosome instability in human cells. *PLoS One* **10**, e0123200 (2015).
201. MediSapiens In Silico Transcriptomics Online. (http://ist.medisapiens.com/, 2011).
202. van Pel, D.M. *et al.* An evolutionarily conserved synthetic lethal interaction network identifies FEN1 as a broad-spectrum target for anticancer therapeutic development. *PLoS Genet* **9**, e1003254 (2013).
203. Gari, K., Decaillet, C., Stasiak, A.Z., Stasiak, A. & Constantinou, A. The Fanconi anemia protein FANCM can promote branch migration of Holliday junctions and replication forks. *Mol Cell* **29**, 141-8 (2008).
204. Wang, X. *et al.* Genomic instability and endoreduplication triggered by RAD17 deletion. *Genes Dev* **17**, 965-70 (2003).
205. Stolz, A., Ertych, N. & Bastians, H. Loss of the tumour-suppressor genes CHK2 and BRCA1 results in chromosomal instability. *Biochem Soc Trans* **38**, 1704-8 (2010).
206. Asbaghi, Y., Thompson, L.L., Lichtensztejn, Z. & McManus, K.J. KIF11 silencing and inhibition induces chromosome instability that may contribute to cancer. *Genes Chromosomes Cancer* **56**, 668-680 (2017).
207. Ducker, G.S. *et al.* Human SHMT inhibitors reveal defective glycine import as a targetable metabolic vulnerability of diffuse large B-cell lymphoma. *Proc Natl Acad Sci U S A* **114**, 11404-11409 (2017).

208. Network, C.G.A.R. Comprehensive molecular profiling of lung adenocarcinoma. *Nature* **511**, 543-50 (2014).
209. Network, C.G.A.R. Comprehensive molecular characterization of human colon and rectal cancer. *Nature* **487**, 330-7 (2012).
210. Network, C.G.A.R. Comprehensive molecular portraits of human breast tumours. *Nature* **490**, 61-70 (2012).
211. Terzoudi, G.I. *et al.* Stress induced by premature chromatin condensation triggers chromosome shattering and chromothripsis at DNA sites still replicating in micronuclei or multinucleate cells when primary nuclei enter mitosis. *Mutat Res Genet Toxicol Environ Mutagen* **793**, 185-98 (2015).
212. Pathak, R. & Prasanna, P.G. Premature chromosome condensation in human resting peripheral blood lymphocytes without mitogen stimulation for chromosome aberration analysis using specific whole chromosome DNA hybridization probes. *Methods Mol Biol* **1105**, 171-81 (2014).
213. Sundin, L.J., Guimaraes, G.J. & Deluca, J.G. The NDC80 complex proteins Nuf2 and Hec1 make distinct contributions to kinetochore-microtubule attachment in mitosis. *Mol Biol Cell* **22**, 759-68 (2011).
214. Nithianantham, S. *et al.* Tubulin cofactors and Arl2 are cage-like chaperones that regulate the soluble alphabeta-tubulin pool for microtubule dynamics. *Elife* **4**(2015).
215. Kudalkar, E.M. *et al.* Regulation of outer kinetochore Ndc80 complex-based microtubule attachments by the central kinetochore Mis12/MIND complex. *Proc Natl Acad Sci U S A* **112**, E5583-9 (2015).
216. Beghin, A., Matera, E.L., Brunet-Manquat, S. & Dumontet, C. Expression of Arl2 is associated with p53 localization and chemosensitivity in a breast cancer cell line. *Cell Cycle* **7**, 3074-82 (2008).
217. Vleugel, M. *et al.* Sequential multisite phospho-regulation of KNL1-BUB3 interfaces at mitotic kinetochores. *Mol Cell* **57**, 824-35 (2015).
218. Dahms, T.E., Sainz, G., Giroux, E.L., Caperelli, C.A. & Smith, J.L. The apo and ternary complex structures of a chemotherapeutic target: human glycinamide ribonucleotide transformylase. *Biochemistry* **44**, 9841-50 (2005).
219. Anderson, D.D., Quintero, C.M. & Stover, P.J. Identification of a de novo thymidylate biosynthesis pathway in mammalian mitochondria. *Proc Natl Acad Sci U S A* **108**, 15163-8 (2011).
220. Miyo, M. *et al.* The importance of mitochondrial folate enzymes in human colorectal cancer. *Oncol Rep* **37**, 417-425 (2017).
221. Kohnken, R., Kodigepalli, K.M. & Wu, L. Regulation of deoxynucleotide metabolism in cancer: novel mechanisms and therapeutic implications. *Mol Cancer* **14**(2015).
222. Motley, W.W., Talbot, K. & Fischbeck, K.H. GARS axonopathy: not every neuron's cup of tRNA. *Trends Neurosci* **33**, 59-66 (2010).
223. Ohishi, K., Inoue, N. & Kinoshita, T. PIG-S and PIG-T, essential for GPI anchor attachment to proteins, form a complex with GAA1 and GPI8. *EMBO J* **20**, 4088-98 (2001).
224. Fujita, M. & Kinoshita, T. GPI-anchor remodeling: potential functions of GPI-anchors in intracellular trafficking and membrane dynamics. *Biochim Biophys Acta* **1821**, 1050-8 (2012).

225. Network, C.G.A.R. Genomic and epigenomic landscapes of adult de novo acute myeloid leukemia. *N Engl J Med* **368**, 2059-74 (2013).
226. Bassermann, F., Eichner, R. & Pagano, M. The ubiquitin proteasome system - implications for cell cycle control and the targeted treatment of cancer. *Biochim Biophys Acta* **1843**, 150-62 (2014).
227. D'Angiolella, V. *et al.* Cyclin F-mediated degradation of ribonucleotide reductase M2 controls genome integrity and DNA repair. *Cell* **149**, 1023-34 (2012).
228. Kondo, T. *et al.* Rapid degradation of Cdt1 upon UV-induced DNA damage is mediated by SCFSkp2 complex. *J Biol Chem* **279**, 27315-9 (2004).
229. Busino, L. *et al.* Degradation of Cdc25A by beta-TrCP during S phase and in response to DNA damage. *Nature* **426**, 87-91 (2003).
230. D'Angiolella, V. *et al.* SCF(Cyclin F) controls centrosome homeostasis and mitotic fidelity through CP110 degradation. *Nature* **466**, 138-42 (2010).
231. Gstaiger, M., Marti, A. & Krek, W. Association of human SCF(SKP2) subunit p19(SKP1) with interphase centrosomes and mitotic spindle poles. *Exp Cell Res* **247**, 554-62 (1999).
232. Network, C.G.A.R. Integrated genomic characterization of oesophageal carcinoma. *Nature* **541**, 169-175 (2017).
233. Beltran, H. *et al.* Divergent clonal evolution of castration-resistant neuroendocrine prostate cancer. *Nat Med* **22**, 298-305 (2016).
234. Lehman, N.L. *et al.* Oncogenic regulators and substrates of the anaphase promoting complex/cyclosome are frequently overexpressed in malignant tumors. *Am J Pathol* **170**, 1793-805 (2007).
235. Reimann, J.D. *et al.* Emi1 is a mitotic regulator that interacts with Cdc20 and inhibits the anaphase promoting complex. *Cell* **105**, 645-55 (2001).
236. Reimann, J.D., Gardner, B.E., Margottin-Goguet, F. & Jackson, P.K. Emi1 regulates the anaphase-promoting complex by a different mechanism than Mad2 proteins. *Genes Dev* **15**, 3278-85 (2001).
237. Rhodes, J. *et al.* Emi1 maintains genomic integrity during zebrafish embryogenesis and cooperates with p53 in tumor suppression. *Mol Cell Biol* **29**, 5911-22 (2009).
238. Verschuren, E.W., Ban, K.H., Masek, M.A., Lehman, N.L. & Jackson, P.K. Loss of Emi1-dependent anaphase-promoting complex/cyclosome inhibition deregulates E2F target expression and elicits DNA damage-induced senescence. *Mol Cell Biol* **27**, 7955-65 (2007).
239. Bartkova, J. *et al.* DNA damage response as a candidate anti-cancer barrier in early human tumorigenesis. *Nature* **434**, 864-70 (2005).
240. Machida, Y.J. & Dutta, A. The APC/C inhibitor, Emi1, is essential for prevention of rereplication. *Genes Dev* **21**, 184-94 (2007).
241. Chan, C.H. *et al.* The Skp2-SCF E3 ligase regulates Akt ubiquitination, glycolysis, herceptin sensitivity, and tumorigenesis. *Cell* **149**, 1098-111 (2012).
242. Penin, R.M. *et al.* Over-expression of p45(SKP2) in Kaposi's sarcoma correlates with higher tumor stage and extracutaneous involvement but is not directly related to p27(KIP1) down-regulation. *Mod Pathol* **15**, 1227-35 (2002).
243. Latres, E. *et al.* Role of the F-box protein Skp2 in lymphomagenesis. *Proc Natl Acad Sci U S A* **98**, 2515-20 (2001).

244. Li, Q., Murphy, M., Ross, J., Sheehan, C. & Carlson, J.A. Skp2 and p27kip1 expression in melanocytic nevi and melanoma: an inverse relationship. *J Cutan Pathol* **31**, 633-42 (2004).
245. Tsvetkov, L.M., Yeh, K.H., Lee, S.J., Sun, H. & Zhang, H. p27(Kip1) ubiquitination and degradation is regulated by the SCF(Skp2) complex through phosphorylated Thr187 in p27. *Curr Biol* **9**, 661-4 (1999).
246. Carrano, A.C., Eytan, E., Hershko, A. & Pagano, M. SKP2 is required for ubiquitin-mediated degradation of the CDK inhibitor p27. *Nat Cell Biol* **1**, 193-9 (1999).
247. Neelsen, K.J. *et al.* Deregulated origin licensing leads to chromosomal breaks by rereplication of a gapped DNA template. *Genes Dev* **27**, 2537-42 (2013).
248. Kamran, M. *et al.* Aurora kinase A regulates Survivin stability through targeting FBXL7 in gastric cancer drug resistance and prognosis. *Oncogenesis* **6**, e298 (2017).
249. Bagheri-Yarmand, R., Biernacka, A., Hunt, K.K. & Keyomarsi, K. Low molecular weight cyclin E overexpression shortens mitosis, leading to chromosome missegregation and centrosome amplification. *Cancer Res* **70**, 5074-84 (2010).
250. Kuhn, E. *et al.* CCNE1 amplification and centrosome number abnormality in serous tubal intraepithelial carcinoma: further evidence supporting its role as a precursor of ovarian high-grade serous carcinoma. *Mod Pathol* **29**, 1254-61 (2016).
251. Miyachika, Y. *et al.* Centrosome amplification in bladder washing cytology specimens is a useful prognostic biomarker for non-muscle invasive bladder cancer. *Cancer Genet* **206**, 12-8 (2013).
252. Ekholm-Reed, S. *et al.* Deregulation of cyclin E in human cells interferes with prereplication complex assembly. *J Cell Biol* **165**, 789-800 (2004).
253. Karst, A.M. *et al.* Cyclin E1 deregulation occurs early in secretory cell transformation to promote formation of fallopian tube-derived high-grade serous ovarian cancers. *Cancer Res* **74**, 1141-52 (2014).
254. Shaye, A. *et al.* Cyclin E deregulation is an early event in the development of breast cancer. *Breast Cancer Res Treat* **115**, 651-9 (2009).
255. Dosaka-Akita, H. *et al.* A risk-stratification model of non-small cell lung cancers using cyclin E, Ki-67, and ras p21: different roles of G1 cyclins in cell proliferation and prognosis. *Cancer Res* **61**, 2500-4 (2001).
256. Kawasaki, H. *et al.* Expression of survivin correlates with apoptosis, proliferation, and angiogenesis during human colorectal tumorigenesis. *Cancer* **91**, 2026-32 (2001).
257. Fu, Q. *et al.* miR-203 is a predictive biomarker for colorectal cancer and its expression is associated with BIRC5. *Tumor Biology* **37**, 15989-15995 (2016).
258. Zhou, X. & Lin, C. Survivin and angiotensin-converting enzyme polymorphisms with risk of colorectal cancer: a systematic review and meta-analysis. *World J Surg Oncol* **13**(2015).
259. Karam, J.A., Lotan, Y., Ashfaq, R., Sagalowsky, A.I. & Shariat, S.F. Survivin Expression in Patients with Non-Muscle-Invasive Urothelial Cell Carcinoma of the Bladder. *Urology* **70**, 482-486 (2007).
260. Chen, L. *et al.* Survivin status affects prognosis and chemosensitivity in epithelial ovarian cancer. *Int J Gynecol Cancer* **23**, 256-63 (2013).
261. Xia, R. *et al.* A chromosomal passenger complex protein signature model predicts poor prognosis for non-small-cell lung cancer. *Onco Targets Ther* **8**, 721-6 (2015).
262. Zhou, X.L. & Wang, M. Expression levels of survivin, Bcl-2, and KAI1 proteins in cervical cancer and their correlation with metastasis. *Genet Mol Res* **14**, 17059-67 (2015).

263. Roylance, R. *et al.* Expression of regulators of mitotic fidelity are associated with intercellular heterogeneity and chromosomal instability in primary breast cancer. *Breast Cancer Res Treat* **148**, 221-9 (2014).
264. Guardavaccaro, D. *et al.* Control of chromosome stability by the beta-TrCP-REST-Mad2 axis. *Nature* **452**, 365-9 (2008).
265. Hsu, C. *et al.* Cyclin E1 Inhibition can Overcome Sorafenib Resistance in Hepatocellular Carcinoma Cells Through Mcl-1 Suppression. *Clin Cancer Res* **22**, 2555-64 (2016).
266. Ayhan, A. *et al.* CCNE1 copy-number gain and overexpression identify ovarian clear cell carcinoma with a poor prognosis. *Mod Pathol* **30**, 297-303 (2017).
267. Janssen, A., van der Burg, M., Szuhai, K., Kops, G.J. & Medema, R.H. Chromosome segregation errors as a cause of DNA damage and structural chromosome aberrations. *Science* **333**, 1895-8 (2011).
268. Fremont, S. & Echard, A. Studying cytokinesis and midbody remnants using correlative light/scanning EM. *Methods Cell Biol* **137**, 239-251 (2017).
269. Penner-Goeke, S. *et al.* The temporal dynamics of chromosome instability in ovarian cancer cell lines and primary patient samples. *PLoS Genet* **13**, e1006707 (2017).
270. Theriault, B.L., Portelance, L., Mes-Masson, A.M. & Nachtigal, M.W. Establishment of primary cultures from ovarian tumor tissue and ascites fluid. *Methods Mol Biol* **1049**, 323-36 (2013).
271. Gaglio, T. *et al.* Opposing motor activities are required for the organization of the mammalian mitotic spindle pole. *J Cell Biol* **135**, 399-414 (1996).
272. Theoclitou, M.E. *et al.* Discovery of (+)-N-(3-aminopropyl)-N-[1-(5-benzyl-3-methyl-4-oxo-[1,2]thiazolo[5,4-d]pyrimidin -6-yl)-2-methylpropyl]-4-methylbenzamide (AZD4877), a kinesin spindle protein inhibitor and potential anticancer agent. *J Med Chem* **54**, 6734-50 (2011).
273. Huszar, D., Theoclitou, M.E., Skolnik, J. & Herbst, R. Kinesin motor proteins as targets for cancer therapy. *Cancer Metastasis Rev* **28**, 197-208 (2009).
274. Skaar, J.R., D'Angiolella, V., Pagan, J.K. & Pagano, M. SnapShot: F Box Proteins II. *Cell* **137**, 1358, 1358 e1 (2009).
275. Coon, T.A., Glasser, J.R., Mallampalli, R.K. & Chen, B.B. Novel E3 ligase component FBXL7 ubiquitinates and degrades Aurora A, causing mitotic arrest. *Cell Cycle* **11**, 721-9 (2012).
276. Zhu, S. *et al.* A Motif from Lys(216) to Lys(222) in Human BUB3 Protein Is a Nuclear Localization Signal and Critical for BUB3 Function in Mitotic Checkpoint. *J Biol Chem* **290**, 11282-92 (2015).
277. Méndez, J. *et al.* Human Origin Recognition Complex Large Subunit Is Degraded by Ubiquitin-Mediated Proteolysis after Initiation of DNA Replication. *Molecular Cell* **9**, 481-491.
278. Nishitani, H. *et al.* Two E3 ubiquitin ligases, SCF-Skp2 and DDB1-Cul4, target human Cdt1 for proteolysis. *EMBO J* **25**, 1126-36 (2006).
279. Fukushima, H. *et al.* SCF-mediated Cdh1 degradation defines a negative feedback system that coordinates cell-cycle progression. *Cell Rep* **4**, 803-16 (2013).
280. Nakayama, K.-I., Hatakeyama, S. & Nakayama, K. Regulation of the Cell Cycle at the G1–S Transition by Proteolysis of Cyclin E and p27Kip1. *Biochemical and Biophysical Research Communications* **282**, 853-860 (2001).

281. Kitao, H. *et al.* DNA replication stress and cancer chemotherapy. *Cancer Sci* **109**, 264-271 (2018).
282. Ganem, N.J., Godinho, S.A. & Pellman, D. A mechanism linking extra centrosomes to chromosomal instability. *Nature* **460**, 278-82 (2009).
283. Kleylein-Sohn, J. *et al.* Plk4-induced centriole biogenesis in human cells. *Dev Cell* **13**, 190-202 (2007).
284. Pannu, V. *et al.* Centrosome-declustering drugs mediate a two-pronged attack on interphase and mitosis in supercentrosomal cancer cells. *Cell Death Dis* **5**, e1538- (2014).
285. Chavali, P.L. *et al.* A CEP215-HSET complex links centrosomes with spindle poles and drives centrosome clustering in cancer. *Nat Commun* **7**, 11005 (2016).
286. Kawamura, E. *et al.* Identification of novel small molecule inhibitors of centrosome clustering in cancer cells. *Oncotarget* **4**, 1763-76 (2013).
287. Cepeda, D. *et al.* CDK-mediated activation of the SCF(FBXO) (28) ubiquitin ligase promotes MYC-driven transcription and tumourigenesis and predicts poor survival in breast cancer. *EMBO Mol Med* **5**, 999-1018 (2013).
288. Zhang, Q. *et al.* Domain-specific c-Myc ubiquitylation controls c-Myc transcriptional and apoptotic activity. *Proc Natl Acad Sci U S A* **110**, 978-83 (2013).
289. Crum, C.P. *et al.* The distal fallopian tube: a new model for pelvic serous carcinogenesis. *Curr Opin Obstet Gynecol* **19**, 3-9 (2007).
290. Perets, R. *et al.* Transformation of the fallopian tube secretory epithelium leads to high-grade serous ovarian cancer in Brca;Tp53;Pten models. *Cancer Cell* **24**, 751-65 (2013).
291. Bardi, G. *et al.* Cytogenetic comparisons of synchronous carcinomas and polyps in patients with colorectal cancer. *Br J Cancer* **76**, 765-9 (1997).
292. Stoler, D.L. *et al.* The onset and extent of genomic instability in sporadic colorectal tumor progression. *Proc Natl Acad Sci U S A* **96**, 15121-6 (1999).
293. Shih, I.M. *et al.* Evidence that genetic instability occurs at an early stage of colorectal tumorigenesis. *Cancer Res* **61**, 818-22 (2001).
294. Teng, Z., Kuang, X., Wang, J. & Zhang, X. Real-time cell analysis--a new method for dynamic, quantitative measurement of infectious viruses and antiserum neutralizing activity. *J Virol Methods* **193**, 364-70 (2013).
295. Justus, C.R., Leffler, N., Ruiz-Echevarria, M. & Yang, L.V. In vitro Cell Migration and Invasion Assays. *J Vis Exp* (2014).
296. Ponti, D. *et al.* Isolation and in vitro propagation of tumorigenic breast cancer cells with stem/progenitor cell properties. *Cancer Res* **65**, 5506-11 (2005).
297. Ji, X. *et al.* Establishment and evaluation of four different types of patient-derived xenograft models. *Cancer Cell Int* **17**, 122 (2017).
298. Measday, V. *et al.* Systematic yeast synthetic lethal and synthetic dosage lethal screens identify genes required for chromosome segregation. *Proc Natl Acad Sci U S A* **102**, 13956-61 (2005).
299. Sajesh, B.V., Guppy, B.J. & McManus, K.J. Synthetic genetic targeting of genome instability in cancer. *Cancers (Basel)* **5**, 739-61 (2013).
300. Kim, G. *et al.* FDA Approval Summary: Olaparib Monotherapy in Patients with Deleterious Germline BRCA-Mutated Advanced Ovarian Cancer Treated with Three or More Lines of Chemotherapy. *Clin Cancer Res* **21**, 4257-61 (2015).

301. McManus, K.J., Barrett, I.J., Nouhi, Y. & Hieter, P. Specific synthetic lethal killing of RAD54B-deficient human colorectal cancer cells by FEN1 silencing. *Proc Natl Acad Sci U S A* **106**, 3276-81 (2009).
302. Chatr-Aryamontri, A. *et al.* The BioGRID interaction database: 2017 update. *Nucleic Acids Res* **45**, D369-D379 (2017).
303. Sajesh, B.V. & McManus, K.J. Targeting SOD1 induces synthetic lethal killing in BLM- and CHEK2-deficient colorectal cancer cells. *Oncotarget* **6**, 27907-22 (2015).
304. Society, A.C. Cancer Facts & Figures. (2017).
305. Patton, E.E. *et al.* Cdc53 is a scaffold protein for multiple Cdc34/Skp1/F-box proteincomplexes that regulate cell division and methionine biosynthesis in yeast. *Genes Dev* **12**, 692-705 (1998).
306. Stemmann, O., Neidig, A., Kocher, T., Wilm, M. & Lechner, J. Hsp90 enables Ctf13p/Skp1p to nucleate the budding yeast kinetochore. *Proc Natl Acad Sci U S A* **99**, 8585-90 (2002).
307. Gardner, R.D. *et al.* The spindle checkpoint of the yeast Saccharomyces cerevisiae requires kinetochore function and maps to the CBF3 domain. *Genetics* **157**, 1493-502 (2001).
308. DeLillo, N., Romero, C., Lin, H. & Vancura, A. Genetic evidence for a role of phospholipase C at the budding yeast kinetochore. *Mol Genet Genomics* **269**, 261-70 (2003).
309. Yong-Gonzalez, V., Wang, B.D., Butylin, P., Ouspenski, I. & Strunnikov, A. Condensin function at centromere chromatin facilitates proper kinetochore tension and ensures correct mitotic segregation of sister chromatids. *Genes Cells* **12**, 1075-90 (2007).
310. NCBI. National Center for Biotechnology Information - Basic Local Alignment Search Tool. (U.S. National Library of Medicine, 8600 Rockville Pike, Bethesda, MD 20894, 2009).
311. Zaarur, N., Gabai, V.L., Porco, J.A., Jr., Calderwood, S. & Sherman, M.Y. Targeting heat shock response to sensitize cancer cells to proteasome and Hsp90 inhibitors. *Cancer Res* **66**, 1783-91 (2006).
312. McCabe, N. *et al.* Deficiency in the repair of DNA damage by homologous recombination and sensitivity to poly(ADP-ribose) polymerase inhibition. *Cancer Res* **66**, 8109-15 (2006).
313. Guppy, B.J. & McManus, K.J. Synthetic lethal targeting of RNF20 through PARP1 silencing and inhibition. *Cell Oncol (Dordr)* **40**, 281-292 (2017).
314. McAndrew, E.N., Lepage, C.C. & McManus, K.J. The synthetic lethal killing of RAD54B-deficient colorectal cancer cells by PARP1 inhibition is enhanced with SOD1 inhibition. *Oncotarget* **7**, 87417-87430 (2016).
315. Bajrami, I. *et al.* Genome-wide profiling of genetic synthetic lethality identifies CDK12 as a novel determinant of PARP1/2 inhibitor sensitivity. *Cancer Res* **74**, 287-97 (2014).
316. Lord, C.J., McDonald, S., Swift, S., Turner, N.C. & Ashworth, A. A high-throughput RNA interference screen for DNA repair determinants of PARP inhibitor sensitivity. *DNA Repair (Amst)* **7**, 2010-9 (2008).
317. Min, A. *et al.* RAD51C-deficient cancer cells are highly sensitive to the PARP inhibitor olaparib. *Mol Cancer Ther* **12**, 865-77 (2013).
318. Koppensteiner, R. *et al.* Effect of MRE11 loss on PARP-inhibitor sensitivity in endometrial cancer in vitro. *PLoS One* **9**, e100041 (2014).

319. Turner, N.C. *et al.* A synthetic lethal siRNA screen identifying genes mediating sensitivity to a PARP inhibitor. *EMBO J* **27**, 1368-77 (2008).
320. Liu, Y.Q. *et al.* Skp1 in lung cancer: clinical significance and therapeutic efficacy of its small molecule inhibitors. *Oncotarget* **6**, 34953-67 (2015).
321. Sakamoto, K.M. *et al.* Protacs: chimeric molecules that target proteins to the Skp1-Cullin-F box complex for ubiquitination and degradation. *Proc Natl Acad Sci U S A* **98**, 8554-9 (2001).
322. Hines, J., Gough, J.D., Corson, T.W. & Crews, C.M. Posttranslational protein knockdown coupled to receptor tyrosine kinase activation with phosphoPROTACs. *Proc Natl Acad Sci U S A* **110**, 8942-7 (2013).
323. Bondeson, D.P. *et al.* Catalytic in vivo protein knockdown by small-molecule PROTACs. *Nat Chem Biol* **11**, 611-7 (2015).
324. Neklesa, T.K., Winkler, J.D. & Crews, C.M. Targeted protein degradation by PROTACs. *Pharmacol Ther* **174**, 138-144 (2017).
325. McClelland, S.E. Role of chromosomal instability in cancer progression. *Endocr Relat Cancer* **24**, T23-T31 (2017).
326. Thompson, L.L., Jeusset, L.M., Lepage, C.C. & McManus, K.J. Evolving Therapeutic Strategies to Exploit Chromosome Instability in Cancer. *Cancers (Basel)* **9**(2017).
327. Jamal-Hanjani, M. *et al.* Extreme chromosomal instability forecasts improved outcome in ER-negative breast cancer: a prospective validation cohort study from the TACT trial. *Ann Oncol* **26**, 1340-6 (2015).
328. Birkbak, N.J. *et al.* Paradoxical relationship between chromosomal instability and survival outcome in cancer. *Cancer Res* **71**, 3447-52 (2011).
329. Burrell, R.A., McGranahan, N., Bartek, J. & Swanton, C. The causes and consequences of genetic heterogeneity in cancer evolution. *Nature* **501**, 338-45 (2013).
330. Bester, A.C. *et al.* Nucleotide deficiency promotes genomic instability in early stages of cancer development. *Cell* **145**, 435-46 (2011).
331. Manning, A.L. *et al.* Suppression of genome instability in pRB-deficient cells by enhancement of chromosome cohesion. *Mol Cell* **53**, 993-1004 (2014).
332. Orr, B., Talje, L., Liu, Z., Kwok, B.H. & Compton, D.A. Adaptive Resistance to an Inhibitor of Chromosomal Instability in Human Cancer Cells. *Cell Rep* **17**, 1755-1763 (2016).
333. Ertych, N. *et al.* Increased microtubule assembly rates influence chromosomal instability in colorectal cancer cells. *Nature cell biology* **16**, 779-791 (2014).
334. Sansregret, L. *et al.* APC/C Dysfunction Limits Excessive Cancer Chromosomal Instability. *Cancer discovery* **7**, 218-233 (2017).
335. Zasadil, L.M. *et al.* Cytotoxicity of paclitaxel in breast cancer is due to chromosome missegregation on multipolar spindles. *Sci Transl Med* **6**, 229ra43 (2014).
336. Sparano, J.A. Taxanes for breast cancer: an evidence-based review of randomized phase II and phase III trials. *Clin Breast Cancer* **1**, 32-40; discussion 41-2 (2000).
337. Cimini, D., Wan, X., Hirel, C.B. & Salmon, E.D. Aurora kinase promotes turnover of kinetochore microtubules to reduce chromosome segregation errors. *Curr Biol* **16**, 1711-8 (2006).

APPENDIX A: SOLUTIONS

CELL CULTURE

DMEM Complete Cell Culture Media (10% fetal bovine serum [FBS])

Name	Amount
Dulbecco's modified Eagle's medium (HyClone)	450.0 mL
FBS (Sigma-Aldrich)	50.0 mL
Total Volume	500.0 mL

McCoys 5A Complete Cell Culture Media (10% FBS)

Name	Amount
McCoys 5A (HyClone)	450.0 mL
FBS	50.0 mL
Total Volume	500.0 mL

10× PBS (stock solution)

Name	Amount
NaCl	80.0 g
KCl	2.0 g
Na_2HPO_4	14.4 g
KH_2PO_4	2.4 g
Milli-Q Water	up to 1.0 L total volume
Total Volume	1.0 L

- Titrate to pH 7.4

1× PBS

Name	Amount
10× PBS (stock)	100.0 mL
Milli-Q Water	900.0 mL
Total Volume	1.0 L

Cupric Sulfate Pentahydrate

Name	Amount
Cupric Sulfate Pentahydrate	26.0 g
Milli-Q Water	up to 1.0 L
Total Volume	1.0 L

GENE SILENCING

1× siRNA Buffer

Name	Amount
5× siRNA Buffer	100.0 µL
DEPC-treated Water	400.0 µL
Total Volume	500.0 µL

MITOTIC CHROMOSOME SPREADS

Colcemid (working dilution - 100 ng/mL)

Name	Amount
KaryoMAX Colcemid (stock - 10 µg/mL)	10.0 µL
Complete Cell Culture Media	990.0 µL
Total Volume	1.0 mL

1M KCl (stock solution)

Name	Amount
KCl	7.5 g
Milli-Q Water	up to 100.0 mL total volume
Total Volume	100.0 mL

75mM KCl (Hypotonic Solution)

Name	Amount
1M KCl	750 µL
Milli-Q Water	up to 10.0 mL total volume
Total Volume	10.0 mL

3:1 Methanol:Acetic Acid (Fixative)

Name	Amount
Methanol	3.0 mL
Acetic Acid	1.0 mL
Total Volume	4.0 mL

WESTERN BLOT

Modified RIPA Buffer

Name	Amount
50 mM Tris Base - pH 8.0	5.0 mL
150 mM NaCl	7.5 mL
0.1% SDS	500.0 µL
0.5% Sodium Deoxycholate	0.5 g
1% NP40	1.0 mL
Milli-Q Water	up to 100 mL
Total Volume	100.0 mL

- Store at 4°C protected from light

25× Protease Inhibitor

Name	Amount
Protease Inhibitor cOmplete EDTA-free (Roche)	1 tablet
Milli-Q Water	2.0 mL
Total Volume	2.0 mL

- Vortex until dissolved, store at -20°C in 50µL aliquots

Protein Extraction Buffer (RIPA)

Name	Amount
Modified RIPA Buffer	960.0 µL
25× Protease Inhibitor	40.0 µL
Total Volume	1.0 mL

4× Tris-HCl/SDS, pH 6.8 (0.5M Tris-HCl containing 0.4% SDS)

Name	Amount
Tris	6.05 g
SDS	2.0 g
Milli-Q Water	up to 100 mL
Total Volume	100.0 mL

- Titrate to pH 6.8 with 1N HCl
- Mix, store at 4°C

6× SDS Sample Loading Buffer (β-mercaptoethanol)

Name	Amount
4× Tris-HCl/SDS	6.5 mL
Glycerol	3.0 mL
SDS	1.0 g
β-mercaptoethanol	600.0 µL
Bromophenol Blue	1.2 mg
Total Volume	~10.0 mL

- Mix, store 0.5 mL aliquots at -80°C, bring to room temperature before use

10× Running Buffer

Name	Amount
Tris Base	30.0 g
Glycine	144.0 g
SDS	10.0 g
Milli-Q Water	up to 1.0 L
Total Volume	1.0 L

1× Running Buffer

Name	Amount
10× Running Buffer	100.0 mL
Milli-Q Water	900.0 mL
Total Volume	1.0 L

Transfer Buffer

Name	Amount
10× Running Buffer	50.0 mL
Methanol	100.0 mL
Milli-Q Water	350.0 mL
Total Volume	500.0 mL

Copper phthalocyanine 3,4′,4″,4‴-tetrasulfonic acid tetrasodium salt (CPTS)

Name	Amount
CPTS	50.0 mg
HCl	1.0 mL
Milli-Q Water	up to 1.0 L
Total Volume	1.0 L

10× Tris Buffered Saline (TBS)

Name	Amount
NaCl	80.0 g
KCl	2.0 g
1 M Tris - pH 7.5	250.0 mL
Milli-Q Water	up to 1.0L
Total Volume	1.0 L

1× TBS-Tween20 (TBST)

Name	Amount
10× TBS	100.0 mL
Tween-20	1.0 mL
Milli-Q Water	up to 1.0 L
Total Volume	1.0 L

5% Non-fat Milk (w/v) Blocking Solution

Name	Amount
Non-fat Milk Powder (Carnation)	5.0 g
TBST	up to 100.0 mL
Total Volume	100.0 mL

FLUORESCENT LABELLING

8% Paraformaldehyde fixative (w/v)

Name	Amount
Paraformaldehyde (VWR Canlab)	2.4 g
1× PBS	30.0 mL
Total Volume	30.0 mL

- Bring to slight boil with stirring, cool to room temperature prior to use

4% Paraformaldehyde fixative (w/v)

Name	Amount
Paraformaldehyde (VWR Canlab)	0.4 g
1× PBS	10.0 mL
Total Volume	10.0 mL

- Bring to slight boil with stirring, cool to room temperature prior to use

10% BSA

Name	Amount
Bovine Serum Albumin	5.0 g
1× PBS	50.0 mL
Total Volume	50.0 mL

- Mix gently, pass through 0.22µm filter prior to use
- Store at 4°C protected from light

1% BSA

Name	Amount
10% BSA	200.0 µL
1× PBS	1.8 mL
Total Volume	2.0 mL

PBS 0.5% Triton X-100

Name	Amount
Triton X-100	5.0 mL
1× PBS	995.0 mL
Total Volume	1.0 L

PBS 0.1% Triton X-100

Name	Amount
Triton X-100	1.0 mL
1× PBS	999.0 mL
Total Volume	1.0 L

4’,6-Diamidino-2-phenylindole (stock dilution - 50 µg/mL [DAPI])

Name	Amount
DAPI 5 mg/mL stock (Sigma-Aldrich)	10.0 µL
1× PBS	990.0 µL
Total Volume	1.0 mL

- Store at 4°C protected from light

DAPI Mounting Media (working dilution - 0.5 µg/mL)

Name	Amount
DAPI (50 µg/mL)	10.0 µL
Vectashield Mounting Media (Vector Laboratories)	up to 1.0 mL
Total Volume	1.0 mL

- Store at 4°C protected from light

Hoechst 33342 (stock dilution - 1 mg/mL)

Name	Amount
Hoechst 33342 stock (Thermo Scientific)	10.0 mg
1× PBS	up to 10.0 mL
Total Volume	10.0 mL

- Store at -20°C protected from light

Hoechst 33342 (working dilution - 300 ng/mL)

Name	Amount
Hoechst 33342 stock dilution (1 mg/mL)	12.0 µL
1× PBS	up to 40.0 mL
Total Volume	40.0 mL

- Store at 4°C protected from light

Wheat Germ Agglutinin (WGA) Alexa Fluor 488 Conjugate (stock dilution - 1 mg/mL)

Name	Amount
WGA (Life Technologies - Invitrogen)	5.0 mg
1× PBS	5.0 mL
Total Volume	5.0 mL

- Store at -20°C protected from light

Wheat Germ Agglutinin (WGA) Alexa Fluor 488 Conjugate (working dilution - 5 µg/mL)

Name	Amount
1mg/mL WGA stock solution	5.0 µL
1× HBSS	955.0 µL
Total Volume	1.0 mL

5-ethynyl-2'-deoxyuridine (EdU) (stock dilution - 10mM)

Name	Amount
EdU (Component A)	5.0 mg
Dimethylsulfoxide (Component C)	955.0 µL
Total Volume	1.0 mL

- Mix well, store at -20°C

5-ethynyl-2'-deoxyuridine (EdU) (working dilution - 20µM)

Name	Amount
10mM stock EdU	24.0 µL
Complete Cell Culture Media	12.0 mL
Total Volume	12.0 mL

- Warm to 37°C before use

Alexa Fluor Azide

Name	Amount
Alexa Fluor Azide (Component B)	1 vial
Dimethylsulfoxide (Component C)	70.0 µL
Total Volume	70.0 µL

- Store at -20°C

1× Click-iT® EdU Reaction Buffer

Name	Amount
10× Reaction Buffer (Component D)	4.0 mL
Deionized Water	36.0 mL
Total Volume	40.0 mL

- Store at 4°C

10× Click-iT® EdU Buffer Additive

Name	Amount
EdU Buffer Additive (Component F)	400.0 ng
Deionized Water	2.0 mL
Total Volume	2.0 mL

- Store at -20°C

1× Click-iT® EdU Buffer Additive

Name	Amount
10× Click-iT EdU Buffer Additive	50.0 µL
Deionized Water	450.0 µL
Total Volume	500.0 µL

- Store at -20°C

Click-iT® Reaction Cocktail

Name	Amount
1× Click-iT EdU Reaction Buffer	430.0 µL
100mM aqueous $CuSO_4$ (Component E)	20.0 µL
Alexa Fluor Azide	1.2 µL
1× Click-iT EdU Reaction Buffer Additive	50.0 µL
Total Volume	500.0 µL

- Add components in the order listed and use within 15 minutes

DNA DAMAGE-INDUCING COMPOUNDS

Hydroxyurea (stock - 100 mM)

Name	Amount
Hydroxyurea (Sigma-Aldrich)	7.6 mg
Milli-Q Water	1.0 mL
Total Volume	1.0 mL

Hydroxyurea (working dilution - 10 mM)

Name	Amount
Hydroxyurea (100 mM stock)	200.0 µL
Complete Cell Culture Media	1800.0 µL
Total Volume	2.0 mL

Bleomycin (stock - 1 mg/mL)

Name	Amount
Bleomycin (MJS Biolynx)	1.0 mg
Milli-Q Water	1.0 mL
Total Volume	1.0 mL

Bleomycin (working dilution - 0.1 µg/mL)

Name	Amount
Bleomycin (1 mg/mL stock)	0.2 µL
Complete Cell Culture Media	1999.8 µL
Total Volume	2.0 mL